HIGH PRECISION HYPERNUCLEAR SPECTROSCOPY STUDY BY THE (e,e′K$^+$) REACTION

A Dissertation

By

LULIN YUAN

Submitted to the Graduate College of
Hampton University
in partial fulfillment of the requirements
for the degree of

DOCTOR OF PHILOSOPHY

August 2002

This dissertation submitted by Lulin Yuan in partial fulfillment of the requirements for the degree of Doctor of Philosophy at Hampton University, Hampton, Virginia, is hereby approved by the committee under whom the work has been completed.

Liguang Tang, Ph.D.
Chair

Oliver K. Baker, Ph.D.

Cynthia E. Keppel, Ph.D.

Rolf Ent, Ph.D.

Khin Maung Maung, Ph.D.

Donald A. Whitney, Ph.D.
Dean of the Graduate College

Date

ABSTRACT

HIGH PRECISION HYPERNUCLEAR SPECTROSCOPY STUDY BY THE (e,e′K$^+$) REACTION. (August 2002)

Lulin Yuan, B.S., Beijing Normal University;

M.S., Beijing Normal University; Ph.D., Hampton University

Chair of Advisory Committee: Dr. Liguang Tang

Jefferson Lab experiment E89009 is the first experiment to study hypernuclear spectroscopy by (e,e′K$^+$) reaction. The $^{12}_{\Lambda}$B spectrum was observed from carbon target with the best energy resolution ever achieved from direct measurement of hypernuclear spectrum. The comparisons of the $^{12}_{\Lambda}$B spectrum with theoretical predictions were provided in terms of excitation strength and level separations. The overall excitation is in accord with theoretical calculations. The binding energies of p-shell and s-shell Λ states were extracted. The photo-production cross section of the $^{12}_{\Lambda}$B ground state was also extracted. The experiment is also the pioneer in detecting scattered electrons at near zero degrees. The benefit and lessons learned from this method was also discussed.

ACKNOWLEDGMENTS

First, I would like to thank my parents. For these long years of education, they always support me and encourage me. They are caring father and mother yet they give me freedom to pursue the path of life I choose. I know they will share my happiness at this time. The person I owe most to during my years at Hampton and Jefferson Lab is Dr. Liguang Tang, my advisor. I learned a great deal from his knowledge and experience, some time hand-in-hand instructions. His persistence in attacking experimental problems also influenced me. Because of his support, I have had many chances to go to conferences and to participate in experiments at Brookhaven National Lab. These trips helped me to gain a broad view of our research program at JLab. As to this dissertation, I have benefited from his advice on every aspect. I discussed with him about the layout of the skeleton. He has read the drafts of this dissertation several times. Some of his suggestions brought major changes to the dissertation which made it more solid in physics. I should also give special thanks to the other members of my dissertation committee: Keith Baker, Cynthia Keppel, Rolf Ent and Khin Maung, for taking time to read this work and give valuable suggestions. Dr. Keppel read through this whole dissertation meticulously. Her suggestions improved this work both in physics and in language. Thanks to Dr. Baker for his encouragement always. He went through my transparencies with me before the

day of defense. Thanks to Dr. Ent for his cold-witted suggestions and questions. Dr. Maung is an outstanding teacher. I enjoyed sitting in his quantum classes. These classes have been proved very instructional and I also like his light-hearted jokes. I learned a lot from the people who participated in this experiment and made it successful. Thanks to Ed Hungerford and Osamu Hashimoto for their encouragement and suggestions. Thanks to Dave Mack for his help on data analysis during the experiment. I am also grateful to Lipin Gan, Jinhua Liu, Henry Juengst, Toshiyuki Takahashi, Yoshinori Sato, Yu Fujii, for the effort they put on the experiment and the help on the data analysis. And of course, I want to express my thanks to my fellow graduate students on this experiment: Murad Sasour, Toshinobu Miyoshi and Xiaofeng Zhu, for their hard work and long hours they devoted to the experiment and data analysis. I enjoyed working with them and I hope them all good luck in their future careers. I would like to express my thanks to the current and former Hampton University staff, postdocs and students for their help and advice: Ashot Gasparian, Paul Gueye, Michael Christy, Jinseok Cha, Gabriel and Ioana Niculescu, Bitao Hu, Mark Harvey, Windy Hinton, Steven Avery, Alicia Uzzle, Yongguang Liang and Leon Cole. Thanks also to the staff of Physics Department and of GPRC. Thanks to Dr. Donald Whitney for his kind help to students. Finally, I want to express my thanks to the person I hold dearest to my heart, my wife Xiaoyan. Her care and support when I was busy with work and her encouragement when I felt depressed provided invaluable contribution to this work.

TABLE OF CONTENTS

Page

Page

LIST OF TABLES

LIST OF FIGURES

FIGURE Page

CHAPTER 1

PHYSICS INTRODUCTION

1.1 Why Study Hypernuclei

A hypernucleus is formed by replacing one or more of the nucleons in a normal nucleus by a hyperon, such as Λ, Σ or Ξ hyperon. This hyperon is bound to the nuclear core. A hypernucleus is a particle-stable nuclear system. It has a typical lifetime around 200 ps [1], comparable to that of a free Λ hyperon which is 263 ps.

The first observation of a hypernucleus was made by M. Danysz and J. Pniewski in 1952 in a balloon-flown emulsion stack [2]. In this event, a Λ hypernucleus was produced by a cosmic ray interacting with emulsion atom and identified by its decay product. Since then, the case of Λ hypernuclei in which a single Λ is bounded to the nuclear core has been extensively studied [3]. Events have also been found with the formation of $S = -2$ $\Lambda\Lambda$ hypernuclei [4]. For the case of Σ and Ξ hypernuclei, because they are unstable and decay via the strong interaction $\Sigma + N \rightarrow \Lambda + N$ and $\Xi + N \rightarrow \Lambda + \Lambda$ reactions, respectively. Thus they should have very short life time and their bound states have large width. A width less than 5 MeV or so would be remarkable. Experiments suggesting the formation of Σ hypernuclei up to now only yield peak structures with widths of 7-8 MeV [5, 6].

Why should one study the hypernucleus? The answer is while the Λ hyperon contains u and d quarks like other nucleons, it also contains another kind of quark: the

s quark. Therefore, the Λ has a strange number S=-1. A Λ embedded in a nucleus thus introduces a new degree of freedom to the nucleus – strangeness. The Λ is distinguishable from a nucleon. The new degree of freedom means that the Λ is not blocked by the Pauli principle, therefore the hypernucleus offers access to a new many-body spectroscopy, where dynamical symmetries may appear which are forbidden for ordinary nuclei. Theoretical and experimental study of hypernuclei will help us address questions which can not be solved by studying ordinary nuclei, such as properties of hyperon-nucleon interactions, structure changes of the nuclei when a hyperon is bound to the nuclear core and the weak decay of hypernuclei.

1.1.1 Understanding Hyperon-nucleon Interactions

Hyperons and nucleons are baryons. The properties of baryon-baryon interactions are still not understood very well. The study of hyperon-nucleon(YN) interactions will provide us information on the relation of YN and nucleon-nucleon forces and lead us to a unified understanding of baryon-baryon interaction [7].

Several novel features of the Λ-N interaction play a significant role in hypernuclear physics. Because the Λ possesses no isospin (T=0) while the nucleon does (T=1/2), they cannot exchange a single pion (T=1), and there is no dominant one-pion-exchange (OPE) force as exists in the NN interaction. The two-pion-exchange (ΛNN three body) interaction, which is overshadowed by OPE in the NN force in conventional nuclear physics, becomes an important long-range component of the ΛN interaction inside nuclear medium. The absence of a direct ΛN OPE force ensures that shorter range properties of the baryon-baryon interaction are extremely important in Λ-hypernuclei. A

question awaiting answer is whether the short range nuclear forces, such as the repulsive core and the spin orbit force, should be described by a quark-gluon picture rather than the meson exchange picture. In addition, the Λ-Σ mass difference is only 80 MeV, thus the Λ (T=0) and the Σ (T=1) couple more strongly than the N and D in the non-strange sector. This strong coupling leads to a nonnegligible tensor force in the ΛN channel and could be responsible for the glue-like role of the Λ in the nuclear medium which shrinks the nuclear size.

Due to the unavailability of a hyperon beam, the YN scattering data are very limited in scope and accuracy. To extract information about the YN interaction, we have to study the bound hyperon state – the hypernucleus and compare experimental information with theoretical calculations based on models of the baryon-baryon interaction. One such topic that has been intensively investigated through hypernuclei is the ΛN spin-orbit force.

It has been found that the weak coupling model which assumes that the Λ couples weakly to the ground and excited states of the core nucleus is well reproduced by the measured hypernuclear ground and excited level structures [8]. The Hamiltonian for this particle-hole shell model configuration can be expressed as [9, 10]:

$$H = H_N + H_\Lambda + V_{\Lambda N} + V_{\Lambda NN}, \tag{1.1}$$

where $V_{\Lambda N}$ is the $\Lambda - N$ interaction. H_N and H_Λ are the nuclear core and Λ single-particle term, respectively. In the weak-coupling basis, these two terms are diagonal and the energies can be taken from experiment. Generally, the ΛN interaction Hamiltonian

$V_{\Lambda N}$ is often expressed in phenomenological effective interaction by G-matrix method based on free YN interaction:

$$V_{\Lambda N} = V_C + V_\sigma + V_T + V_{LS} + V_{ALS}, \tag{1.2}$$

where the components are central, spin-spin, tensor, spin-orbit (LS) and antisymmetric-LS forces. The different Λ spin orientations with respect to the core nucleus cause a single energy level of the core nucleus to split into doublet levels of the hypernucleus. The spin-orbit splittings predicted by different models vary widely [11].

For the case of p-shell hypernuclei with a Λ in an s orbit, the $p_N s_\Lambda$ interaction can be expressed in terms of five radial integrals V, Δ, S_Λ, S_N and T, assumed to be constant across the p-shell and associated with the average central, spin-spin, Λ spin-orbit, induced nucleon spin-orbit and tensor terms in the potential [7] as:

$$V_{\Lambda N}(r) = V_0(r) + V_\sigma(r)\vec{s}_N \cdot \vec{s}_\Lambda + V_\Lambda(r)\vec{l}_{N\Lambda} \cdot \vec{s}_\Lambda + V_N(r)\vec{l}_{N\Lambda} \cdot \vec{s}_N + V_T(r)S_{12}, \tag{1.3}$$

where $\vec{l}_{N\Lambda}$ is the relative orbital angular momentum and

$$S_{12} = 3(\sigma_N \cdot \hat{r})(\sigma_\Lambda \cdot \hat{r}) - \sigma_N \cdot \sigma_\Lambda$$

with $\vec{r} = |\vec{r}_N - \vec{r}_\Lambda|$. The r-dependent coefficients $V_\alpha(r)$ of the terms above can be simulated by a number of Gaussian functions with different ranges [12]:

$$V_\alpha(r) = \sum_i (a_i + b_i k_F + c_i k_F^2) \exp[-(r/\beta_i)^2].$$

Here α denote different components and k_F is the Fermi momentum.

The "standard interaction" of Millener et al. [13, 10] based on Nijmegen Model D one boson exchange model [14] has:

$$\Delta = 0.50, S_\Lambda = -0.04, S_N = -0.47, T = 0.04.$$

Doublet splittings are determined mainly by Δ, S_Λ and T. The energy separations of spin-doublet states can be calculated base on these parameters and compared with experimental data. One example is the ${}^{7}_{\Lambda}$Li spin doublet states $\frac{3}{2}^+$ and $\frac{1}{2}^+$ formed by s_Λ coupled with ^{6}Li core 1^+ state. Their energy separation is $1.444\Delta + 0.054S_\Lambda + 0.016S_N - 0.271T = 712$ keV. It is quite close to the measured separation of 692 ± 2 keV from KEK experiment E419. However, these parameters fail to explain the small energy separation of ${}^{9}_{\Lambda}$Be spin doublet states $\frac{5}{2}^+$ and $\frac{3}{2}^+$ ($s_\Lambda \otimes {}^{8}\mathrm{Be}(2^+)$). The energy separation calculated from these parameters is 121 keV, while the measured seperation is 31.4 ± 3 keV from BNL experiment E930. These Comparisons will further constaint the interaction parameters and help to improve the theoretical ΛN potentials which are not well constrained so far. Figure 1.1 shows the strengths of different components of the ΛN interaction matrix elements according to various Nijmegen models.

For the p-shell Λ case, the energy separation of ${}^{13}_{\Lambda}$C spin doublet states $\frac{1}{2}^-$ and $\frac{3}{2}^-$ ($p_\Lambda \otimes {}^{12}\mathrm{C}(0^+)$ was measured to be 154 ± 54 keV from BNL E929 experiment, while different versions of Nijmegen soft-core model NSC97a–f give 0.67–1.09 MeV with the LS only, and they become 0.39–0.78 MeV with the antisymmetric (ALS) components. (Figure 1.1). The small splitting suggests possible direction of fine tuning of the potential

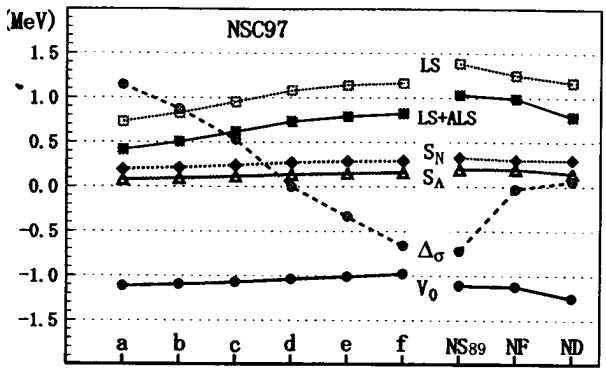

Figure 1.1: Strengths of different components in the spin-orbit splitting of p-state Λ according to various Nijmegen models ([11]). See text for definitions of the notations.

models.

1.1.2 Probing Interior Structure of Nuclei

As mentioned before, the Λ is distinguishable from nucleons, so a bound Λ is not blocked by the Pauli principle and thus can drop deep inside a nucleus. This provides us a way to investigate the interior structure of nuclei which can not be accessed by excitation of normal nuclei. In an ordinary nucleus, deeply bound nucleon-hole states are very broad, because they will decay by emitting nucleons. For a hypernucleus, an embedded Λ can bring down the energy of the nuclear system and deeply bound Λ states can be particle-stable and form narrow level structures.

Well defined series of such single-particle states have been identified in hypernuclei up to A= 208 through (K^-, π^-) and (π^+,K^+) reactions at BNL and KEK-PS [15]. They provide a textbook example of single particle structure in nuclei. The binding energies B_Λ up to the g shell have been extracted as shown in Figure 1.2 [16]. The data were used to extract information on the Λ-nucleus potential well depth, geometrical shape and effective mass, which characterize the Λ-nucleus potential. The solid curves correspond

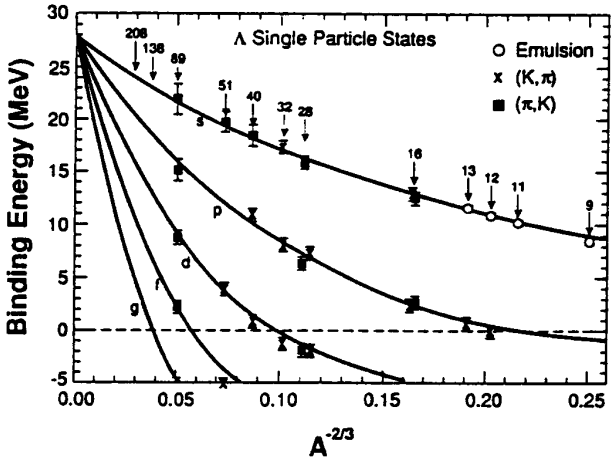

Figure 1.2: A dependence of the binding energies of Λ single particle states. The solid line curves are fittings to the data according to a phenomenological Λ potential based on a spherical Skyrme-Hartree-Fock approach ([7]).

to a phenomenological Λ potential based on a spherical Skyrme-Hartree-Fock approach and fit to the data. As a unique feature of hypernuclei, Λ binding energies vary smoothly as a function of nuclear mass A. The absence of shell structure of nucleon single particle states reveals the distinguishable particle nature of Λ inside nuclei.

The presence of a Λ in a hypernucleus can introduce new dynamical symmetries which are forbidden for ordinary nuclei by the Pauli exclusion principle. The Λ can act as an "impurity" in a nucleus. It can cause drastic change in the nuclear structure, such as changes in size and shape, cluster structure, change of collective motion, etc. Three examples I will mention here are Λ induced parity-mixing inter-shell coupling, supersymmetric (or genuinely hypernuclear) states revealed by the ${}^{9}_{\Lambda}$Be spectrum and the shrinkage of ${}^{7}_{\Lambda}$Li nuclear size by a Λ. The ${}^{12}_{\Lambda}$C binding energy spectrum obtained by the (π^+,K$^+$) reaction from KEK experiment E369 shows three small peaks (#2,#3 and #4) in addition to the two prominent peaks: the 1^- ground state (#1) and the 2^+ p_Λ

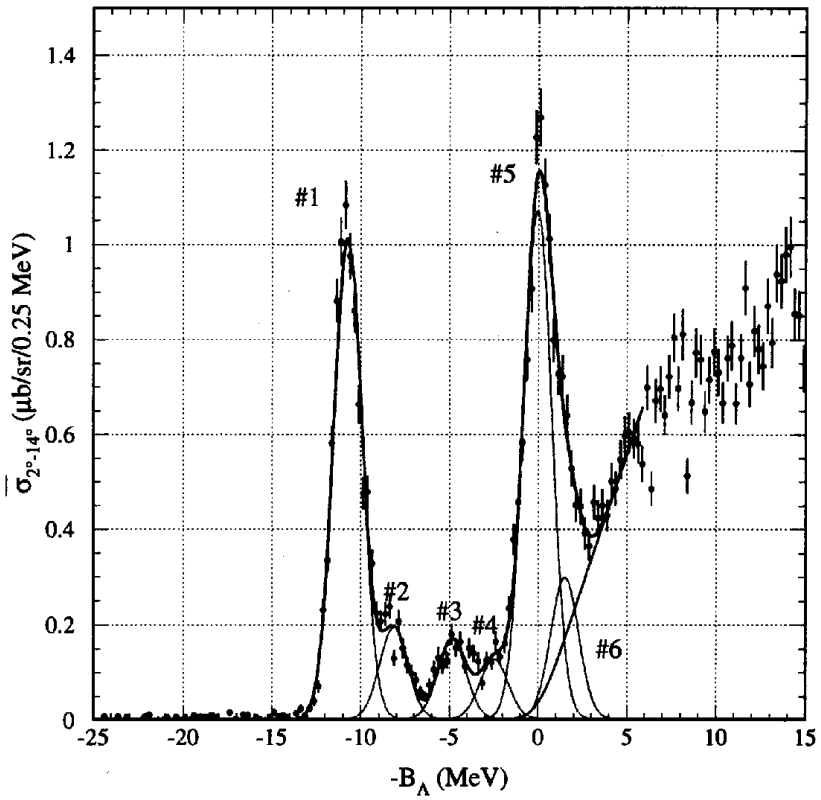

Figure 1.3: $^{12}_{\Lambda}$C binding energy spectrum obtained by the (π^+,K$^+$) reaction from KEK E369 (dots with error bars). The solid curve is a fit to the data by six Gaussian peaks and a quasi-free component. The energy resolution is $\sim$1.85 MeV [17].

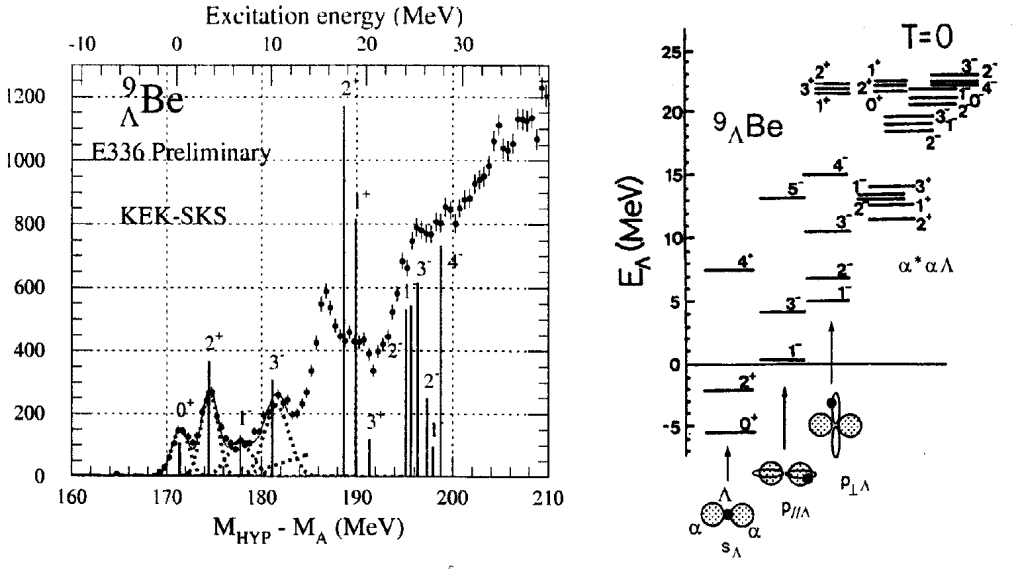

Figure 1.4: Left: ${}^{9}_{\Lambda}$Be spectrum by (π^+,K$^+$) reaction from KEK E336. The y-axis is counts/0.5 MeV. Right: cluster model prediction of ${}^{9}_{\Lambda}$Be energy levels. Same energy levels are marked in the left figure but also indicate relative strength.

states at $E_x = 11$ MeV (#5) (Figure 1.3) [17]. These three peaks are explained as core excited states, in which a s-shell Λ coupled with excited states of ^{11}C core. The peaks #2 and #3 are assigned as the $1^-[^{11}\mathrm{C}(1/2^-)\otimes s_\Lambda]$ and $1^-[^{11}\mathrm{C}(3/2^-)\otimes s_\Lambda]$. However, the position and strength of speak#4 can not be explained by the p-shell core-s_Λ coupling. A configuration called parity-mixing inter-shell coupling was proposed to interpret this peak [18]. It was assigned 2^+ having a ^{11}C $5/2^+[s^4p^6(sd)^1]\otimes s_\Lambda$ configuration but with a mixture of $[(p_{3/2})_n^{-1}\otimes p_\Lambda]$ component. Such coupling mediated by Λ particle, is a unique feature of hypernuclei. Study of ${}^{9}_{\Lambda}$Be structure has revealed the existence of supersymmetric states. ${}^{9}_{\Lambda}$Be is treated as two α and a Λ by the cluster model [19]. The configuration where a p_Λ orbit is parallel to the axis of the two α clusters has a larger overlap between the Λ and αs than the other p_Λ configurations thus has lower energies (Figure 1.4). But these states can't exist in ordinary nuclei because they are forbidden

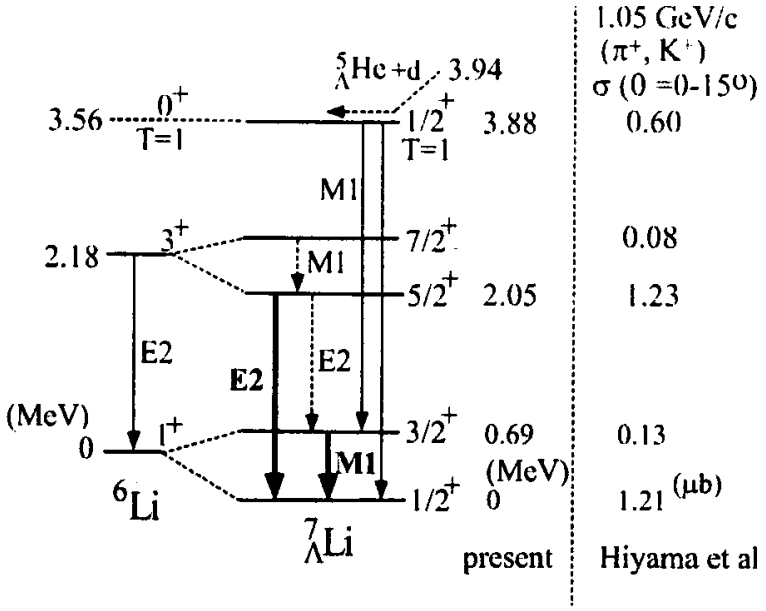

Figure 1.5: Energy Levels and γ transitions of ${}^{7}_{\Lambda}$Li. The thick arrows indicate the γ transitions measured in KEK E419. The numbers show the energy levels calculated from γ-ray energy. numbers in the right of the dot line shows the calculated cross sections [21].

by the Pauli principle. They have been observed in the ${}^{9}_{\Lambda}$Be spectrum by the (π^+,K$^+$) reaction in KEK E336 [20].

Another remarkable example of the unique feature of hypernucleus is the size shrinkage of ${}^{7}_{\Lambda}$Li nuclear size by embedding a Λ in a nucleus [22, 23]. ${}^{7}_{\Lambda}$Li can be treated as $\alpha + d + \Lambda$ in cluster model (Figure 1.5). The γ-ray transition probability B(E2) of the $5/2^+ \rightarrow 1/2^+$ E2 transition is measured by (π^+,K$^+\gamma$) coincidence experiment KEK E419 with Hyperball. It is much smaller than the corresponding $3^+ \rightarrow 1^+$ B(E2) transition in the core nuclei. This is interpreted as the contraction of inter-cluster distance of ${}^{7}_{\Lambda}$Li by 19% compared with ^{6}Li. In this case, a s-shell Λ is acting as "glue" to shrink a loosely bound nucleus due to the attractive Λ-N force.

1.1.3 Medium Effect of Baryon Interaction

At the hadron level, Λ is distinguishable from other nucleons. At quark level, the u and d quark in the Λ must be antisymmetrized with non-strange quarks in other nucleons. The quark-gluon degree of freedom should have observable effects on the hypernuclear structure, such as repulsive shift in binding energies, decrease in decay widths of hypernuclear particle-hole states of the type $s_\Lambda \otimes s_N^{-1}$, isospin mixing in hypernuclear wave function. The explicit quark effect maybe shadowed in many-body system by the effective density dependent ΛN interaction. In heavy nuclei and when the Λ drop deeply into the s-shell which can be favorably produced by (e,e'K^+) reactions, this quark presence may be more evident. Also the detailed study of density and spin dependence of ΛN interaction in nuclear medium, and the comparison with the NN case, remains a interesting topic.

1.1.4 Weak Decay of Hypernuclei

A free Λ decays via the mesonic decay mode:

$$\Lambda \rightarrow p + \pi^-, \tag{1.4}$$

$$\Lambda \rightarrow n + \pi^0. \tag{1.5}$$

When a Λ is embedded in a nuclear, this mesonic decay mode is Pauli blocked, since the recoil nucleon has a momentum $\leq$ 100 MeV/c, below the typical Fermi Momentum of

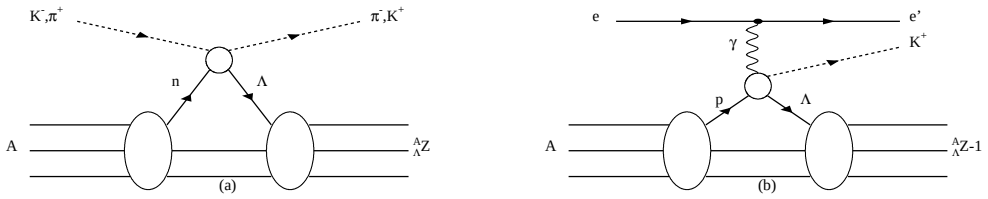

(a) Hadronic production (b) Electroproduction

Figure 1.6: Hypernuclear production mechanisms.

nuclei (≈ 270 MeV/c) except the lightest ones. So the nucleon-catalyzed mode:

$$\Lambda + p \rightarrow n + p \quad \text{or} \quad \Lambda + n \rightarrow n + n$$

dominates in all but the lightest nuclei. Nonmesonic decay with $\Delta S = 1$. It contains rich information about baryon-baryon weak interaction since both parity-conserving and parity-violating partial rates can be measured, while in weak NN interaction, the PC signal is masked by the strong interaction. Two key questions are: (1) Does the $\Delta I = 1/2$ rule, which applies to kaon and hyperon decay, also hold on the nomesonic decay? and (2) What is the ratio of nn to np decays, which deviate strongly from theoretical expectation?

1.2 Overview of Hypernuclear Experiments

1.2.1 Hypernuclear Production Mechanisms

Hypernuclei can be produced by the strangeness exchange (K^-,π^-) and associated production (π^+,K^+) or (γ, K^+), (e,e'K^+) reactions (Figure 1.6). In (K^-,π^-) and

(π^+,K$^+$) reactions, a neutron in the target nucleus ${}^{A}Z$ is converted into a Λ. This Λ is coupled to the nuclear core to form a hypernucleus ${}^{A}_{\Lambda}Z$. The reactions can be expressed as:

$$K^- + n \rightarrow \pi^- + \Lambda, \tag{1.6}$$

$$\pi^+ + n \rightarrow K^+ + \Lambda. \tag{1.7}$$

Photoproduction of hypernucleus convert a Proton in a nucleus ${}^{A}Z$ to Λ, which can be expressed as:

$$\gamma + p \rightarrow \Lambda + K^+$$

and forms a hypernucleus ${}^{A}_{\Lambda}(Z-1)$.

Hypernuclear production cross section depends mainly on the momentum transfer to the Λ, the nature of the elementary amplitudes, and the target and hypernuclear wave functions. They are also affected by distorted waves of the mesons (K and π) involved in the process.

The elementary process cross section of the strangeness exchange reaction of (K$^-$,π^-) is about 4 mb/sr near $p_K = 800$ MeV/c at forward angle after Fermi-averaging over the nucleons [7]. It is one order of magnitude larger than the strangeness production (π^+,K$^+$) reaction which has a maximum cross section of about 280 μb/sr at $p_\pi = 1.05$ GeV/c. The photoproduction process has a much smaller cross section of about 0.3 μb/sr, two order of magnitude less than (π^+,K$^+$) [24]. But this drop in the elementary

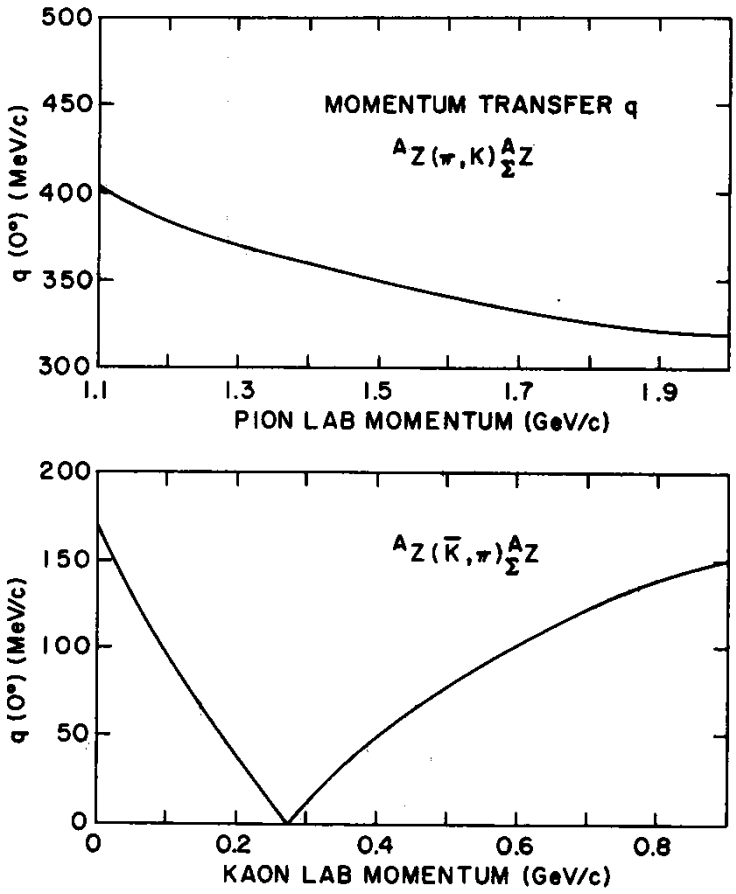

Figure 1.7: Momentum transfer $q(0°)$ as a function of meson lab momentum for the (π^+,K^+) and (K^-,π^-) reactions on heavy nuclear targets.

amplitude can be partly compensated by the high intensity and high quality electron beam, especially in CEBAF.

Another factor that shapes the hypernuclear production rate is the momentum transfer q to the Λ. Nuclear form factor drops off sharply with increasing momentum transfer, if q exceeds the peak value (around 250 MeV/c for Carbon) [25]. The (K^-,π^-) process is exoergic, while the (π^+,K^+) and (γ,K^+) reactions are both endoergic. The π^+ lab momentum has a threshold value of 0.89 GeV/c to induce (π^+,K^+) process. As shown in Figure 1.7, the typical momentum transfer for (K^-,π^-) process is 100–150

MeV/c, while it is about 400 MeV/c for (π^+,K^+) reaction at 0 degree.

With the sizable momentum transfer in the (π^+,K^+) process, it will favorably excite high-spin stretched configuration of hypernucleus with maximum aligned angular momentum: $J = L_{max} = l_n + l_\Lambda$ for the $0^+ \rightarrow J^\pi[(lj)_n^{-1}(lj)^\Lambda]$ transition. For the (K^-,π^-) reaction, due to the recoilless or low momentum transfer, the configuration of $\Delta L \leq 1$ and $\Delta S = 0$ is especially favored.

Photoproduction (γ,K^+) also features large momentum transfer comparable to (π^+,K^+) reaction. The threshold photon energy for ^{12}C(γ,K^+) at 0 degree is 687 MeV/c. The typical momentum transfer for (γ,K^+) reaction at forward angle has a value of 250–400 MeV/c. So high-spin states is favored. However, unlike the psudeoscalar mesons π and K, γ carries spin, the spin-flip amplitude will dominate in the (γ,K^+) process. These two factors – high spin states and spin-flip – constitutes the unique feature of photoproduction: excitation of high spin unnatural parity state. The highest spin state in hypernucleus is favored: $J = J_{max} = l_p + l_\Lambda + 1$. Before going into the detail of photoproduction which is the subject of this thesis, I will first review the current status of hypernuclear experiments with hadron beam.

1.2.2 Current Status of Hypernuclear Experiments

The first series of (π^+,K^+) experiments were proposed and carried out at BNL AGS [26, 27]. After that, extensive experiments have also been performed at KEK PS using the Superconducting Kaon Spectrometer (SKS) [20, 22, 28, 29], which has a large solid angle (100 msr maximum) and good resolution (0.1%). Hypernuclear excited states including deeply bound states have been identified up to a target mass ^{208}Pb. The excita-

tion spectra of hypernuclei revealed the unique features of hypernuclear structure because Λ is a distinguishable particle from other nucleons. The best missing mass resolution obtained before the present experiment was 1.45 MeV (FWHM) for the ^{12}C(π^+,K$^+$)$^{12}_{\Lambda}$C reaction from KEK E336 using the SKS spectrometer system.

Resolving hypernuclear spin-orbit splitting is the key to understand spin-dependent ΛN force. To improve the resolution, (π^+,K$^+\gamma$) and (K$^-$,$\pi^-\gamma$) coincidence experiments have been carried out at KEK and BNL to tag the hypernuclear γ decays. Using "Hyperball", a large-acceptance Ge detector array, high resolution of 3–4 keV for γ energy was achieved. The measurements of energy splittings of the spin-doublet states helped to constraint ΛN interaction parameters and suggested possible ways to improve the existing ΛN potential models.

Despite considerable progress in this field, the status is far from satisfactory. The spin-dependent part of the ΛN potential is still unclear and the experiments give contradictory results. The BNL $^{13}_{\Lambda}$C and $^{9}_{\Lambda}$Be γ-ray measurements suggested a very small spin-orbit splitting thus a small spin-orbit force. On the other hand, reanalysis of $^{16}_{\Lambda}$O gives a p-shell Λ spin-orbit splitting of 0.3-0.6 MeV [18]. The $^{89}_{\Lambda}Y$ spectrum also suggested a 1.7 MeV splitting for f-shell Λ [17]. Direct measurement of spin-orbit splitting by (π^+,K$^+$) and (K$^-$,π^-) reaction is hampered by poor resolution. Although γ-ray measurement has high resolution, it is limited to particle stable states. For heavy hypernuclei, other decay channels like particle emission will prevail other than γ decay. And the observed γ-transitions are difficult to interpret for heavy nuclei. Furthermore, the hadronic reactions (π^+,K$^+$) and (K$^-$,π^-) also have their intrinsic shortcomings. They both convert n in a nucleus to Λ, thus only produce isospin $T > 0$ hypernuclei.

The Charge Symmetry Breaking (CSB) effect cannot be studied by these reactions. Both π and K^- are strong absorptive inside nucleus, so deeply bound particle-hole state has a small cross section, this along with the poor resolution makes it difficult to search for explicit quark effect in a nuclear medium.

With the advent of CEBAF high intensity, high quality electron beam, high resolution hypernuclear electroproduction experiments become possible.

1.3 Electroproduction of Hypernuclei

As mentioned before, the virtual photon γ^* from electron scattering carries spin, so the (e,e'K^+) reaction will preferentially excites spin-flip unnatural parity states with $J = J_{max} = l_n + l_\Lambda + 1$ in hypernuclei. These states are suppressed in (K^-,π^-) and (π^+,K^+) reactions.

In contrast to the purely hadronic processes, in photoproduction target nuclei are essentially transparent to the incident photons and the distortion of K^+ is also modest, so deeply bound particle-hole states can be formed and Λ can drop deep inside nuclei for heavy nuclei. The (e,e'K^+) reaction acts on proton rather than neutron, so for zero isospin $T = 0$ nuclei, it will excite neutron rich $T > 0$ mirror hypernucleus to (K^-,π^-) and (π^+,K^+) reactions. Observation of high resolution heavy hypernuclear level structures and comparison with their mirror hypernuclei will definitely further our understanding of nuclear structure and the Charge Symmetry Breaking effect. Quantitative search of quark-gluon presence in nuclei will also be possible.

Furthermore, (e,e'K^+) reaction uses the high energy stability ($< 10^{-4}$) and low emittance primary beam, so the beam energy uncertainty is small. The high beam

intensity allow us to use thin target thus target energy straggling is minimized. Combined with carefully designed spectrometers, we can get much improved resolution (up to 300 keV FWHM) which may allow us to directly observe the spin-orbit splittings for high orbital states. Another advantage of using thin target is large varieties of rare isotopes can be assembled as target.

Therefore, hypernuclear electroproduction taking advantage of the high energy resolution and high beam intensity can study a complete series of hypernuclear states in a single spectrum including bound and unbound states rather than several particle stable states investigated by γ-ray experiments, and with better resolution than hadronic reactions using secondary beams. The electroproduction excitation strength can be measured. Because the mechanism of electro-weak interaction is well know, the measured strength will provide valuable information on nuclear structure and nuclear forces. Electronproduction also provides us a way to produce hypernuclear systems and states which are difficult to access by conventional hadronic reactions.

This dissertation will talk about Jefferson Lab experiment E89009. As the world's first high-resolution hypernuclear electroproduction experiment, E89009 demonstrated the feasibility of high precision hypernuclear spectroscopic study by (e,e'K^+) reaction and tested our experimental technique.

1.4 Experimental Considerations for the First Hypernuclear Electron Production Experiment

Carbon target run which produces ${}^{12}_{\Lambda}$B by ^{12}C(e,e'K^+)${}^{12}_{\Lambda}$B is the benchmark of hypernuclear experiments. Observation of high resolution level structure of ${}^{12}_{\Lambda}$B is a test

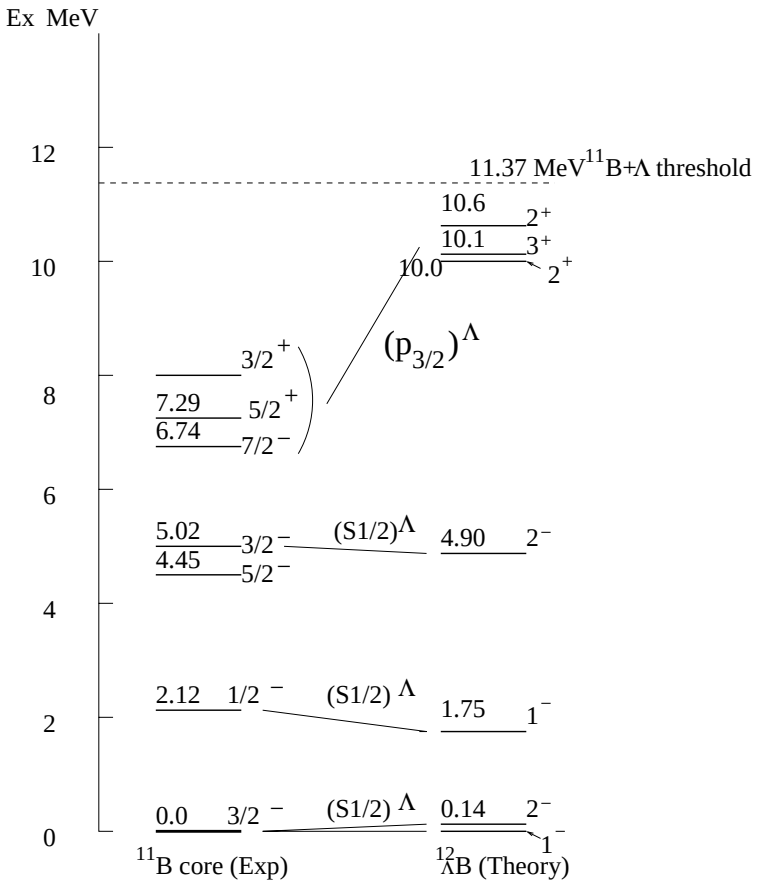

Figure 1.8: Theoretical shell model predictions of ${}^{12}_{\Lambda}$B energy levels. Only bound states are shown.

Table 1.1: Target materials prepared for E89009. ^{7}Li,^{12}C and CH_2 are actually used within them in the experiment.

Target	Thickness (mg/cm^2)	X_0 (g/cm^2)
^{7}Li	19.0	80.52
^{9}Be	9.25	64.54
^{12}C	22.0	42.67
^{28}Si	5.2	21.92
CH_2	9.2	47.9

of the experimental system. Figure 1.8 shows the level diagram of $^{12}_{\Lambda}$Be and the ^{11}Be core [24]. The unnatural parity states have the most strength within the same $\hbar\omega$ group: 2^- in GS and 3^+ in the substitute states. These unnatural parity states have never been observed by other experiments before. Small peaks may also be seen formed by s_Λ coupled to core excited states with possible configuration mixing. Of physics interest is the position and strength of these states compared with its mirror $^{12}_{\Lambda}$C and energy separation of the p_Λ spin-orbit doublet 2^+ and 3^+, formed by $(p_{1/2})_\Lambda$ or $(p_{3/2})_\Lambda$ coupled to a $(p_{3/2})_p^{-1}$ ^{11}B core. Several other targets are also prepared as shown in Table 1.1. The hypernuclear systems: $^{7}_{\Lambda}$He, $^{9}_{\Lambda}$Li and $^{28}_{\Lambda}$Al that can be produced by the (e,e'K$^+$) reaction will also reveal interesting physics.

To achieve the physics goals of this experiment, we need to maximize hypernuclear yield (keep in mind the much lower electroproduction cross section compared to hadron beam), suppress background noise and improve energy resolution. Hypernuclear yield for a specific reaction depends mainly on the momentum transfer to the nucleus and the nature of the elementary amplitudes.

The elementary process for strangeness electroproduction is : $\gamma + p \rightarrow K^+ + \Lambda$. We first consider photoproduction.

The total cross section for the elementary process rises with photon energy from the threshold at 911 MeV to a broad maximum near 1.5 GeV [30].

For the (γ,K$^+$) reaction on nuclear target, by a plane wave approximation, the essential dependence of cross section on momentum transfer q is contained in a factor $F^2(q)$ [25]. The peak value of $F^2(q)$ occurs for

$$q^2 = \frac{2\Delta L}{b^2} \approx 2\Delta L A^{-1/3},$$

where b is the harmonic oscillator parameter. For the $p \rightarrow p$ transitions in carbon, the above equation gives a q value of 340 MeV. The cross section decreases sharply with increasing q after the peak value. As mentioned in the last part, photoproduction also features a large momentum transfer of several hundred MeV. Because of the sizable momentum transfer, the probability of forming hypernuclear bound states by the (γ,K$^+$) reaction is rather small. Summing over all hypernuclear states f, including both bound and continuum Λ, we have

$$\sum_f (\frac{d\sigma}{d\Omega_K})^{0^\circ}_f = Z(\frac{d\sigma}{d\Omega_K})^{0^\circ}_{\gamma p \rightarrow K^+\Lambda} \tag{1.8}$$

in plane wave approximation. We can define the "sticking probability" [31] by restricting the sum to bound states b as:

$$P = \frac{Z_{eff}}{Z} = \sum_b (\frac{d\sigma}{d\Omega_K})^{0^\circ}_b \Big/ \sum_f (\frac{d\sigma}{d\Omega_K})^{0^\circ}_f . \tag{1.9}$$

For the reaction $^{12}C(\gamma, K^+)^{12}_\Lambda$B, the estimated P is from 0.06 to 0.13 for photon energy

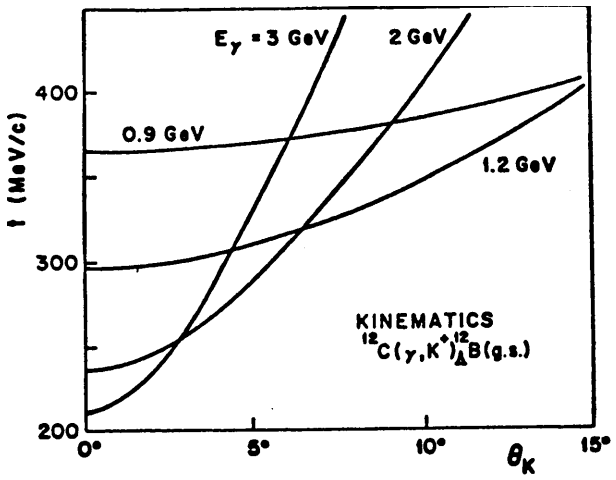

Figure 1.9: The momentum transfer $q = |\mathbf{p}_\gamma - \mathbf{p}_K|$ in the lab system as a function of kaon angle θ_K, for several photon energies E_γ.

1.2 GeV to 2.0 GeV. Thus most of the (γ, K^+) cross section on nuclear targets will correspond to quasi-free Λ production.

For a hypernucleus of mass $M_{HY} = M_A + \omega$, where $\omega = m_\Lambda - m_p + B_p - B_\Lambda$, the momentum transfer can be calculated by iterating

$$p_K^2 = [E_\gamma - (\omega + T_R)]^2 - m_K^2 \tag{1.10}$$

$$q^2 = p_K^2 + p_\gamma^2 - 2p_K p_\gamma \cos(\theta_K), \tag{1.11}$$

starting with $T_R = q^2/2M_{HY}$ initially. Figure 1.9 shows q as a function of kaon angle θ_K for several photon energies between 1.2 and 2.5 GeV. We can see that with a reasonable Kaon solid angle acceptance, $\theta_K < 6^\circ$ and $E_\gamma = 1.5$ GeV is a good selection. Although q at 0° drops with increasing photon energy, the reasonable range for θ_K becomes narrower and the elementary cross section will drop too. Photon energy also

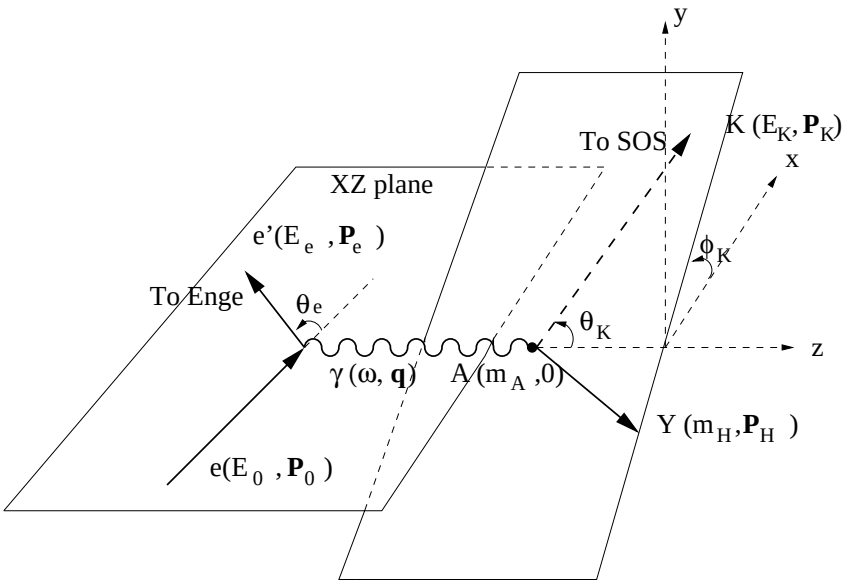

Figure 1.10: A(e,e′K$^+$)Y kinematic variables. The numbers in the brackets are the four-momentum of the particles.

need to be keep below the threshold for kaon production from resonance states to reduce background kaon rate.

Now let us turn to electroproduction, the kinematics variables of (e,e′K$^+$) are shown in Figure 1.10. The triple differential cross section for the elementary electroproduction can be written as [32]

$$\frac{d^6\sigma}{d\Omega d\omega d\Omega_k dE_k} = \Gamma(p_0,\omega,\theta)\{\epsilon\frac{d^3\sigma_L}{d\Omega_k dE_k} + \frac{d^3\sigma_T}{d\Omega_k dE_k} - \cos(\phi_k)\epsilon_{TL}\frac{d^3\sigma_{TL}}{d\Omega_k dE_k} - \cos(2\phi_k)\epsilon_{TT}\frac{d^3\sigma_{TT}}{d\Omega_k dE_k}\}, \quad (1.12)$$

where Γ is the virtual photon flux factor in the lab frame. It measures the number of virtual photons per unit photon energy, per unit electron solid angle and per incident

electron. It has the form

$$\Gamma = \frac{\alpha}{2\pi^2 Q^2} \frac{\omega}{1-\epsilon} \frac{E_e}{E_0}. \tag{1.13}$$

The polarization factor ϵ is

$$\epsilon = [1 + (2\frac{q^2}{Q^2} \tan^2 \frac{\theta}{2}]^{-1}.$$

At exactly 0°, this factor has a form as:

$$\Gamma = \frac{\alpha}{2\pi^2} \frac{1}{\omega} \frac{E_e^2}{m^2}.$$

Notice that Γ has an extremely forward peaking shape of distribution. To maximum our virtual photon acceptance, we will detect 0° scattering electrons.To increase hypernuclear yield, kaons also need to be detected in as forward angle as possible (see Figure 1.11). The Hall C kaon spectrometer SOS (Short Orbit Spectrometer) has a minimum forward angle of 12.5°. To separate forward angle electrons from kaons, a dipole magnet called splitter is used right after the target to bend electrons and kaons in opposite direction to their respective spectrometers.

One drawback for detecting 0° scattering electrons is the electron spectrometer will accept most of the bremsstrahlung electrons, because bremsstrahlung electrons have a even narrower angle distribution around 0° than virtual photons. This causes very high background rate at the electron spectrometer. To keep the e' rate below the limit the detectors can handle and have a reasonable signal to accidental ratio, beam luminosity

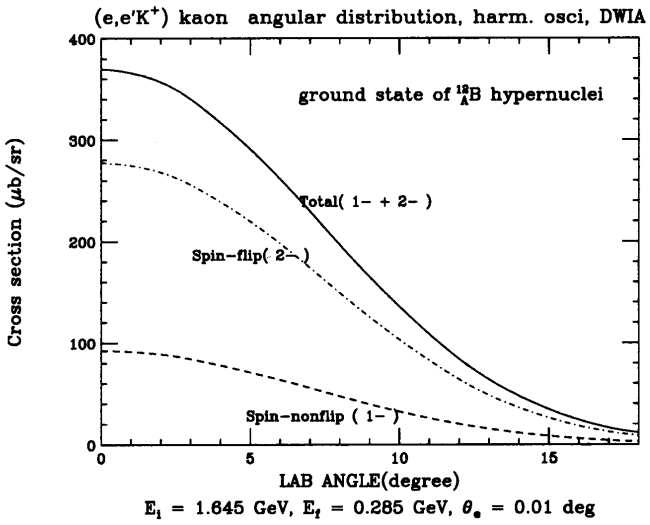

Figure 1.11: The angle distribution of $^{12}_{\Lambda}$B ground state by (e,e$'$K$^+$) reaction calculated by DWIA with the harmonic oscillator potential [33].

has to be lowered. This in turn restricts hypernuclear yield. A more practical selection seems to be detecting electrons at as small angle as possible but avoid 0°. However, a 0° experiment as a extreme case will provide valuable information about spectrometer design and data handling under high rate. So the present experiment chose to tag at 0°.

Tagging 0° electrons also simplifies the design of electron arm spectrometer and detectors. The concentration of e$'$ flux at 0° along with the focusing property of the electron spectrometer allow the determination of e$'$ momentum with good resolution by electron focal plane 1-D position in bending direction. Otherwise, a full tracking of the e$'$ at focal plane will be difficult at high rate.

Due to the limited momentum resolution of the kaon spectrometer (0.6–1.0 MeV) in the present experiment, it contributes the main part to the overall hypernuclear spectroscopic energy resolution. New experiment has been planned to improve it by replacing

the present kaon spectrometer [33].

In summary, the goal of JLab E89009, as the first hypernuclear spectroscopy experiment via electroproduction, is (1) to examine and test the feasibility of using electromagnetic probe and the associated technique and (2) to measure the first spectrum that is dominated by spin-flip structures with a resolution < 1 MeV. ^{12}C was chosen to be the primary target. The experimental design was optimized to achieve this goal. A a new experimental configuration – detecting 0° scattered electrons – was used in this experiment. Detectors were designed to run in this situation (high rate) and their performance was tested. Through the experiment, we can evaluate the advantage and disadvantage of this technique. The knowledge is especially useful in future small angle experiments.

CHAPTER 2

EXPERIMENTAL APPARATUS

2.1 Overview

Jefferson Lab experiment E89009, spectroscopic study of hypernuclei produced by the (e,e′K$^+$) reaction , took place at Jefferson Lab Hall C from February 2000 to May 2000. The CEBAF electron linac delivered 100% duty cycle continuous wave (CW) electron beam to three experimental halls: Hall A, B and C. Three beam energies were used during the experiment: 1.953 GeV for commissioning, 1.864 GeV and 1.721 GeV for production runs. The carbon target was the primary production target. There were also limited data from the ^{7}Li target. The aluminized Mylar and CH_2 targets were used for momentum calibration but the Mylar yield was too low due to smaller H content. Hypernuclear Spectrometer System (HNSS) was used to detect the reaction particles. It consisted of a dipole magnet ("splitter"), an Enge split-pole spectrometer (ESPS) and the Hall C Short Orbit Spectrometer (SOS). The near zero degree scattering electrons were tagged by ESPS. The forward angle (2–4 degrees) scattering positive kaons were detected and momentum analyzed by SOS. The splitter was used to separate the e′ and K$^+$ oppositely into the ESPS and SOS spectrometers.

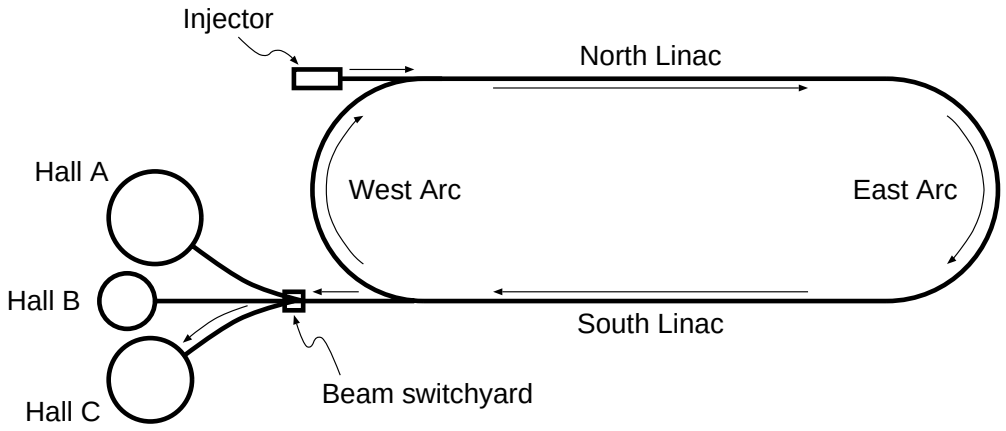

Figure 2.1: Schematic top view of CEBAF beamline and experimental halls.

2.2 CEBAF Accelerator

CEBAF is an electron linear accelerator, capable of accelarating electrons up to 5.5 GeV using superconducting RF technology (Figure 2.1). The accelerator uses a state-of-the-art photocathode gun system. It is capable of delivering beams of high polarization and high current to Hall A and Hall C, while maintaining high polarization low current beam delivery to Hall B. However, only unpolarized beam was used in experiment E89009. In the injector, an RF chopping system operating at 499 MHz is used to develop a 3-beam 1497 MHz bunch train at 100 KeV. The beam is longitudinally compressed in the bunching section to provide 2 picosecond bunches, which are then accelerated to just over 1% of the total machine energy in the injector section. The beam polarization, optics and energy are verified in the injector matching region prior to injection into the main machine.

The beam from the injector is accelerated through a unique recirculating beamline

with two linear accelerators – the north and south linac – and joined by two 180° arcs with a radius of 80 meters – the east and west arcs. Twenty cryomodules, each containing eight superconducting niobium cavities, line the two linear accelerators. Liquid helium, produced at the Lab's Central Helium Liquefier (CHL), keeps the accelerating cavities superconducting at a temperature of 2 Kelvin. Quadrupole and dipole magnets in the tunnel steer and focus the beam as it passes through each arc. The injector first sends beam to the north linac. The electron beam is accelerated by an identical energy at the north and south linac by the cavities. After gaining 400 MeV at the north linac under "standard" mode, it is steered to the south linac by the east arc, then gains another 400 MeV at the south linac. At this point, it can be directed into experimental halls or be recirculated into the linacs by the west arc for additional passes of acceleration. The electron beam gains 800 MeV from every pass up to 5 passes.

The beams of different passes go through the same linac. Because every pass has different energy, different fields are required in the steering magnets of the arcs to steer the beams. Thus there are separate arcs for every pass. They are recombined before being sent into the linac.

Beam is directed into a hall's transport channel using magnetic or RF extraction at the beam switch yard (BSY). The 499 MHz RF modules kick out every third bunch of the 1497 MHz bunch train to every hall. This produces a beam structure of 2 ps length bunches in every 2 ns. The accelerator can deliver the first four passes to one hall only. The fifth pass can be sent to all three halls.

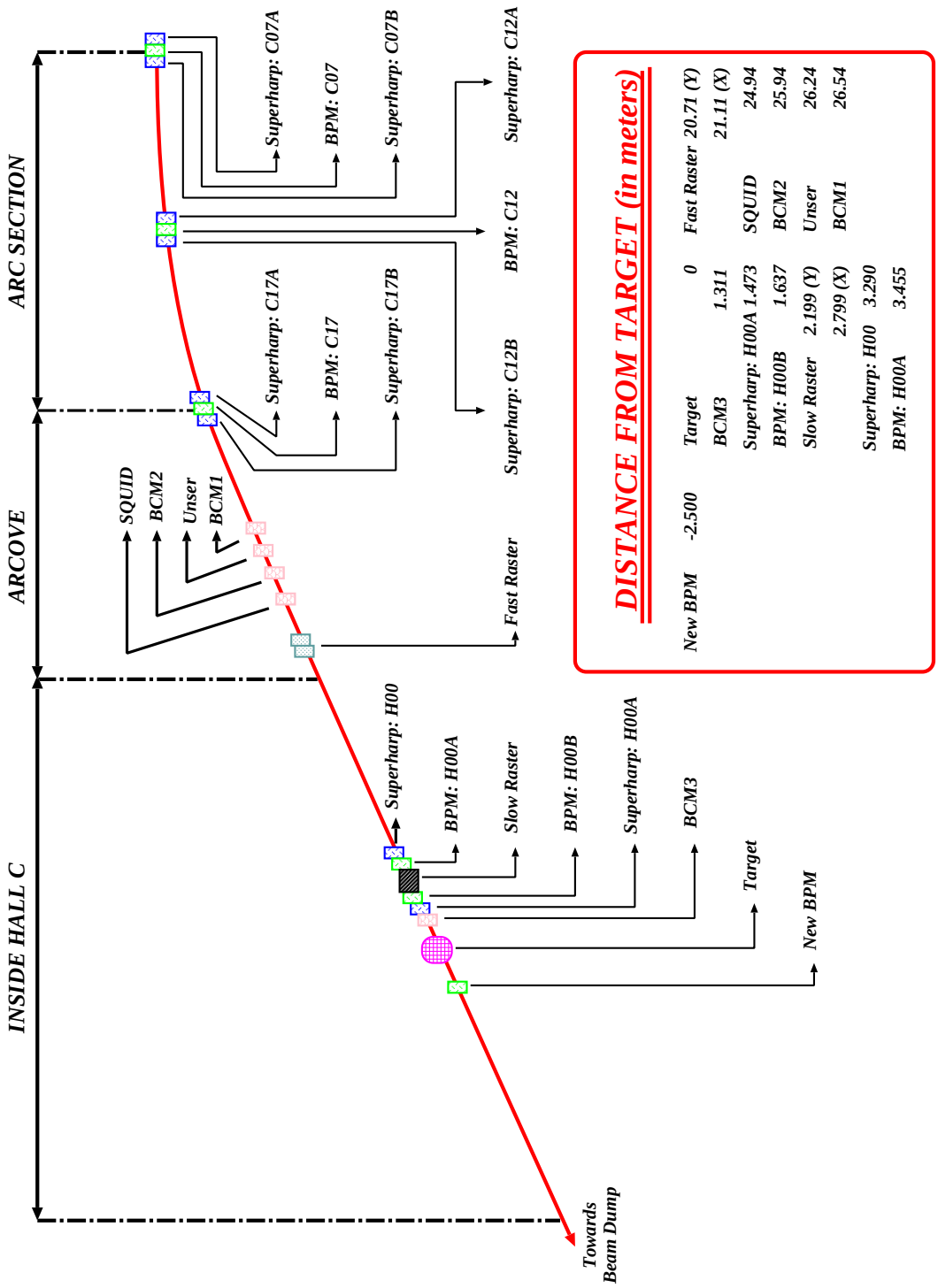

Figure 2.2: Hall C beamline [34]. The positions of various BPMs, BCMs and harps are shown. The target is located normally in the Hall C pivot, while in the HNSS experiment, it was shifted upstream from the Hall C pivot.

2.3 Hall C Arc and Beamline Instruments

After the beam is split from the accelerator BSY into Hall C, it is transported to the experiment target through the Hall C Arc and beamline. The Hall C Arc is composed of a series of dipole and quadruple magnets to steer and focus the beam onto the target along with beam diagnostic devices to measure the beam positions, beam profile, beam current and beam energy (Figure 2.2).

Several harps and superharps are located in different portions of the Hall C Arc and beamline for beam profile measurements and absolute beam position calibration [35]. The superharp consists of a wooden fork holding a 22 μm tungsten wire segmented in three sections: two in the vertical direction and one in the horizontal direction. This fork can be inserted in and out of the beam pipe, causing an interaction between the wires and the electron beam. An Analog to Digital Converter collects the charges induced in the wire and reads in the encoder positions of the fork ladder as they pass through the beam. Three signals are produced for each scan, two from the vertical wires to determine the horizontal position and one from the horizontal wire to determine the vertical position of the beam. The position is measured with an accuracy of about $\pm$50 μm for each direction. Because the beam-wire interaction spreads the beam, this is a destructive method which can not be operated coincident to data taking. A superharp scan is conducted between run periods to calibrate the absolute positions of other less destructive beam position monitors (BPMs), which are also used to measure the beam energy in Hall C.

There are a series of BPMs throughout the Hall C beamline which can measure

the beam positions simultaneously with data taking [36]. The BPM is a cavity with four antennae rotated 45° from the horizontal and vertical direction. Two antennae are located on each side of the beam in both directions. When beam passes through the cavity, the amplitudes of the induced signals in the antennae are proportional to the distance between the beam and antennae. The relative positions to the cavity center are calculated by the gravity center of the signals. The absolute positions are obtained by calibration with superharp measurements to find the offsets of the cavity center to the ideal beam trajectory. The accuracy for relative beam position with constant beam current is ~ 0.1mm while the final accuracy for absolute position is about 1.0 mm.

Three BPMs situated at the start, middle and end point of the Hall C Arc beside superharps can be used for beam energy measurements [37]. Three BPMs (IPMH00A, IPMH00B, IPMH00C) measure beam positions before the target in both vertical and horizontal directions. These measurements are used to determine the beam position and direction at the target. They are monitored throughout an experiment.

To ensure the kinematic resolution of this experiment, the energy of beam electrons must be known to $\delta E/E \leq 1.0 \times 10^{-4}$ (FWHM). This requires a relative beam energy stability less than 10^{-4} and an energy spread $\leq 10^{-4}$. The accelerator can provide beam of this resolution with the energy feedback system. This system used the real-time data from BPMs placed along the accelerator and Hall C arc with an optical matrix to extract beam energy deviations. The last accelerator cavity was adjusted by this feedback. The lock system included fast feedback and slow feedback energy and position lock with different length of feedback cycles to correct the slow and fast energy drift.

The beam position and spot size also affect the kinematic resolution. A 1 mm offset in the target in the SOS bending direction (vertical) will cause about 10^{-3} momentum shift in the Kaon spectrometer. The offset in the horizontal direction is not so crucial but also has some effect. We required the beam spot size to be horizontal $\delta x \leq 120$ μm, $\delta y \leq 60$ μm. The stability of beam position on target was required $\delta x \leq 250$ μm, $\delta y \leq 60$ μm (all in FWHM).

The accelerator energy feedback system assumed a constant field over beamline magnets. Thus, during the experiment, we also monitored change of integral BdL of beamline magnets.

Hall C current was measured by three sets of Beam Current Monitors (BCMs) continuously during the data taking in the Hall C beamline [38]. Two sets, BCM1 and BCM2, use cylindrical RF resonance cavities. Harmonic EM waves are excited in the cavity. Antennae in the cavities pick up the power of the EM wave which is converted to frequencies. The relative current can be calculated from the output frequencies.

To calibrate gains and offsets of BCM1 and BCM2, we have another kind of BCM, a parametric current transformer (Unser monitor), which has very good gain stability and can measure absolute current. It can be used to calibrate the other two BPMs. However, the Unser monitor has low S/N ratio and has unacceptable error below a beam current of 2 μA, which was the beam current range of E89009. Thus we didn't use the Unser monitor for calibration. Instead, the beam was collected in an accelerator Faraday Cup and the charge was compared with the Hall C BCM measurements to obtain the gains and offsets. The systemic error for this procedure was $\sim 5\%$.

Since E89009 used a splitter magnet after the target, pass-through electrons from

the target were deflected by the field of the magnet, heading away from the Hall C standard beam dump. Therefore, four correction magnets were installed on the exit beamline to ensure the pass-through beam to be directed to a temporary local beam dump in the hall. The straight through bremsstrahlung photons were aimed to the regular Hall C dump.

2.4 Hall C Beam Energy Measurement

Table 2.1: Parameters of the Hall C Arc spectrometer.

Parameter	Figure
Overall length of spectrometer	46 m
Nominal beam deflection angle	34.3°
Length of matching section	27 m
Object/Image distance	45.38 m
Momentum range	0.8 - 6 GeV/c
Momentum acceptance	10^{-3}
Momentum dispersion	13.6 cm/%
Momentum resolving power (RP)	6.8×10^{5}
Horizontal angular acceptance	$\pm$ 0.1 mr
Vertical angular acceptance	$\pm$ 0.1 mr
Beam current range	1 - 30 μA
Beam operating mode	Pulsed and CW

The Hall C Arc has a set of magnets to bend beam from the linac to Hall C. When it is running in dispersive mode, all the 8 dipole magnets are powered by the same power supply in a string and the quadruple and sextuple are set at zero field. The Hall C Arc acts like a dipole spectrometer in this case. Using the beam position information from the three groups of superharps at the entrance, mid-point and exit of the Arc, the beam energy can be calculated from an optical code relating position to energy (momentum). Another way is to use the three BPMs, C07 at entrance, C12 at mid-point and C17 at

end of Arc, to calculate the beam bending radius.

If P_0 and $R_0 = 40.09$ m are the nominal beam energy and radius in the Arc, respectively, the X-axis is along the direction from the center of the Arc to the position of BPM C12, $(x_{i0}, y_{i0}), i = 1, 2, 3$ are the nominal positions of the beam trajectory at BPMs C7, C12 and C17, B is the dipole field and assumed to be constant, we have the relations:

$$P_0 = eBR_0, \quad P = eBR. \tag{2.1}$$

$$\text{thus,} \qquad \delta P/P_0 = \delta R/R_0. \tag{2.2}$$

We can calculate δR by fitting a circle through the three beam positions dx_1, dx_2, dx_3 from C07, C12 and C17. The center of the new circle (x_c, y_c) will satisfy

$$(x_{i0} + dx_i - x_c)^2 + (y_{i0} - y_c)^2 = (R_0 + \delta R)^2 \quad \text{where i=1,2,3.} \tag{2.3}$$

Ignoring the second order of δR and dx_i and using $(x_{i0})^2 + (y_{i0})^2 = R_0^2$, we have:

$$\frac{\delta R}{R_0} + \frac{x_{i0}}{R_0}(\frac{x_c}{R_0}) + \frac{y_{i0}}{R_0}(\frac{y_c}{R_0}) = \frac{x_{i0}dx_i}{R_0^2} \qquad \text{i=1,2,3.} \tag{2.4}$$

This is a group of three linear equations with three unknowns: $\frac{\delta R}{R_0}$, $\frac{x_c}{R_0}$ and $\frac{y_c}{R_0}$. It can be solved directly. Because the BPMs can be operated continuously with the data taking, this method provided a way to monitor the beam energy shift in an event-by-event basis. Figure 2.3 shows the beam energy offsets calculated by this method. One can see that,

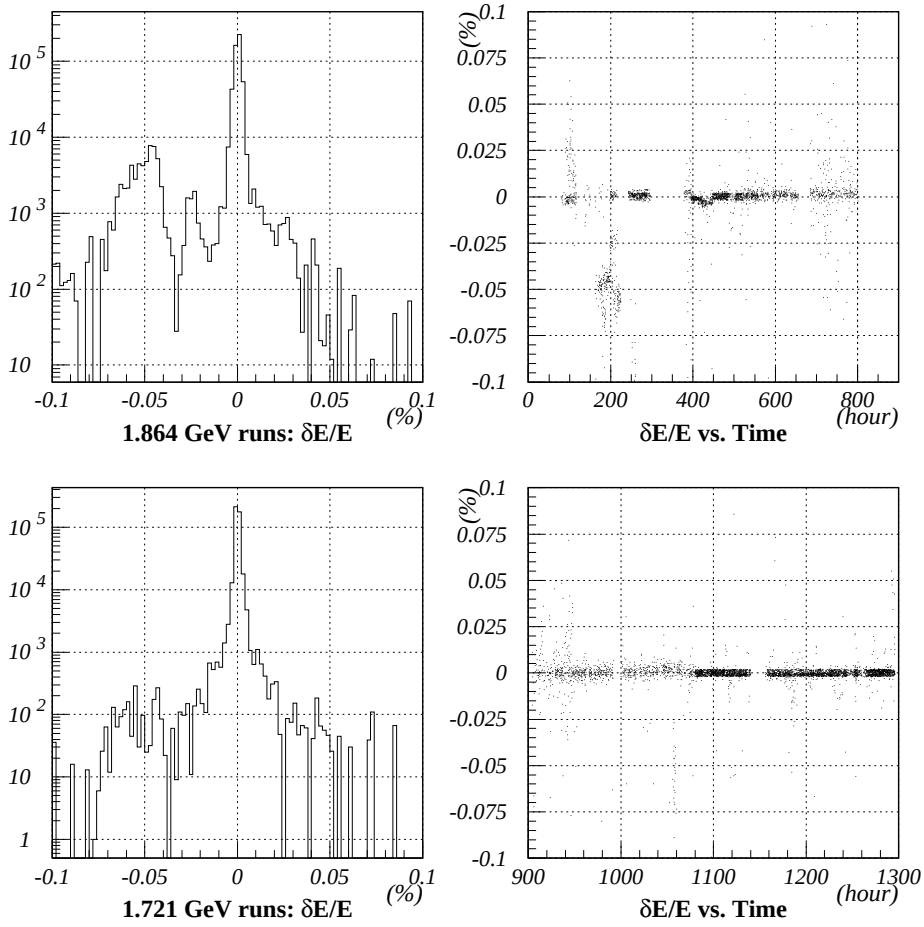

Figure 2.3: Beam energy spreading in $\delta E/E\%$. The horizontal axis is the time from the beginning of the experiment. The Y-axis is in logarithm scale for the 1-D histograms. The gaps in the 2-D graphs are due to the beam down time between run periods. Notice that the outlying points may possibly due to dis-functioning of BPMs and not beam energy drift.

except for some very short period, for most of the events, the beam energy was well within 10^{-4} of the nominal value. This means that the accelerator energy feedback worked effectively.

During the experiment, we also used the known masses of the Λ and Σ^0 from the $H(e,e'K^+)\Lambda(\Sigma^0)$ reaction on CH_2 target to calibrate the beam energies and spectrometer central momenta. Such special calibration runs were taken throughout the experiment.

2.5 Beam Rastering

The CEBAF electron beam is a high intensity CW beam with small transverse size. To prevent damage to the target and avoid local boiling effects in cryogenic targets, the beam is spread out by two rastering systems [39]. The fast raster system, 25 meters upstream from the target, is designed to spread beam on the target. The slow raster system located before the target is used to prevent damage to the beam dump. In E89009, we only used low current beam (≤ 2 μA), so the slow raster was not used.

The fast raster system has two sets of steering magnets to spread the beam in the horizontal and vertical directions. The driving current of the magnets is sinusoidally. To achieve a more uniform illumination within the beam spot, current frequencies in the two directions are not multipliers of each other so that a stable pattern will not be formed at the target. The sweeping frequencies are 16.7 kHz in the vertical direction and 23 kHz in the horizontal direction.

During E89009, in order to achieve high missing mass resolution, no rastering was used on the carbon target. This was possible because only low beam current ($< 0.6\mu$A) was used. Whereas for the CH_2 target, a 2.2 mm width $\times$ 1.1 mm height raster pattern

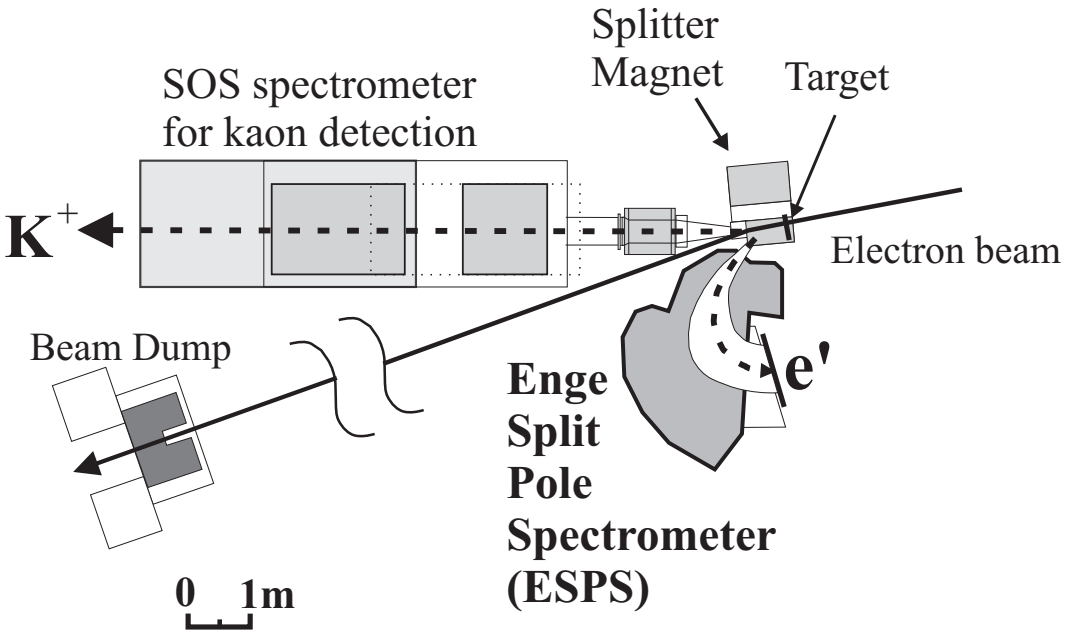

Figure 2.4: Schematic top view of HNSS beam line and magnets.

was used to spread the beam and avoid melting the target.

2.6 HNSS Spectrometer

The HNSS was a two arm spectrometer system that measured the e′ and K^+ in coincidence. It had a fixed geometric configuration shown in Figure 2.4. The splitter bent K^+ to SOS (enlarging the angle from 2° to 16°) for momentum and angular analysis, while the 0° scattered e′ was deflected to ESPS (from 0° to 33°). The whole system was under vacuum all the way to the exit windows of the spectrometers of both arms, including the beam line. It was so designed to minimize the multiple scattering effect to the overall energy resolution.

2.6.1 0° Electron Tagging

By tagging the near 0° scattered electrons, the produced photons in the electromagnetic interaction were nearly real because the square of 4-momentum transfer was almost zero ($Q^2 = p_0 p_e \sin(\theta) \approx 0$ at $\theta \approx 0$). The purpose of using this method was to maximize the virtual photon acceptance which is heighest at small scattering angles. Although the HNSS electron arm had a moderate solid angle acceptance of about 10 msr in average, it could accept about 35% of all the virtual photon flux over the momentum acceptance. To maximize hypernuclear yield, kaons were also detected at extremely forward angles. The HNSS kaon arm covered an angular range of in-plane -1.8° to 1.8° and out-of-plane 0° to 4.6° (Figure 2.5). However, the center cone around 0° was also the density peak of the (e, e^+) pairs created by electron bremsstrahlung and pair production in the target. We measured high bremsstrahlung electron rate in the e′ arm.

For a target of radiation length t, the flux of pair production is given by [32]:

$$\phi_{pair}(\omega) = \phi_{brems}(\omega)\sigma_{pair} X_0 t, \tag{2.5}$$

where ϕ_{brems} is the bremsstrahlung rate from the target and σ_{pair} is the pair production cross section. Since energy loss in the target was dominated by bremsstrahlung followed by pair production [40], and we have the pair production cross section: $\sigma_{pair} \sim \frac{7}{9}\frac{1}{X_0}$, or $\sigma_{pair} X_0 \sim 7/9 \sim 1$, the flux can be written as:

$$\phi_{pair}(\omega) = \phi_{brems} t. \tag{2.6}$$

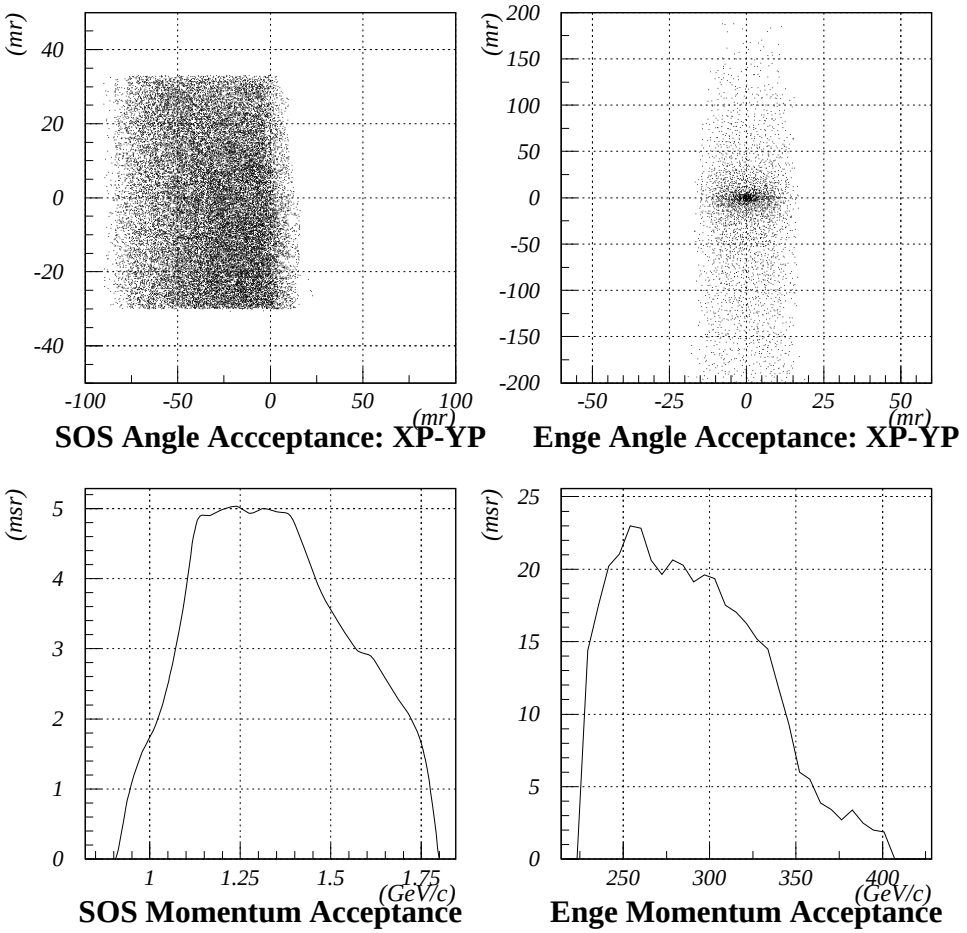

Figure 2.5: HNSS angle and momentum acceptance. The top two panels are scatter plots of SOS and ESPS angle acceptance, both in target coordinate system. Particles were bent in the X-direction in ESPS, so acceptance was large in the X-direction but narrower in the Y-direction. Bottom panels show the SOS and ESPS solid angle acceptance as a function of particle momentum.

Since $t \ll 1$ in our experiment, the flux of pair-produced electrons was a negligible background compared with the rate of bremsstrahlung electrons in the electron spectrometer. However, the pair-produced positrons were enormous compared with the kaon rate in the kaon arm.

The e$'$ single rate was dominated by the bremsstrahlung process. Assuming a recoilless target nuclei, the bremsstrahlung e$'$ angle distribution can be calculated from the photon momentum and angle distribution by the following kinematic relations [41]:

$$\frac{d\sigma_b}{d\Omega dk} = \frac{2\alpha^3}{\pi k}\frac{E^2}{m^4}\{[\frac{2y-2}{(1+l)^2} + \frac{12l(1-y)}{(1+l)^4}]G_2(\infty) + [\frac{2-2y+y^2}{(1+l)^2} - \frac{4l(1-y)}{(1+l)^4}] \cdot [X - 2Z^2 f((\alpha Z)^2)]\}. \quad (2.7)$$

where $G_2(\infty) = Z^2 + Z$, $y = k/E$ and $l = \theta_k^2 E^2/m^2$. k is photon momentum and E is the beam energy. The meaning of other parameters in the formula can be found in [41]. The angle spread due to multiple scattering can be calculated from Equation (23.9) of [41]. It was 0.7 mr (σ) for a carbon target with thickness of 22 mg/cm^2.

Using the formula above, we have calculated both the virtual photon and bremsstrahlung electron's integrated acceptance ratio plotted in Figure 2.6. Almost all of the electrons from bremsstrahlung within Enge momentum acceptance were accepted by the HNSS electron arm. This caused a very high e$'$ rate at the ESPS focal plane: 130 MHz at beam current $0.66\mu A$, dominated by the bremsstrahlung electrons. All these events contributed to the accidental background of the real (e,e$'$K$^+$) process. Thus, as the price for increasing virtual photon acceptance by tagging the 0° electrons, we got overall lower signal to accidental ratio S/A, around 0.3 for 0.66 μA beam current for the carbon target

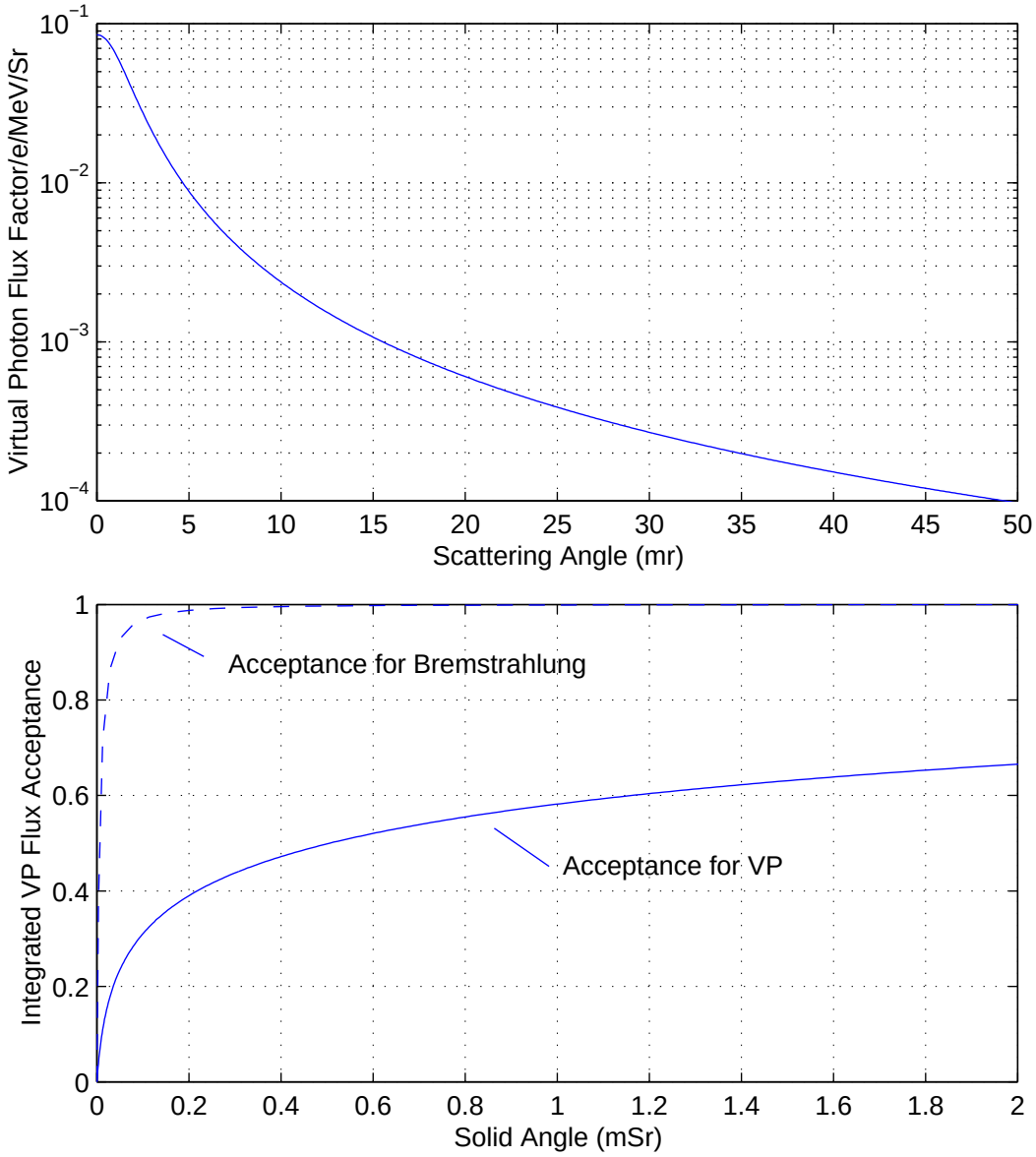

Figure 2.6: The top panel shows the virtual photon flux factor as a function of e′ scattering angle. The bottom panel depicts the integrated acceptance ratio for bremsstrahlung and virtual photo production processes. This assums a circular entrance collimator, p_0=1864 MeV/c and p_e = 306.06 MeV/c.

runs.

The e′ rate distribution over the ESPS focal plane can be estimated by a Monte-Carlo method. The total bremsstrahlung photon rate in photon energy $d\omega$ after an electron has passed through a target of dT radiation length is:

$$d\phi_{brems} d\omega dT \sim \frac{1}{\omega} d\omega dT = 3.25 \times 10^9 I[\mu A] \frac{dp_e}{p_0 - p_e}. \tag{2.8}$$

We have used $dT = 5.2 \times 10^{-4}$ for the carbon target. The bremsstrahlung electron were generated at the target randomly according to the momentum distribution in Equation 2.8. Their corresponding coordinates at the spectrometer focal plane were calculated by a spectrometer simulation program called Raytrace which takes into account the spectrometer acceptance and optical properties. Only events which can pass through the whole spectrometer will appear in the final output. The number of events from Monte-Carlo simulation, scaled up according to the beam current, gave the bremsstrahlung electron rate. At a beam current I=0.62 μA, Figure 2.7 shows the e′ rate distribution at the ESPS focal plane. The total bremsstrahlung electron rate was $\sim$ 126 MHz by this calculation.

2.6.2 Kinematics Settings

Table 2.2 shows the kinematic settings of HNSS. The beam energies of 1.864 GeV and 1.721 GeV were used for the production runs. 1.645 GeV was the nominal beam energy in the original design. The kinematics points were selected so that the virtual photon energies from electron scattering were around 1.5 GeV, the optimal energy for

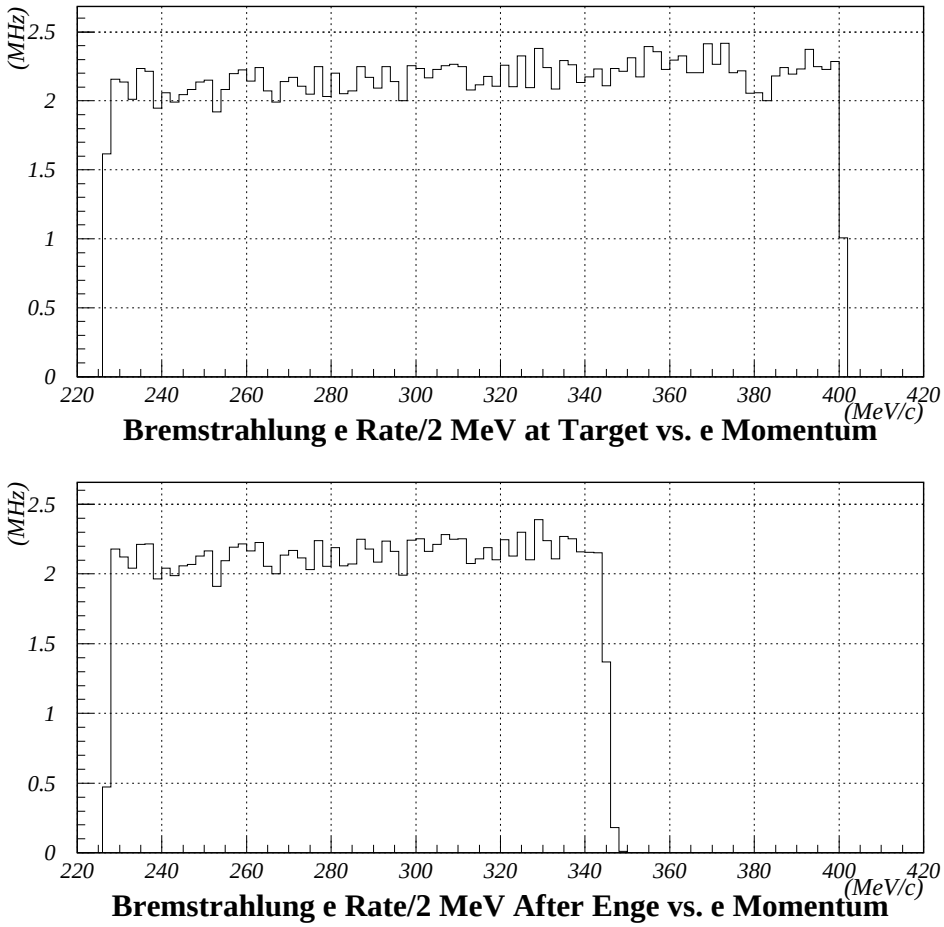

Figure 2.7: Top panel shows the bremsstrahlung e$'$ momentum distribution. It is generated by Equation 2.7. Bottom panel shows the e$'$ momentum distribution at ESPS focal plane after it was cut by the ESPS acceptance. The integration of bottom histogram gives the total bremsstrahlung e$'$ rate at focal plane: 126 MHz. It is very close to experimental measurement of $\sim$ 130 MHz at 0.62 μA for carbon target runs.

Beam (GeV)	SOS P_0 (GeV/c)	P_e Range (MeV/c)	Field Scaling Factor	Run Mode
1.645	1.055	228.47 - 338.14	1	nominal setting
1.953	1.313979	284.55 -421.14	1.245478	commissioning
1.864	1.239800	268.49 - 397.37	1.175166	production, CH2 calibration
1.721	1.119519	242.44 - 358.82	1.061156	production, CH2 calibration

Table 2.2: HNSS momentum and field settings.

hypernuclear production. Another constraint of our kinematic settings arose from the fact that the kaon arm and electron arm shared the same splitter. When beam energy change, the magnets fields of kaon arm, electron arm and splitter has to be scaled by the same factor to keep both arms having the same optics.

According to the three body A(e,e′K)H_Y kinematics, we have:

$$\mathbf{P}_0 = \mathbf{P}_e + \mathbf{P}_K + \mathbf{P}_H \tag{2.9}$$

$$E_0 + m_A = E_e + E_K + E_H. \tag{2.10}$$

The meanings of the notations are shown in Figure 1.10. We have

$$m_H^2 + m_K^2 - m_A^2 + 2(-p_K \cos\theta_K + E_K - m_A)(p_0 - p_e) + 2E_K m_A = 0, \tag{2.11}$$

where $\theta_K = 1.85^\circ$ is the lab angle of kaon arm central w.r.t. the incoming beam direction.

When the beam energy need to be scaled up from the nominal 1.645 GeV to 1.864 GeV, the scale factor is $s_b = 1.1331$, assuming HNSS kinematics setting need to be scaled

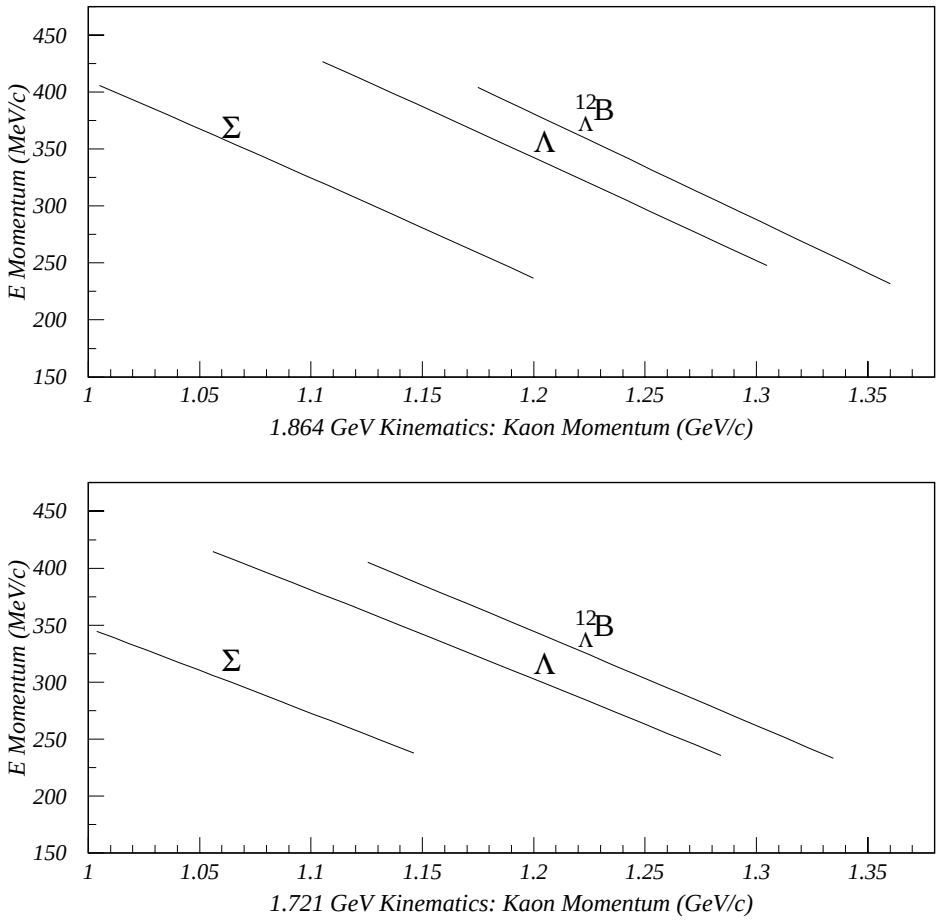

Figure 2.8: HNSS electron arm and kaon arm momentum correlations for 1.864 GeV and 1.721 GeV kinematics settings for different reaction products. The three lines in the graphs represent Σ, Λ and $^{12}_{\Lambda}C$ ground state, respectively.

up s_k, we have equation:

$$m_H^2 + m_K^2 - m_A^2 + 2(-s_K p_K \cos\theta_K + \sqrt{s_K^2 p_K^2 + m_k^2} - m_A)(s_b p_0 - s_k p_e) + 2\sqrt{s_K^2 p_K^2 + m_k^2} m_A = 0. \quad (2.12)$$

Taking nominal values of the p_0, p_k and p_e: 1.645 GeV, 1.055 GeV/c and 291.8 MeV/c, the above equation can be solved numerically to get $s_k = 1.175$. Same calculation can be done for beam energy 1.721 GeV/c, the scale factor is $s_k = 1.061$.

In Figure 2.8 , the momentum range of kaon and e$'$ corresponding to production of the ${}^{12}_{\Lambda}$B ground state (GS), Λ and Σ are shown. Our HNSS kinematics settings put the ${}^{12}_{\Lambda}$B GS and Λ at center of then spectrometer acceptance. Σ was also included in the acceptance. We could use the known masses of Λ and Σ for momentum calibration.

2.6.3 Splitter and Target Chamber

Splitter was a C-type dipole magnet which was located right after the target to separate the 0° scattered electrons and forward angle kaons. It had a pole gap of 3 inches. The field in the mid-plane was mapped before the experiment. The effective field boundary (EFB) of the splitter field was fitted from the field map and the Raytrace optical code was obtained to describe the field. The position of the EFB x_{EFB} is defined so that the integral of BdL from a point x_0 in the uniform field region to x_{EFB} along X or Y axis is equal to the integral of BdL over the total path length,

$$B(x_{EFB} - x_0) = \int_{x_0}^{\infty} BdL. \quad (2.13)$$

The target chamber was installed in the splitter pole gap. It held the target in vacuum and also served as a vacuum connection from beam line to SOS, ESPS and exit beam line. It also had window for target viewer. This viewer helped to check the correct beam position by viewing the beam spot on BeO target. There was a pipe inside the chamber to hold a hall probe for field measurement. 7 targets were held on a target ladder. A remote controlled motor drove the target ladder along a track to allow target change during the experiment.

The target ladder was positioned so that the target was right at the EFB of the splitter field and is 32.9 cm upstream from the Hall C pivot. The splitter was rotated 7° to the incoming beam direction to get better focusing for e′ at ESPS focal plane. Kaon was bend to 16° to SOS and e′ to 33° to ESPS by the splitter field. The path of the exit beam (pass-through electrons) passed through the corner of the splitter field. At the corner of the splitter field there were field gradients in both X and Y directions, the trajectory of the exit beam calculated by a uniform field inside EFB was not correct. To calculate the actual bending angle of the exit beam, we solved the Lorenz equation by fourth-order Lounge-Kutta method point by point over the trajectory. Field values were calculated from the actual field mapping plus interpolating between the mapping points. The actual bending angle was found to be 8.0°, which was 0.5° less than the angle calculated using uniform field assumption.

The splitter was also powered before the experiment to measure the excitation curves and to determine the proper excitation procedure to the desired field (Figure 2.9). The saturation started from 1.5 Tesla, well above our desired field settings. A Hall probe was inserted in a pipe built into the chamber to measure the field during the

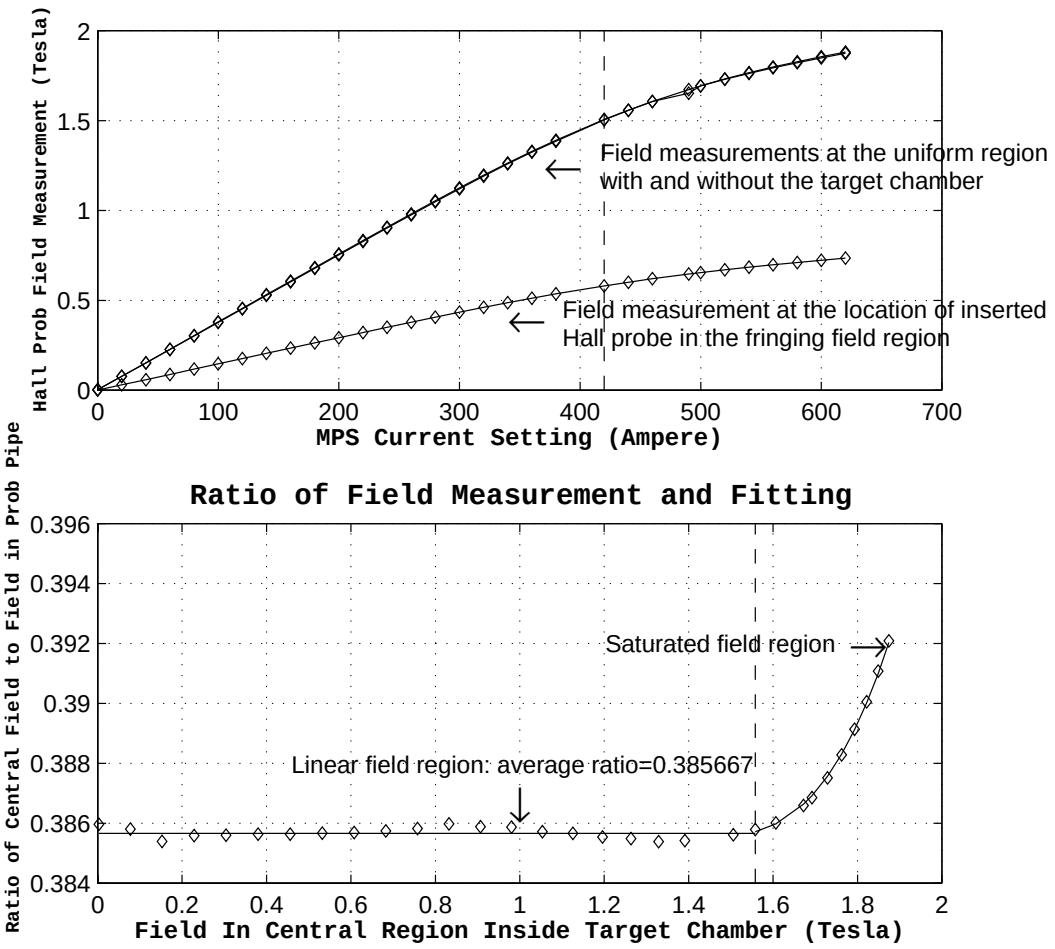

Figure 2.9: Splitter I-B curve and the ratio of Hall probe measurement at the location of the inserted Hall probe to the uniform field strength. The ratio when field was partially saturated was not a constant and depended on B. The magnetic fields with and without target chamber were almost same.

experiment. To avoid interfere with the particle trajectory, the tip of probe was not put in the uniform region of the splitter field. Therefore, we compared the measurement of the Hall probe in the uniform field region and at the monitor position. A function was introduced to describe the ratio of two Hall probe measurements over a wide range of field strength. Below saturation point of 1.5 Tesla, the variation of the ratio was less than 2×10^{-4} and was around a constant of 0.38567. The ratio was used to calculate the real field strength in the uniform region from Hall probe measurement at the monitoring position in the fringing field region during the experiment.

2.6.4 Enge Split-Pole Spectrometer

Scattered electrons were analyzed in the ESPS (Figure 2.4). Table 2.3 [42] shows the main characteristics of the magnet. Electrons were bended horizontally in the spectrometer. The ESPS focal plane was well formed. The ESPS had the advantage of small size and high resolution. The small solid angle acceptance was sufficient to match well with the forward peaking nature of the near zero degree virtual photon production. Combined with good focusing property the ESPS provided excellent resolution even if only the 1-D position of the electron along the focal plane was measured. Therefore, focal plane tracking with angular measurement was not required. Such tracking would be difficult under the high e$'$ flux. Figure 2.10 shows the e$'$ momentum δp ($= dp/p_0$ in %) vs. the focal plane X position by Raytrace simulation using virtual photon distribution on target. If we simply fit δp as a polynomial function of x, the fitting error is $4.4 \times 10^{-4} \sim 121$ keV/c.

Enge Split-pole was also powered before the experiment and an I-B excitation

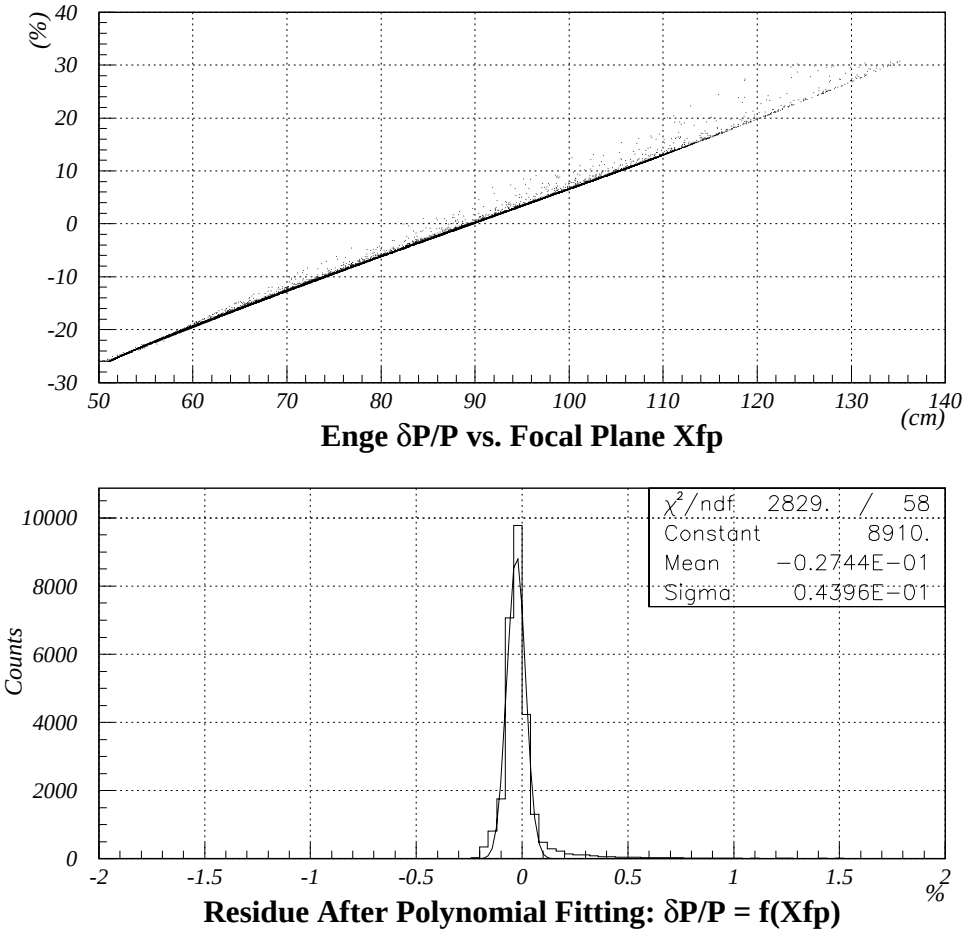

Figure 2.10: Correlation of ESPS focal plane δp to focal plane X position. We can see that e$'$ momentum can be very well determined by ESPS focal plane 1-D position.

Table 2.3: Main characteristics of ESPS.

Parameter	Value
Momentum	228 - 338 MeV/c (nominal)
Design Central Momentum	276 MeV
Total Length	∼5m
Solid Angle Acceptance	1.6 msr
Horizontal	25 mr
Vertical	20mr
Momentum Bite	±20%
Focal Plane Geometry:	
Length	74 cm
Tilt	48.8°
Dispersion	1.5 cm/%

curve was measured (Figure 2.11). We can see that the magnet can be operated up to 1.6 Tesla without significant saturation.

2.6.5 Hall C Short Orbit Spectrometer

Hall C Short Orbit Spectrometer is a Hall C standard equipment specially designed to detect short lived particles such as kaon and pion. It has been used in previous Hall C experiments to detect hadrons in (e,e′π^+) and (e,e′K^+) reactions. It has a moderate energy and angular resolution. The main characteristics are tabulated in Table 2.4 [43].

The spectrometer consists of a horizontally focusing quadrupole (Q) followed by a vertically +33° upward bending dipole (BM01) and a −15° vertically downward bending dipole (BM02). The optical axis of the spectrometer at the focal plane is at an angle of 18° relative to the horizontal direction. The spectrometer is very compact because both dipoles share the same iron yoke. The center of BM01 is far from the edges, on the other

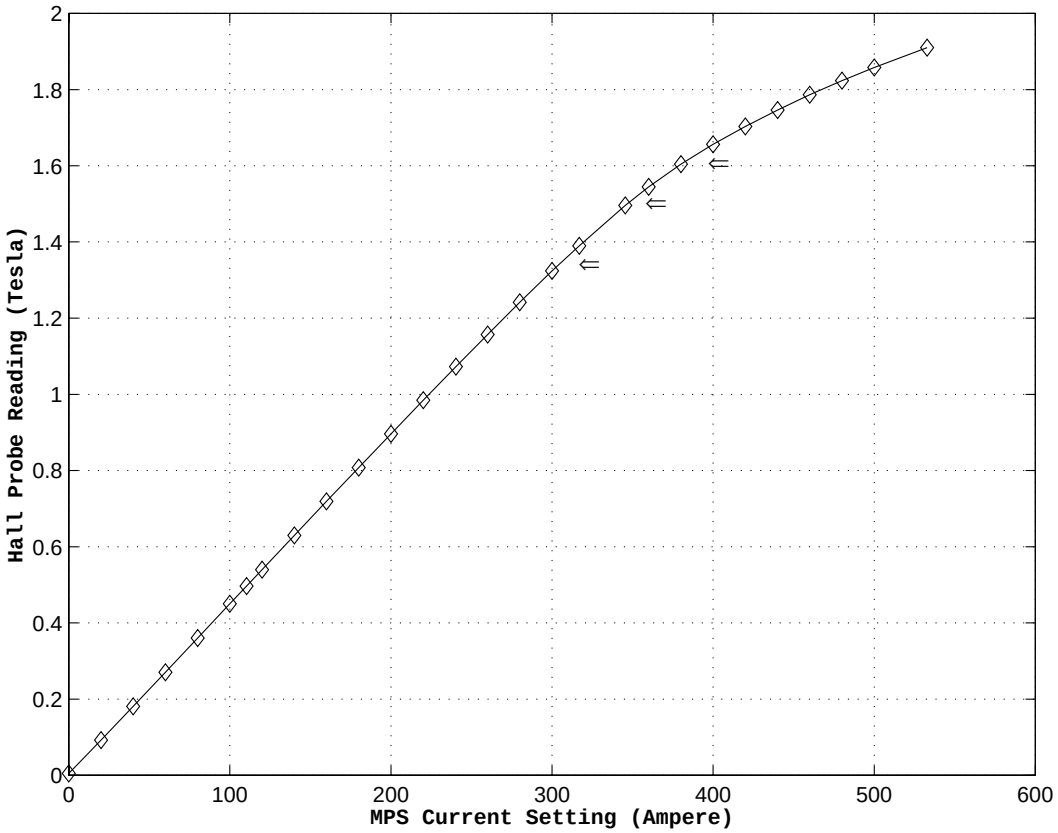

Figure 2.11: ESPS I-B excitation curve tested at Test Lab. the arrows point to 3 setting points of field for 1.721 GeV, 1.864 GeV and 1.950 GeV beam energies.

Table 2.4: Parameters for the QD$\bar{\text{D}}$ SOS Design.

Parameter	Value
Solid angle	9 msr
Central momentum at B_{nom}	1.5 GeV/c
Momentum Acceptance	40%
Dispersion	< 0.92 cm/%
Optical Length	7.4 m
Horizontal Opening Angle	120 mr
Vertical Opening Angle	80 mr
Focal Plane size	40×120 cm
Focal Plane Tilt Angle	70°
Distance Target-Q1	1.5 m
Out of Plane Angle Range	$< 20°$

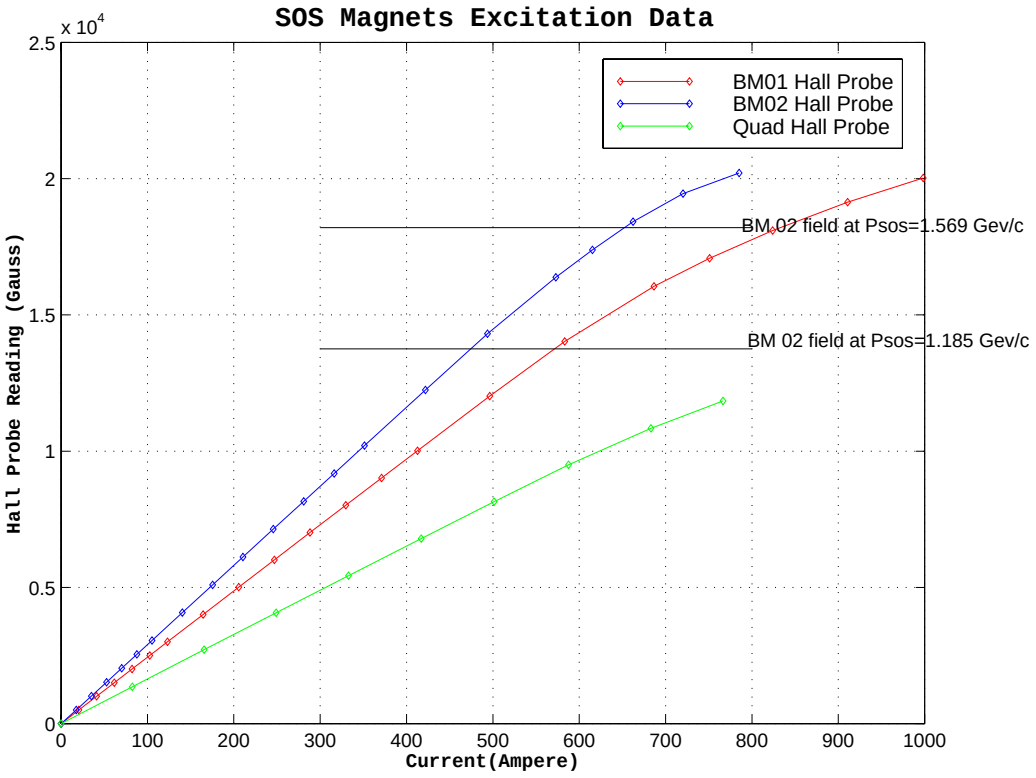

Figure 2.12: SOS magnetic field excitation curves. Note that our SOS field settings were close to the 1.185 GeV/c line.

hand, BM02 is a thin magnet, and there is no region that isn't close to the entrance and exit edges. To determine the proper relative excitation of these magnets, extensive field mapping was done on BM01 and BM02 except some corner area of the dipoles because of the inaccessibility of field probes. The SOS field excitation curve is shown in Figure 2.12. The bending power of BM01 and BM02 is: 11379.3 Gauss/GeV/c, for SOS quadruple, 498.152 Gauss/cm/GeV/c (point-to-point tune). The spectrometer can be operated at maximum central momentum of 1.75 GeV/c. But the magnets begin to saturate at $\sim$ 1.6 GeV which is still well above the E89009 momentum settings: 1.1195 GeV/c for 1.721 GeV beam, 1.2398 GeV/c for 1.864 GeV beam.

There is a slit box installed in front of Q entrance. It allows the use of different

collimators in front of the spectrometer. There are three HEAVYMET (machinable Tungsten with 10% CuNi; density=17 g/cc) collimators which may be selected remotely. These three collimators are shown in Figure 2.13. The top two collimators have oblong holes on the 2.5 inch thick metal where the opening is flared to match the spectrometer acceptance. The larger of the two has an acceptance of roughly 7.55 msr, while the smaller opening about 3.98 msr. The last in the assembly is a sieve slit collimator which is used to tune the optics. The metal in this collimator is only 1.25 inch thick with a matrix of holes. All of the holes except the central hole are 0.2 inch in diameter. The central hole is considerably smaller and is used to identify the optical axis of the spectrometer. There are two holes missing on the sieve slit so that one can easily identify which way is up etc. All positions of the holes are known and the distance of the sieve slit plane to the target are fixed. Thus events passing through the sieve slit holes will have known angles. During E89009 the large collimator was used in the production runs. The sieve slit was used for optical study. However, the addition of the splitter caused the sieve slit holes lost the angle selectivity (see detailed discussion later).

The SOS spectrometer uses a point to point tune(PT-PT) featuring point to point focusing in both the bend and no-bend planes.

The SOS has a short path length to reduce decay of short-lived particles. The path length from nominal target to focal plane is 7.4 meter.

The HNSS optics calibration is an important issue and details will be left to next chapter. Due to the existence of splitter field around target as mentioned above, we used Raytrace simulation method in comparison to sieve slit data for optical tuning. This was a different method from previous Hall C experiments. Generally speaking, initial

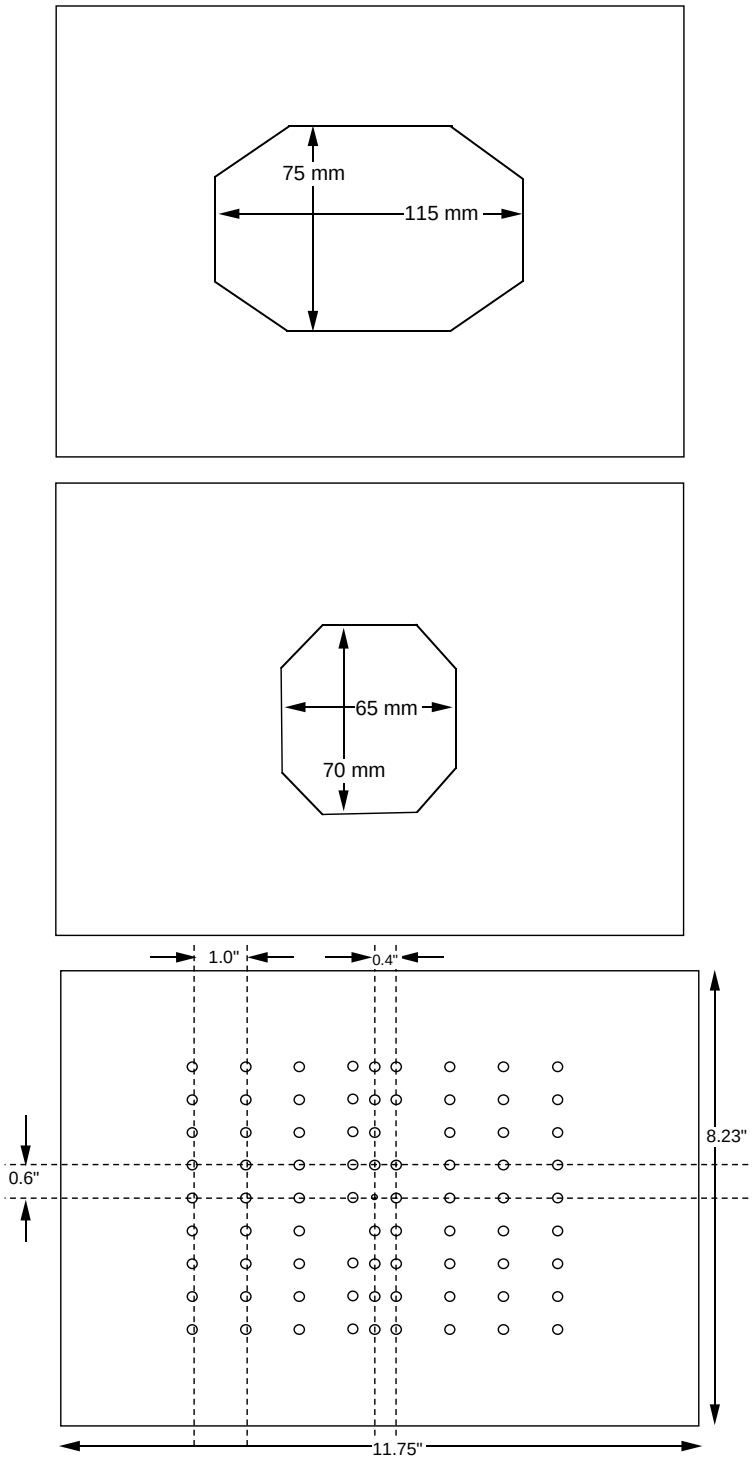

Figure 2.13: Dimensions of aperture placed in front of the SOS quadrapole.

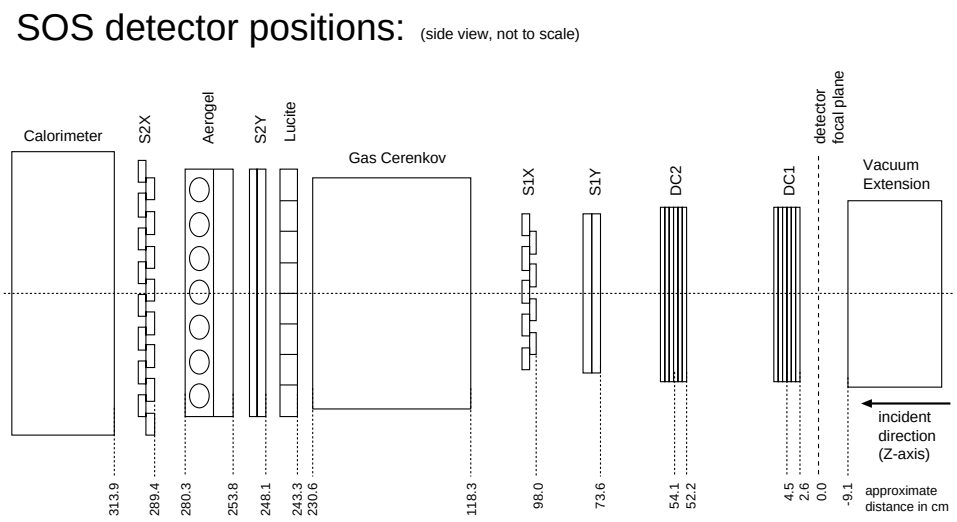

Figure 2.14: SOS detector package showing the approximate locations (Z) along the central ray (the center dotted line).

Raytrace optical code was obtained from field map. This Raytrace code was further tuned during the experiment according to sieve slit data. The reconstruction matrix was then fitted from the Raytrace simulation.

2.7 HNSS Detector Package

In the SOS side, there are detectors for particle tracking, kaon particle identification, time determination and trigger. They are drift chambers, scintillation hodoscopes, gas Čerenkov counter, aerogel Čerenkov counter, lucite Čerenkov counter and lead glass shower counter. All these detectors are housed in a concrete shielding house against background particles (Figure 2.14)

In the e′ side, because no tracking was needed, we used array of Silicon Strip

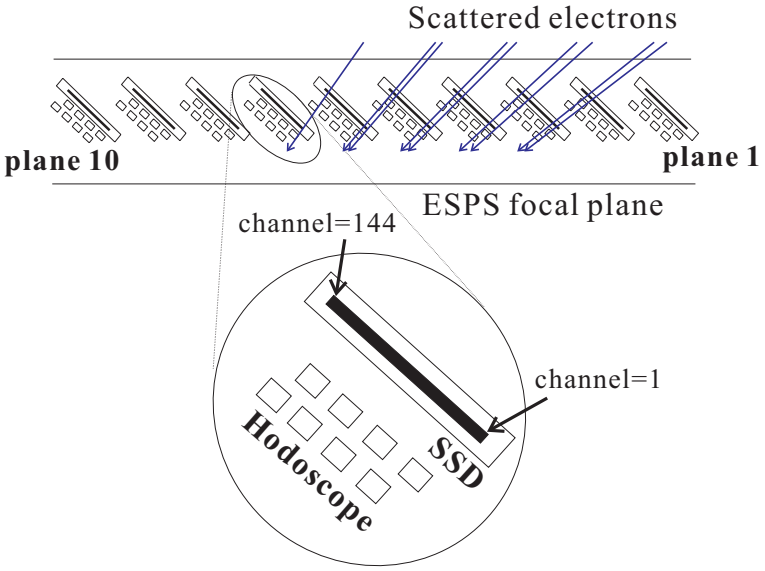

Figure 2.15: ESPS focal plane detectors layout. The arrowed lines illustrate the directions of incident electrons. Some incoming particles could pass through two adjacent SSD planes. Some hodoscope channels had overlap.

Detectors (SSD) to measure electron positions in the focal plane. The reason to select SSD is its ability to handle the high e′ rate of more than 100 MHz over the focal plane length of 74 cm in our experiment. The e′ timing was measured by the scintillation hodoscope strips. The segmentation of the hodoscope was to improve its rate capability (Figure 2.15).

2.7.1 SOS Drift Chambers

There are two identical sets of drift chambers (DC1 and DC2) placed directly after the dipole to reconstruct tracks at the focal plane. They are placed before any other detectors to reduce multiple scattering. The two drift chambers are 49.5 cm apart. DC1 is about 6.3 cm from the focus of central momentum of SOS. The planes of DC1 and DC2 are parallel and normal to optical Z axis and are 17° tilt about the optical axis.

The configuration of the SOS drift chambers is shown in figure 2.16. It is a

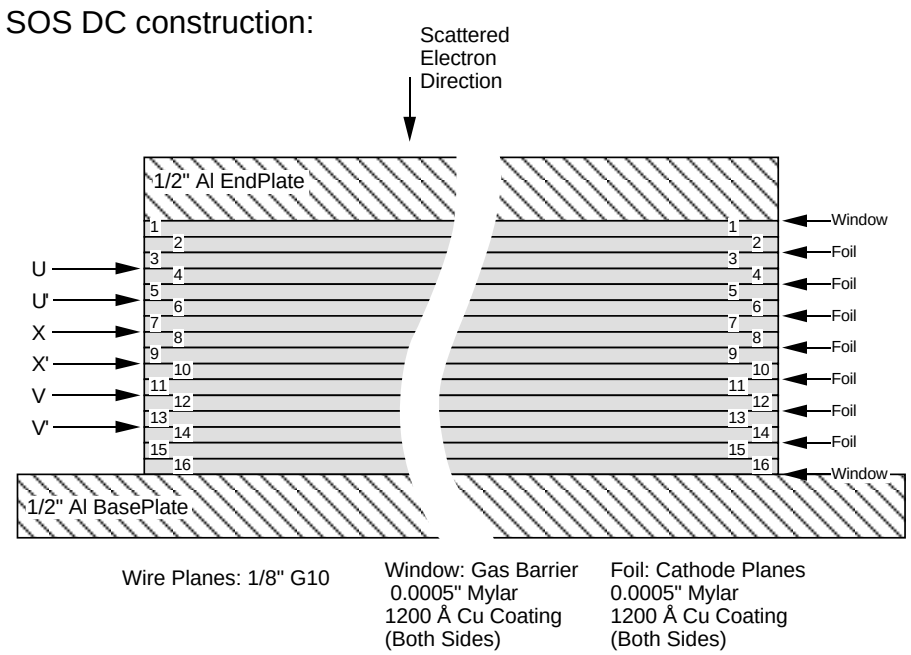

Figure 2.16: SOS DC configuration.

sandwich of 1/8 inch thick G10 plates with 1/2 inch thick Al plates as entrance and exit flanges. The entire assembly is therefore 3 inches thick. There are 6 separate measurement planes in each drift chamber. In the sequence of U, U', X, X', V and V'. The X and X' planes measure the particle coordinate in the dispersive direction of the spectrometer.U and V axes are rotated 60° clockwise and counterclockwise w.r.t. X, respectively (Figure 2.17).

The drift cell of the SOS drift chambers is 1 cm as shown in Figure 2.18. The basic drift cells are formed by 60 μm potential wires alternating with 30 μm anode wires with a 5 mm spacing between wires. The anode wires are kept at ground potential while the potential wires and cathode foils are biased to negative high voltages. The difference between the regular and "primed" planes is also shown in Figure 2.17 In the "primed"

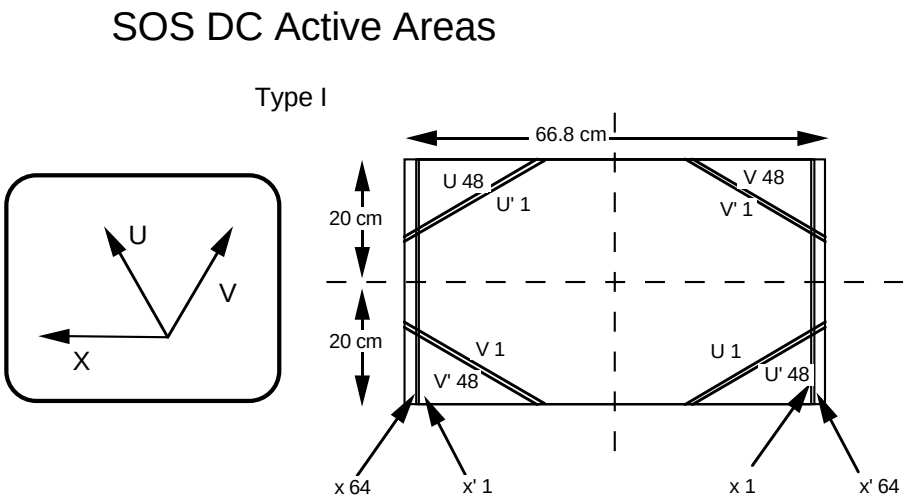

Figure 2.17: SOS DC active area. NOTE: Gravity is in the same direction as x.

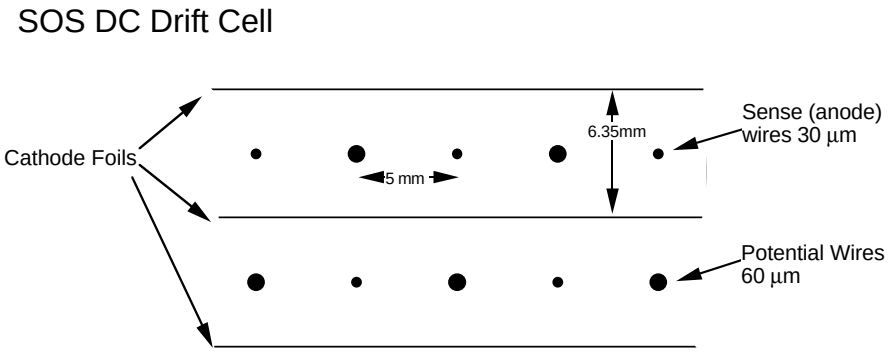

Figure 2.18: SOS DC drift cell.

plane, the anode wires are offset by 5 mm (1/2 of the cell size w.r.t. regular planes). The information from these planes are used to resolve the left-right ambiguity.

The coordinate system and active area of the SOS drift chamber is shown in Figure 2.17. The entrance window size for a drift chamber is about 67 cm in X by 40 cm perpendicular to X.

The operation of all drift chambers depend on the phenomenon of ionization avalanches. A particle traversing the chamber liberates electrons in the gas which then drifting towards the anode. At the same time, the fast signal from the scintillator starts a TDC. The signal created at the anode as the drifting electrons arrive then stops the TDC to yield the drift time. From the drift time and distance relationship of the drift chamber, drift distance can be calculated and hit position can be found.

The drift chambers work on individual wire readout. A hit on a wire which produces a signal with amplitude large than a threshold level (typically 1.5 V) will start a TDC. The TDC readout occurs only after a trigger signal has been sent to the SOS to stop the TDC. The the wire number information and TDC values for all the above threshold "hits" in the 4 μs before the trigger are send to the analyzer. These TDC values give a measure of the drift time of the track to the wire. For the Ar-Ethane gas mixture used and the 0.5 cm cell size, the maximum drift time is about 150 ns. This information is passed to the tracking algorithm to measure the coordinate of the track (in each plane) relative to the center of the drift chamber. Then a Least-Square fit is used to fitting the particle track through all the drift chamber planes. The average position resolution is about 280 μm (σ) per plane.

During E89009, SOS had a very high trigger rate up to 1.2 kHz due to the high

positron rate. SOS drifting chamber had been working well under this high rate with detection efficiency of $\sim 97\%$ and negligible multiple tracks.

2.7.2 SOS Hodoscopes

Two pairs of scintillation hodoscopes S1Y, S1X and S2Y, S2X are used for triggering on passing through charged particles and measuring the time of flight (TOF) between the hodoscope planes. Hodoscopes S1X, S2X are segmented in X direction (vertical and bending direction), S1Y, S2Y are segmented in Y direction. S1Y and S1X are located upstream of the Čerenkov detector. S2Y and S2X are located between the Čerenkov detectors and the shower counter. Each pair (S1X-S1Y and S2X-S2Y) in combination also provides rough position determination. The two pairs are $\sim$174 cm apart in Z direction to provide the longest possible flight path to improve TOF measurement precision.

The SOS hodoscopes are constructed by long narrow strips of BC404 scintillators which are readout on each end with light guide coupled to photo-multiplier tubes (PMT). The strips are slightly overlapped (5 mm) to ensure full coverage of the active area. All the hodoscope strips are 10mm thick but with different width and length. The first three hodoscopes, S1Y,S1X and S2Y, have 9 strips of scintillator, while the last one, S2X, has 16 strips to cover enlarged particle profile in the bending direction. The positions and active areas of these hodoscopes are listed in Table 2.5.

When charged particle pass through the scintillator, the light produced from energy loss is transmitted to the PMT on each end and is converted to electric pulse. This signal is sent to a splitter in upstairs counting house by coaxial cable and is divided into 1/3 and 2/3. the larger signal is properly delayed and then sent to a fastbus ADC

Table 2.5: Active areas of SOS detectors in horizontal (X) and vertical (Y) directions and center Z positions of the detectors at 1/2 of thickness (unit: cm).

	-x	+x	-y	+y	z	thickness
DC1	-28.894	37.976	-19.405	20.595	6.25	1.905
DC2	-33.047	33.753	-19.618	20.382	55.77	1.905
S1Y	-36.8	36.8	-18.423	18.423	74.61	1.0
S1X	-32.75	30.75	-23.5	23.5	99.01	1.0
GC					174.45	55.5
LC	-43.0	40.0	-20.	20.	244.6	1.25
S2Y	-57.15	57.15	-18.423	18.423	249.11	1.0
AC	-48.0	+48.0	-19.5	19.5	258.3	4.5
S2X	-50.0	50.0	-34.00	34.00	290.53	1.0

1.864 GeV run32178-32421:

	-x	+x	-y	+y	z	thickness
S1X	-17.2	17.2	-23.5	23.5	99.01	1.0

[LRS1881M] for pulse size analysis. The smaller one is sent to a leading edge discriminator [PS7105]. The discriminator signal is used for timing and analyzed by a fastbus TDC [LRS1872A] after a appropriate delay. In addition the signal is used for forming trigger. Majority coincidence in restricted time period between signals from different hodoscope planes, 3/4 or 4/4, forms the first level trigger without kaon identification.

The TDC signals from the hodoscopes provide a timing in reference to the trigger. Subtraction of TDCs between hodoscope planes measures TOF of passing-through particles. The ADC signal is used to correct the "time walk" from leading edge discriminator due to pulse height variation relative to a constant threshold. TOF or the particle velocity β is one of the criterion for particle identification, since particles with different masses have different β range (Table 2.6). The β of a particle is related to its momentum

Table 2.6: β ranges for particles in SOS.

Beam (GeV)	e^+	π^+	K^+	p^+
1.864	1	0.992–0.995	0.914–0.940	0.765–0.824
1.721	1	0.991–0.994	0.898–0.928	0.732–0.795

p by:

$$\beta = p/\sqrt{p^2 + m^2}. \tag{2.14}$$

where m is the particle mass. In the present experiment, within the SOS momentum acceptance, the β of protons had a range 0.765–0.824 for the beam energy of 1.864 GeV and 0.732–0.795 for that of 1.721 GeV. They can be well separated from other faster particles by TOF (β). Kaons and pions cannot be completely separated by β. Additional Čerenkov detectors were used for kaon identification.

For HNSS experiment, since the zero degree scattering angle of hadrons was covered by the SOS angular acceptance, the positron single rate was high and concentrated on one side in X direction. To reduce this high trigger from positron, we disabled the outside 4 scintillators in the S1X scintillator array for some run periods when high beam current was used. The active area of the hodoscope and thus the solid angle acceptance were reduced after these scintillators were disabled (Table 2.5).

2.7.3 Lead Glass Shower Counter

Shower counter is the last detector in the sequence of detector array for the SOS. It is constructed from Pb glass blocks. This counter is used to provide a total energy

measurement of the detected electrons or positrons and to provide additional information for particle identification. It was used to discriminate the large amount of positrons from other particles in E89009.

The lead-glass counter is an electromagnetic calorimeter that detects the energy deposited when an electron or positron enters the lead-glass. When a high-energy electron or photon is incident into this thick absorber, it initiates an electromagnetic cascade as pair production and bremsstrahlung generate more electrons and photons with lower energies. Electrons and positrons will deposit their entire energy in the calorimeter. Hadrons can not produce electromagnetic shower so only a fraction of their energy is deposited in the calorimeter. For example, pions typically deposit $\sim$ 300 MeV in the calorimeter [44]. If calculate the ratio of energy detected in the calorimeter to the particle momentum measured by spectrometer, the value is one for electrons and positrons, other particles will have a value well below one. So electrons and positrons are separated from other particles.

The shower counter was constructed from 10 cm by 10 cm by 70 cm blocks of TF1 lead glass. This glass was arranged in 4 layers, every layer has 11 blocks stacked transversely. Each block is readout by a phototube on one end. The blocks were stacked to put the best performing blocks at the outer edges of the active area where the signals are smaller.

The signals from the PMT are fanned out in a splitter [UVA122B] with 1/2 of the signal to a fastbus ADC [LRS1881M] for offline pulse size (energy) analysis. The remainder of the signal are summed together to form a total summed signal for each stack (e.g. SUM-A). A further linear sum occurs of the SUM-A and SUM-B signals

forms a preshower sum (PRSUM) and the sum of SUM-C and SUM-D signals forms a shower sum (SHSUM). The PRSUM signal is useful because electrons and positron will loss most of their energy in the first 2 calorimeter layers. These signals were used in trigger as online particle ID.

2.7.4 Gas Čerenkov

The Čerenkov counters in the SOS provided important particle identification information. Gas Čerenkov provided additional discrimination of $\beta = 1$ positrons against other particles. Aerogel Čerenkov was used mainly to veto pions. Lucite Čerenkov was used to reject slower protons.

Čerenkov counters work by detecting the Čerenkov radiation. When particle travels through medium in a speed faster than that of light in the medium c/n (n is the index of refraction of the medium), it will emit light in a forward pointing cone with an opening angle θ_c. This light is called Čerenkov radiation. The opening angle θ_c can be calculated as

$$\cos(\theta_c) = \frac{1}{\beta n} \quad \text{when} \quad \beta > \beta_c = \frac{1}{n}. \tag{2.15}$$

Only particles which have a β large than threshold β_c can emit Čerenkov radiation. Thus by detecting the Čerenkov radiation. particles with β large than threshold β_c can be distinguished from particles traveling slower than β_c. This is called threshold Čerenkov.

In E89009, the gas Čerenkov counter signal was used in the online trigger to suppress $\beta = 1$ positron from other slower particles along with shower counter because

gas Čerenkov has a very high threshold β: $\beta_c = 0.9989$, higher than all the other $\beta < 1$ particles. In offline analysis, positron events were further removed by shower counter signals.

The SOS gas Čerenkov is a rectangular Al box with interior dimensions 99 cm high (X) by 73.7 cm wide (Y) by 111 cm long (Z). It is filled with Freon 12 gas (CCl_2F_2) which has an index of refraction of 1.00108. Particles with the speed of light traversing this gas produce Čerenkov light in a cone with a polar angle of 2.7° with respect to the particle momentum vector. This light is reflected backwards by four spherical mirrors which focus the light to four PMTs. Each PMT is placed in the gas just to the left or right (in Y) of the active area of the detector. The entrance and exit windows of the detector are shaped to reflect the focusing characteristics of the spectrometer optics. Both windows consist of 254 μm (0.010") Lexan graphic film covered by 50.8 μm (0.002") Tedlar film for complete opacity. The total thickness of this window material is 39 mg/cm^2. Thin material is used to reduce the knock-on electrons . Other particles can produce knock-on electrons from window material. These electrons have sufficient energy to emit Čerenkov radiation. Therefore, these particles may be misidentified as positrons.

The signals from the four PMTs are split and 1/2 of the signal is sent to a fastbus ADC [LRS1881M]. The rest of the four signals are summed in a linear fan-in/fan-out [PS740] and the one output signal is sent to a discriminator [PS708]. The threshold of this discriminator was set to a threshold corresponding to 2.5 photoelectrons (see calibration section below). This signal was used in the trigger to reject positron events in E89009.

Because the signal from the Čerenkov was used in the trigger, the high voltages

for the four PMTs were adjusted so that the average signal heights of the PMTs were matched within 20-30%.

The calibration of the SOS gas Čerenkov is done with beam. Only good electron events selected by tracking and shower counter signals and the events pass through the middle of the mirror were used for calibration. Average number of photoelectrons per event for all the four PMTs were compared to the mean to obtain the gain for that particular phototube (number of ADC channels per photo-electron).

2.7.5 Aerogel Čerenkov

An important requirement for the SOS detector package is kaon particle identification because the small cross section of kaon production compared with that of other particles, positrons, pion and protons. A clean separation of kaon events is important to reduce background noise.

Among the particles in SOS, the mass of Pion (0.1396 MeV) is close to that of kaon (0.4937 MeV). Their β difference is not large enough to be separated completely by the TOF β measurement. Therefore, aerogel Čerenkov counter was used to reject pions.

The aerogel Čerenkov counter is made of silica aerogel ($n(SiO_2) + 2n(H_2O)$) with a index of refraction 1.034 ± 0.001. The threshold β for onset of Čerenkov radiation is 0.967. Thus pions will produce Čerenkov light while kaons can not.

The SOS Čerenkov counter has a aerogel tray which holds the slabs of aerogel material, a diffusion box to collect Čerenkov light and 14 PMTs (Figure 2.19) [45]. Every tile of aerogel is 3 cm thick. The tiles of aerogel material were arranged in three layers. The joints between tiles are in different places in each layer so that particles

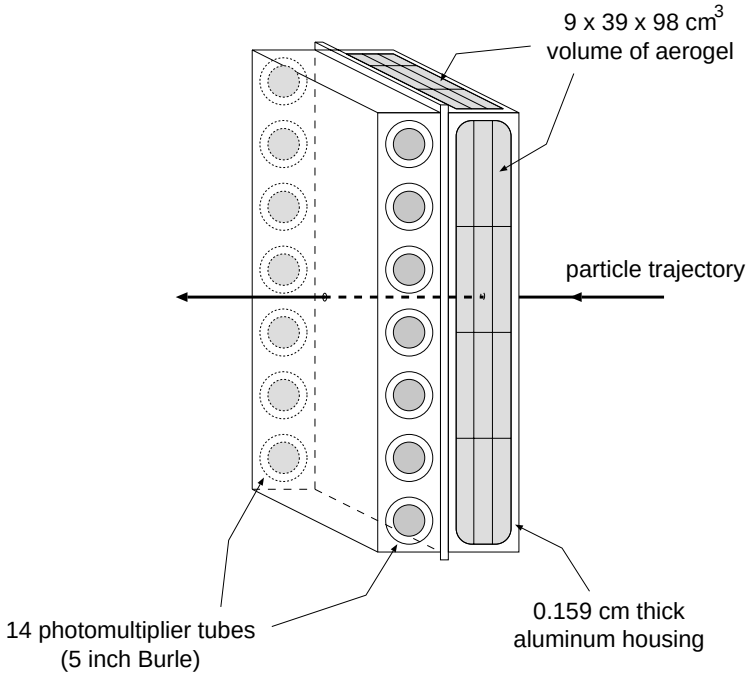

Figure 2.19: Schematic view of SOS aerogel Čerenkov detector.

from all directions can pass through enough aerogel material. All the tiles are covered with 2 layers of aluminized Mylar on all sides except for the side facing the diffusion box. The diffusion box walls, except the PMT cutouts, are covered with Millipore (high-reflectivity) filter paper glued onto thin aluminum plates. On each side of the diffusion box, there mounted 7 Burle 8854 PMTs. The glass surfaces of PMTs penetrate up to about 20 mm into the diffusion box volume.

When particle with $\beta > 0.967$ passes through the aerogel, it emits Čerenkov light in a $\pm 16^{\circ}$ wide forward pointing cone. The Čerenkov light gets into the diffusion box down stream and is diffusely reflected by the diffusion box wall by reflective Millipore

paper until it is collected by one of the PMTs or is absorbed by the walls or material inside. The useful active area is defined to be 95 cm high by 35 cm wide, which assures clearance of all internal structures including phototube faces.

The aerogel material can easily absorb moisture in the air and get contaminated, thus there are two gas feed-through holes on opposite sides of the diffusion box to let dried air flow in continuously during the experiment. The dried air helps to carry away the moisture.

The 14 side-mounted PMTs convert Čerenkov light to electronic signals. These signals are amplified and divided into two groups according to a "shoelace" configuration instead of the simple sum of each side to reduce any y-dependent inefficiency. In this configuration, alternating tubes from +y and -y sides form one group. The signals from each groups are summed together to forms two signal sum-A and sum-B. The two signals are sent into a discriminator. The threshold levels of each discriminator was set to corresponding to about 3.5 photon electron (p.e.). The two discriminated logical signals are then ANDed to form the SOS aerogel pretrigger signal, AERO. This signal joined the SOS pretrigger logics as a veto signal to reject pions at trigger level.

The HVs of the PMTs were gain matched so that the one-photo-electron (OPE) peaks were aligned at about the same position in their ADC spectra. To increase the efficiency of the aerogel Čerenkov counter, the detector had undergone a low temperature but week long baking before the previous experiment (E91016) to remove the moisture (see Hall C experimental log book entry#18709). It gave a $\sim$ 12 p.e. in average for $\beta = 1$ particles after baking.

2.7.6 Lucite Čerenkov

The SOS lucite Čerenkov was installed to suppress the high proton rate in the online trigger. It is a total internal reflection type detector. The lucite material ($C(CH_3)CO_2CH_3$ polymer) has an index of refraction n = 1.49, so that the threshold β for lucite Čerenkov radiation is 0.672 [46]. In E89009, SOS had a central momentum of ~1.2 GeV, the β of protons was 0.73–0.83. Protons also radiated Čerenkov light in lucite material. However, the phenomenon of total internal reflection was employed to discriminate protons from kaons and other faster particles.

When light is transmitted from one medium to another, if the index of refraction n in medium one is larger than that of medium two n_0, it is possible that the transmitted angle θ_t is greater that 90° when the incident angle θ_i is large than a critical angle θ_0. In this case, all the light energy will be reflected inside the medium and no energy will escape out of the medium. We call this phenomenon as total internal reflection (TIR). The critical angle is reached when:

$$sin(\theta_{critical}) = \frac{n_0}{n}. \tag{2.16}$$

By requiring the opening angle for Čerenkov radiation in equation 2.15 equal to critical angle $\theta_{critical}$, we have

$$\beta_{TIRthreshold} = \frac{1}{\sqrt{n^2 - n_0^2}}. \tag{2.17}$$

Therefore for lucite, $\beta_{TIRthreshold} = 0.905$. Protons with small incident angles did not

have Čerenkov radiation transmitted through TIR. When 1.864 GeV beam energy was used, the SOS central momentum setting was $p_0 = 1.2398$ GeV, the β of kaons varies in range of 0.914-0.940, so kaons will produce total TIR Čerenkov radiation. But when beam energy is 1.721 GeV, SOS central momentum setting was $p_0 = 1.1195$ GeV, the β range of kaons was 0.898-0.928. Thus radiations from some low momentum kaons were below the TIR threshold. Therefore, to avoid loss of kaon events, lucite signal was only used in the 1.864 GeV beam energy run period in trigger to suppress proton events. For 1.721 GeV beam energy runs, lucite signal was not used in the online trigger.

Čerenkov radiation has a continuous energy spectrum, with a stronger intensity in the short wavelength, ultra-violet region. In order to minimize the light lose due to absorption, ultra-violet transmitting (uvt) lucite material was used. The SOS lucite detector was designed and built by Hampton and Temple University groups. It consists of eight horizontal lucite bars wrapped in black Teflon foil,each has a dimension of $40 \times 13.7 \times 2.5$ cm. Each bar has two 3 inch Phillip PMTs at both end coupled to the lucite by 15 cm long light guide. The detector was mounted before S2Y on the same metal frame.

The signals from lucite PMT are amplified and split: 2/3 go to ADC for individual channels, 1/3 go to summing module. The summed signal from all the 16 PMTs is sent to a discriminator. The discriminated signal was used in the trigger in ANDed mode.

The PMT HVs were adjusted before the experiment by one photo-electro OPE peaks from cosmics. The OPE peak positions in the ADC spectrum of all the lucite PMTs were aligned at ~ 50 channels above pedestal. The variation were within 20%.

2.7.7 Silicon Strip Detector

As mentioned before, at the focal plane of the HNSS electron arm, there was a high rate of bremsstrahlung e$'$ (150 MHz). Efficient tracking of particle trajectory would be difficult. However, we have shown that the sharp angular distribution of scattered electrons from bremsstrahlung and virtual photon process and the good focusing property of the ESPS allow us to determine e$'$ momentum with good resolution through the measurement of only the hit position along the bending direction on the focal plane. This measurement was performed by silicon strip detectors backed by scintillation hodoscope along e$'$ arm focal plane (Figure 2.15). The SSD measured the positions of electrons with a 500 μm resolution and the scintillators behind it provided the time measurement with a 250 ps (σ) resolution.

The silicon strip detector consisted of 10 SSD planes mounted near the 74 cm long focal plane. Each SSD plane had 144 strips with a strip width 500 μm. Thus in total it had 1440 channels for the whole focal plane. The positions of SSD planes were precisely measured and coded in the optical raytrace simulation. The center positions of the SSD planes were about 40–50 cm downstream from the ESPS vacuum extension window and titled about 42° relative to the exit pole boundary of the second split-pole piece. The planes were laid along the central line but inclined 45° to the central line in order to be about normal to the incident particles. The planes had overlap region between each other. The main specification are summarized in Table 2.7 [47].

The SSD was constructed in MOS (Metal-Oxide-Semiconductor) technology and had a $P^+N^-N^+$ coupling structure. The top and side views of the SSD are shown in

Table 2.7: SSD characteristics.

Active Area	72 mm×50 mm
Strip Pitch	0.50 mm
P^+ Strip Width	0.36 mm
Al Electrode Width	0.352 mm
Thickness	0.325±0.015 mm
Number of Channels Per Plane	144
poly-Si Resistance	10 MΩ
Strip Capacitance	$\leq$ 20 pF
Maximum Bias Voltage	150 V

Figure 2.20. Each strip was a 0.36mm wide P^+ type diode with aluminum contacts implanted on n-type base material. The strip pitch was 0.50 mm. The width of the P^+ strip was optimized based on the inter-strip capacitance and full depletion voltage. An N^+ electrode was similarly implanted on the other side. A bias voltage of 80 V was applied to the N^+ side of all SSD channels to obtain full depletion. When a particle passes through the P-N junction, it can excite a electron-pole pair from valence band to conduction band in the depletion region. The electrons and poles are driven by the bias field and the electrons are collected by the N^+ layer and the holes are collected by one of the P^+ strip. By calculating the center of gravity of the charge collected, the position of the impinging particle can then be determined with a resolution better than the strip pitch.

All the P^+ strips were AC coupled to the signal channel to reduce leakage current. The signal picked up by the Al electrode was sent by a 40 μm Al wire to the front-end board (FEB), on which three TEKZ preamplifier-shaper-discriminator (ASD) chips were mounted. The TEKZ was a low power, bipolar preamplifier with a shaping time of 20 ns. The threshold voltage of the discriminator, V_{th}, can be set by two ways. It can be

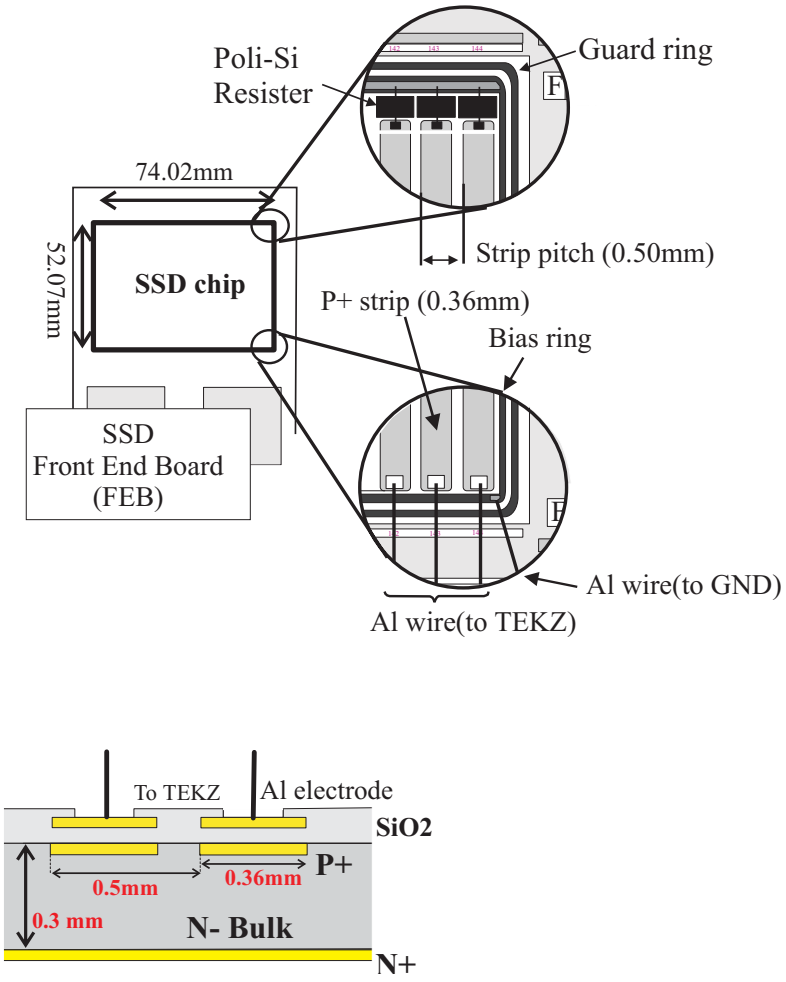

Figure 2.20: Top and side views of one SSD chip.

set manually using a voltage meter on the FEB. The minimum value of V_{th} (default) 1.0 fC. The threshold can also be varied remotely through a CAMAC 12 bit DAC to a value above the minimum value. This was used to scan the detector noise level during the experiment as a monitor of radiation damage to SSD. The discriminator output from each TEKZ was sent to the ECL Driver Boards (EDB) through a short flat cable. The EDBs clocked the ASD outputs into 15 fastbus multihit TDCs (LeCroy 1877) with a frequency of 50 MHz. The TDC was started by the SOS trigger signal. The full width of SSD TDC signals is $\sim$ 50 ns, 30 ns variation from charge-collection and 20 ns from electronic latches [48].

SSD is very sensitive to environmental noise and light, therefore, the SSD detectors were mounted in a RF shielded and light tight box on a metal frame. The same box also contained the scintillator hodoscope. The height of the frame can be adjusted. The whole frame can also be moved around the focal plane.

One concern with the silicon detector was radiation damage. During E89009, the SSDs received an estimated total dose of 22-23 kGy. As an effect of radiation damage, the leakage current rose from 0 to 6.5 μA as radiation dose accumulated for SSD plane #2 which received the highest radiation. The noise σ changed from 0.235 fC before the experiment to 0.25 fC after the experiment. However, throughout the experiment, SSDs were operated normally with a threshold voltage 340 mV, 3–5 times higher than the noise level. Under this threshold, the detection efficiency remained greater than 95% with a negligible level of radiation damage. The noise counts for all planes is 10 kHz compared with the 100 MHz total e$'$ rate at ESPS focal plane. Figure 2.21 shows a typical SSD hit pattern. The discontinuity at the beginning of each SSD plane is due

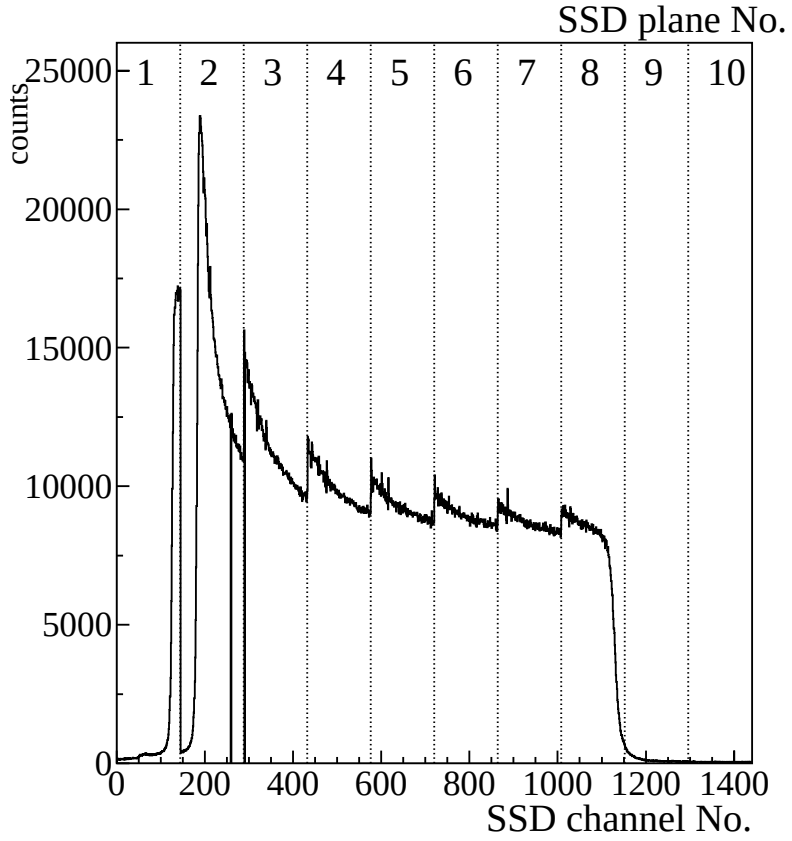

Figure 2.21: Typical SSD hit pattern. The vertical lines denote the start channel of SSD planes. Plane 1, 9 and 10 got little hit due to ESPS acceptance.

to the overlap between two adjacent SSD planes (Figure 2.15). The lower momentum side (lower channel number) received higher radiation as a consequence of ESPS optics and flux change as functions of the e$'$ energies. The SSD efficiency had been $\sim$ 96% throughout the experiment.

2.7.8 ESPS Hodoscope

There were 8 scintillator strips behind each SSD plane for time determination and suppressing background noise by requiring coincidence between SSD and hodoscope hits. Total 80 hodoscope elements covered the 74 cm focal plane (Figure 2.15). The plane of the scintillators was parallel to the SSD plane in order to be about normal to the incident e′s. Each group of scintillators were arranged in two layers to gain space for PMTs. The two layers were overlapped slightly to reduce gaps between them. However, due to the incident angles changed from 35–65° over the entire focal plane, there were still some remaining gaps between them for some incident directions, especially at high momentum planes. This contributed to the loss of efficiency for detecting electrons. Comparison of the hodoscope hit pattern with the simulation showed an efficiency of about 87% for 1.864 GeV runs and 84% for 1.721 GeV runs.

The scintillator strips were coupled to the Hamamasu PMTs by long light guides. These light guides also provided the support for the scintillators. The performance of PMTs are easily affect by straying magnetic field. At the position of hodoscopes, the fringe field of ESPS was $\sim$ 20 Gauss. Therefore, iron tubes with 0.25 inch think wall were mounted on the PMTs.

The signals from the PMTs were first sent to linear amplifiers. The 80 amplified signals were sent upstairs. They were split into 1/3 and 2/3or total charge after a 388 ns delay. The larger signals were sent to ADCs, while the smaller ones were sent to CAMAC discriminators. The output of discreminators were then fed into FASTBUS TDCs (FASTBUS TDC 1875A) which were started by the SOS trigger signal.

During the experiment, the ESPS hodoscope scintillators accepted high e′ rate. For example, one of the scintillator strip behind the second SSD plane, channel #12 got 5.5 MHz e′ hits at 0.6 μA beam current on carbon target. To handle this high rate, specially designed transistor-type booster card was added to each PMT base. This improved the rate capability of PMTs. But the charge pile-up effect still showed up for high rate runs when count rate for a single scintillator exceeded 1.5 MHz, as we can see from Figure 2.22. The figure shows the hodoscope ADC distributions for ESPS hodoscope channel #12, at rate 5.4 MHz, 4.2 MHz, 2.2 MHz and 1.2 MHz. The channel got the highest e′ rate among the ESPS scintillators. The ADC peak broadened and a bump showed up at the slope as rate increased. The pile-up affected efficiency and cause "time walk". Since the experiment used a few different beam current, the data were grouped accordingly and timing calibration was done separately. Despite the high rate, an overall ESPS hodoscope efficiency of $\sim 96\%$ was achieved for the experiment.

The hodoscope timing parameters were calibrated by the time difference between two neighbouring scintillators using overlap and coincidence events. The ESPS hodoscope time resolution after the calibration was 325 ps (σ) in Figure 2.23.

2.8 HNSS Trigger

The HNSS trigger was formed at SOS. Due to the high e′ rate at electron arm, no separated trigger from electron arm was formed and there was no coincidence trigger. The (e′K$^+$) time coincidence was done by offline analysis only. The SOS kaon PID signals were used in SOS trigger to select kaon events and suppress background events.

Figure 2.24 shows the trigger diagram for SOS. The basic trigger was formed from

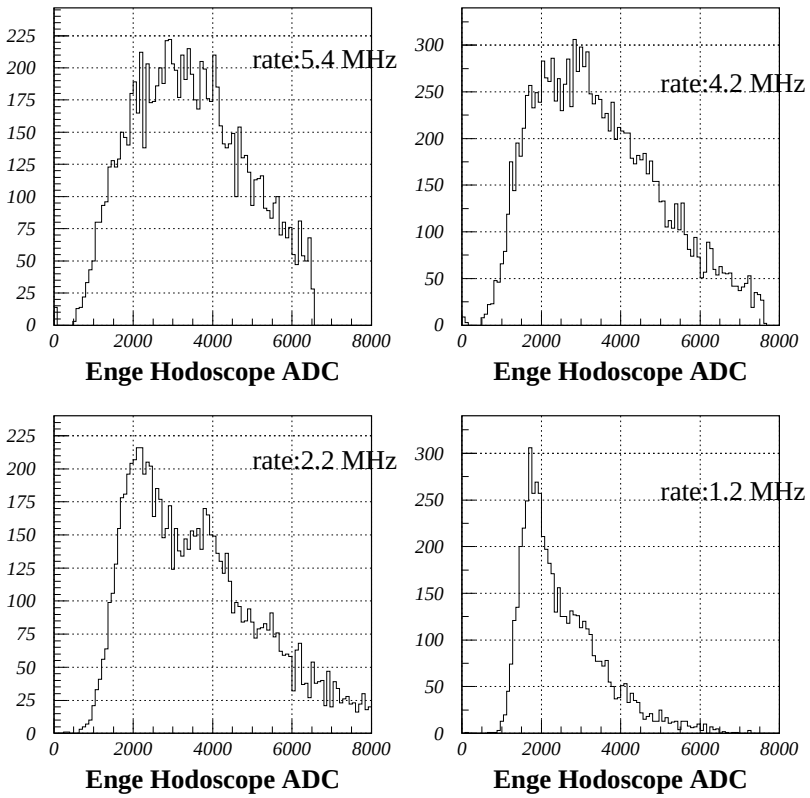

Figure 2.22: ESPS hodoscope ADC distributions for hodoscope channel #12 under different counting rates. The 1.2 MHz rate distribution was taken at a later stage of the experiment.

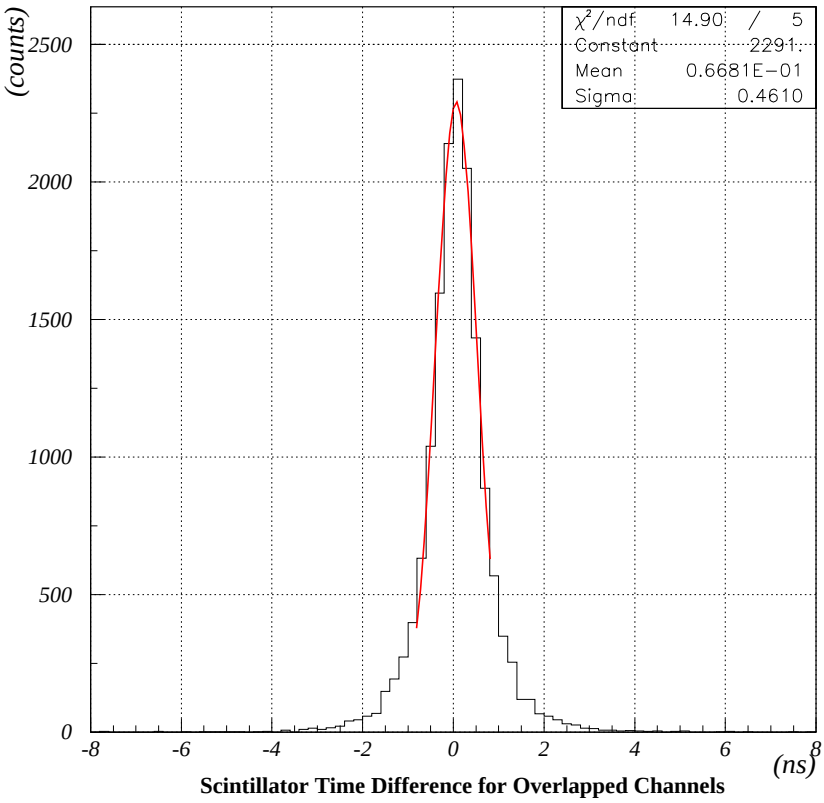

Figure 2.23: Time difference of ESPS overlapped scintillators. The tail was due to the pile-up effect and was excluded from Gaussian fitting.

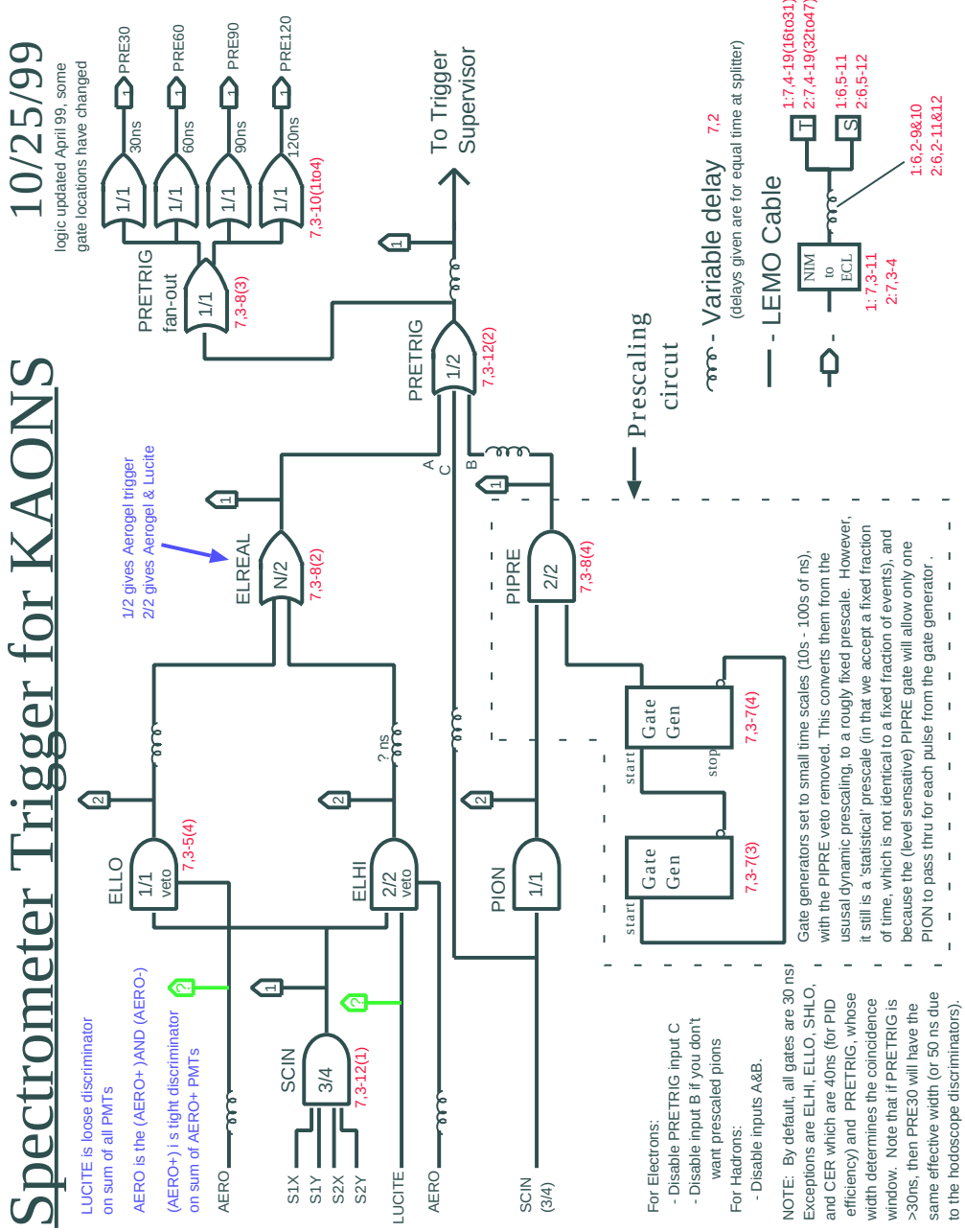

Figure 2.24: SOS trigger diagram. The gas Čerenkov and shower counter SHLO signals go into the ELHI gate, which is not shown in the diagram.

the hodoscope signals. Each hodoscope plane formed its own signal to be used in this logic. These signals were generated by requiring an above threshold signal in at least 2 PMTs in the hodoscope plane (at least one on each side). These signals were sent to a majority coincidence [LRS4564] module. The first level trigger for charged particles was formed in the module marked SCIN by requiring 3 out of the 4 scintillator planes have fired (3/4) or 4 out of the 4 scintillator planes have fired (4/4). This trigger signal was required for all other types of triggers. The ELHI signal was then formed by adding other kaon PID signals: vetoed by the PRLO or SHLO signal from the shower counter to remove the positron event as positron tends to deposit all its energy in the shower counter by electromagnetic shower; vetoed by the gas Čerenkov and aerogel Čerenkov to suppress positron and pion respectively; coincided with the lucite Čerenkov signal for 1.864 GeV beam energy runs only to remove proton event. The ELLO signal was formed by the SCIN vetoed by the AERO signal. ELLO and ELHI were then ANDed to generate the ELREAL, the SOS single arm trigger with kaon PID.

The PION trigger was directly formed from the SCIN signal. This trigger was prescaled as desired using a prescaling circuit which was essentially two gate generators in a loop. The ratio of the widths of these two gate generators determined the scaling factor. The prescaled pion trigger formed PIPRE, denoted as B in the trigger algorithm. The ELREAL and the PIPRE were ORed to generate the pretrigger PRETRIG.

In previous Hall C experiments, SCIN was normally set at 3/4 mode. But E89009 had high positron rate at the SOS arm, the SCIN 3/4 coincidence mode took too many accidental coincidence noise from the hodoscopes. Thus SCIN was set at 4/4 mode for most part of this experiment. The SCIN 4/4 mode greatly reduced data size with little

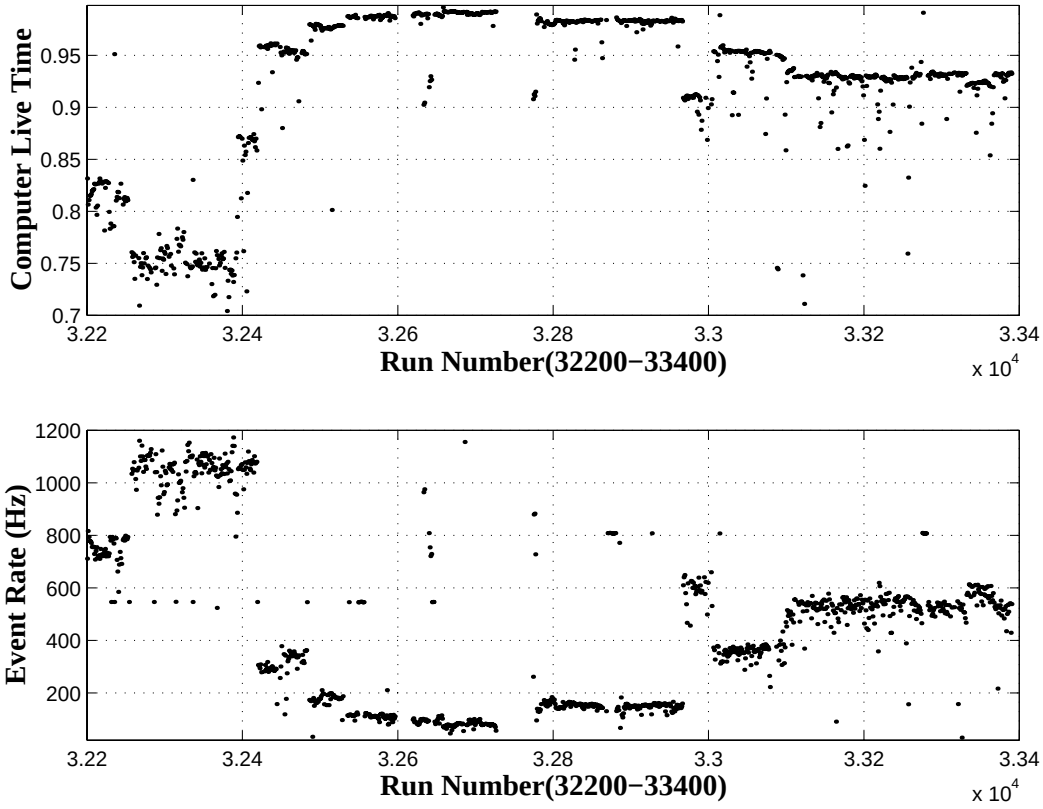

Figure 2.25: Event rate and computer live time for the runs. SOS SCIN trigger mode was 3/4 before run 32421. After that, it was changed to 4/4. DAQ was in buffered mode after run 32394.

lose of kaon events. The trigger rates versus run number are shown in Figure 2.25. With 3/4 mode, the trigger rate was about 1 kHz for 0.6 μA beam. When changed to 4/4 trigger started from run 32421, the trigger rate dropped to below 400 HZ with the same current.

The SOS PRETRIG was converted to ECL for input into a LeCroy 8LM programmable logic matrix. The busy output from the CEBAF Trigger Supervisor (TS) was the third input into the 8LM. The 8LM, in general case in parallel, produces the coincidence signal, singles HMS, and singles SOS. In our case, we didn't use HMS (Hall

C High Momentum Spectrometer) and coincidence. Only single SOS signal was produced by the 8LM. The other input signal to the 8LM were PEDPRE trigger and the run control signals TS EN1 and TS GO generated by the trigger supervisor.

Trigger Supervisor is the interface between the trigger hardware and the computer data acquisition system (DAQ). To reduce the data rate, the TDCs and ADCs are typically run in "sparsified" mode controlled by the TS. In this mode, TDCs don't give a output for a channel without stop signal after a preset time. A threshold is set for each channel of ADC (LeCroy 1881M) by TS and signal lower than the threshold will not be recorded. That means no pedestal values recorded for ADC during normal data taking. Thus a fixed number (typical 1000) of PEDPRE trigger signals generated by a pulser is created at the begining of each run as a random trigger for which sparsified mode is disable. This allows the DAQ to record a fixed number of pedestal events. The TS GO signal is just at the start of each run to signal the DAQ to start. The EN1 signals the end of PED trigger.

The final SOS kaon triggers used in most of the runs of 1.864 GeV beam energy were: $(SCIN3/4) \bullet \overline{GC} \bullet \overline{AC} \bullet LC \bullet \overline{SH}$ and $(SCIN4/4) \bullet \overline{GC} \bullet \overline{AC} \bullet LC \bullet \overline{SH}$. For some run period, the outside 4 scintillator bars (S1X1, S1X2, S1X8, S1X9) of SOS hodoscope plane S1X were used as veto ($\overline{S1X}$). For 1.721 GeV beam energy, it was $(SCIN4/4) \bullet \overline{GC} \bullet \overline{AC} \bullet \overline{SH}$. Prescaled pion trigger B was also taken in for some runs. The output SOS trigger signal from TS was sent to TDCs as start or stop and also to ADCs as gate signal.

2.8.1 Trigger Rates

The rate at which triggers can be taken was limited by the time required for the DAQ system to read out the data. Currently the time required is 100 μs for fastbus conversion plus 300 μs for fastbus readout and transporting the fastbus information through VME to the FDDI in parallel mode [44]. This is about 400 μs per event and limits the trigger rate to $\sim$ 2 kHz. However, the dead time is still large for rates well below this limit. For trigger rate of 700 HZ, the computer dead time is $\sim$ 17%. To improve this, the fastbus modules can operate in buffered mode in which they buffer 8 events in the memory before being read out by the computer. This allows the trigger supervisor to accept new triggers as soon as the fastbus conversion is done, instead of waiting for the additional readout time.

Figure 2.25 plots the computer live time (= 1 – dead time) with run number. We can see the computer dead time was greatly reduced after buffered mode was used after run 32394.

2.9 Data Summary

The E89009 data composed of $\sim$ 3100 runs, among them $\sim$ 2500 were production runs. The total charge of production runs is $\sim$ 1050 mC. Table 2.8 lists the run conditions and accumulated electron charges on ^{12}C and CH_2 targets in each run period.

Table 2.8: Run conditions and accumulated charges for different run periods.

Data Set No.	Beam Energy (GeV)	Beam Current (μA)	Target	Trigger ($\overline{GC} \bullet \overline{AC} \bullet \overline{SH} \bullet T$)	Beam Charge (mC)
1	1.864	0.4	^{12}C	T=(3/4or4/4) • LC	23
2	1.864	0.5-0.6	^{12}C	T=(3/4)•LC(or•$\overline{S1X}$	177
3	1.864	1.0	CH_2	T=(3/4) • LC • $\overline{S1X}$	82
4	1.864	0.35	^{12}C	T=(4/4) • LC	38
5	1.864	0.6	^{12}C	T=(4/4) • LC	62
6	1.864	0.5	CH_2	T=(4/4) • LC	235
7	1.721	0.22	^{12}C	T=(4/4)	99
8	1.721	1.	CH_2	T=(4/4)	154
9	1.721	0.6	^{12}C	T=(4/4)	212

CHAPTER 3

DATA ANALYSIS AND CALIBRATION

3.1 Overview

The raw quantities from ADCs, TDCs and scalers are converted into physical quantities by event reconstruction program. The event reconstruction program reads in the raw events, decodes the detector hits, extracts particle tracks, timing and particle identification information for each event. Hardware scaler information from different scalers to monitor the detectors is also extracted and software scalers are created. Other than the spectrometer information, the beam line information such as the beam position, beam current, magnetic current and field which were fed in by the DAQ system is extracted. The reconstruction software outputs the result in three formats: PAW Ntuple, PAW histogram or plain data format. The histogram format is especially useful to monitor the experiment running online.

The HNSS event reconstruction software is composed of three parts: the SOS reconstruction part, ESPS part and the coincidence part. The SOS event reconstruction performs particle tracking, time of flight measurement and extracts particle identification (PID) information. The particle momentum and target quantities including angle and time are calculated from focal plane quantities by a reconstruction matrix. It is part of Hall C standard data analysis software and has been tested in previous Hall C experiments. The electron arm – ESPS part and coincidence part were specially developed for

HNSS data analysis. It extracts particle hit position on the SSD detectors, determines the electron time and momentum, and calculates the coincidence time with kaon arm.

3.2 SOS Event Reconstruction

The SOS event reconstruction procedure is shown in the flow chart Figure 3.1 [49]. After the raw TDC, ADC hits and scalers stored by different slots, channel numbers in the DAQ crates have been decoded and the corresponding detector variables have been filled by the SOS reconstruction program according to a detector-DAQ channel map file, the physical analysis starts by reading in pedestal events from the first 1000 events of each run. Pedestal values are updated for the ADCs. Warning messages are generated if the new calculated pedestal values are significant different from the DAQ ADC threshold settings.

Next, preliminary hodoscope timing information is extracted without tracking because it is required to determine the drift chamber starting time. The hodoscope TDCs are corrected for the light propagation in the scintillator, pulse height and cable delays. Scintillator time outside a predefined window (usually 100 ns wide) are discarded to reduce random hits. Without tracking informations, SOS central momentum is used for all the events and the path assumed to follow the central ray. Initial time-of-flight beta is fitted from these conditions. The time at which the particles pass the focal plane is extrapolated from the hodoscope time. This is used as start time for the SOS DC drift time measurement. The drift time is converted into drift distance from a calibrated SOS DC drift distance-drift time correlation. In addition, small corrections are also made for the time it takes for the signal to transmit along the wire.

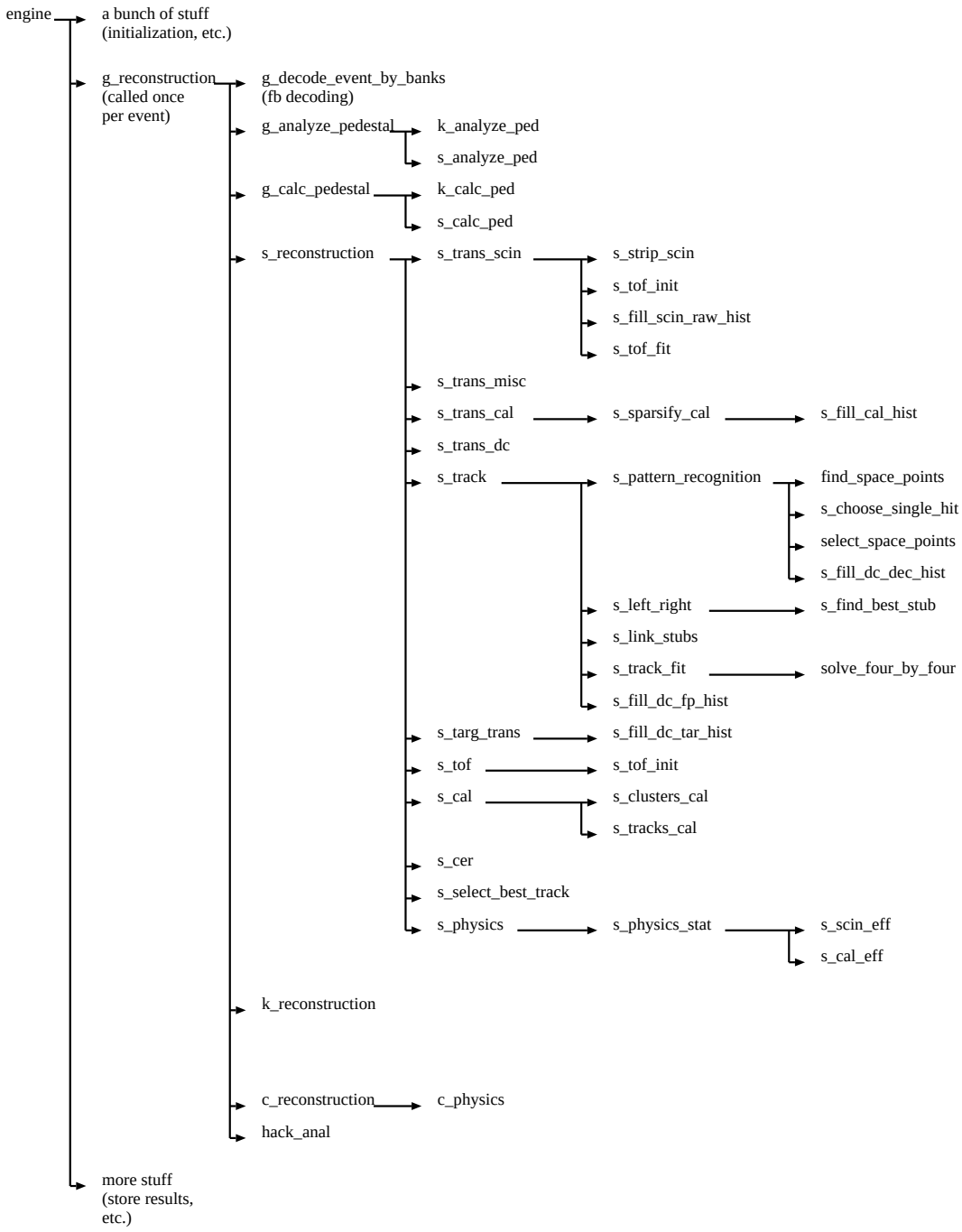

Figure 3.1: Flow chart of Hall C data analysis software, *engine.f*. The SOS aerogel and Lucite analysis subroutines,*s_aerogel.f* and *s_lucite.f* are not shown.

Next, the SOS shower counter and Čerenkov hits are decoded and track independent quantities are calculated and tracking routine is called.

3.2.1 Tracking

Particle trajectory in the SOS is determined by two sets of drift chambers, each has 6 wire planes. The hit position of a particle on a wire plane is determined by the wire position which gets the hit plus an offset with a closet-approach distance to the wire. The tracking algorithm is based on the assumption that the incident particles in the focal plane have a small angle spreading and are nearly normal to the drift chamber [50], as is the case for SOS: the angle spreading is within $\pm 6^\circ$ in the bending direction and $\pm 2^\circ$ out-of-plane direction.

Each two crossed wires that fired constitute a "pair". For the pair, the position can be determined by their intersection without the drift time information. In each chamber package, all of the pairs are then grouped into "combinations". The criterion to assign pairs to one combination is the square root of sum of their squared distance between the intersections. For one combination, the value should be less than a constant – the space point criterion – which is usually set at 1.2 cm. A space point is recognized if it is belong to at least one hit-pair combination.

When a wire gets hit, the particle can pass through left or right of the wire. To solve this left-right ambiguity, all three of the SOS wire planes X, U, V have their primed planes X', U', V' which have 0.5 cm , half the drift cell size, offset from unprimed planes. Thus if both primed and unprimed planes fires, we can require the hit point to be located between the wire centers. In the case of one of the two planes is missing, we can fit a

track to each chamber package and pick the fit with the best χ^2 to solve the left-right ambiguity. This track is called "stub" because it only uses hits information from one chamber set. Then stubs from the front and back chamber packages are combined into tracks if the difference of each of the stub fit track parameters is less than the test criterion. Finally, a track is fitted from all the space points by minimizing χ^2.

After proper calibration, the SOS wire planes should have good position resolution. During HNSS experiment, the tracking residues for all chamber planes were within 0.02 cm (average is 0.017 cm) in σ.

3.2.2 Hodoscope Timing Measurement

Time of flight of charged particles in SOS is measured using the scintillation hodoscopes. The time of flight β are calculated track by track. For each track, only the hits that come from the scintillators that on the track of the particle are selected, other hits are discarded to reduce noise hits. The hit position on the scintillator is calculated as the intersection of the track with the scintillator. Then the distance to the PMTs at both ends and therefore light transmitting time can be calculated. Hodoscope TDCs are corrected for light propagation in the scintillator, the pulse height and the cable delays. If PMTs at both ends of scintillator have hits, the average time of both PMTs are taken.

From the particle coordinates and angles at the SOS focal plane, the traveling distance of the particle from the virtual focal plane to each hodoscope plane is calculated, combined with the time when particles pass through each scintillator relative to SOS trigger, the time of flight β can be extracted by a least square fitting. Valid fitting of β requires at least two scintillator hits, one comes from the front two hodoscope planes

S1X or S1Y and the other from the back two hodoscope planes S2X or S2Y. Otherwise β is undetermined. This TOF β information can be used in PID, because β is directly related to particles mass as in equation 2.14.

The focal plane time (the time when the particle passes through the virtual focal plane) relative to SOS trigger is also extrapolated from the time measurements of hodoscope planes. For this purpose the particle velocity β is calculated by the formula 2.14 from the reconstructed particle momentum p and assumed particle mass, which is generally the kind of particle that SOS is looking for, in our case, the kaons. Because the p measurement is very precise ($\sim 10^{-4}$), the β calculated by this method is generally more accurate than the TOF β. A focal plane time can be extrapolated from each hodoscope plane time measurement. Their average is taken to be the proper focal plane time of the event.

During the 1.864 GeV running period, hodoscope S2X8+ PMT used accidentally a longer delay cable, this caused a 15 ns more delay than other hodoscope channels. In the SCIN 4/4 trigger mode, the signals from S2X8+ for the events passing through this scintillator caused the delay of the trigger for 15 ns. Figure 3.2 shows the TDC spectrum of S2X8+. We can see the sharp (almost single bin) self-timing peak containing events triggered (thus started) by S2X8+ signal and stopped by S2X8+ itself. The calculated focal plane time relative to SOS trigger also had a 15 ns offset. Due to this long delay, scintillator timing parameters had a little change. Thus a special timing calibration for the events associated with this PMT was done.

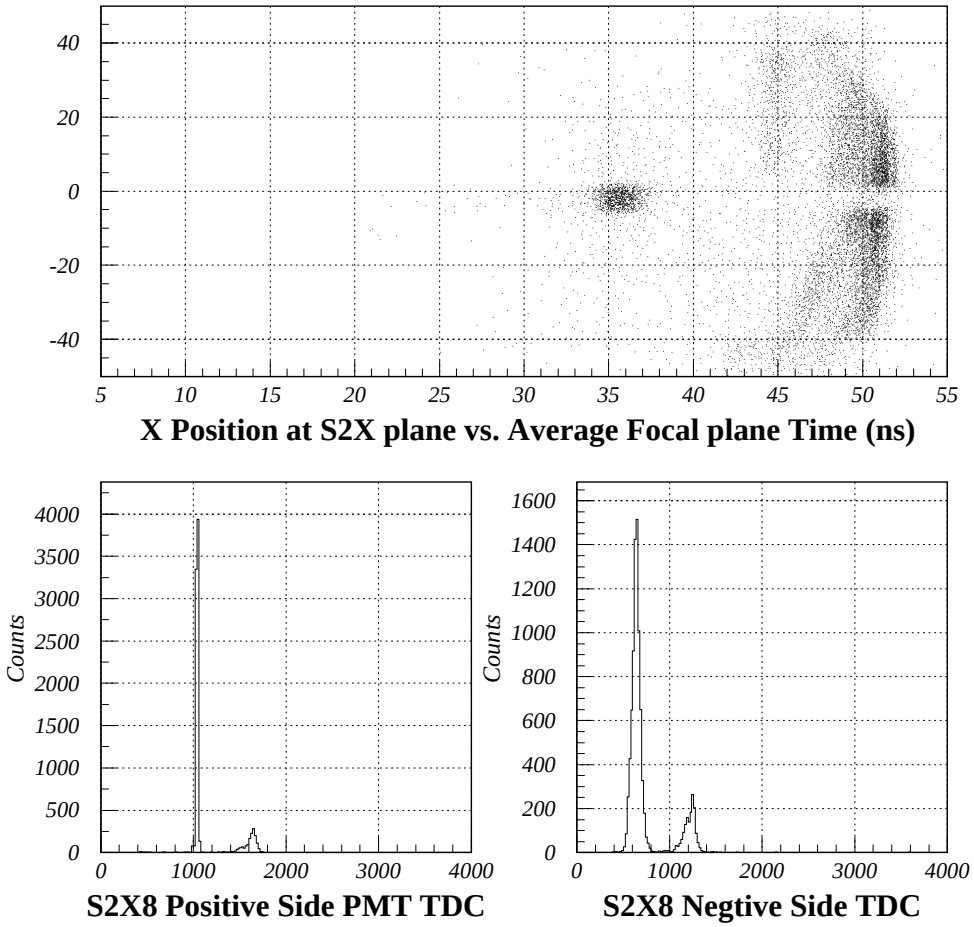

Figure 3.2: Time shift of SOS hodoscope S2X8+ PMT. Bottom two histograms show the TDCs from the two PMTs at both ends of the scintillator.

3.2.3 SOS Shower Counter and Čerenkovs

SOS shower counter information was used in E89009 to remove e^+ events. The shower counter ADCs from each block was converted to energy and summed together. The ratio of total energy to the particle energy calculated from momentum:

$$\text{sshtrk} = \frac{\text{shower energy}}{p} \tag{3.1}$$

gives the PID information. For electron (and positron) this value is close to 1 because they tend to deposit all their energy in calorimeter by EM shower. For $\beta \neq 1$ particles, this value is 0.5 or lower.

The ADCs from the Čerenkov counters were converted into number of photoelectrons. Except the lucite Čerenkov, the signals from all counters of one type of Čerenkov were summed together to give the total n.p.e. The SOS lucite Čerenkov was segmented. Thus tracking information was used and only Čerenkov signals from the counters on the particle track were summer together. This helped to reduce background noise hits.

3.2.4 SOS Target Reconstruction

The target physical quantities were calculated from the focal plane quantities. SOS spectrometer is what we called a "software spectrometer", which means the full coordinates and angles in the focal plane are measured and used in the reconstruction of target quantities. In point-to-point tune, four measured quantities in the reconstruction plane are X_FP, XP_FP, Y_FP, YP_FP, where X_FP and Y_FP are the coordinates in the bending and nonbending directions, respectively. XP_FP and YP_FP are tangent of

in-plane and out-of-plane angles θ and ϕ,

$$XP\_FP = \tan(\theta) = V_x/V_z \tag{3.2}$$

$$XP\_FP = \tan(\phi) = V_y/V_z. \tag{3.3}$$

In the SOS coordinate system, X points down, Y points to the left and Z follows the central trajectory. The corresponding four target quantities are XP_TAR, Y_TAR, YP_TAR and δp ($= \frac{p-p_0}{p_0}$ in %). Target position in the bending direction X_TAR is fixed. The target quantities and the focal plane quantities are related by the transformation:

$$Y_i = \sum_{j,k,l,m=0}^{N} R^i_{jklm}(X\_FP)^j(XP\_FP)^k(Y\_FP)^l(YP\_FP)^m, \tag{3.4}$$

where Y_i is one of the four target quantities and N is the order of the transformation. R^i_{jklm} is commonly referred to as a reconstruction matrix element.

In E89009, point targets was used. Target position was fixed both in X (X_TAR) and Y (Y_TAR) direction.

A high missing mass resolution relied heavily on the reconstruction precision, especially δp, because kaon momentum was the largest contribution to the missing mass resolution For HNSS. Thus the reconstruction matrix was carefully calibrated. It was fitted from a Raytrace simulation that was tuned based on the sieve slit data.

The focal plane time calculated from hodoscope timing had to be corrected by the particle flying time from the target to the focal plane to get the time when it was produced from the target. Different events have different trajectories, hence different

flying times. The total path length can be expressed as the central path length plus path length correction, so that we have,

$$\text{Time of Flight in Spectrometer} = \frac{\text{Central Path Length} + \text{Path Length Correction}}{\text{Velocity}} \tag{3.5}$$

and

$$\text{SOS Target Time} = \text{SOS Focal plane time} - \text{Time of Flight in Spectrometer.} \tag{3.6}$$

The central path length was extracted from SOS optics simulation Raytrace as 752.3 cm. The path length correction can be expressed as a function of focal plane quantities. Initial path length correction can be extracted from the Raytrace simulation. But the final expression was further calibrated by utilizing the RF structure of CEBAF beam.

3.3 ESPS Event Reconstruction

As previously mentioned, no focal plane tracking needed for ESPS and there was no online trigger signal from ESPS. PID was needed neither for ESPS because no other negative charged particles had significant presence in the electron arm other that e$'$ (e^- to π^- ratio was larger than 10^4 and no physical real (π^-,K^+) coincidence within kinematic acceptance of HNSS). The objective of ESPS event reconstruction was to extract hit position on SSD detector and determine the hit time from hodoscope. The event analysis of ESPS was relatively simple compared with SOS. However, due to more than 100 MHz e$'$ rate in the ESPS arm, a careful event selection had to be carried out

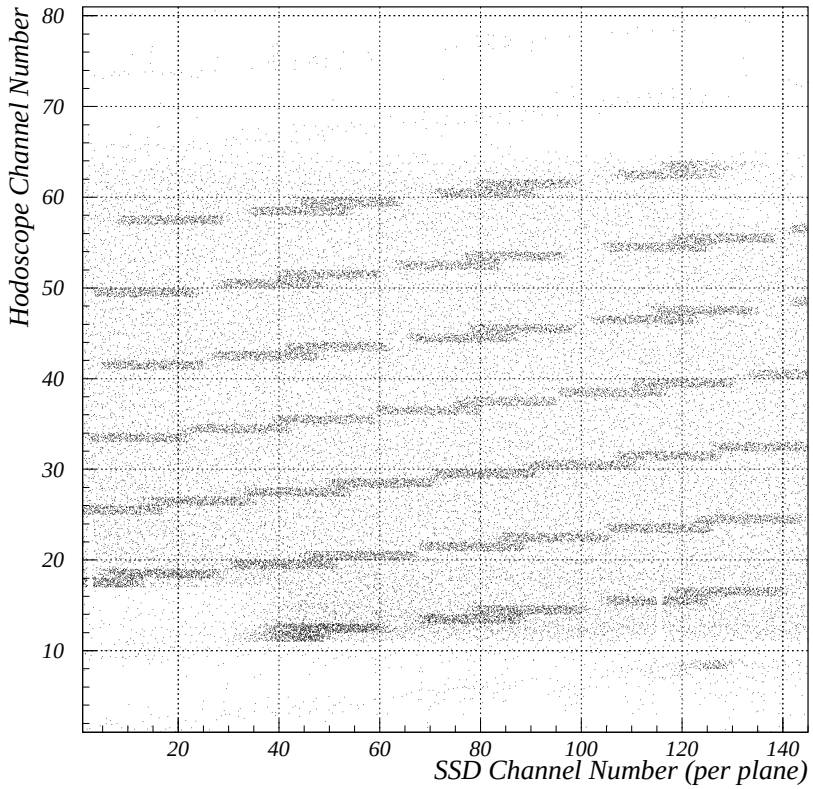

Figure 3.3: SSD and hodoscope channel number correspondence. The dense lines represent real events, each segment representing one scintillator channel, one tilted row representing one SSD plane. From bottom up, they are plane 1 to 9.

to reduce the huge background noise and hodoscope multiplicity.

Each SSD plane had 8 hodoscope elements behind them. For fixed optics, real e' events from the target incident into the SSD and hodoscope with almost fixed angles. This caused a correspondence between the SSD channel number and hodoscope channel number. In Figure 3.3, the events satisfying this channel correspondence can be clearly seen as dense line. The background events were those SSD hits without a correspondent hodoscope hits. Thus each hodoscope channel was assigned a SSD channel gate, only events within this gate could survive the selection. Another selection criterion was the

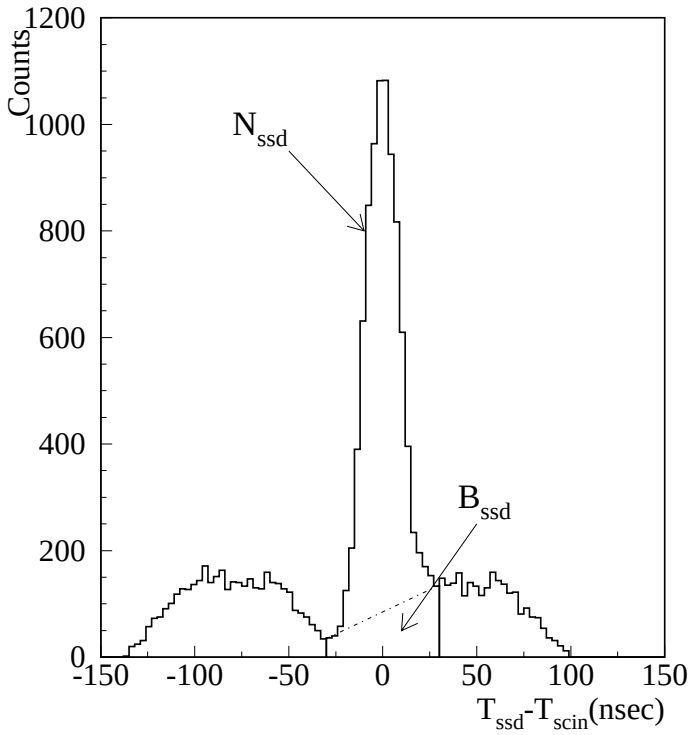

Figure 3.4: SSD and hodoscope time difference. A gate at ±30 ns was used to select real events. N_{ssd} denote the counts in the real coincidence window. B_{ssd} denote the accidental background under the real coincidence peak. The reason for the asymmetry of background to the left and right of the true peak is explained in the text.

hodoscope and SSD time coincidence. SSD and hodoscope were mounted closely hence their time difference should be close to zero. Figure 3.4 is the time difference spectrum. SSD had a wide time resolution of 50 ns (full width). A gate at ± 30 ns was used to select real events. The accidental background at the left and right of the true peak show asymmetry because SSD used multihit TDCs but hodoscope used single hit TDC. The events in which a hodoscope hit with a time earlier than the real hit accidentally coincident with a SSD hit later than it were present in the accidental background at the right of the true peak. However, its counterparts, events in which a hodoscope hit later than the real hit accidentally coincident with a SSD hit earlier than it were greatly suppressed because the real hodoscope hit already stopped the single hit TDC. After the event selection, SSD hit were combined with hodoscope hit (single or multiple hits) to form a track.

To reduce the double counts from the particles passing through two overlapped scintillator strips, their time differences were tested (Figure 2.23). If the two overlapped hodoscopes had hits within 3 ns of each other, the two tracks were combined into one track with an average time.

Next, SSD multiple hits were treated. If the firing channels were connected, they formed a cluster and their average position was extracted. Thus different tracks could be combined to form events. Adjacent SSD planes also had overlap channels. Particle passing through this region would have double hits. To recognize these events, momentum of each event was calculated from the SSD channels. If their momentum were close enough, these events registered separately by two SSD planes were treated as one event. Because the precise relation between SSD channel and momentum was

not available before the experiment, a loose test $|dP| \leq 1$ MeV (corresponding to 5–8 SSD channels) was applied. For particle which hit two overlapped SSD planes, only the position in the front SSD plane was taken. A more complete treatment of the SSD overlapped channels was in offline analysis after the precise overlapped SSD channel to channel correspondence for adjacent SSD planes was obtained from SSD hit pattern.

The ESPS hodoscope time needed also be corrected for the pulse height, cable delay and flying time in the spectrometer. The ESPS-SOS coincidence time in the target is:

$$\text{coincidence time} = \text{corrected ESPS time} - \text{SOS Target time}. \tag{3.7}$$

The e$'$ momentum was calculated offline because SSD channel-momentum relation was not available before the experiment.

3.4 SOS Detector Calibration

3.4.1 Drift Chamber Calibration

The signal from the drift chambers is drift time: the time starting from the moment when particle pass through the wire plane to the ionized electrons reach the sense wire. The time is correlated to the distance of the hit position from the wire. The analysis program converts the drift time to drift distance by a time-to-distance map, one for each chamber plane. To determine this map. we used the drift time distribution from each wire of a plane (Figure 3.5). First, the start offset of drift time for each plane was corrected to move the front edge of the distribution to zero because the cable delays

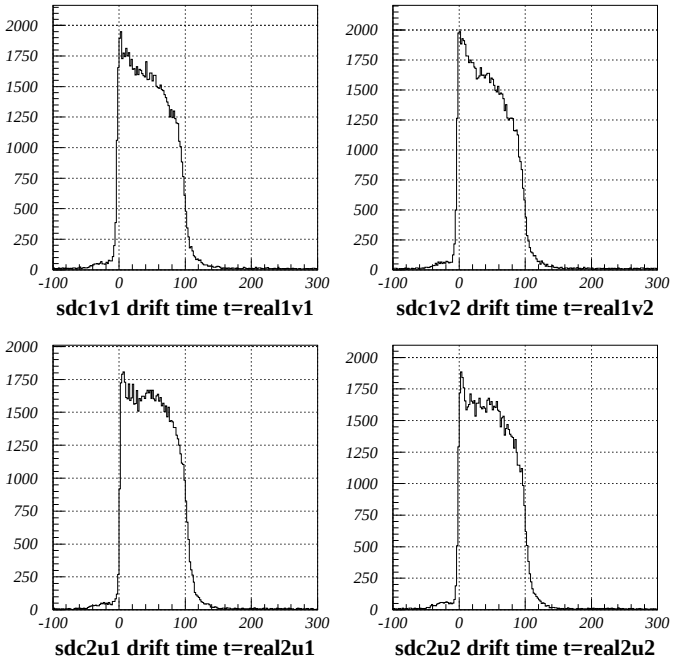

Figure 3.5: Sample SOS drift chamber drift time distributions. These distribution were used to do the time-to-distance map calibration.

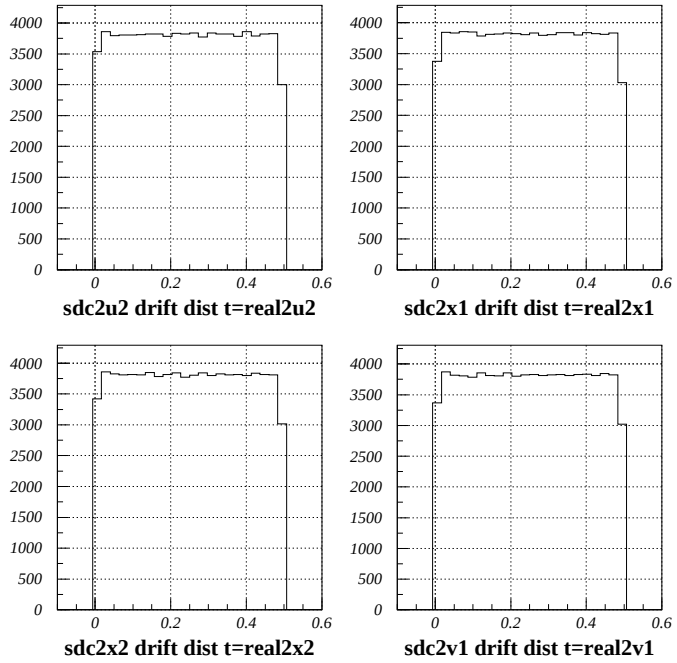

Figure 3.6: Sample SOS drift chamber drift distance distributions after the calibration of time-to-distance map . The flat top means the calibration was done properly.

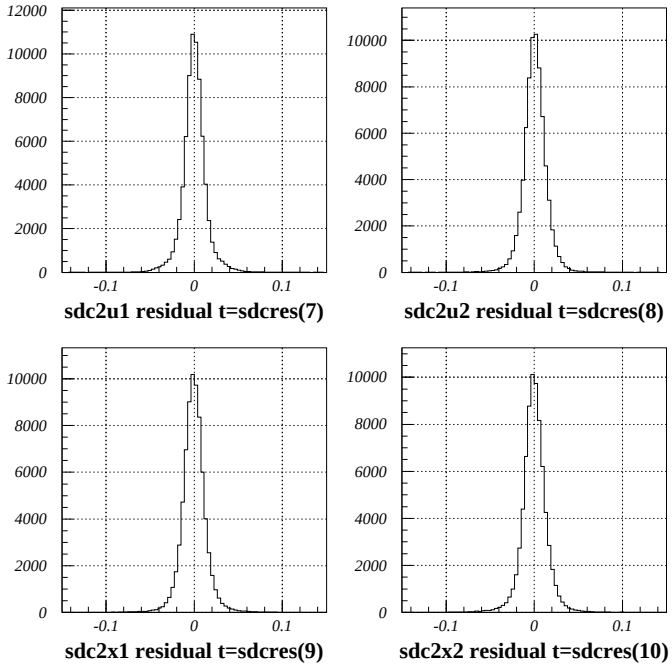

Figure 3.7: Typical SOS drift chamber track fitting residues. These residues are the differences between the hit position on a wire plane and the intersection of the fitted tracks. The width of the distribution indicate the tracking error.

and the distances of the chambers to focal plane were different. After averaging over all wires from one plane, the drift chamber should be uniformly illuminated in a half drifting cell range (0.5cm). This corresponds to a uniform drift distance distribution or constant drift velocity. The time-distance map that can produce this uniform distribution is:

$$D = D_{max} \frac{\int_{t_{min}}^{T} F(\tau) d\tau}{\int_{t_{min}}^{t_{max}} F(\tau) d\tau}, \tag{3.8}$$

where D is the drift distance, D_{max} is the maximum drift distance, or the size of half drift cell, 0.5 cm. $F(\tau)$ is the drift time distribution. T is the drift time. The time interval between t_{min} and t_{max} is the drift time gate to reject noise hit. These background noise hits are shown in 3.5 as the flat background. The gate was set from -24 ns to 250 ns.

After drift chamber calibration, the residues of tracking fitting for all the planes were below 0.017 cm(σ), generally about 0.013 cm.

3.4.2 Hodoscope Timing Calibration

The SOS hodoscope TDC can be varied from the real time when the scintillator bar gets the hit relative to the trigger. The sources include: time variations for the light to transmit from the hit point to the PMTs at ends of the scintillator bar; traveling time variations for the signal to be sent through long cables upstairs; time walk from pulse height variations relative to the fixed discriminator threshold. All these variations need to be corrected.

The first step in the calibration process was to calibrate the hodoscope TDC scales (ps/channel). Then corrections had to be made for timing variations caused by

light propagation time in the scintillators. They are generally very stable. On the other hand, time offsets change when electronics room temperature and counting rate varies significantly, thus they need to be calibrated more frequently.

For the fixed discriminator threshold, the time when the signal passes the threshold depends on the shape and height of the pulse. There was a clear correlation between time variation and pulse height for one kind of particle (Figure 3.8). The function used to correct for the time variation caused by pulse height was:

$$\Delta t = PHC * \sqrt{\max(0, \frac{ADC}{PHOFF} - 1)} + t_0 \tag{3.9}$$

where ADC is the raw ADC from the corresponding scintillator PMT, t_0 is the time offset between two counters and PHC and PHOFF are the parameters to be determined for every counter of hodoscopes by calibration procedure.

The calibration procedure used the time difference between two counters. To reduce the effect of light propagation time difference in the scintillator, "crossed pair" scintillators were used, i.e., one scintillator in X direction, the other one in Y direction, so that the particles passed through both scintillator had limited transverse illumination range along the scintillators [51]. Generally, the scintillators in the center region of the hodoscope planes get the most hits and tend to have better calibration, thus in order to increase statistics, one of the scintillators in the cross pair was from a sets of "reference counters" located near the center of hodoscope planes: in X direction, they were 3,5,7, while 4 and 6 in Y direction. The S1X5 counter in the center was the "absolute reference", meaning that all the time differences thus all the timing parameters of other

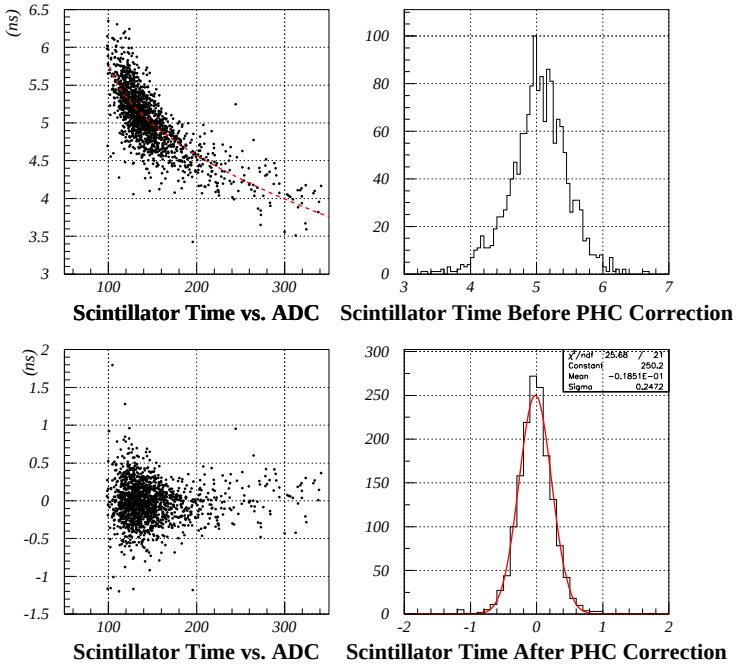

Figure 3.8: Scintillator pulse height correction for scintillator S1X04p. The scintillator time in the Y-axis of the scatter plots is actually time difference between S1X04p and a reference counter. The dash line is overlaid function relation of time to ADC according to Equation 3.9 with parameters: $PHC = -1.4$ and $PHOFF = 98.2$. The time resolution after PHC correction was $0.25/\sqrt{2} = 0.18$ ns (σ).

Table 3.1: Time resolutions (σ) of SOS hodoscope planes.

Plane	S1X	S1Y	S2X	S2Y
Time Resolution σ (ns)	0.19	0.19	0.22	0.16

counters were relative to S1X5. Calibration was first done on the cross pairs within the reference counters: S1Y4 to S1X5, S1Y6 to S1X5. Then S1X3 and S1X7 to both reference counters S1Y4 and S1Y6. After that, all the other counters were calibrated relative to their crossed pairs from the set of reference counters. The input data for the timing calibration came from the output of Hall C SOS analysis code. For the purpose of calibration, a single type of particles must be selected so that the particle velocity β can be calculated from the momentum and known mass without TOF information. To calibrate pulse height correction for kaons, it is desirable to select kaons. But due to the scarcity of kaons, to get enough statistics for the calibration, many runs had to be accumulated. If just checking the validity of pulse height correction, pions with β close to kaons may be used. For each PMT to be calibrated, the calibration program used the tracking information, scintillator position and the known β with initial timing parameters of its crossed reference scintillator to calculate the path length corrected time difference to the reference scintillator. The time from the the reference scintillator was the mean time of the PMTs on both ends.

A sample SOS scintillator time difference distribution is shown in Figure 3.8. The time resolution of a hodoscope plane is the average of all its elements. Table 3.1 lists the time resolution of each hodoscope plane.

During E89009, it was found that due to the high positron rate and change of beam

currents, the SOS scintillator time offsets were varied between run periods. Especially for S1X5, the one which got the most positron hits, time offset changed more frequently. This can be seen by path length corrected S1X and S1Y time difference (Figure 3.9). It should be around zero for a proper time offset calibration. Because a large amount of data is required for the TOF calibration, pulse height correction was done by using both pion and kaon events accumulated from several runs. The time offset was corrected from run to run using proton events because of its larger amount.

Particle velocity (TOF β) measurement depends sensitively on the SOS time parameter calibration. For properly calibrated SOS hodoscope time parameters, the difference between TOF β and β_{mK}, $\Delta\beta = \beta_{TOF} - \beta_{mK}$, where β_{mK} is the β calculated by assuming kaon mass and using the known momentum from tracking (Equation 2.14), will be a Gaussian centered at zero and is momentum independent. In SOS, the $\Delta\beta$ resolution (σ) for kaon should be around 0.02. Figure 3.10 shows the kaon $\Delta\beta$ resolution: $\sigma = 0.023$, after subtracting the pion mixed in the tail.

3.4.3 SOS Path Length Calibration

To obtain the time when the particle was scattered from the target, the SOS focal plane time need to be corrected for the flying time of the particle through the spectrometer from target to focal plane. As explained in Section 3.2.4, this correction was expressed as the central path length (constant) plus a correction depending on particle trajectory. The particle velocity inside spectrometer was calculated by Equation 2.14, by assuming a particle mass and using the reconstructed momentum. The trajectory correction can be fitted from Raytrace simulation as a polynomial function of focal plane

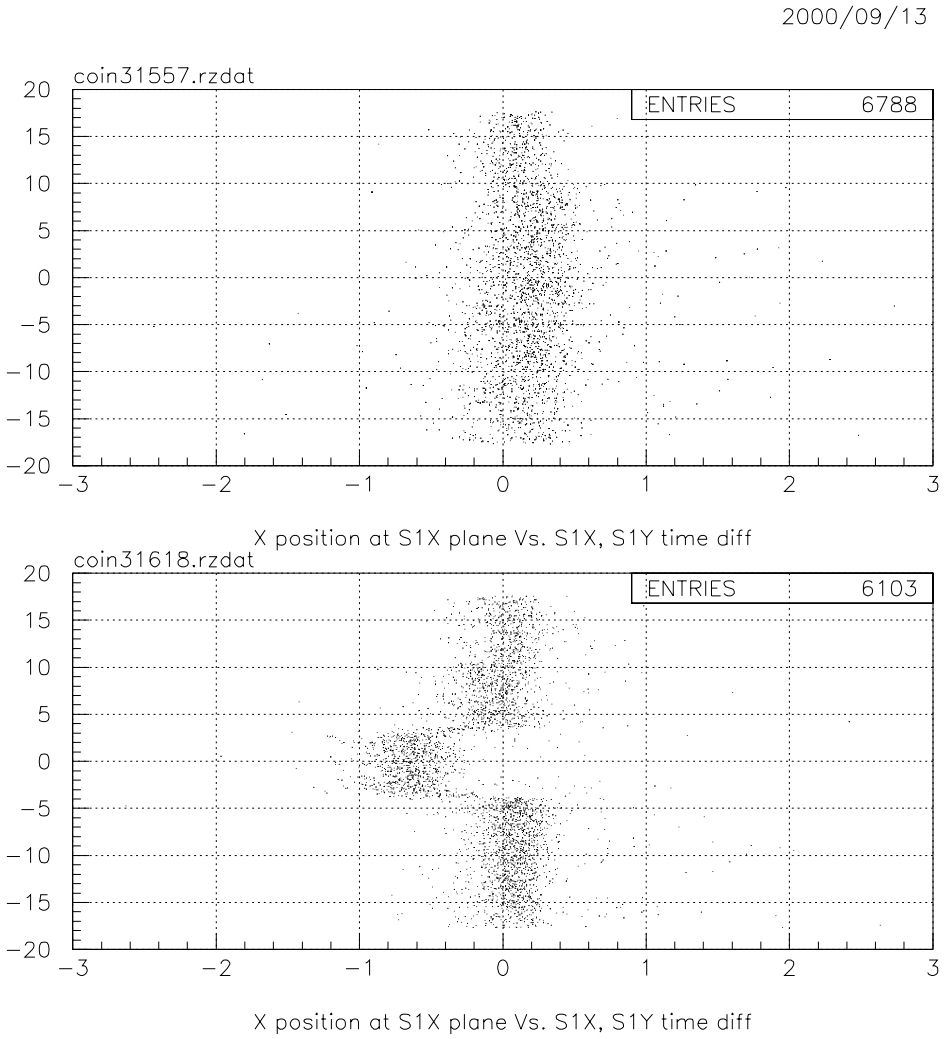

Figure 3.9: SOS scintillator S1X5 time offset. The top plot is for run 31557, the bottom one is for a later run 31618. For run 31557, the time offset for all the scintillators at plane S1X were properly aligned, while for run 31628, the misalignment of S1X5 means its time offset had moved.

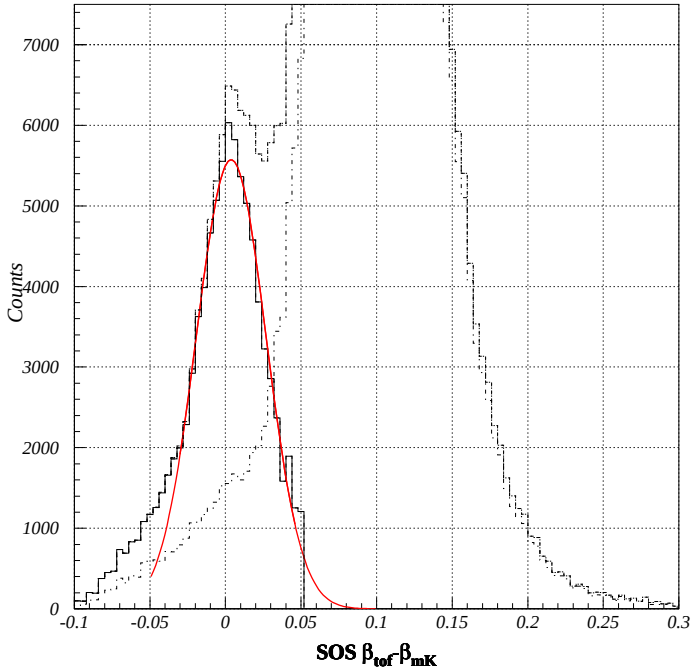

Figure 3.10: SOS kaon $\Delta\beta$ distribution (solid line). The outside dashed line is the summed distribution of kaons and pions. The dash-dot line is the pion distribution.

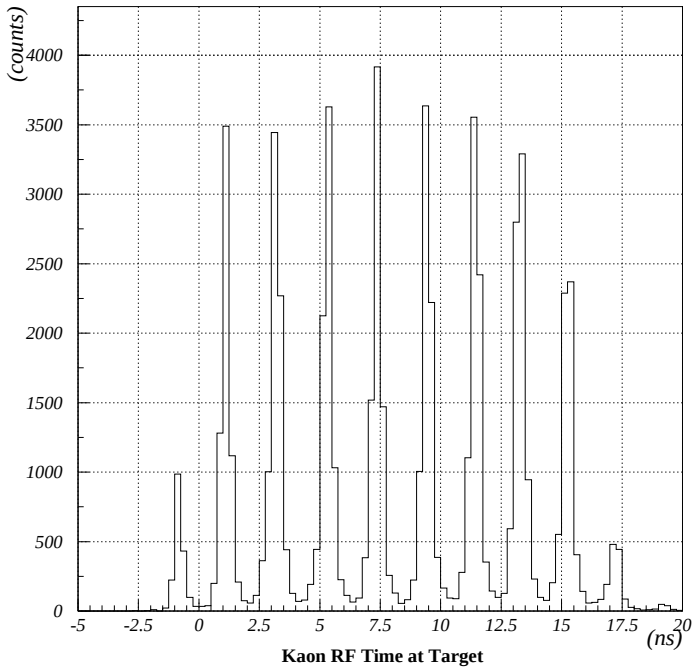

Figure 3.11: SOS target RF time spectrum after correction for path length. The 2 ns beam bucket structure is clearly seen.

quantities. This initial expression was calibrated during the experiment by utilizing the CEBAF 2 ns beam structure.

The CEBAF electron beam has a 499 MHz beam bucket structure. Each bunch has only 2 ps width. This provided a precise time tick on the target. A 499/8 MHz RF signal synchronous with the beam was used to stop a TDC started by SOS trigger. For every 8 beam buckets, such an RF signal was sent out once. Each event from the target originated from one of the eight bunches preceded the RF signal. Thus the target RF time, the RF TDC we mentioned above after corrected the flying time through the spectrometer, must be an integer multiplier of 2 ns. As in shown in Figure 3.11, we can see clearly the 2 ns beam structure. The first and 9th bunches came from the same beam

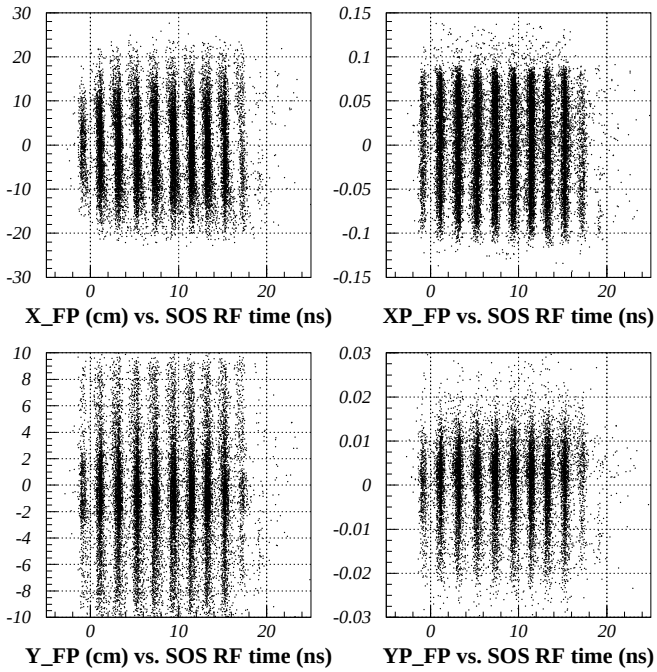

Figure 3.12: Correlation of SOS target RF time with target quantities X_FP, YP_FP, Y_FP and YP_FP after correction for path length. Kaon mass was used in the calculation of particle velocity. The tails in the top and bottom of RF time-X_FP correlation came from pions because wrong mass was used.

bucket. The reason 9th peak appeared is some SOS triggers arrived after the correct RF signal therefore they matched the next RF signal 16 ns later.

If the path length correction is done correctly, the target RF time will all located in an 2 ns grid. Its correlation with target quantities, X_FP, YP_FP, Y_FP, YP_FP, are all straight lines. If there are residue correlations, the average residue correlations can be fitted by a polynomial function. This function need to be added to the initial path length correction to correct for the residue correlations.

The calibrated HNSS kaon arm (splitter+SOS) path length correction was obtained as:

Path Length Correction

$$= 2.519 * XP\_FP - 4.894 * XP\_FP^2 + 0.001 * X\_FP + 0.002 * Y\_FP - 0.01. \quad (3.10)$$

3.4.4 ESPS Hodoscope Time Calibration

The ESPS hodoscope time measurement also need to be corrected for the time variation caused by pulse height, cable delay and path length in the spectrometer. From the optics of ESPS, one hodoscope element got the hits from events with a very small momentum range. The trajectories and path lengths were very close for all events which passed through one scintillator strip and were fixed. Hence time offsets between different scintillators already contained the contributions from the path length variations due to momentum differences and the cable delays.

The time difference of two TDC signals from a event which passed through two

overlapped hodoscope channels was used to calibrate ESPS hodoscope pulse height and time offset (Figure 2.15). The correlation of time difference and scintillator ADC can be corrected by the function:

$$\text{corrected time} = \text{raw time} - \frac{p1}{ADC}, \tag{3.11}$$

where $p1$ is the parameter which was obtained from pulse height calibration. When count rate for a single scintillator exceeded 1.5 MHz, the PMT pulse pile-up effect will showed up. This effect is shown as the big bunch of tail in the scintillator TDC-ADC correlation histogram (Figure 3.13). These events can not be well corrected for the pulse height, hence introduce error in the ESPS time resolution and the final e′K coincidence time.

One problem with this hodoscope calibration method is that not all scintillators had overlapped partners. To overcome this problem, the time measurement from each ESPS hodoscope element was combined with the SOS time measurement to calculate the coincidence time between the two arms. ESPS time calibration can be done by aligning the centers of real coincidence peaks for all the elements. Due to high background, large amount of events was needed for each hodoscope element to accumulate enough statistics to recognize clearly the center position of real coincidence peak. Thus special runs for ESPS hodoscope time calibration with SOS triggered on positrons were taken during the experiment at each different run period. Proton events were used off-line to check the coincidence time spectrum for all the elements and time offset parameters were corrected when necessary.

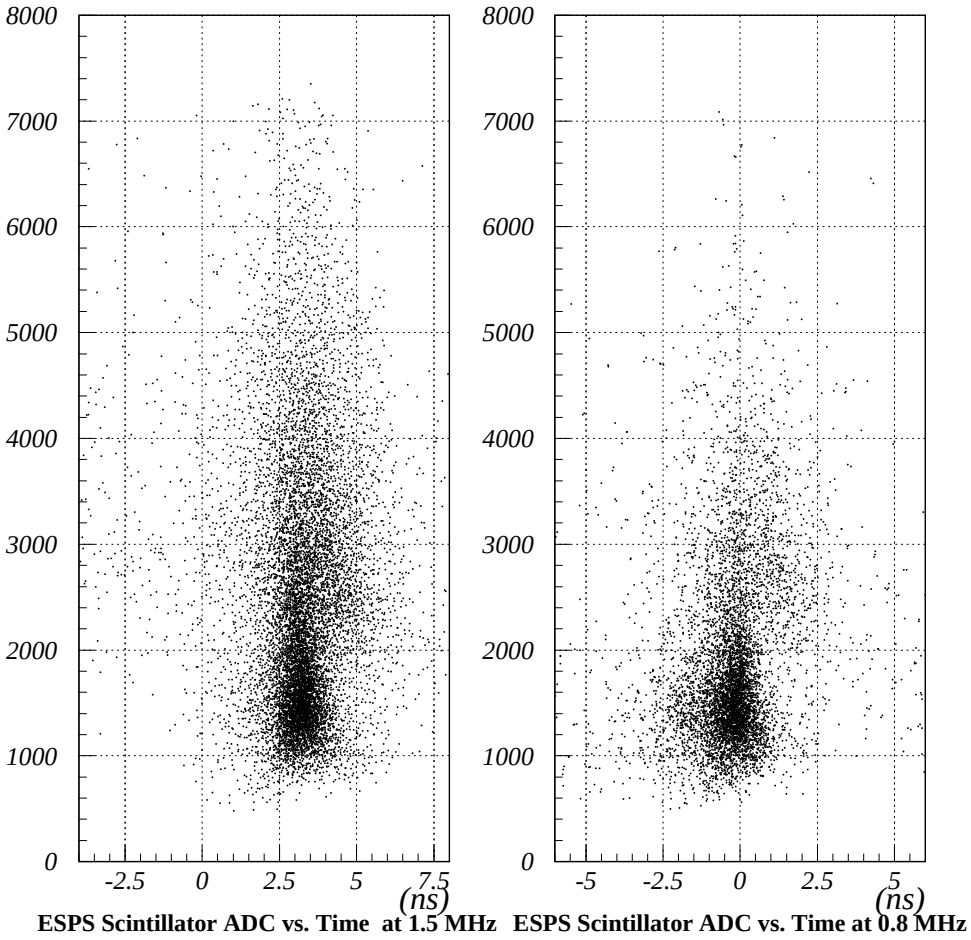

Figure 3.13: ESPS scintillator ADC vs. time after PHC correction. At high e′ rate, the PMT pulse pile-up effect showed up as dense tail in the graph.

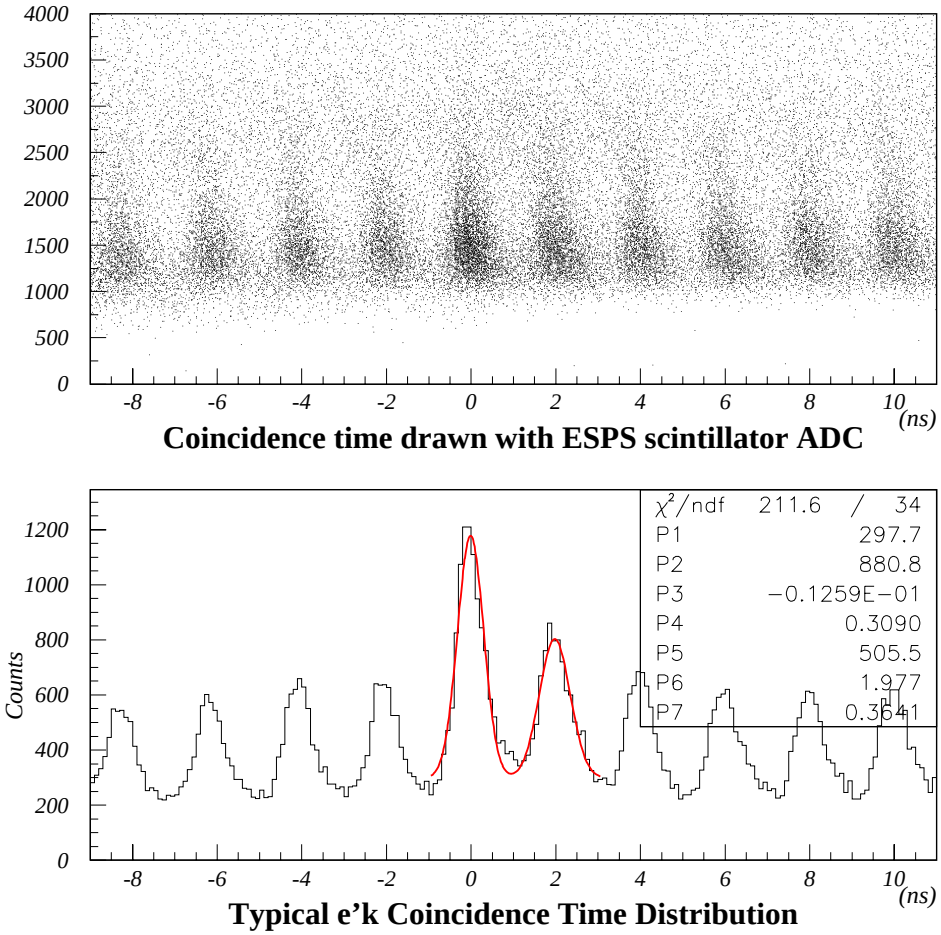

Figure 3.14: Top, e′K coincidence time drawn with ESPS scintillator ADC. The dense band around 0 ns contains the in-time events. Bottom, a typical e′K coincidence time spectrum. The overlaid function is a fit to the in-time peak and the first out-of-time peak to the left. The fitting function is two Gaussian plus a flat background.

A typical e′K coincidence time spectrum is shown in Figure 3.14. The background under the peaks came from ESPS multiplicity events and the hodoscope pile-up effect due to high e′ rate. The average resolution of the coincidence time was $\sigma = 0.36$ ns.

3.5 SOS and Splitter Optics Calibration

The standard procedure to obtain SOS reconstruction matrix is using sieve-slit runs: fitting the coefficients of equation 3.4 according to the correlation between measured focal plane quantities and the known target angles and position for the events that come from corresponding sieve slit holes. Each hole selects a specific pair of in-plane and out-of-plane angles independent on momentum [52].

In HNSS case, due to the existence of splitter before the sieve-slit, target angles were already deflected by the splitter field before particles entering the sieve-slit. Angle-momentum correlation arose from the splitter field. Therefore, the target angles were no longer known by the slit hole locations and depend on splitter optics. The Hall C standard procedure to get the reconstruction matrix cannot be used for HNSS. Instead, we used Raytrace simulation method for optical tuning. Our approach was first getting a precise Raytrace description for SOS using existing sieve slit data from previous experiments, then adding the splitter part to have combined code. This raytrace code was further tuned during the experiment from the sieve slit data by comparing data to simulations with splitter added. The reconstruction matrix was then fitted from the Raytrace simulation.

3.5.1 Raytrace Overview

Raytrace is an ion-optics simulation program developed at MIT [53]. Its application in spectrometer optics tuning was proposed by L.Tang [54]. Raytrace simulates the motion of charged particle in magnetic and electrical field using step-by-step numerical integration to solve Lorenz equation. A fourth-order Runge-Kutta integration method is used.

Raytrace can treat the optics of both uniform field and non-uniform field magnets of various kinds. Raytrace has a input data card to describe the fringing field effect and the shape of EFB of magnets, as well as collimators.

Figure 3.15 lists part of the Raytrace input data card for HNSS kaon arm. The first two lines of data card provides the general information of the raytrace simulation of a spectrometer: the number of rays to be traced, output coordinate axes option (2 means final output coordinate system is the output coordinate system of the final optics element, see manual for detail), etc. The third line gives the tracking particle information, its central kinetic energy, mass and charge. The following part describes the optical elements of the spectrometer, one paragraph for each element. Each paragraph has a title to denote the kind of ion-optical element it describes. For our HNSS data card, they include: coordinate system shift and rotation (SHRT), field-free drift region (DRIFT), collimator (COLLIMATOR), dipole magnet (DIPOLE), multipole (quadruple, etc.) (POLES). The lines following SENTINEL are the input rays. They give the particle position, incident angles and momentum δp at the target. The first input ray defines the central ray of the spectrometer.

```
SPL+SOS(1.055 GeV/c), mod. quad L.Yuan(10/24/00) from L. Tang (2/26/96)
500002, 201,1,2,0,0,0,
1055.0, 0., 1., 0.0005486, 1.0,
SHRT
0.0, 0.0, 0.0, 0.0, 0.0, 90.0
COLLIMATOR
1.,0.,0.,24.,24.
DIPOLE
4.0, 4.0, 4.0, 4.0, 1.,
0.32, 89.85, 7.62, 275.0467, 1.321    ! 1.27944 --> 1.321
13.45, 5.15, 6.3
0.0, 0.0, 0.0, 0.0,
0.32, -16., -16., 24.
.37503, 1.56166, -.31026, .28577, -.14037, .02153
.37503, 1.56166, -.31026, .28577, -.14037, .02153
0.0, 0.0, 0.0, 0.0, 0.0, 0.0,
0.0, 0.019646,
0., 0., 0., 0., 0., 0., 0.
0., 0., 0., 0., 0., 0., 0.
SHRT
0.0, 0.0, 0.0, 0.0, 0.0, -90.0,
DRIF
23.78
COLLIMATOR
1.,0.,0.,14.,14.
POLES
5.0, 5.0, 5.0,
0.0, 0.0, 70.0, 12.827
-0.60798, -0.00834, 0.0, 0.0, 0.00641,   !-0.61009, -0.00837, 0.0, 0.0, 0.00644
40.0, -16.0, -16.0, 40.0,
0.2486, 5.3626, -2.412, 0.9874, 0.0, 0.0,
0.2486, 5.3626, -2.412, 0.9874, 0.0, 0.0,
0.9, 0.8, 0.7, 0.6, 0.025, 0.05, 0.075, 0.10,
DRIF
-35.0
COLLIMATOR
1.,0.,0.,15.,15.
...

SHRT
0.0, 0.0, 0.0, 0.0, -0.0, 0.3
SHRT
0.8, -0.36, 0.0, 0.037, 0.2, 0.0
SENTINEL
   0.00000   0.00000   0.00000   0.00000   0.00000   0.00000   0.00000
   0.00000   1.00000   0.00000   1.00000   0.00000   0.00000   0.00000
```

Figure 3.15: Part of Raytrace input data card for HNSS kaon arm (splitter+SOS) for 1.864 beam energy setting.

The optical elements that define the optical properties of a magnetic spectrometer are mainly dipoles and multipoles.

The dipole data card includes 12 lines. Line 3 lists information about the magnet pole gap, the field value in central uniform region, the radius of particle trajectory in the central uniform region. The three numbers in line 4 are ϕ, α and β. They are particle bending angle in the magnet along the central trajectory, angles of the central trajectory to the normal direction of effective field boundary at entrance and exit, respectively. Line 7 and 8 give the coefficients C_is used in the expansion of the fringing field fall-off at the entrance and exit of the magnetic element. Consider a particle moving in the median plane of a dipole, the particle will see a magnetic field given by

$$B_y = \frac{B_0 - B_R}{1 + e^S} + B_R, \tag{3.12}$$

which is called a "Enge function", where B_0 is the uniform field, B_R is the asymptotic constant field outside the magnet (normally zero) and S is a function of particle traveling distance from EFB along the central ray Z. S is expressed as:

$$S = C_0 + C_1 s + C_2 s^2 + C_3 s^3 + C_4 s^4 + C_5 s^5 \tag{3.13}$$

and $s = z/D$ where D is the magnet airgap. The coefficients C_is describe the shape of the fringing field fall-off along Z direction. They are generally determined by a least-square fit of function 3.12 to the measured field. As a example, Figure 3.16 shows the entrance fringing field B_y of splitter along the beam path and the fitting with Enge function 3.12.

If the EFB is curved, a correction $\Delta s = \Delta z/D$ is made to Equation 3.12 with Δz

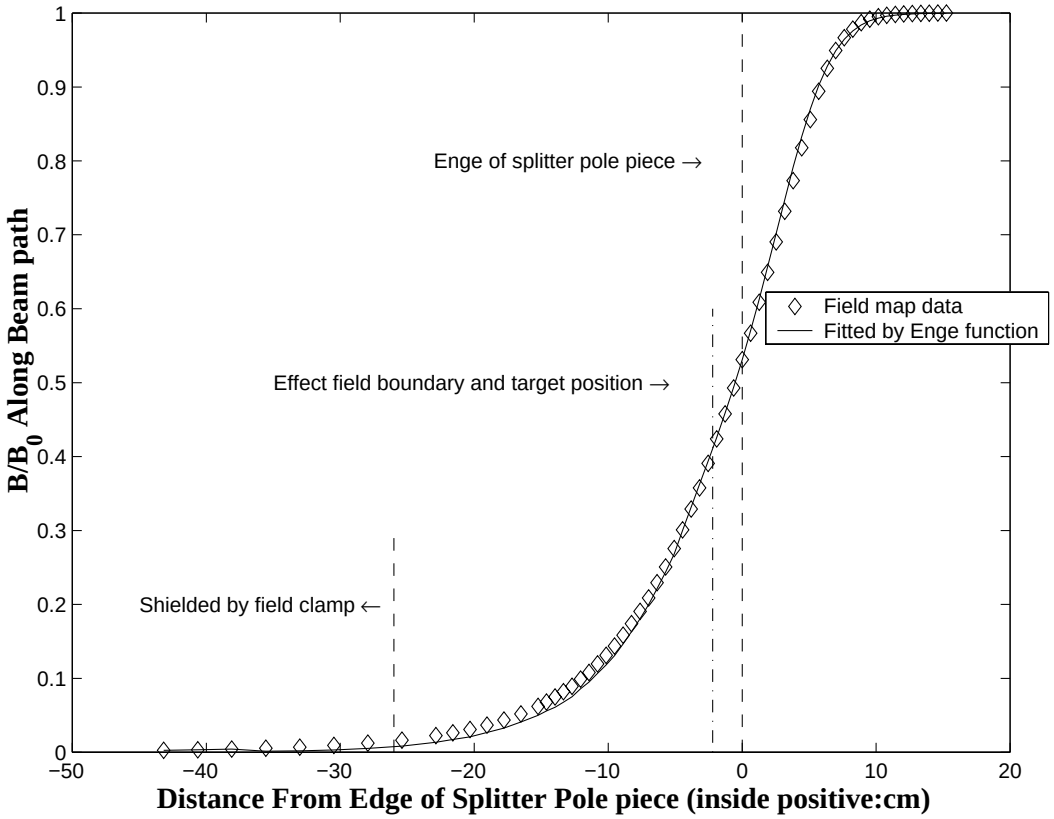

Figure 3.16: B_y/B_0 along the beam path at splitter entrance,where B_y is the fringing field, B_0 is the uniform field inside splitter. The solid line is the fitting with Enge function (Equation 3.12). The dot-dashed line denote the position of EFB and the target position. The gap between the field clamp and the target is unshielded. The field deflected the beam incident angle.

given by

$$\Delta z/R = -[S_2(x/R)^2 + S_3(x/R)^3 + \cdots + S_8(x/R)^8]. \tag{3.14}$$

Here R is the radius of central ray in uniform region. The coefficients S_is are in lines 11 and 12 of dipole data card for dipole entrance and exit. They describe the shape of EFB in the particle bending direction.

For the quadrupole data card, most of the lines are very similar to those of dipole except one line which gives the multipole components of the quadrupole, including quadrupole, sextuple, octuple, decapole, etc. These multipole components change the focusing properties of the spectrometer in the unbending direction.

In addition, the effect of misalignment or rotation of the magnet elements can be expressed in the data card SHRT, by shifting or rotating the coordinate systems.

3.5.2 HNSS Raytrace Data Card Tuning

There was already a Raytrace data card for SOS obtained by the original magnet design file and field mapping. But due to the existence of corners in the magnets (Figure 3.17), the mapping only covered the center field region, whereas the second dipole BM02 has narrow pole width, the field map only covered a small portion of its field. This initial data card was not accurate, especially the shape of the EFB. In addition, although saturation of SOS magnets in general occurs at central momentum setting > 1.6 GeV/c (our high momentum setting is ~ 1.24 GeV/c), field in some edge and narrow regions may already saturate. Thus the initial version cannot precisely describe the SOS optics.

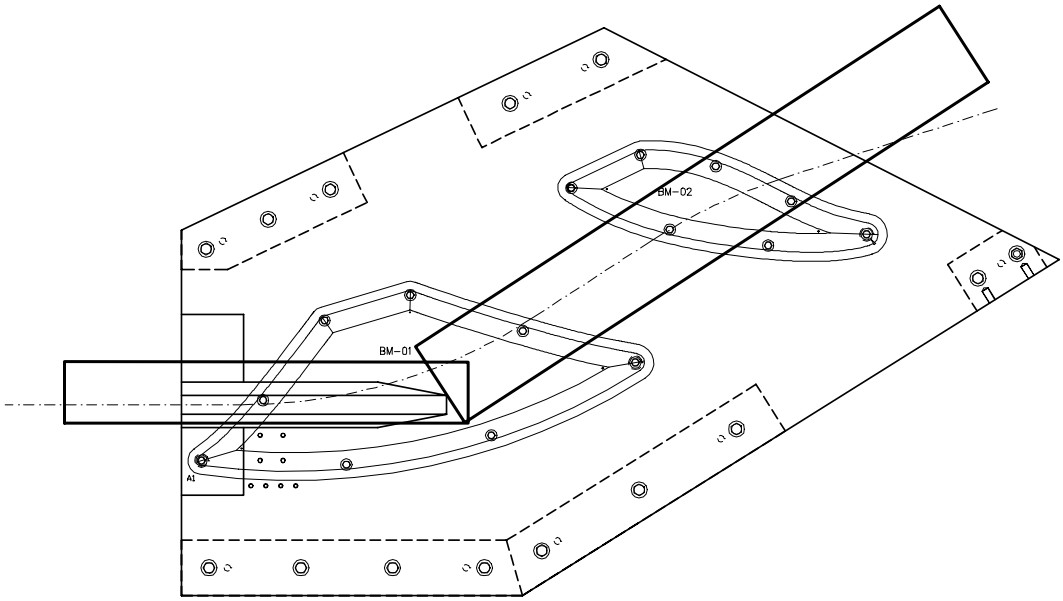

Figure 3.17: Outline of field map regions for SOS dipole. The area inside the two rectangular box has been field mapped.

This was evident when we compared the Raytrace generated focal plane sieve slit pattern with data from SOS sieve slit runs.

The raytrace simulation procedure is: first, events are generated from the target by Monte-Carlo method with fixed X, Y position (point target) and uniformly distributed angles XP and YP. The XP and YP distribution need to cover the whole sieve slit plane. Then these events are sent through the splitter by Raytrace simulation and transported to SOS collimator plane, there, a test is applied to see if the events can pass the sieve slit holes. The thickness of the sieve slit is taken into account by test both at the front and back faces of sieve slit plane. The events which pass through the sieve slit will be sent through the SOS magnets and their focal plane coordinates can be obtained.

From simulation, it was found that the SOS sieve slit patterns at focal plane were sensitive to the entrance and exit EFB shape of BM02: the coefficients C_is. Other

parameters that had been tuned were the multipole components of SOS quadrupole. We added higher order multipole components to make SOS Y-focusing properties consistent with sieve slit run data. The position and orientation of the final focal plane was also adjusted slightly.

For the splitter, we did a field mapping for the entire field area. Raytrace data card was calculated based on this field map.

After adding the splitter data card to the SOS data card, we got the Raytrace data card for HNSS kaon arm: the splitter+SOS spectrometer. We compared the simulated HNSS sieve slit pattern at focal plane by raytrace with the data from experimental sieve slit runs. To check the experimental sieve slit pattern at SOS focal plane, hadron events were selected. This is because that positron events in SOS, though abundant, were concentrated in a very small core from target. Only a small portion of focal plane was illuminated by positrons while hadron distribution was more uniform over the focal plane. The focal plane correlations which were compared with simulation were: Y_FP vs. X_FP, YP_FP vs. X_FP and XP_FP vs. X_FP. The sieve slit holes were grouped into 7 raws in Y direction. Raytrace simulation was compared with real data raw by raw. The events which passed through one sieve slit hole from a point target dispersed into a "band" by the magnets because of the momentum difference. As mentioned in Section 2.6.3, the Hall probe used to measure the splitter field was not put in the uniform field region in order to avoid interference with particle trajectory. Consequently, a small position shift of the probe would cause significant error of field measurement. Actually, the splitter field in the Raytrace data card needed to be adjusted slightly from ideal setting to produce a simulated sieve slit pattern consistent with real data (Figure 3.18).

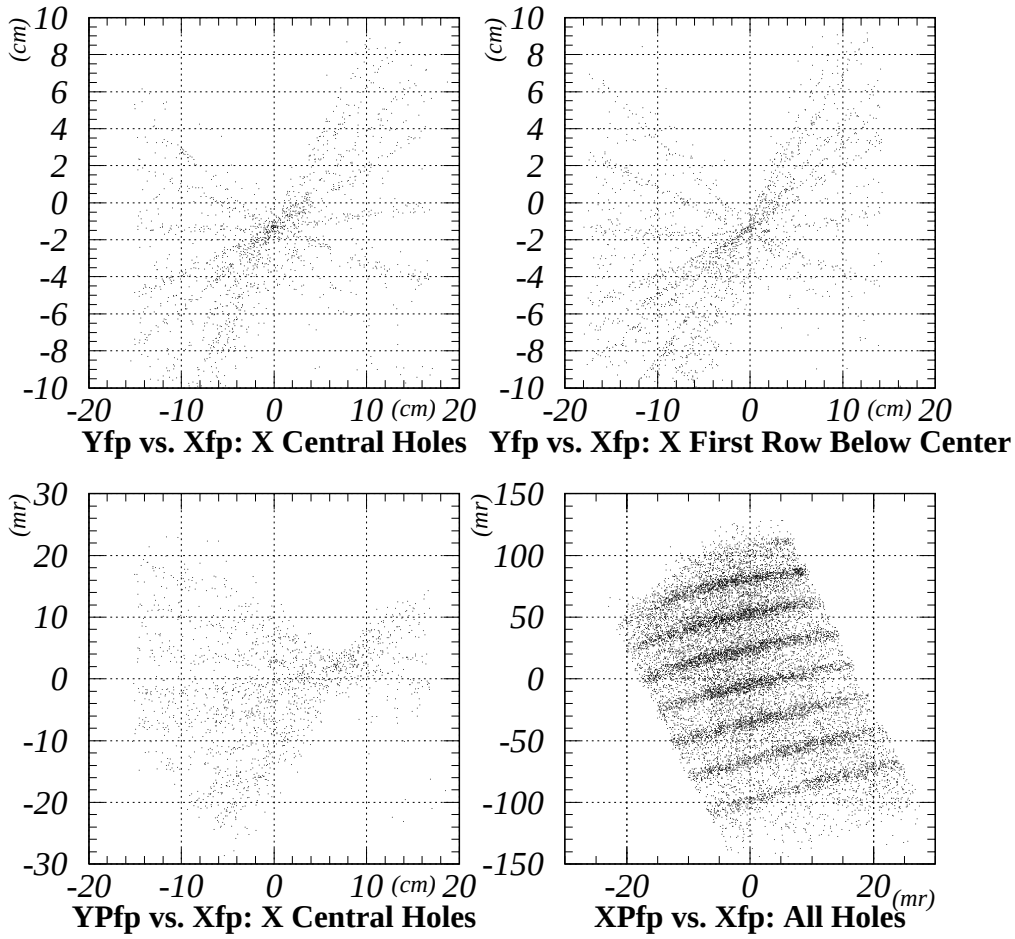

Figure 3.18: Correlations of focal plane quantities from real sieve slit data.

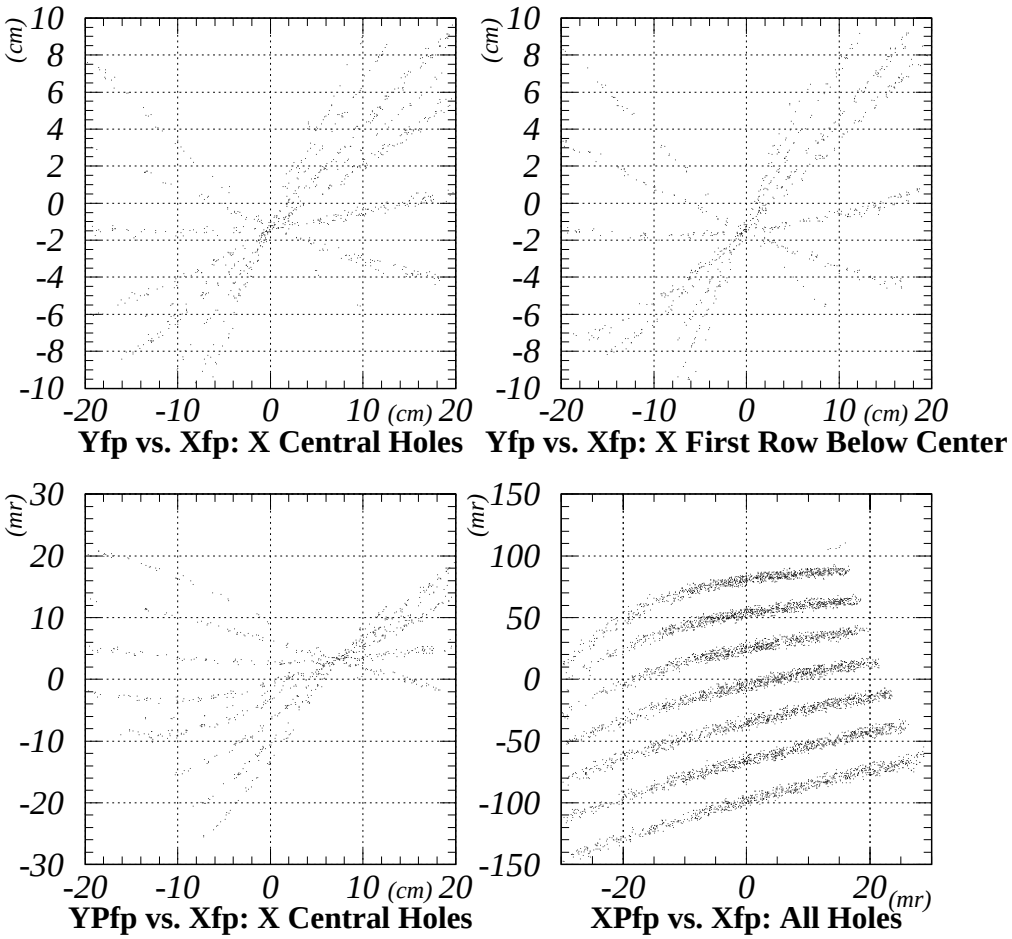

Figure 3.19: Comparison of Raytrace simulated focal plane patterns with data from HNSS sieve slit run 32767 (Figure 3.18). The four plots show the correlations from Raytrace simulation. Only comparison of the central row in X direction and the first row below it are shown. We used a larger opening SOS collimator in Raytrace data card for optics study, so the acceptance is larger than data.

During the experiment, we ran a series of sieve-slit runs in both beam energy 1.721 GeV and 1.864 GeV periods. Comparing with the simulation, our tune of Raytrace parameters yielded consistent result with real data (Figure 3.19). The asymmetry of the pattern about X and Y was due to the distortion of particle angles by the splitter.

3.5.3 Fitting Reconstruction Matrix from Raytrace

With the HNSS kaon arm raytrace data card at hand, we did a simulation with random generated target events with angles (XP_TAR, YP_TAR), position (Y_TAR) and momentum δp. Their corresponding focal plane quantities X_FP, Y_FP, XP_FP and YP_FP were obtained by raytrace simulation. After Substituting the known target and focal plane quantities into the polynomials Equation 3.4, the equation became group of linear equations of the unknown coefficients which were the reconstruction matrix elements. Each event gave one equation. The number of coefficients depended on the order of polynomial 3.4. The equation can be solved by a least-square fitting method because the number of equations (equal to the number of simulated events) were much more than the number of coefficients. For HNSS target reconstruction, a 6th order polynomial was used, so there were totally 210 coefficients. At 6th order, the error of target reconstruction from fitting is already much less than the error from drift chamber resolution and optical code.

To check the reconstruction matrix, we used it to reconstruct the real sieve slit data from the focal plane quantities to obtain the event positions at the sieve slit plane. The X and Y positions were output on the same plane as the sieve slit (Figure 3.20). We can see the reconstructed holes are aligned and well separated. The centers of the

reconstructed holes are in good agreement with measured sieve slit hole positions. The background came from the punch through hadrons.

The error of HNSS kaon arm angle reconstruction can be derived from the width of the reconstructed holes. We know all the sieve slit holes have 0.2 inch diameter except the center hole. The path length from target to SOS collimator plane through the splitter is about 155 cm. Figure 3.21 shows the fittings of width of the reconstructed holes, both in X and Y direction. Also shown in Figure 3.21 is the simulated hole distributions calculated by ideal sieve slit dimensions without reconstruction. Fitting to the simulation distribution gives a $\sigma = 0.12$ cm intrinsic hole width. The fitting of the reconstructed hole width was done on the out-of-center holes which was wider than the center holes, hence it represents the upper limit of the angular resolution. For X direction, we got $\sigma_x = 0.21$ cm, and $\sigma_y = 0.81$ cm. Subtracting the contribution of intrinsic width, we got the angular resolutions: $\sigma_{xp} = 0.17/150 = 1.1$ mr, $\sigma_{yp} = 0.8/150 = 5.3$ mr.

Raytrace simulation was also used to determine the offset of the SOS quadruple field setting from the nominal values in order to moved the SOS focal point back to the acceptance center after we added the splitter. A scale factor of 91.5% from nominal quadruple field setting was determined and applied in the experiment.

3.6 Splitter Fringing Field Effect on The Beam

Before beam hit the target, it met already the splitter fringing field. To alleviate the field deflection effect on the incoming beam, a field clamp was put around the beam pipe to shield the splitter field outside the flange of target chamber. Due to space restriction, the clamp was in up to ~ 24 cm upstream from the target. The gap between

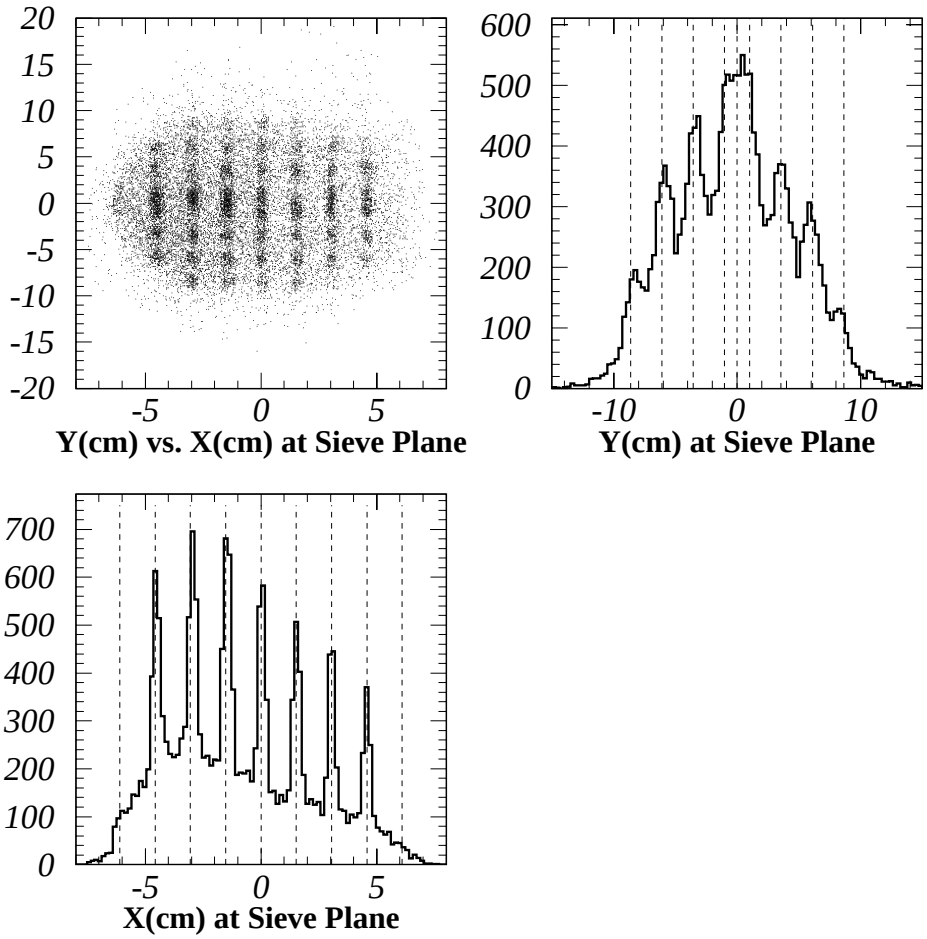

Figure 3.20: Raytrace reconstructed sieve slit pattern from the focal plane quantities of sieve slit run 32767. The dashed lines denote the correct positions of the sieve slit holes. The background came from the punch through hadrons.

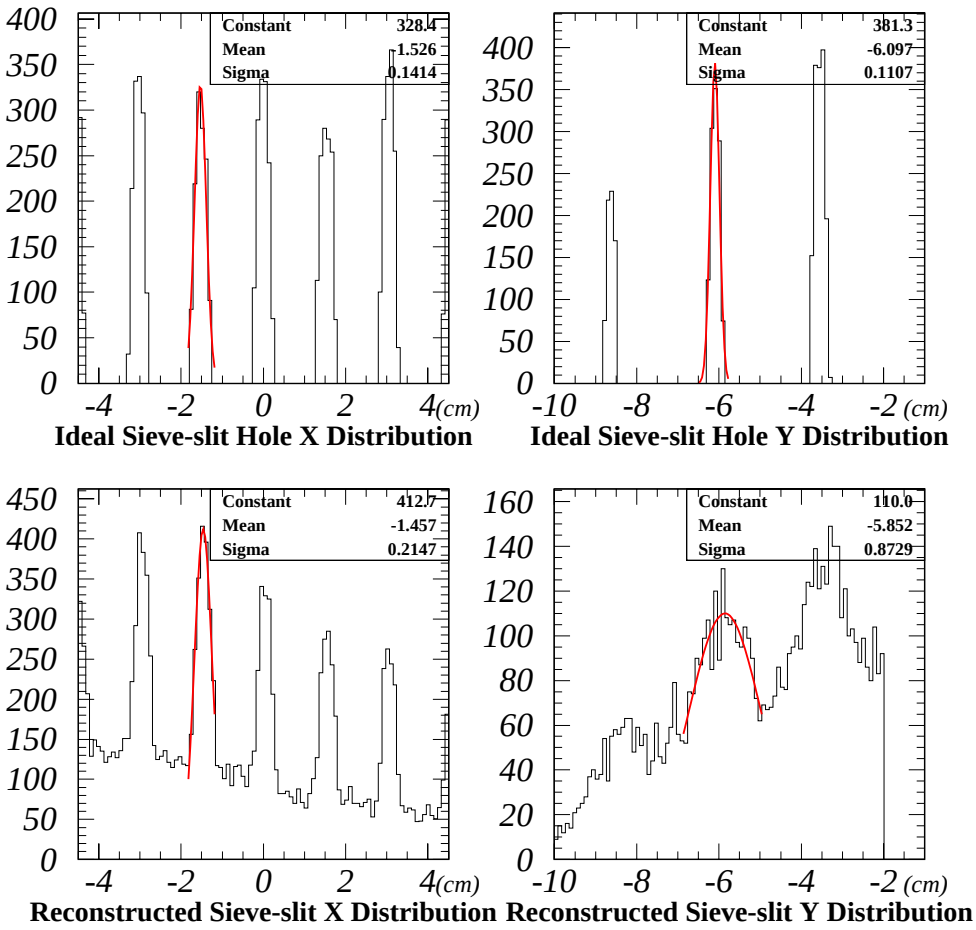

Figure 3.21: Reconstructed and ideal sieve slit hole patterns showing the resolution of reconstructed angles at target. The width of the ideal sieve-slit hole represents the intrinsic hole width.

the field clamp and the target was unshielded. The field would deflect the beam incident angle slightly.

Figure 3.16 plots the entrance fringing field B_y of splitter along the beam path. Based on the splitter field map, We did a field integration point by point along the beam trajectory as in Section 2.6.3 within the gap. The calculation showed that the incoming beam was deflected 0.32° before hitting the target. After adding this to the nominal kaon scattering angle (1.85°), the actual central scattering angle for the kaons was determined as 2.17°.

CHAPTER 4

PHYSICS ANALYSIS

As an $e'K^+$ two arm coincidence experiment, the first task of physical analysis is naturally select a clean sample of e' and kaons, the detected particles from the reaction. Because the cross section of kaon electroproduction is much smaller than other processes which produce positrons, protons and pions, etc., the kaon events we are looking for were embedded in a huge background from other processes. The data analysis needs to reject these background events. Background was also produced by events which were outside HNSS acceptance but re-scattered into the focal plane by spectrometer magnet structures. Secondly, the real ($e'K^+$) coincidence events have to be distinguished from the accidental coincidence. In addition, to determine the momentum of scattered electrons , we need to calibrate the ESPS focal plane SSD channel number-e' momentum correlation. The method was to use known particle masses and the geometrical and optical information of ESPS. After that, the missing mass spectrum of $^{12}_{\Lambda}$B can be calculated.

Moreover, to extract the cross section of hypernuclear production, HNSS spectrometer acceptance and total accumulated charge need to be studied. The various corrections due to the detector inefficiencies, cuts, dead time, kaon decay are to be considered.

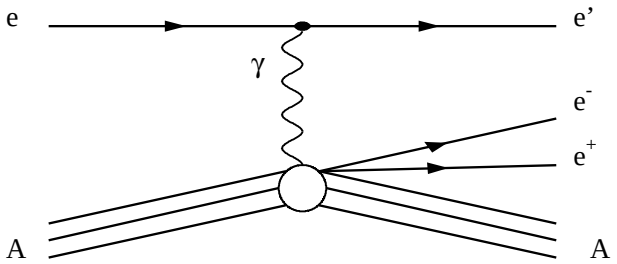

Figure 4.1: Feynman diagram for the production of Dalitz pair, C(e,e′e$^-$e$^+$)C.

4.1 SOS Collimator Cut

Not all the events we took at SOS focal plane came directly from the target. Some events were outside the SOS spectrometer acceptance but still made to the focal plane by re-scattering from the magnet irons and vacuum structures. These events contributed part of the background for our physics events. In E89009, This background was quite significant due to the high positron rate at SOS. These positrons were produced by the electron bremsstrahlung process in the carbon target: C(e,e′e$^-$e$^+$)C (Figure 4.1). These positrons concentrated in a very small angle around zero. The hot spot of positrons was at the right edge of the SOS angle acceptance (Figure 2.5). SOS has a relatively small momentum acceptance range at edge of collimator. A large part of the positrons with momentum outside the acceptance could not go directly through the spectrometer to the focal plane, instead they hit into the magnets. Some of them were absorbed by the magnets, part of them was re-scattered by the magnets into the focal plane detector acceptance and formed the background.

After these events were reconstructed to the target, most of them lay outside the SOS acceptance, represented by the collimator size in the reconstructed event distribution. Figure 4.2 shows the distribution of reconstructed events at the target. The dimension and shape of the SOS large collimator can be recognized as the dense region. Splitter caused a distortion in Y direction. A SOS shower counter cut was already applied to reject main part of positrons. A loose cut on target in-plane and out-of-plane angle according to the SOS collimator can be applied to reject these background events. The cut was made loose considering the SOS drift chamber resolution, uncertainties in the reconstruction matrix especially for large scattering angles, etc. The cut was slightly larger than the size of SOS collimator, |XPtar| $<$ 50 mr and |YPtar| $<$ 100 mr. Thus, this ensured a negligible amount of kaon within SOS acceptance will be outside the cut after reconstructed back to the target. No correction for kaon lose due to this collimator cut was considered.

4.2 SOS Shower Counter Cut

To reject the high positron background, SOS shower counter information was used in both the online trigger and offline analysis. For positrons, the ratio of total energy deposited in the calorimeter to the particle energy sshtrk was close to 1 (Figure 4.3), while other $\beta \neq 1$ particles had a value less than 0.7. A cut on sshtrk$<$ 0.8 will reject most positrons with very little loss of $\beta < 1$ particles.The sshtrk spectrum of kaon events with $sshtrk < 0.8$ and other kaon PID cuts (SOS aerogel Čerenkov, SOS TOF β) is shown in Figure 4.4. Most of the kaon events have a value less than 0.7. Negligible amount of kaon events ($< 0.1\%$) have $ssshtrk > 0.7$. Thus the cut of $ssshtrk < 0.8$ will

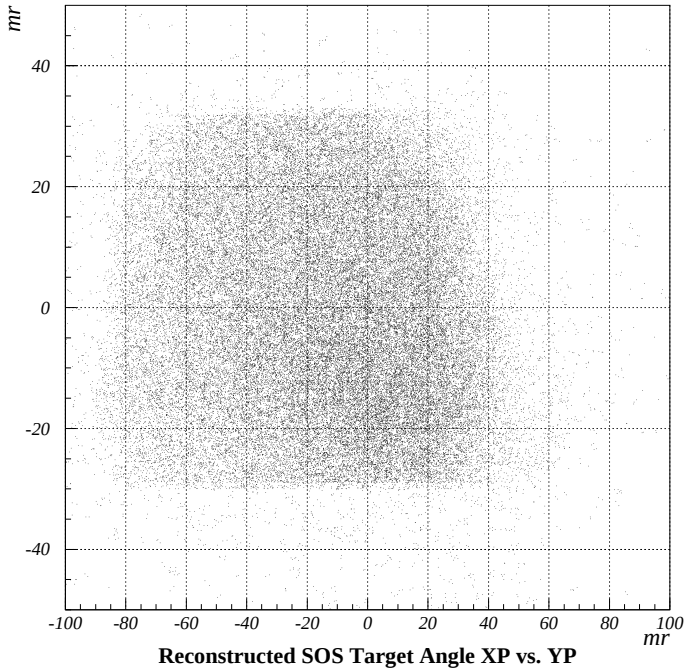

Figure 4.2: SOS target reconstructed XP_TAR-YP_TAR correlation. The dense region shows the shape of the SOS entrance collimator after distorted by the splitter.

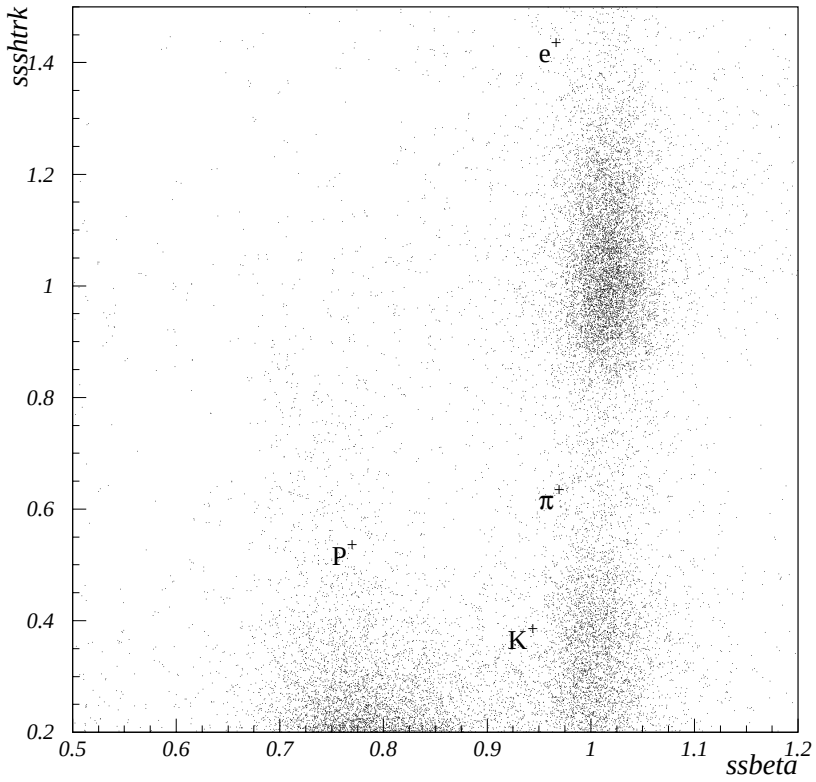

Figure 4.3: Fraction of energy deposit in the SOS calorimeter, *ssshtrk*, versus SOS TOF β. Large part of the positrons have already been rejected by online calorimeter and gas Čerenkov veto.

not cause a lose of kaon events.

4.3 Data Reduction

Because of the high SOS trigger rate, our raw data contained a large amount of background events including positrons and events re-scattering from magnets. Especially, in SCIN 3/4 trigger mode, a lot of SOS scintillator noise hits were taken as acciental triggers. The real physics events were only a small portion of the total raw events. The analysis became very slow because the analysis program spent most of the computer

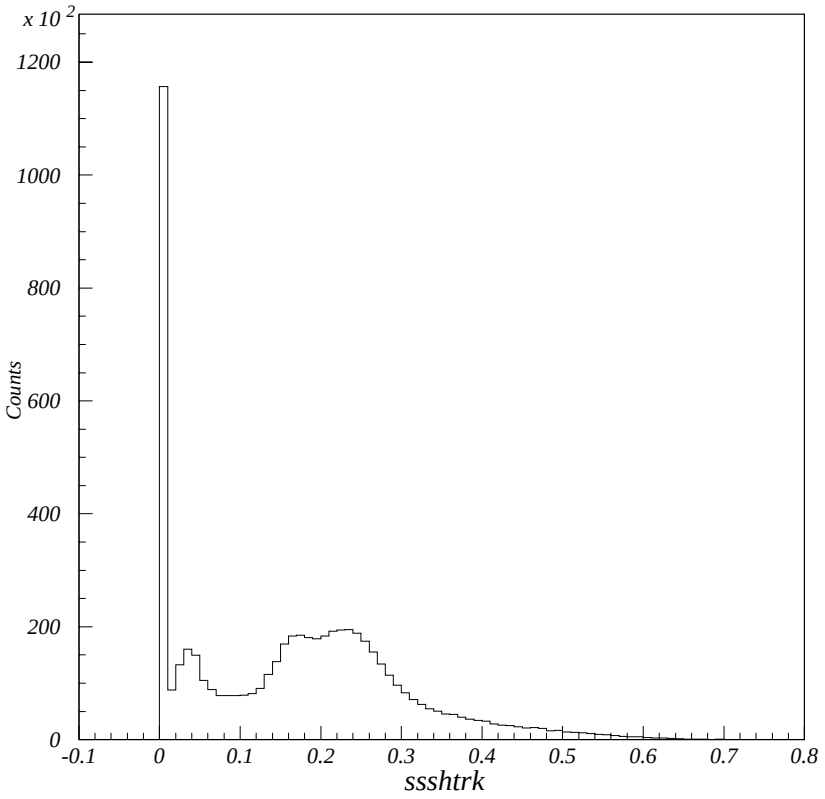

Figure 4.4: *ssshtrk* distribution for kaon events.

handling the background events. To facilitate the analysis, we took advantage of the "preprocess" feature of the Hall C data analysis code which instruct the program to perform some preliminary analysis and events selection and put the output data in the same format as the raw data. We applied the SOS collimator and shower counter cut to the raw data in the first round of replay and produced data for future analysis. This reduced data to 10-30% fo the original size. Although only very loose cuts were used in the preprocess, it turned out that small amount of real kaon events were lost after this data reduction. This event loss is related to the SOS tracking. Detailed study on this are still under way by Tohuku University group.

4.4 SOS Kaon Particle Identification

4.4.1 Aerogel Čerenkov Cut

Only very loose aerogel Čerenkov veto on number of photoelectrons was used in the online trigger level to avoid lose Kaon events. At offline level, after careful calibration of the PMTs gains, tighter cuts can be used to reject pions more efficiently. Figure 4.5 shows the particle velocity (TOF β) versus Aerogel Čerenkov number of photoelectrons. Pion β should be 0.991–0.995 at these beam energies. Note that the online aerogel Čerenkov trigger had already rejected more than 2/3 of the total pions. Protons had been cut by TOF β. Pions generally produce an average $\sim$12 n.p.e. in the aerogel Čerenkov detector. But in E89009 experiment, due to the problem with one PMT (#3) and age or moisture of aerogel materials, some pion events had Čerenkov light $<$ 2 n.p.e.. This caused the overlap of pion and kaon in the region where saer_npe$\sim$1 and

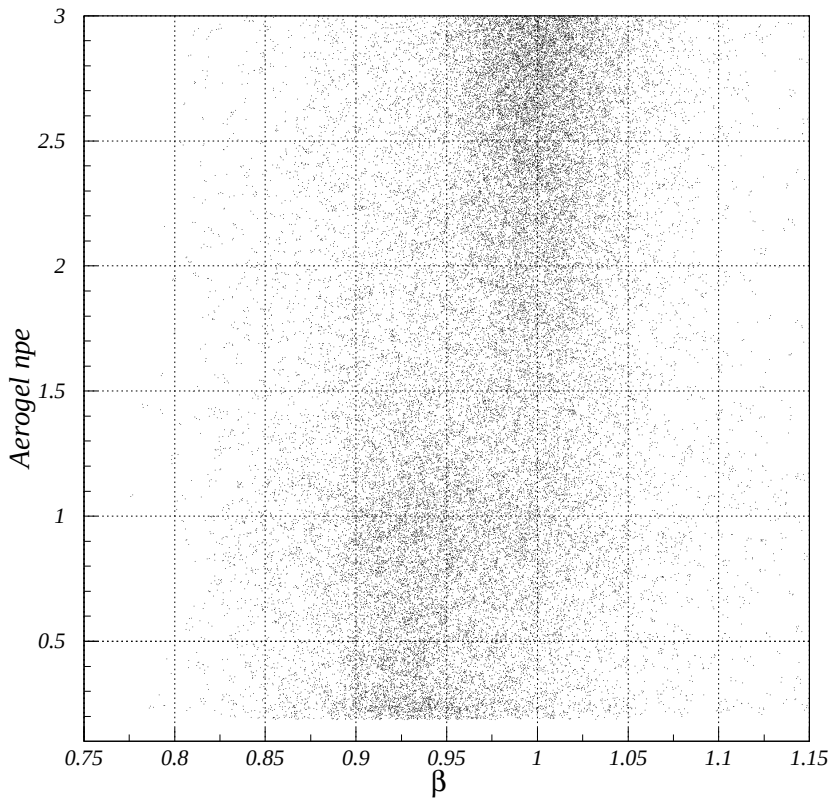

Figure 4.5: Aerogel Čerenkov n.p.e. vs. particle velocity (TOF β). The events with β around 1 are pions. The events in the lower part are kaons. Protons are already rejected by sos β cut.

TOF $\beta \sim 0.95$. We used a cut of aerogel npe$<$ 1.6 for 1.864 GeV run period and npe$<$ 2 for 1.721 GeV run period. These cuts will eliminate most pions and keep the kaon events basically intact. Figure 4.6 shows the $\Delta\beta$ ($= \beta_{TOF} - \beta_{mK}$) of kaons and pions before and after aerogel Čerenkov cut.

It was clear that the aerogel Čerenkov cut only cannot separate kaon from pion completely. Therefore, another cut on particle velocity (TOF β) was used to further clean up the pions.

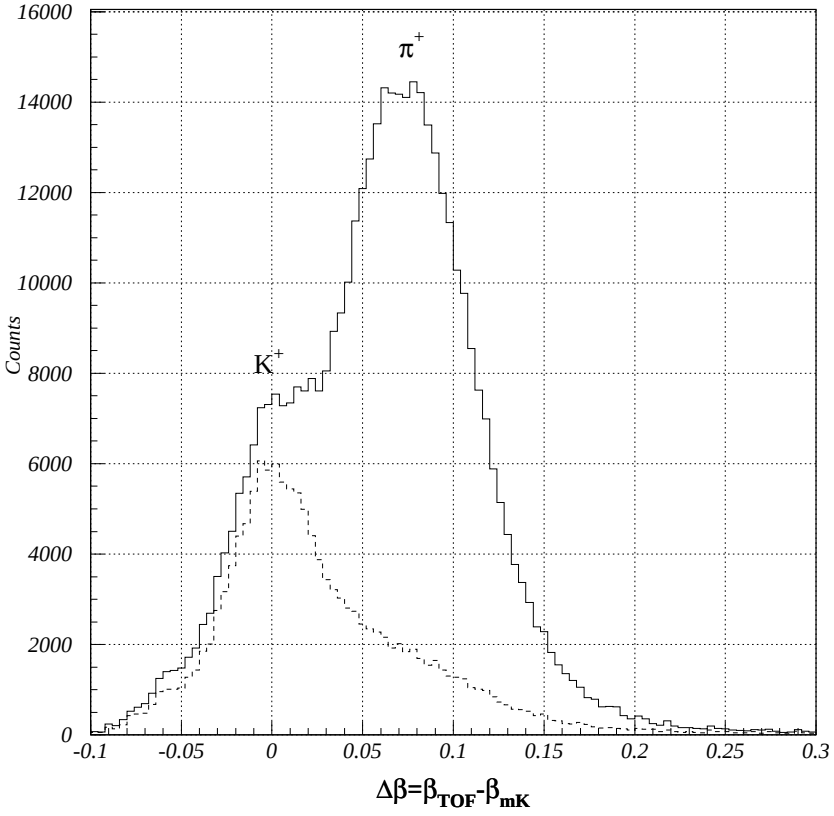

Figure 4.6: The $\Delta\beta$ distribution for kaons and pions before and after aerogel Čerenkov cut. Most of the pions were rejected after aerogel cut. But some remain in the right tail of the kaon distribution.

4.4.2 Lucite Čerenkov and Time of Flight β Cut

Particle velocity β depends on particle mass and momentum (Equation 2.14). In the SOS arm, the particles kaons, pions and protons had different range of β that didn't overlap (Table 2.6). β was an effective way for PID. But β itself is momentum dependent. For better Kaon PID, we used the difference of TOF β to β_{mk}, $\Delta\beta$. Because particle momentum can be accurately determined by tracing in the order of 10^{-4}. β_{mK} will be a more reliable estimate for particle velocity if the particle was actually kaon. Thus we expected the $\Delta\beta$ will be a Gaussian centered at zero and was momentum independent. Other particles with different mass will be separated from Kaon peak.

Figure 4.7 shows the $\Delta\beta$ of kaons, protons and pions, versus SOS lucite Čerenkov n.p.e. for 1.721 GeV and 1.864 GeV runs. We can see that for protons and kaons a cut on $\Delta\beta$ can separate protons and pions very well. We used cut $\Delta\beta > -0.032$ for 1.864 GeV runs, $\Delta\beta > -0.05$ for 1.721 GeV runs to reject proton events.

SOS lucite Čerenkov can also be used for proton/kaon separation for 1.864 running period. But for 1.721 GeV running period, SOS central momentum was 1.113 GeV/c, the kaons in SOS had a β range 0.898–0.928, part of them were already below the lucite Čerenkov TIR threshold 0.905. This caused significant reduction in Čerenkov light collection. At lower SOS momentum setting, the average npe dropped to 6 from 8.5 n.p.e. at higher momentum setting. Hence, for 1.864 GeV runs, we used a lucite cut npe>4, but for 1.721 GeV runs, we only used a very loose cut npe>1 to avoid reduce kaon events.

Because kaon's and pion's β were close in our SOS momentum settings, in Figure

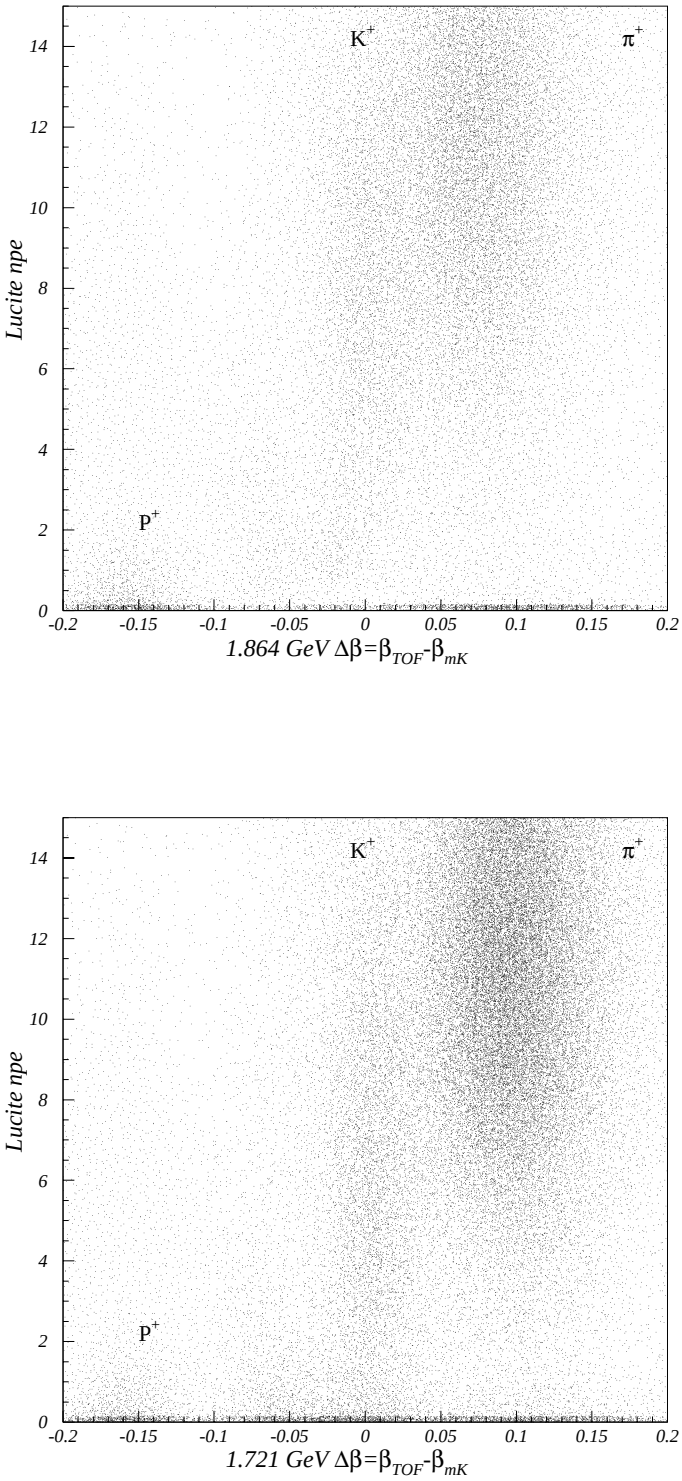

Figure 4.7: Lucite Čerenkov n.p.e. vs. $\Delta\beta$ for 1.864 GeV (top) and 1.864 GeV runs (bottom). Note the change in lucite npe distribution for kaons due to the difference of SOS central momentum at two beam energy settings.

4.5, we can see some overlaps between kaon and pion events. After the aerogel Čerenkov cut, we can still see the presence of pions in the right tail of kaon peak. A $\Delta\beta$ cut will further separate kaons and Pions. Best cut should be the compromise of keeping as many kaon events as possible while keeping pion contamination minimum. The cuts we used were: $-0.032 < \Delta\beta < 0.04$ for 1.864 GeV $-0.05 < \Delta\beta < 0.05$ for 1.721 GeV runs.

4.4.3 SOS PID Cut Efficiencies

To estimate the PID cut efficiencies, a clean sample of kaons needs to be selected. We used the Gaussian distribution of kaon $\Delta\beta$ around zero, as in Figure 4.6, the $\Delta\beta$ spectrum for kaons and pions. First, pions were separated by an aerogel Čerenkov cut and its $\Delta\beta$ distribution was estimated by a Gaussian fitting. The total distribution subtracted the pion distribution then can be fitted by a Gaussian to estimate the kaon distribution. The counts within this Gaussian peak were assumed to be all kaons.

To estimate the aerogel Čerenkov cut efficiencies, we varied the aerogel Čerenkov cut threshold from 1 n.p.e. to 5 n.p.e. and calculated the counts under the Gaussian distribution fitted to the distribution of remaining kaons . The ratio of this count to the total kaon count without aerogel cut gave us the aerogel cut efficiency. The efficiency appeared to have some beam current dependence. It dropped at high beam current. This change of cut efficiency may come from drop of Čerenkov gain at high rate. Table 4.1 shows the aerogel cut efficiency versus cut threshold at both beam energies after averaging low and high current runs. We can see that for our threshold settings, the aerogel cut efficiencies were 0.90 for 1.864 GeV runs, 0.93 for 1.721 GeV runs.

The systematic error for the aerogel cut efficiency came from two sources: The

Table 4.1: Aerogel Čerenkov cut efficiencies for both beam energies.

Aerogel cut threshold (npe)	Ratio of kaon survive	
	1.864 GeV	1.721 GeV
5.0	0.975	0.966
4.5	0.970	0.962
4.0	0.963	0.958
3.5	0.953	0.952
3.0	0.945	0.943
2.5	0.935	0.932
2.0	0.921	0.916
1.5	0.902	0.893
1.0	0.865	0.843

current dependence and the error in estimation of survived kaon counts. Compare the cut efficiencies at low and high current conditions, a $\sigma \sim 1.5\%$ error can be assigned. Since we estimated the kaon count by fitting the kaon $\Delta\beta$ peak, thus the error of kaon count can be calculated from the errors for kaon Gaussian fittings: error for the amplitude A was about 0.5% and for σ about 2%. The total area under Gaussian curve was $\sqrt{2\pi}\sigma A$. Thus we expect an error of $\sim 2\%$ for the estimation of kaon counts and $\sim 2.8\%$ error for the ratio. The error from the kaon count combined with the beam current dependence of cut efficiency gives the total systematics error, which was 3.2%.

The same procedure was followed to determine lucite cut efficiencies for 1.721 GeV runs. the result is shown in Table 4.2. The cut efficiency is 84% when require n.p.e.> 4 for 1.864 GeV runs and 85% when require n.p.e.> 1 for 1.721 GeV runs. The systematic error for the efficiency is dominated by the error of the estimated surviving kaon count: 2.8%.

As seen from the $\Delta\beta$ fitting in Figure 3.10, the β resolution of kaon was $\sigma = 0.022$

Table 4.2: Lucite Čerenkov cut efficiencies for both beam energies.

Lucite cut threshold (npe)	Ratio of kaon survive	
	1.721 GeV	1.864 GeV
5.0	0.6071	0.772
4.5	0.6409	0.907
4.0	0.6758	0.837
3.5	0.7102	0.866
3.0	0.7402	0.888
2.5	0.7684	0.911
2.0	0.7947	0.936
1.5	0.8210	0.960
1.0	0.8507	0.984
0.5	0.8830	0.998

for low current runs and $\sigma = 0.023$ for high current runs. There is small dependence of β resolution on beam current that can be related to the SOS scintillator time shift under high rate. The efficiency of $\Delta\beta$ cut can be calculated as the ratio of events within the $\Delta\beta$ gate to the total events in the fitted kaon $\Delta\beta$ peak. The β cut efficiencies are: 88% for 1.864 GeV runs, 97% for 1.721 GeV runs. The σ of kaon $\Delta\beta$ distribution has an 2% uncertainty. This will cause about 0.4% systematic error on the cut efficiencies.

4.5 SSD Overlapped Channel

The layout of SSD planes was zigzagged. Adjacent SSD planes had overlaps to cover the gaps between SSD planes. To eliminate the double counts caused by these overlapped SSD channels, the precise overlapped SSD channel to channel correspondence for adjacent SSD planes were obtained from the SSD hit patterns. If corresponding to one SOS event, there were two SSD hits on two adjacent SSD planes which satisfy this channel correlation, they were treated as one event, only the hit on the front plane was

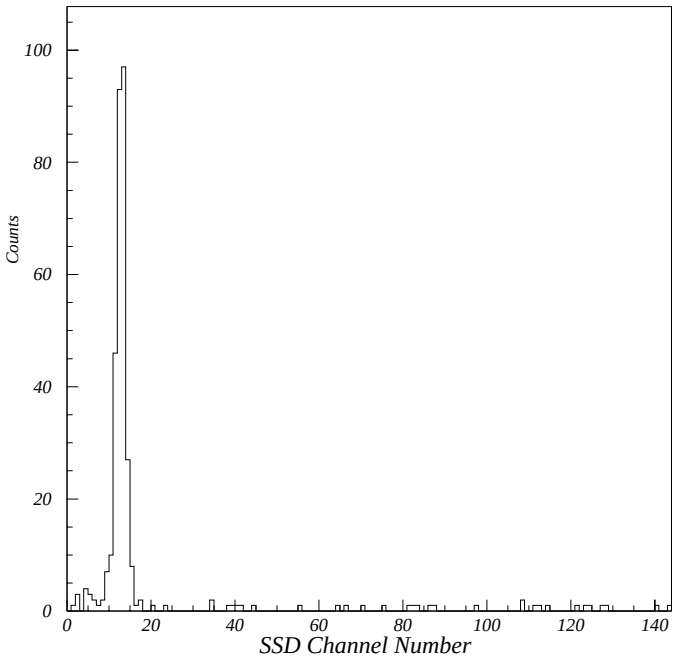

Figure 4.8: The overlap channel distribution in SSD plane 3 corresponding to channel 130 of the front plane 2.

selected.

To find the SSD overlapped channel correspondence, first, we did a analysis with all the other event selections active except the SSD overlapped channels, i.e., set the momentum difference *dp* in Section 3.3 to 0. Thus all hits including those came from overlapped SSD channels were kept in these events. If two hits were from the same event from two overlapped SSD channels, the two channels would always be fired simultaneously. For a fixed channel in the front plane, the channel number in the back plane would form a narrow distribution centered at the corresponding overlapped channel of the front plane. Figure 4.8 shows the distribution of the back channels corresponding to a fixed front channel. The center of the Gaussian

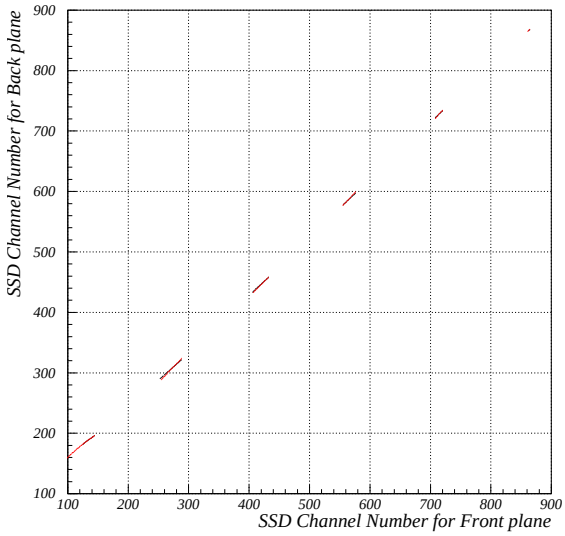

(a) SSD plane overlap at 1.864 GeV beam energy

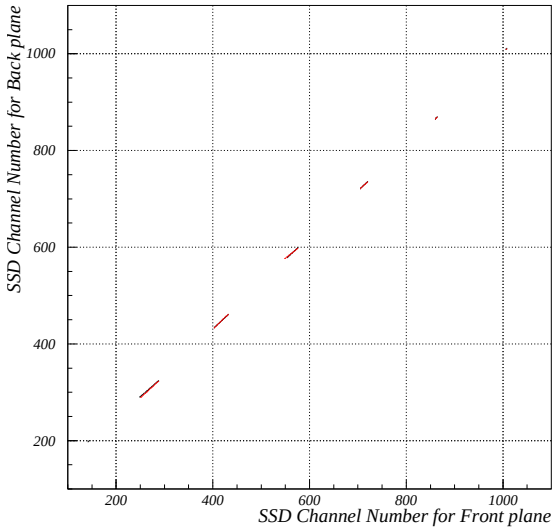

(b) SSD plane overlap at 1.721 GeV beam energy

Figure 4.9: SSD channel overlap correlation for both beam energies. Every segment corresponds to overlapping between one pair of planes. from bottom to top, they are planes 1 to 7. Overlaid with the experimental data is the SSD overlap correlation calculated from the fitted ESPS focal plane momentum as a function of SSD channel.

fitting to the distribution was taken to be the overlapped channel. The σ width of the distribution was 1–1.6 channels, due to the position resolution of the SSD and the multiple scattering of the particle in the front plane. SSD plane overlap existed from plane 1 up to plane 6. Figure 4.9 shows the SSD channel overlap correlations. The axes are ESPS focal plane SSD channels calculated as: Focal Plane Channels = SSD Channel Number per Plane $+ 144 \times$ (SSD Plane Number $- 1$). Thus all SSD planes are included. This focal plane channel will be referred to as SSD channel hereafter.

The overlap correlations were slightly different for the two beam energies. This change in overlap means the incident angle change of incoming particles on the SSD, which implicit that between the two beam energies ESPS optics had some change. This can be explained by the splitter field offset when scaled to different beam energies. One may recall that the splitter Hall probe was not in the uniform field region so that it was possible that the splitter field was not set precisely.

Based on the accurate channel overlap correlations, SSD double hits were eliminated. Figure 4.10 shows the SSD hit pattern after SSD channel overlap selection. Due to the acceptance restriction, SSD plane 10 didn't get hit and only small region of SSD plane 1 and plane 8 got hit. The gaps between two SSD planes are the channels which were "shadowed" by the front planes. There are also number of small gaps within one SSD plane. They were formed because of the Enge hodoscope gaps. It caused loss of e' detection efficiency.

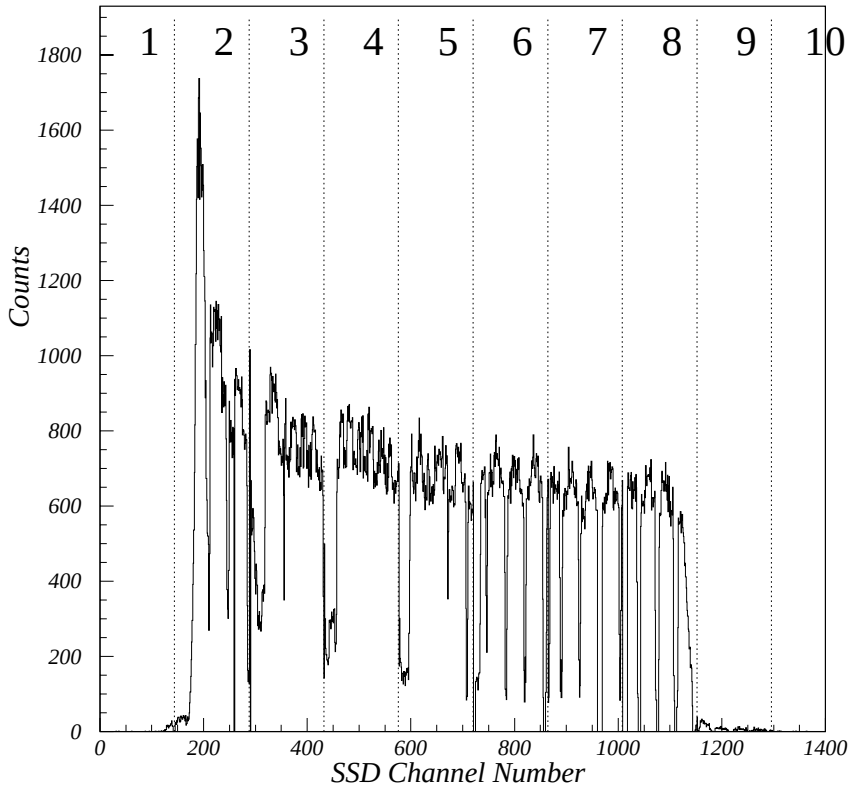

Figure 4.10: SSD hit pattern after SSD channel overlap selection.

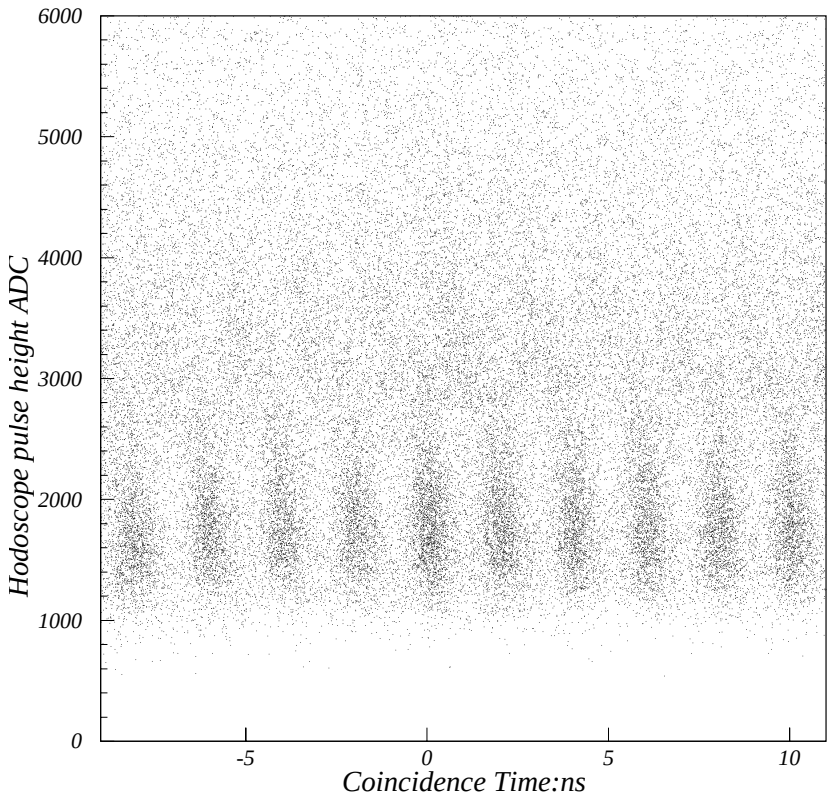

Figure 4.11: The ESPS hodoscope pulse height ADC vs. coincidence time from high rate 1.864 GeV runs.

4.6 Enge Hodoscope Pulse Height Cut

There was no need for tracking and PID at the HNSS e′ arm. The main task of e′ arm event selection was to suppress noise hits. The ESPS event selection was carried out by the analysis program, as described in Section 3.3.

After SOS arm kaon PID and ESPS event selection, the two arm ($e'K^+$) coincidence time was calculated. Figure 4.12 shows the coincidence time spectrum for 1.864 GeV beam energy with beam current 1 μA on CH_2 target. Despite the high level of background, we can recognize the 2 ns beam structure and the real coincidence peak

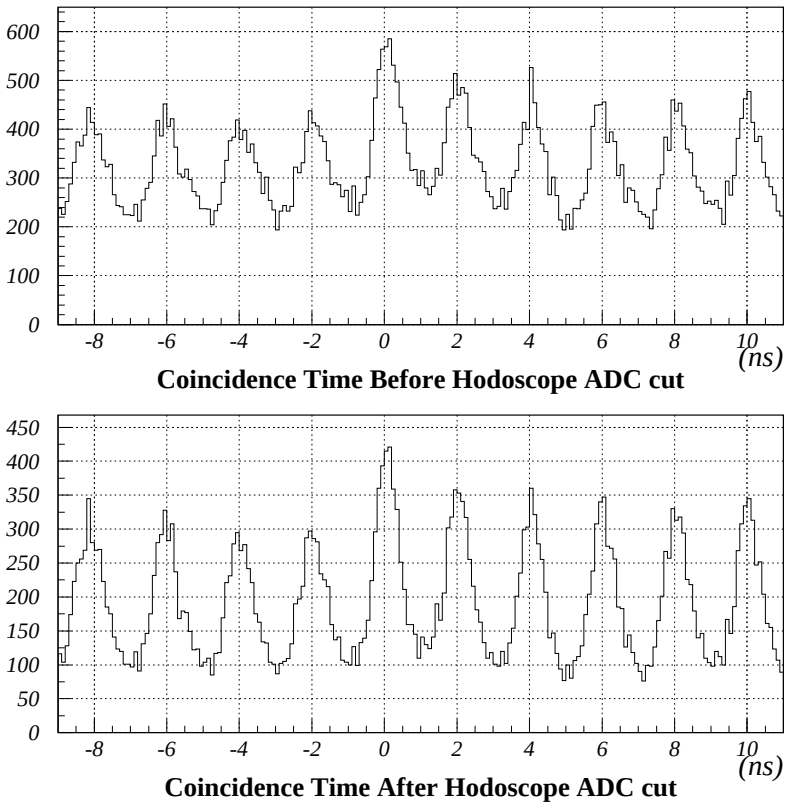

Figure 4.12: Coincidence time spectrum before and after Enge hodoscope ADC cut (hodoscope pulse height < 3000). The peak centers at 0 is the in-time peak.

centering at zero. But the signal to accidental ratio was rather poor. The S/A ratio can be estimated by the count in the real coincidence peak R and average count A from the accidental coincidence peaks as: S/A = (R−A)/A. When e′ rate in ESPS was low (< 100 MHz), S/A ∼ 0.7. Under high e′ rate, S/A ∼ 0.24. The high level of background came from the ESPS multiplicity and the pile-up effect of ESPS hodoscope PMTs. Here ESPS multiplicity means one SOS event was coincided with more than one ESPS separable e′ events. If we draw the coincidence time versus ESPS hodoscope pulse height (Figure 4.11), we can see that when hodoscope pulse height < 3000, the real and all accidental coincidence time peaks are well separated. The major part of the events with hodoscope pulse height above 3000 were affected by the pile-up effect. The ESPS hodoscope time walk caused by the pile-up effect spread the coincidence time structure. Consequently, the real coincidence peak were difficult to separate from accidental peaks when hodoscope pulse height > 3000. We cut at pulse height 3000 and discarded the events above that. This reduced the high level of background and improved signal to noise ratio with the price of losing some statistics (Figure 4.12). After the cut, the S/A ratio increased from 0.24 to 0.27. In addition, ESPS multiplicity also was reduced after this cut (Figure 4.13) . This ESPS pulse height cut was applied to all high current runs with the overall ESPS hodoscope rate greater than 100 MHz. The efficiency of this cut was estimate by the loss of events in the Λ peak. The 1.864 GeV high current CH_2 runs 32165–32255 were used to extract the Λ missing mass spectrum. The Λ was fitted by a Gaussian plus a polynomial for the background. The area within ±2 MeV under the Gaussian distribution was taken to be the Λ count. The Λ count before and after applying the ESPS hodoscope pulse height cut are 155 and 126, respectively, so that

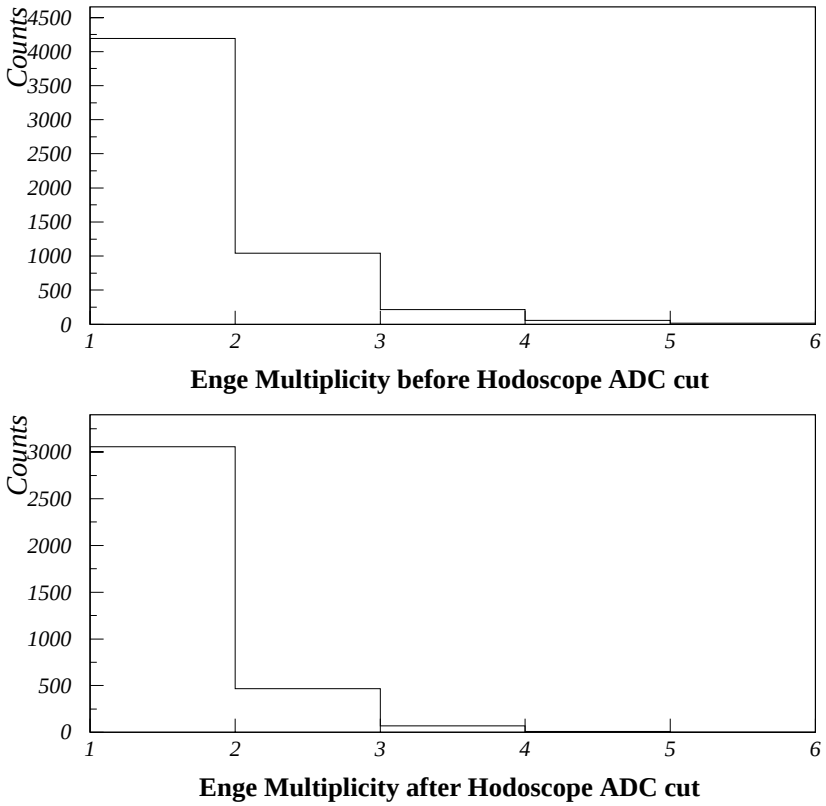

Figure 4.13: ESPS hodoscope multiplicity distribution before and after ESPS hodoscope pulse height cut.

we estimated that the efficiency is 81.3%. The error comes from the Gaussian fitting and the counting rate variation of ESPS hodoscope. It was about 9%. For 1.721 GeV high beam current runs, a tighter cut: ESPS hodoscope ADC < 2500 was used. The efficiency from this cut is 52.1%.

Table 4.3 summarized the efficiencies after the cuts were applied to data and their associated errors.

Table 4.3: List of efficiencies from the cuts and their errors. SOS XP_FP cut will be described in Section 4.9.

Cut type	1.864 GeV	1.721 GeV	Error	Note
SOS Collimator	1.	1.		
Shower Counter	1.	1.		
Aerogel Čerenkov	0.90	0.93	0.032	
Lucite Čerenkov	0.84	0.85	0.028	
TOF β	0.88	0.97	0.004	
SOS Xp_FP	0.86	0.86	0.12	
ESPS Hodo. ADC	0.81	0.52	0.090	High current runs only

4.7 Coincidence Time Cut and Background Estimation

After all these ESPS event selections, considerable amount of ESPS multiplicity still survive. If more than more ESPS events coincided with one SOS event within the 2ns real coincidence window, only one of them can be real. But for for these events, we don't know which one represents the real hit. Thus all these events were kept in the data and contributed to the background of missing mass spectrum. While ESPS multiplicity = 1 events dominated, there were some events with multiplicity =2 and tiny amount of data with multiplicity > 2.

The $(e'K^+)$ coincidence time spectra for high and low current runs for both beam energies are ploted in Figure 4.14.

Figure 4.15 shows $\Delta\beta$ versus coincidence time with protons and pions inside. Different particles are separated by different range of $\Delta\beta$. The real coincidence kaons are in the dense band around $\Delta\beta = 0$ and coincidence time =0. The coincidence time structures of pions and protons are not as well separated as that kaon because the SOS path length correction was based on kaon mass. Thus for pions and protons, the

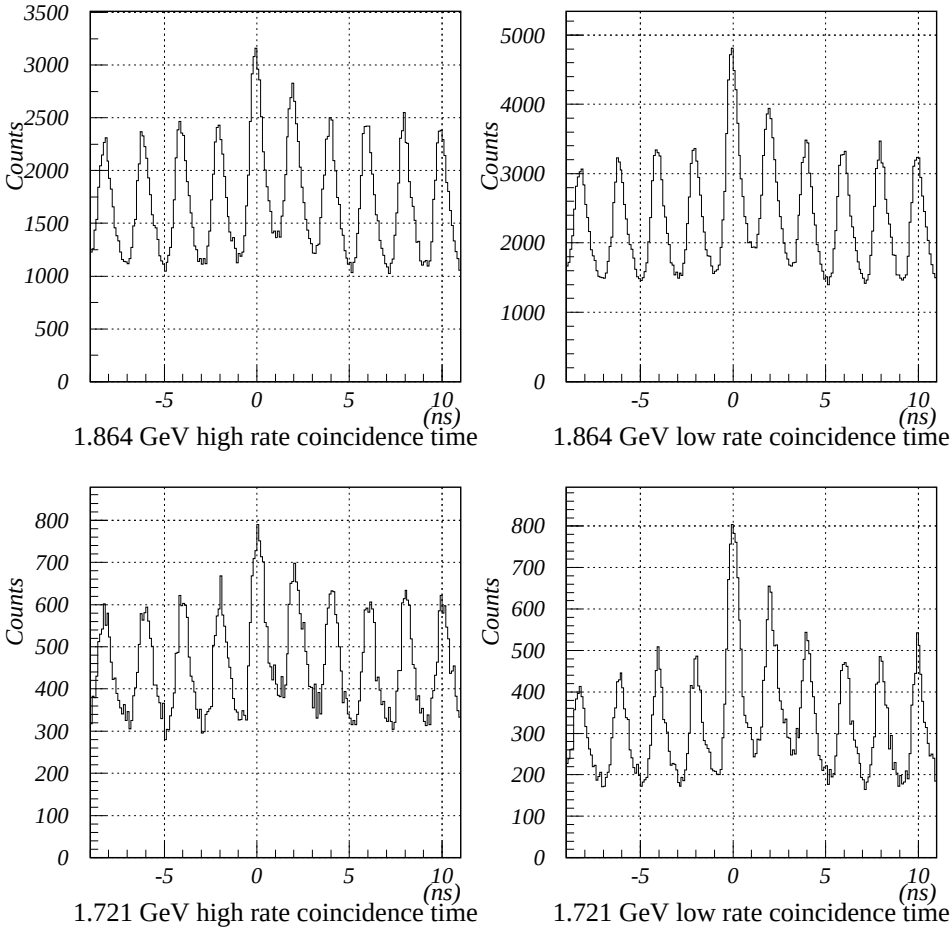

Figure 4.14: e′K coincidence time distributions for different run periods. We can see that the S/A ratio dropped when ESPS e′ rate increased.

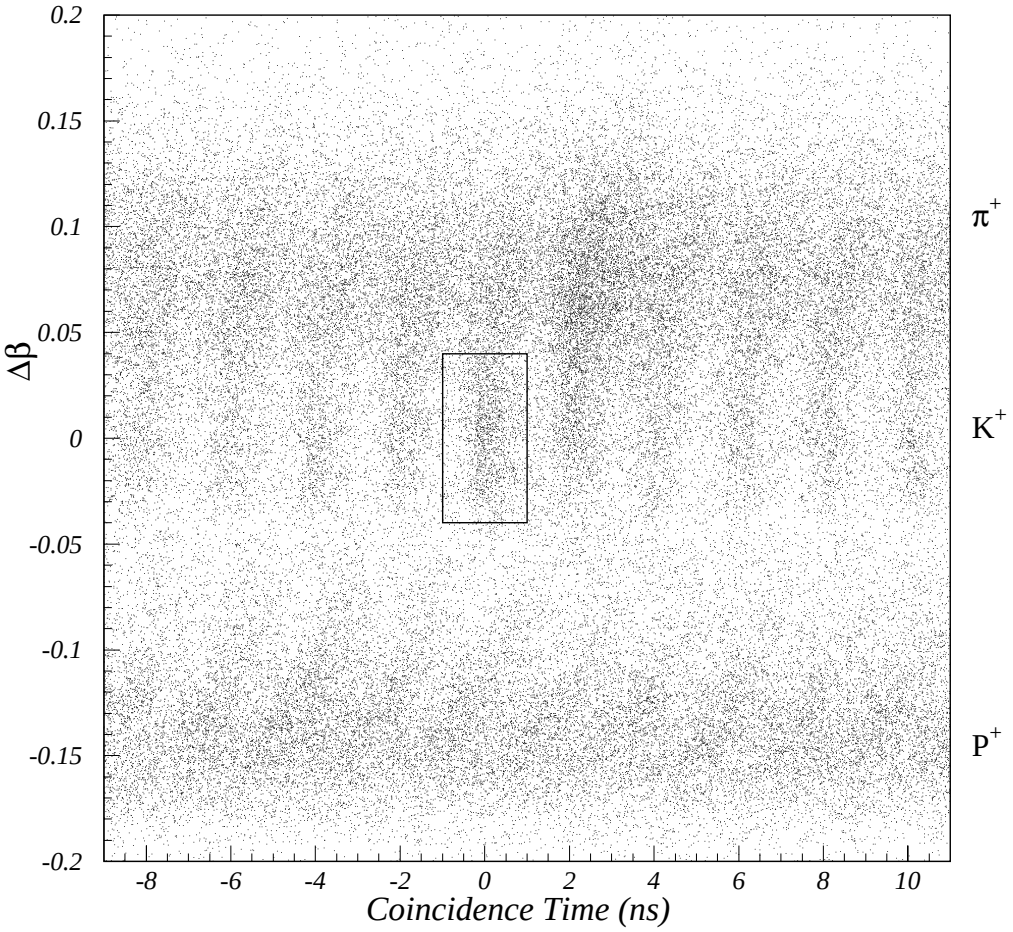

Figure 4.15: Coincidence time drawn with $\Delta\beta$. The three bands in different $\Delta\beta$ ranges are pion, kaon and proton band, respectively. The pion contamination into the kaon region can be reduced after SOS Aerogel Čerenkov cut. The events in the box are in-time kaons.

correction was not correct. Their "in time" or real coincidence ($e'\pi^+$) or ($e'p$) events represented by the dense bands are tilted and shifted from zero due to this reason. To select real coincidence kaon events, we gated at the real coincidence band by 1 ns at both sides from the center of real coincidence band according to the 2 ns beam bucket separation. The hypernuclear and Λ/Σ missing mass spectra were calculated from events within this coincidence time gate. The background for the spectra was dominantly the accidental coincidence events. This background can be estimated from events in the accidental coincidence peaks because all events were taken and analysis under same conditions, so that the accidental coincidence events within the real coincidence window should have the same amount as the accidental events within an average accidental coincidence window.

Note that there is pion and proton contamination to the kaon sample, especially from the pions. These pions spread into the defined real coincidence window thus will be present in the missing mass spectrum. But these pions only present in the spectrum as random background and can be eliminated by random subtraction. Because the real coincidence band and other accidental coincidence band were contaminated by the accidental pions in the same way. There is one concern that because kaon in-time band is close to the pion real coincidence window (about 2 ns away), there may be some in-time pions mixed in. These events can not be subtracted by the accidental subtraction.

To check the contamination of in-time pions in the real coincidence kaon window, we compared the ratio of pion contamination in the real coincidence window and the accidental coincidence window. Because the accidental pion contaminations are in the same amount for both real and accidental window, if there is more pion mix-in in the

Table 4.4: Pion contamination ratios for in-time and out-of-time windows.

Run Period	1.864 GeV	1.721 GeV	Absorber In
In-time Ratio	0.054	0.12	0.12
Out-of-time Ratio	0.10	0.12	0.10

real kaon window, they are from real coincidence pions. The pion contaminations were estimated in the same way as cut efficiency study, fitting the $\Delta\beta$ distribution. First, kaon events within the real coincidence window was selected. Their $\Delta\beta$ distribution had a shape of Gaussian centered at zero representing kaons plus a tail at positive side from the pion contamination. This distribution was fitted by sum of two Gaussians, one centered at zero and the other one around 0.1. The count under the pion Gaussian was the number of pions mixed in. The ratio of this number over the number of total real kaon events was the pion contamination ratio. This ratio in the accidental coincidence window can be calculated the same way. Table 4.4 lists this ratios for the run periods. Pion contamination ratios in the real coincidence window and the accidental coincidence window are basically the same within error. That means all pion contamination in the real coincidence kaon window are accidentals, thus they can be removed by random subtraction.

Unlike the real coincidence peak, the events within accidental coincidence time window [1,3] (the first to the right of real peak) was contaminated by real pions because their coincidence time almost overlap. The spread-in in-time pions enhanced this accidental peak. That is why this accidental peak is higher than others. Thus this accidental peak was not used in the estimation of the accidental background.

4.8 ESPS Momentum Calibration

Before the final missing mass can be calculated, the scattered e′ momentum must be determined. One may recall that the extreme forward peaking distribution of virtual photons and the optical properties of the ESPS enables us to determine the e′ momentum as a function of hit position with good accuracy. The e′ hit positions at ESPS focal plane were measured by the SSD detectors. Electron momentum can be expressed directly as a function of SSD channel number. This momentum-SSD channel correlation was not available before the experiment. It has to be calibrated by actual experimental data.

Because of the zigzagged layout of SSD planes, we anticipated that a single function for the whole focal plane can not describe the momentum-SSD channel relation. Instead, a separate function was used for every SSD plane. This introduced many free parameters in the calibration. According to the initial Raytrace optical simulation of ESPS, the momentum-channel correlation for one SSD plane can be fully described by a 2-order polynomial. There were 8 planes which really got hits. Thus in total we had 24 free parameters, 3 for each plane. We had to find enough constraints to calibrate these parameters. The constraints we can find are:

1. SSD overlapped channel correlation as described in Section 4.5. Because the overlapped channels were fired by the same particle, so these two channel should have the same momentum;

2. The geometry of SSD planes and the spectrometer optics information. The positions of all the SSD planes were surveyed after the experiment. These information can be coded into a Raytrace data card for simulation. The focal plane momentum

hit position relations can be extracted from the focal plane quantities of Raytrace simulation output;

3. The known positions of Λ and Σ^0 in the p(e,e'K^+) missing mass spectrum. We took some calibration runs on CH_2 target for both beam energies.

Calibration by the ground state of $^{12}_{\Lambda}$B was also considered. However, our statistics on bound states are very limited and the precise position of GS is not known (electroproduction dominantly produces GS with J^π : 2^-, while the well known GS binding energy 11.37 MeV is for 1^- GS produced by hadronic reaction). Thus the hypernuclear ground state was only used as a reference in the calibration. None of the constraints mentioned above uniquely confined the momentum-channel relation. Our calibration should combine all these constraints.

Using the reconstructed kaon information from SOS and the known mass of Λ from p(e,e'K^+)Λ reaction from CH_2 target, the electron momentum can be reconstructed by solving Equation 2.10 as:

$$p_e = \frac{m_H^2 + m_K^2 - m_A^2 + 2E_K m_A + 2(-p_K \cos\theta_K + E_K - m_A)p_0}{2(-p_K \cos\theta_K + E_K - m_A)}, \tag{4.1}$$

where M_A is proton mass, m_H is Λ mass and p_0 is the electron beam energies. When p_e was correlated with SSD hit channels, the events which actually came from Λ production formed a segmented dense curve over the background of accidental and carbon quasi-free (QF) (there are carbon nuclei in CH_2 target). The dense curve represented the e' momentum-SSD plane channel correlation at ESPS focal plane. The segmentation was due to the discontinuity of SSD planes. Fig 4.16 shows the reconstructed e' momentum

vs. SSD channel for 1.864 GeV beam current I=0.5 μA and 1.721 GeV I = 1 μA CH_2 target runs. The width of the Λ band was due to the uncertainty in the reconstructed kaon scattering angle and the use of beam raster at target. Due to this width, the momentum-channel correlation can't be precisely determined. In the figure, we can see some gaps in the SSD channel corresponding to the gaps of the ESPS hodoscope. 1.721 GeV CH_2 runs were taken at high current and only had been taken for a very short time, so that the Λ band is barely seen.

The ESPS momentum-SSD channel correlation represented by the Λ band can be compared with the result from Raytrace simulation because the momentum-SSD channel correlation can also be extracted from Raytrace simulation. First, the scattering electrons were generated at target as input to Raytrace simulation according to the angular distribution of virtue photon flux. Using existing Raytrace data card for splitter and ESPS to do a raytrace simulation, the coordinates and angles of the outgoing particles in the ESPS focal plane were calculated. The geometrical positions of the two ends of every SSD plane in (X, Z) plane (the bending plane) were measured with an error of $\pm$1 mm and coded into the Raytrace simulation. The intersections of every outgoing particle with SSD plane were solved from the Raytrace output and the SSD positions. Using the width of every SSD channel: 0.5 mm, the SSD channel number for passing through particles were obtained. This Raytrace simulated momentum-channel correlation was also segmented bands (Figure 4.17). Comparing the simulated relation with initial ESPS raytrace data card with the Λ band, some discrepancies were found. This means that the assumed optics was not totally correct. Further tuning was needed. One correction we have made was the uniformity of the ESPS field. The field B_y may not

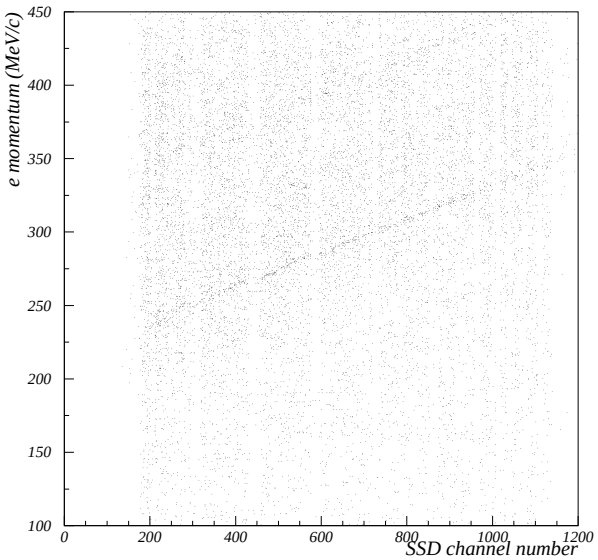

(a) 1.864 GeV e′ momentum vs SSD channel

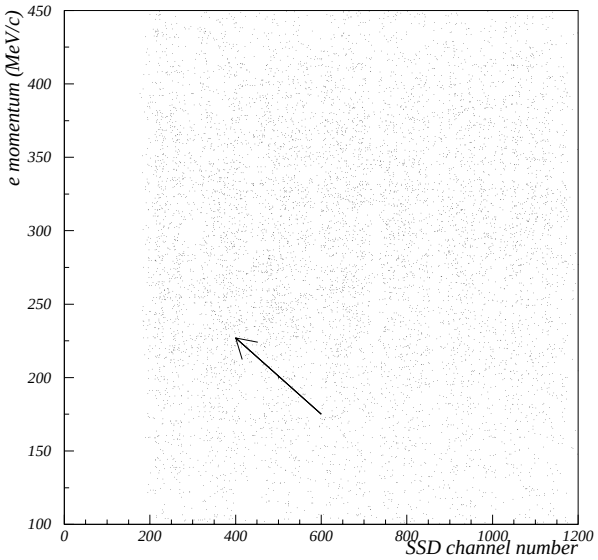

(b) 1.721 GeV e′ momentum vs SSD channel

Figure 4.16: Reconstructed ESPS e′ momentum vs. SSD channel number on CH_2 target. For 1.864 GeV, the Λ band is clearly seen. For 1.721 GeV, the Λ band is pointed by an arrow. It is barely seen.

be uniform in the radius (bending) direction. In Raytrace, this can be described by a dipole field gradient in radius direction and can be expressed as:

$$B_y = B_0[1 - n\Delta r/R + \beta 1(\Delta r/R)^2 + \gamma(\Delta r/R)^3 + \delta(\Delta r/R)^4]. \tag{4.2}$$

The parameters n, $\beta 1$, γ and δ are the numbers listed in line 4 of Raytrace dipole data card.

Another change was the splitter field which had offset when we scaled the magnets field according to beam energies. After the tuning, Raytrace simulation agreed reasonably well with the Λ band.

From the Raytrace data card for ESPS, the simulated SSD hit patterns for both beam energies were obtained by first generating events at the target according to the momentum and angle distributions of bremsstrahlung electrons (Equation 2.7) and then sending them through the ESPS by Raytrace simulation. The intersections of the outgoing electrons with the the SSD planes determined the hit positions. The effect of the ESPS acceptance was taken into account by the Raytrace simulation througn the collimators in the data card. Figure 4.18 shows the comparisons between SSD hit patterns from data and the Raytrace simulated patterns. The gaps within one SSD plane in the real hit patterns are due to the gaps in the ESPS hodoscope acceptance. It can be seen that they are consistent. There are some small discrepancies at low momentum channels. But they only account to about 3% of the total acceptance.

The simulated ESPS momentum-channel correlation also defined a set of SSD channel overlap correlation. From the momentum-channel correlation, a channel in the

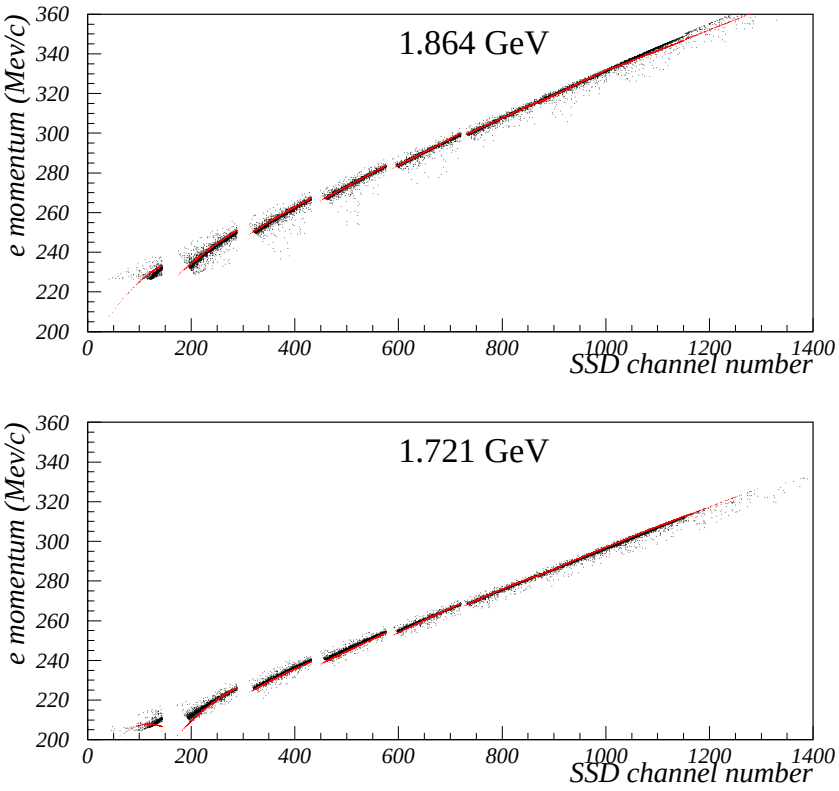

Figure 4.17: ESPS e′ momentum vs. SSD channel number after calibration. The black dots are from Raytrace simulation. The overlaid lines are the calibrated momentum-channel correlation.

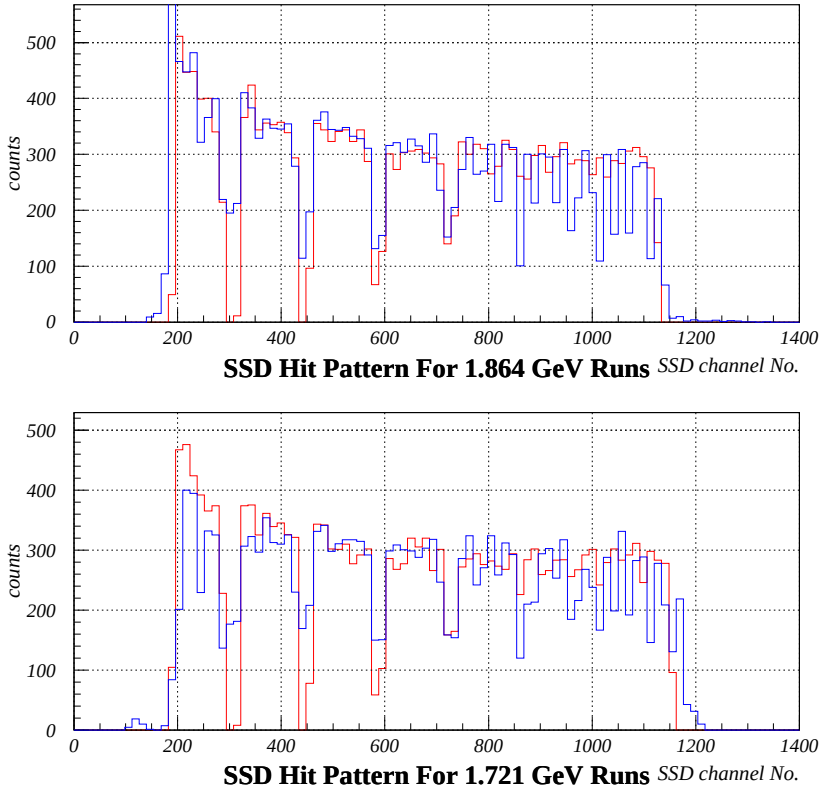

Figure 4.18: The comparisons between SSD hit patterns from data and the Raytrace simulated patterns. The blue histograms are from real data. The red histograms are from Raytrace simulation.

front SSD plane and the channel in the back SSD plane with the same momentum was taken to be overlap channels. This overlap should be consistent with the relation extracted from data (Section 4.5). Due to the position measurement error of SSD planes, the momentum correlation from Raytrace simulation can not be completely accurate. However, the error of position measurement was within a few millimeters. The facts that Raytrace simulated momentum-channel relation were basically consistent with the Λ band and the basic consistency of SSD channel overlap relation shows that the simulated momentum-channel relation is very close to the reality. The offsets from the real correlation is within 1 MeV or so. Notice that the position offset or rotation of SSD planes mostly affect the first order property of momentum-SSD channel relation. The curvature of this relation for every SSD plane will remain largely unaffected . Therefore, we fitted the bands of the momentum-channel relation from Raytrace simulation by two order polynomials, tuning the zeroth and first order coefficients within 2 MeV range while keep the second order parameters unchanged. The known positions and width of Λ and Σ peaks in the missing mass spectrum were used as the tuning criterion under the constraint of SSD channel overlap relations.

The tuning was done plane by plane. Different planes were connected by the channel overlap relation. The missing mass according to $p(e,e'K^+)$ kinematics was calculated from CH_2 data for all the SSD planes. For plane 3 to 9, the Λ peak was well formed and they were used to do the calibration. For plane 2, it was at the low e' momentum end of HNSS acceptance. Only a small part of Λ events were in its acceptance but it had a large acceptance of Σ^0. Thus Σ^0 peak was used to do the calibrations. We changed the offset (zeroth order) and slope (ist order) of momentum-channel relation for every SSD

plane by shifting the two ends of the relation in 100 keV step within ±2 MeV range so that the centers of Gaussian fitting were at correct Λ or Σ^0 masses and the counts under peak were maximized. The statistical quantity we used to describe the merit of missing mass peaks is *sample variance* S^2, which is defined for a random sample $\{X_i, i = 1, ..., n\}$ as:

$$S^2 = \frac{\sum_{i=1}^{n}(X_i - \bar{X})^2}{n-1}, \tag{4.3}$$

where n is the sample size and $\bar{X}$ is the sample mean. In our case, the sample mean is the known mass M_0 of Λ or Σ^0. To calculate the variance of the missing mass peaks, The missing mass peaks were fitted by Gaussian plus a polynomial for the background. If A, μ and σ were the Gaussian amplitude, center and width, we took our sample size n to be the total area under the Gaussian curve $n = \sqrt{2\pi}\sigma A$. Let c_i be the count of the background subtracted missing mass spectrum in bin ΔM with abscissas M_i, then we have:

$$S^2 = \frac{\sum_i c_i(M_i - M_0)^2}{\sqrt{2\pi}\sigma A}. \tag{4.4}$$

In our calculation, we take the sum to be within $\pm 3\sigma$ of Gaussian mean, i.e., $\mu - 3\sigma \leq M_i \leq \mu + 3\sigma$.

A small variance S^2 of Λ missing mass peak means a narrow peak at correct position. A correct momentum-channel correlation should minimize S^2. The tuning of the momentum relation was constrained by the channel overlap between adjacent planes. Sometime, we need to compromise between a better Λ missing mass peak and a better

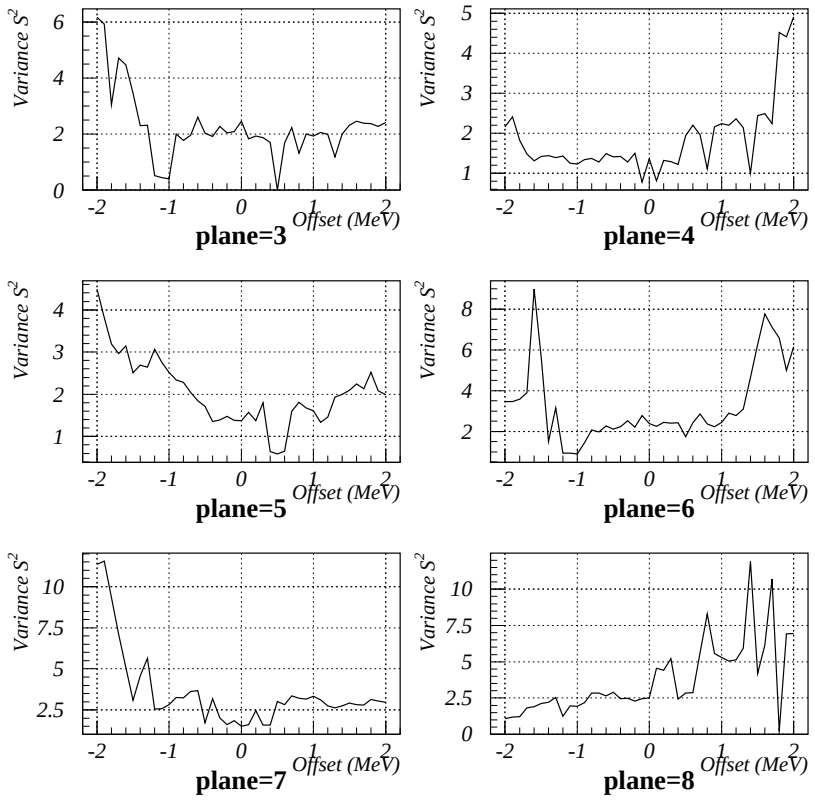

Figure 4.19: Variance S^2 of Λ missing mass peak vs. the slope change of ESPS momentum-SSD channel relation from plane 3 to 8. The way of slope change is shifting both ends of the relation at opposite directions in the same amount, in a 100 keV step, within ± 2 MeV.

agreement of overlap relation with data.

Figure 4.19 and Figure 4.20 show the S^2 of missing mass peaks changing with slopes and offsets of momentum-channel relation for every SSD plane. The offsets and slopes were selected for minimizing the S^2. The reason for some sharp dips in the graphs is due to the split of the missing mass peaks, the S^2 only accounts for the prominent one of the peaks. Apparently the parameters were not correct in these cases. The slopes and offsets at the minimum positions may be varied with ± 100 keV to be more consistent

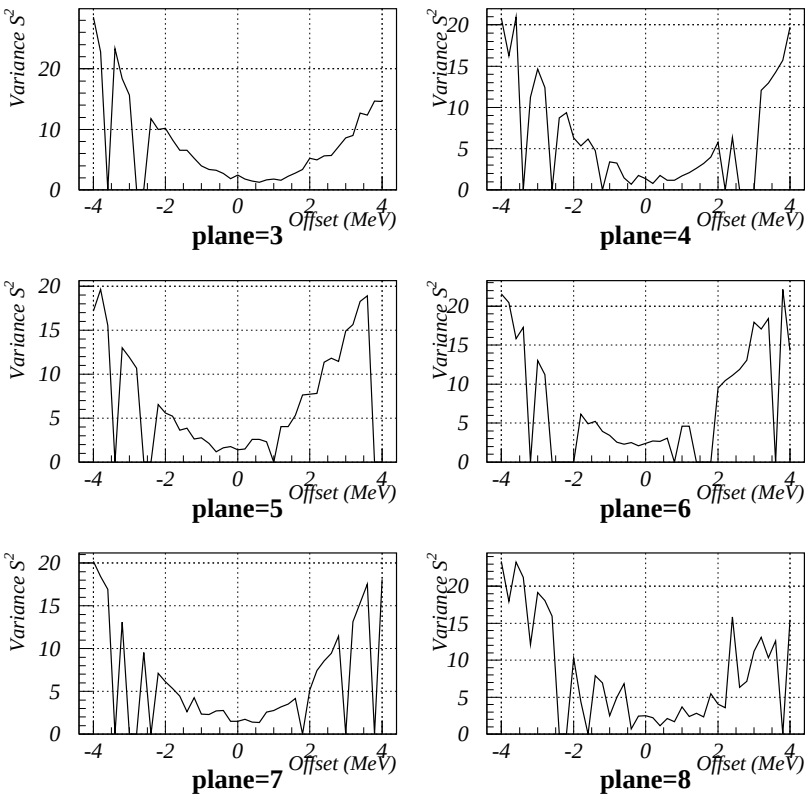

Figure 4.20: Variance S^2 of Λ missing mass peak vs. the offset of ESPS momentum-SSD channel relation from plane 3 to 8. The way of offset is shifting both ends of the relation at same direction in the same amount, in a 200 keV step, within ± 4 MeV.

with overlap relation. The channel overlap relations for adjacent SSD planes are shown in Figure 4.9 corresponding to our momentum-channel correlation. We can see that they are consistent with experimental data within the known error.

For 1.721 GeV runs, due to the high current and low statistics, the background statistical fluctuation sometime caused more uncertainties in the minimum positions of S^2. In these cases we used the ^{12}C(e,e$'$K$^+$)$^{12}_{\Lambda}$B missing mass spectrum as a reference. For runs with the Bremsstrahlung absorbers in, the blocking of the center part of the virtual photon cone changed the e$'$ angle distribution drastically, thus the ESPS focal plane momentum-channel relation also was changed within 1 MeV level of the relation without the absorber . So momentum-channel relation tuning for the absorber runs was based on 1.721 GeV relation and used the $^{12}_{\Lambda}$B missing mass spectrum as a reference.

Using the calibrated momentum-channel relations, the plane by plane Λ and $^{12}_{\Lambda}$B missing mass spectrums for all the run period are shown in Figure 4.21 to Figure 4.25.

4.9 Missing Mass Scale Correction

To determine if the missing mass has any residue correlation with SOS focal plane quantities, the missing mass of p(e,e$'$K$^+$)Λ for 1.864 GeV was drawn in scatter plots correlated with kaon focal plane angles and positions X_FP, XP_FP, Y_FP, YP_FP. From the curve in the missing mass-XP_FP plot, we found there still existed a Λ missing

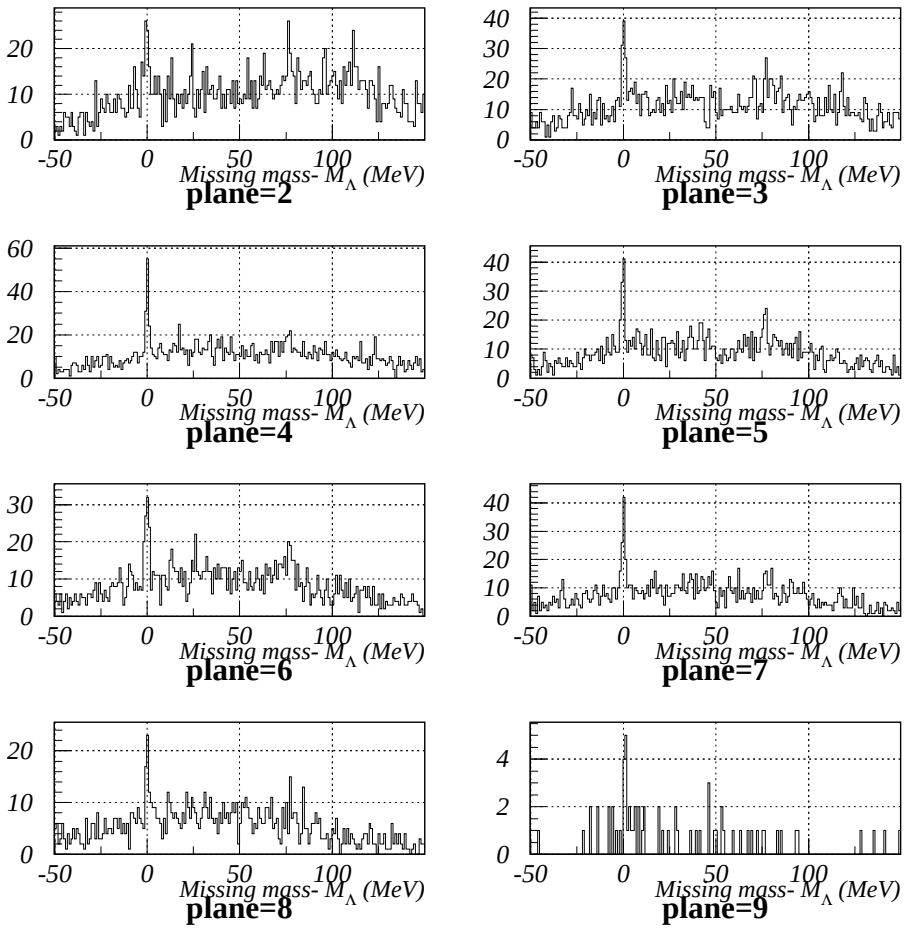

Figure 4.21: 1.864 GeV Λ missing mass spectra plane by plane. The missing mass scale correction has been applied. There is more Σ^0 statistics in low momentum plane than high momentum plane due to the HNSS acceptance

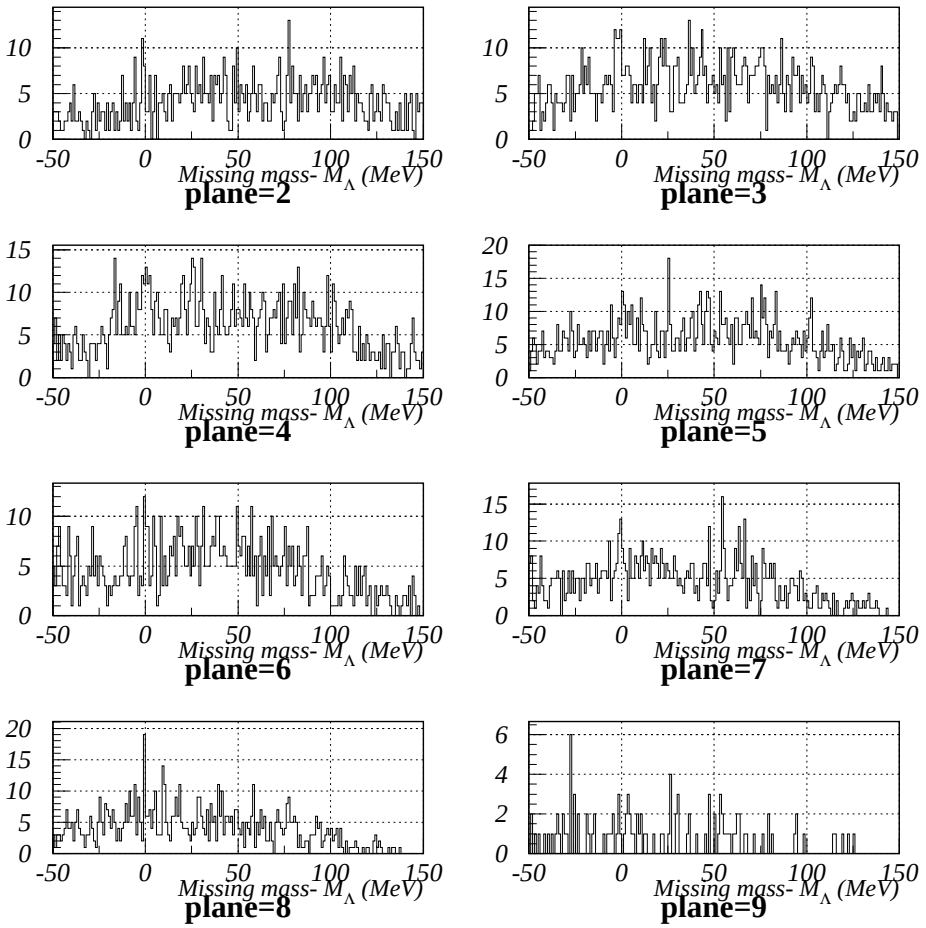

Figure 4.22: 1.721 GeV Λ missing mass spectra plane by plane. The missing mass scale correction has been applied.

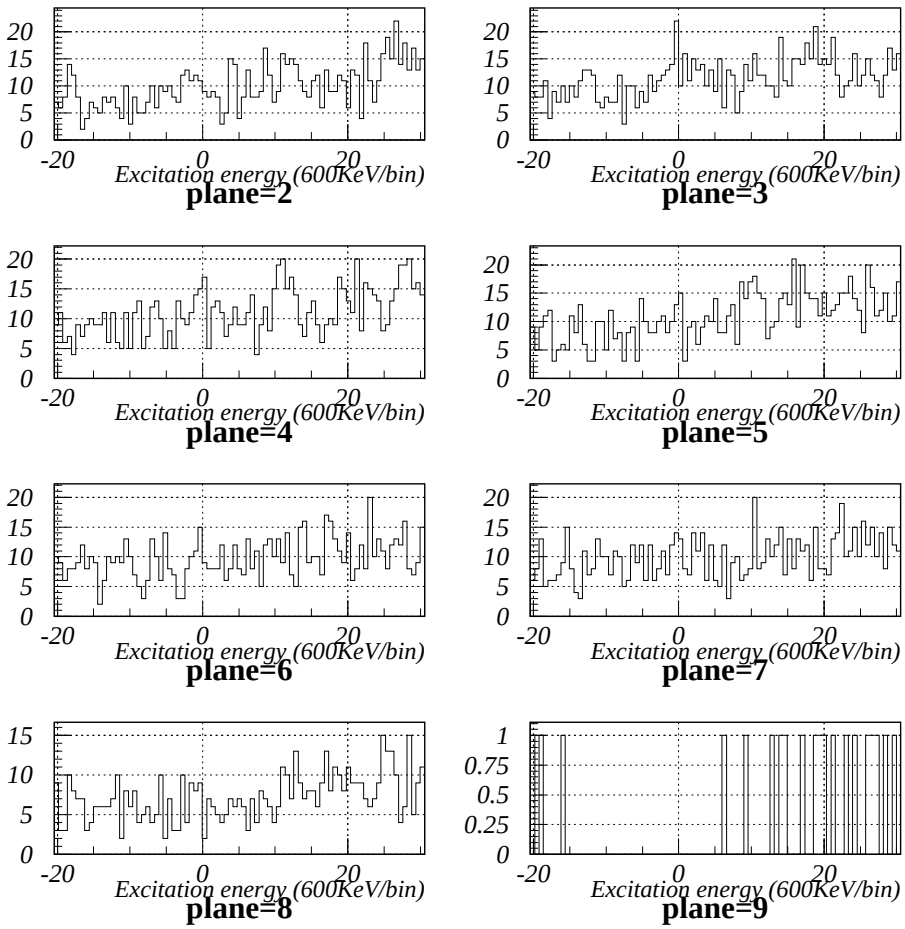

Figure 4.23: 1.864 GeV $^{12}_{\Lambda}$B missing mass spectra plane by plane. The missing mass scale correction has been applied.

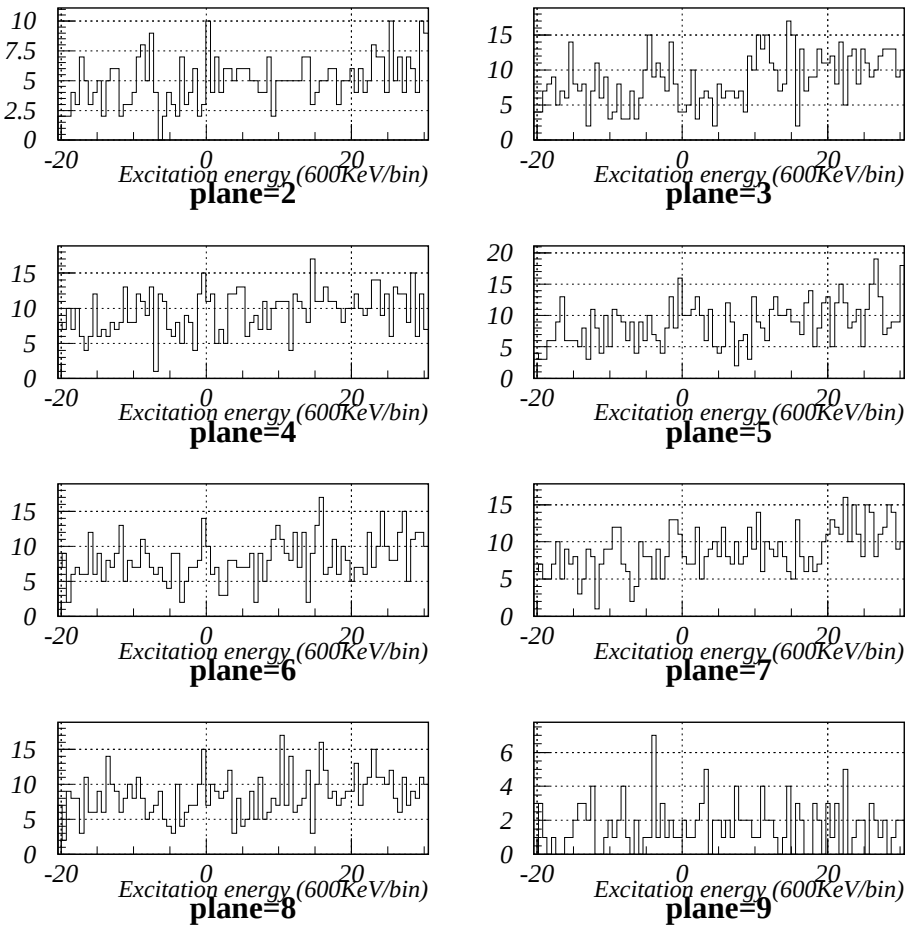

Figure 4.24: 1.721 GeV $^{12}_{\Lambda}$B missing mass spectra plane by plane. The missing mass scale correction has been applied.

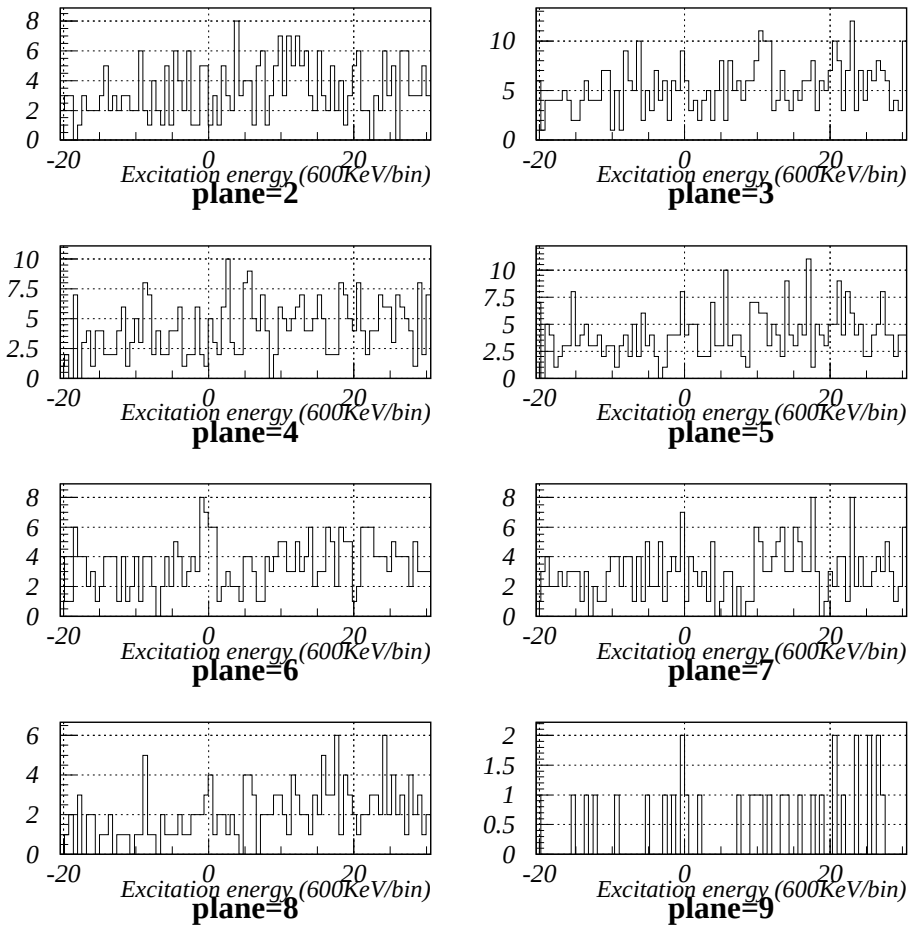

Figure 4.25: $^{12}_{\Lambda}$B missing mass spectra i plane by plane for 1.721 GeV runs with Bremsstrahlung blockers in. The missing mass scale correction has been applied.

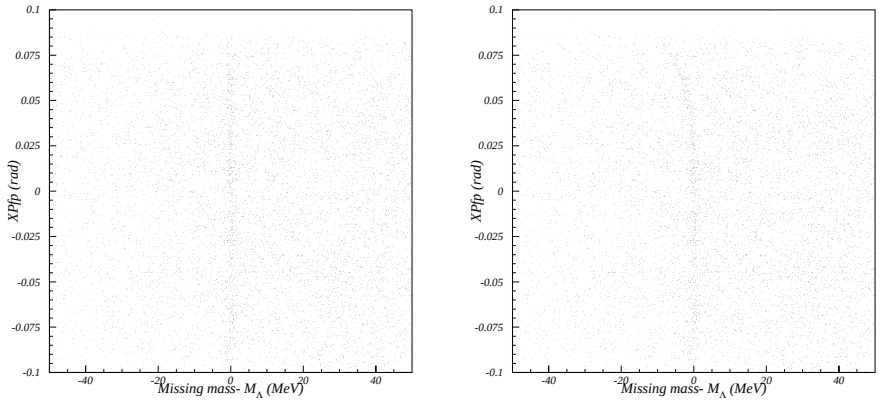

(a) After correction (b) Before correction

Figure 4.26: Λ missing mass versus SOS focal plane in-plane angle XP_FP before and after correction.

mass-XP_FP correlation. This correlation can be corrected by

$$\text{Corrected Missing Mass} = \text{Missing Mass} - 0.883 + 33.31 * XP\_FP + 90.33 * XP\_FP^2 - 18946 * XP\_FP^3 \quad (4.5)$$

Unfortunately, because ^{12}C(e,e′K$^+$) has a different kinematics from p(e,e′K$^+$). This correction can not be directly applied to $^{12}_{\Lambda}$B missing mass. However, there was no correlation when $XP\_FP > 0.05$ rad, Thus we used a cut on XP_FP: $XP\_FP < 0.05$ to plot $^{12}_{\Lambda}$B missing mass spectrum. The loss of events after this cut was estimated by looking at the events in the Λ peak before and after the cut. The counts before and after the cut was estimated by Gaussian fittings. the ratio is 0.855 ± 0.12 (system). The error is from the Gaussian fitting error.

Table 4.5: Λ and Σ^0 peak positions relative to correct Λ mass 1.11568 GeV before scaling and the applied missing mass offsets and scaling factors.

Beam Energy	Λ Position(MeV)	Σ Position(MeV)	Offset (MeV)	Scaling Factor
1.864 GeV	0.703	79.543	0.748	0.976
1.721 GeV	0.794	79.263	0.998	0.984

From the p(e,e$'$K$^+$) missing mass spectrum, we noticed that the Λ and Σ^0 peak still had slight offset from the correct positions. The peak centers of Λ and Σ were fitted by Gaussian plus a background. For 1.864 GeV CH_2 target spectrum, the centers of Λ and Σ peaks were: $M^e_\Lambda = 0.748$ MeV , $M^e_\Sigma = 79.599$ MeV. Their mass difference was: $\Delta M_e = 78.851$ MeV, while the Particle Data Book value for this mass difference is $\Delta M_b = 76.959 \pm 0.023$ MeV. The Λ mass offset can be seen as coming from the error in e$'$ momentum tuning or beam energy, or generally, uncertainty in momentum transfer $q = p_0 - p_e$. A shift E_{off} can be applied to the p(e,e$'$K$^+$) missing mass spectrum to move Λ mass to the correct position. Figure 4.27 shows the derivative of missing mass correlation with momentum transfer q: $\frac{dm_H}{dq}$ for proton and carbon kinematics. We can see that if the same amount of shift E_{off} is applied to ^{12}C(e,e$'$K$^+$) missing mass spectrum as that of p(e,e$'$K$^+$) , an error of $0.2E_{off}$ in $^{12}_{\Lambda}$B missing mass will come from this shift.

The expanse of Σ^0/Λ mass difference can not be explained by error in momentum transfer q. From HNSS kinematics, inaccurate knowledge about SOS central momentum and SOS central angle can all contribute to the expanse of missing mass scale. However, since the ESPS momentum has been tuned under fixed assumption on SOS kinematics parameters, all the contributions were then centroid to SOS central momentum p_0. Thus

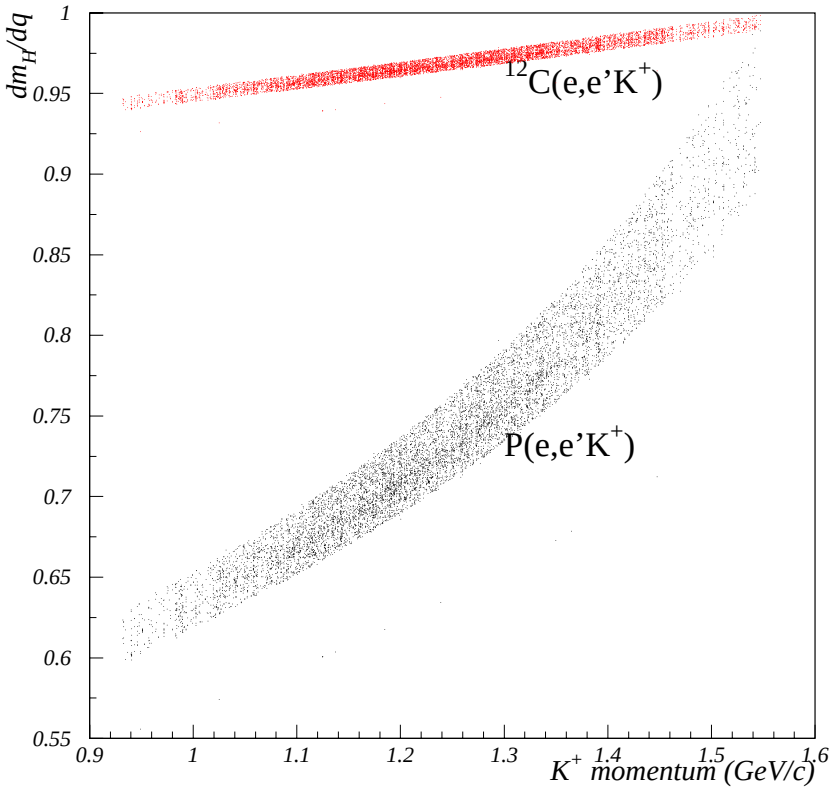

Figure 4.27: $\frac{dm_H}{dq}$, the derivative of missing mass as a function of momentum transfer q for p(e,e$'$K$^+$) and ^{12}C(e,e$'$K$^+$) kinematics, drawn with kaon momentum p_K.

it became the most sensitive parameter. SOS central momentum p_0 was used as a constant in the analysis. The quantity we measured at SOS is relative momentum "δp". Therefore an offset on p_0 does not only shift the kaon momentum, but also expands (or shrinks) the entire SOS momentum scale which in turn expands (or shrinks) the missing mass scale. The relationship between change in missing mass and change in SOS momentum can be derived from Equation 2.11 as:

$$\frac{dM_H}{dp_K} = \frac{[-(E_0 - E_e + m_A)\beta_K + (p_0 - p_e)\cos\theta_K]}{\alpha}, \tag{4.6}$$

where,

$$\alpha = [m_K^2 + m_A^2 + 2m_A(E_0 - E_e) + 2p_K(p_0 - P_e)\cos\theta_K - 2E_K(E_0 - E_e + m_A)]^{\frac{1}{2}}, \tag{4.7}$$

$$\beta_K = \frac{p_K}{\sqrt{p_K^2 + m_K^2}}. \tag{4.8}$$

Figure 4.28 shows $\frac{dM_H}{dp_K}$ for the two kinematics within HNSS acceptance. We can apply an overall scaling factor $scale = \Delta m_b/\Delta m_e$ to correct the Σ^0/Λ mass difference. The same shrinking factor can be applied on ^{12}C(e,e'K$^+$) missing mass spectrum. Because if we take $\frac{dM_H}{dp_K}$ as constant, for p(e,e'K$^+$) kinematics, $\frac{dM_H}{dp_K} \sim S_P = 0.7$, the error is $\pm$ 0.1 (σ); for ^{12}C(e,e'K$^+$) kinematics, $\frac{dM_H}{dp_K}$ is more like a constant, $\frac{dM_H}{dp_K} \sim S_C = 0.9$. If the expanse of Σ^0/Λ mass difference comes from the error in kaon momentum, in other words, experimental value P_K^e is not equal to the correct momentum P_K^r, then the scale

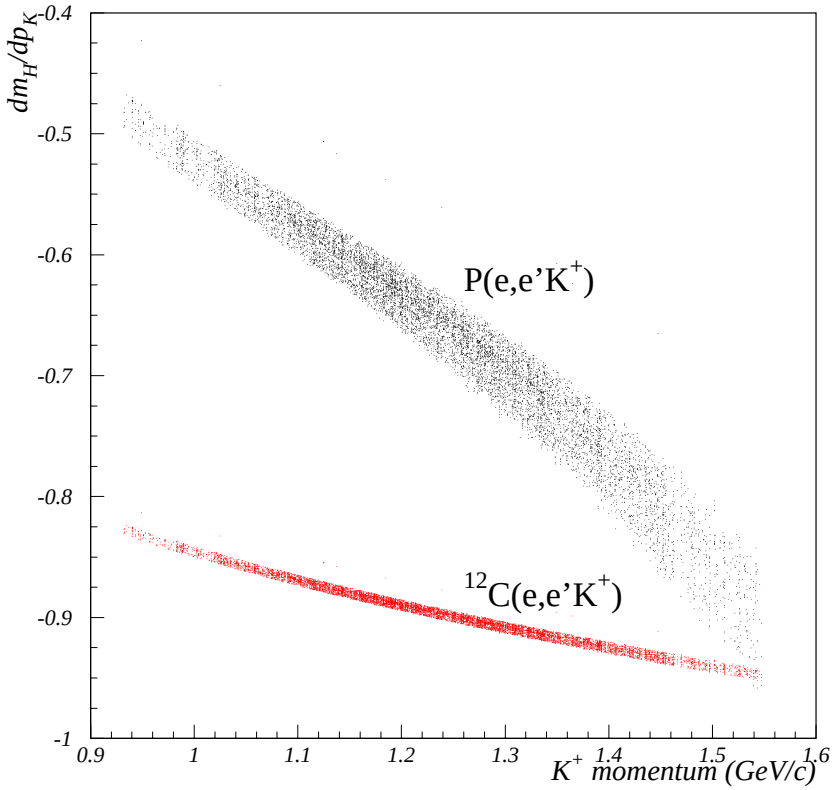

Figure 4.28: $\frac{dm_H}{dp}$, the derivative of missing mass as a function of kaon momentum p_K for p(e,e$'$K$^+$) and ^{12}C(e,e$'$K$^+$) kinematics, drawn with kaon momentum p_K.

factor on ^{12}C(e,e′K$^+$) missing mass:

$$\frac{\Delta m_b'}{\Delta m_e'} = \frac{S_C * \Delta P_K^r}{S_C * \Delta P_K^e} = \frac{S_P * \Delta P_K^r}{S_P * \Delta P_K^e} = \frac{\Delta m_b}{\Delta m_e} = scale, \tag{4.9}$$

where $\Delta m_b'$ and $\Delta m_e'$ are the corrected and uncorrected mass differences in ^{12}C(e,e′K$^+$) kinematics, respectively. Therefore, the two kinematics have the same scaling factor. The correct mass separation between Λ and Σ^0 after the shift and scaling means that the kaon momentum is correct for the Λ events while putting the Λ mass at emission threshold. Same correction then produces the correct mass of $^{12}_{\Lambda}$B with respect to the emission threshold in the ^{12}C(e,e′K$^+$) kinematics. Hence the emission threshold position in the carbon missing mass spectrum is also at correct position. This means that correct mass for p(e,e′K$^+$) kinematics should be expressed as:

$$\text{corrected missing mass} = [(\text{missing mass} + offset) - m_\Lambda] \cdot scale, \tag{4.10}$$

and for ^{12}C(e,e′K$^+$) kinematics,

$$\text{corrected missing mass} = [(\text{missing mass} + offset) - m_{threshold}] \cdot scale. \tag{4.11}$$

The offsets and scale factors calculated from the Λ and Σ^0 peak positions are listed in Table 4.5.

Figure 4.29 shows the Λ and Σ^0 missing mass spectrum after this scaling. Figure 4.30 shows the summed $^{12}_{\Lambda}$B spectrum. Since the absolute missing mass of $^{12}_{\Lambda}$B was calibrated by the know masses of Λ and Σ peaks, the $^{12}_{\Lambda}$B spectrum is shown in Λ

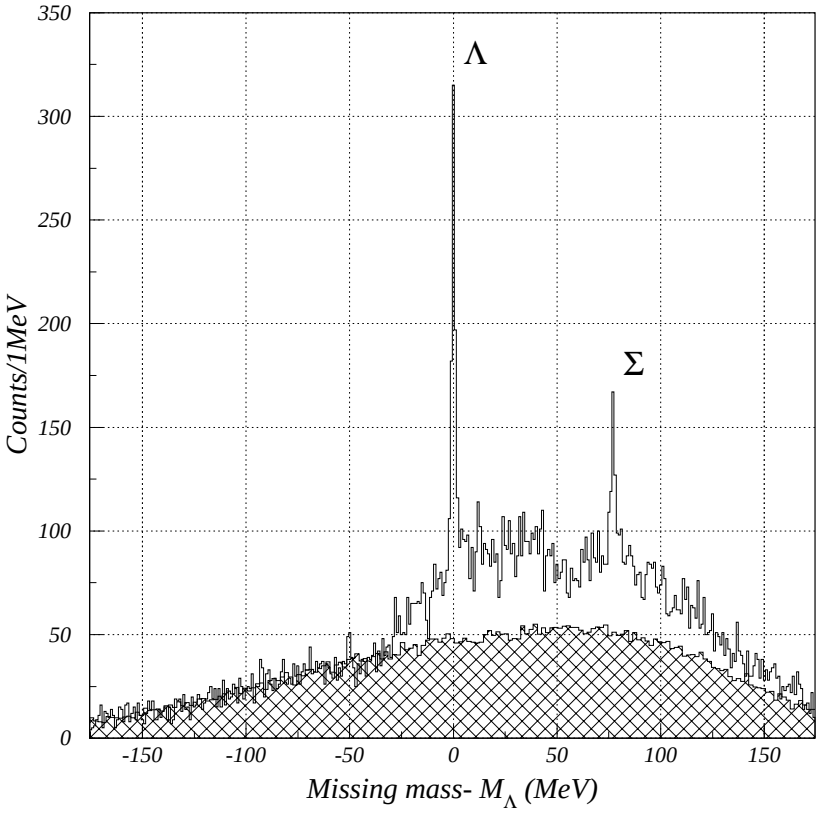

Figure 4.29: Λ and Σ^0 missing mass spectrum after scaling. The shaded area is the background.

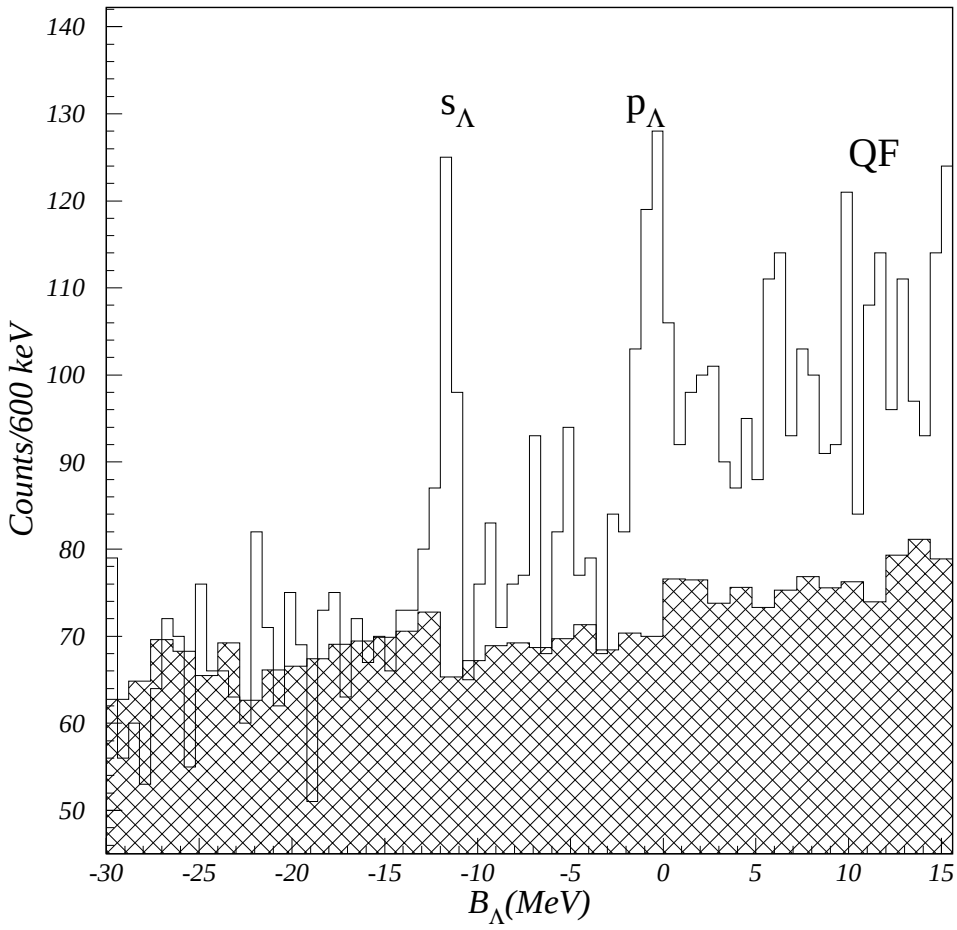

Figure 4.30: Summed $^{12}_{\Lambda}$B binding energy spectrum. The distribution include accidental background and Λ quasi-free contribution. Shaded area is the accidental background calculated from out-of-time events.

binding energy scale. The strength above $\sim$ 11 MeV is from Λ quasi-free contribution. The background distribution was obtained from the events in the 8 accidental coincidence peaks and analyzed with the same kinematics as the real coincidence events.

When coincidence time moved away from the real coincidence window, some coincidence events may be cut by the coincidence trigger gate (80 ns wide). This caused the fall off of the accidental coincidence peak heights. Thus to correctly estimate the statistics of accidental events, we used the statistics of the first accidental peak C_{l1} on the left of the real coincidence peak to scale the summed background distribution of the 8 accidental peaks. The scale factor was: $S_b = C_{1l}/$(summmed statistics of 8 accidental peaks).

Systematic error of the $^{12}_{\Lambda}$B binding energy has two sources: (1) The calculation error of scale factor and offset due to the fitting errors of the Λ and Σ^0 peak and (2) the difference of the two kinematics. The error of scale factor from peak fitting is:

$$\sigma_{scale} \approx \frac{\sigma_{\Delta m_e}}{\Delta m_e} scale. \tag{4.12}$$

The fitting error for peak centers of Λ and Σ^0 are 0.07 MeV and 0.13 MeV respectively. Therefore, we get $\sigma_{scale} = 0.002$.

When using the same scale factor for Λ and $^{12}_{\Lambda}$B spectrum, we assumed $\frac{dM_H}{dp_K}$ is constant for both kinematics. From Equation 4.9 and the error of S_P, this led to an error of 0.0048 for the scale factor. Therefore the total systematic error of the scale factor is 0.005.

If E is binding energy before the scaling and energy offset, E_s is the the binding energy after the scaling, then from Equation 4.11, the total error of the scaled binding

energy is:

$$\sigma_{E_s}^2 = (E + E_{off})^2 \sigma_{scale}^2 + scale^2 \sigma_{Eoff}^2 + scale^2 \sigma_E^2, \tag{4.13}$$

where σ_{Eoff} is the error of the energy offset due to peak fitting error which was 0.07 MeV plus kinematics difference 0.15 MeV. Thus, $\sigma_{Eoff} = 0.17$ MeV. Since *scale* is very close to 1, the additional systematic error introduced by this energy shift and scaling is:

$$\sigma_s = \sqrt{(E + E_{off})^2 \sigma_{scale}^2 + scale^2 \sigma_{Eoff}^2}. \tag{4.14}$$

For ground state, binding energy $E \approx -11.6$ MeV, we get:

$$\begin{aligned} \sigma_s &= \sqrt{11.6^2 \times 0.005^2 + 0.976^2 \times 0.17^2} \\ &= 0.18 \quad MeV. \end{aligned} \tag{4.15}$$

4.10 Energy Resolution

The energy resolution is dominated by the kaon momentum uncertainty measured by SOS spectrometer. An analysis of missing mass spectrum of electron elastics scattering from carbon target detected by SOS obtained in fall of 1997 gives an energy resolution of about 1 MeV for carbon GS. This resolution had the contribution of multiple scattering of electrons through SOS entrance window material and air gap together with target energy straggling. For HNSS, the target chamber was connected to SOS under vacuum. The SOS entrance window was removed. This window was one of the major sources of multiple scattering. In addition, we only used the best region ($\pm 7\%$) of the entire momentum acceptance of the SOS. Thus we expect a 600 – 1000 keV (FWHM)

Table 4.6: Composition of HNSS missing mass resolution.

Component	Resolution (keV)
kaon momentum	600 – 1000
kaon scattering angle	87
e′ momentum	300
Target energy straggling	37
Beam energy	180
Total	650 – 1064

resolution for SOS.

The kaon scattering angle uncertainties are $\sigma_{xp} = 1.1$ mr, $\sigma_{yp} = 5.3$ mr (Section 3.5.3). This will cause $\sim 5.3 \times 10^{-4}$ (FWHM) error in the cosine of the kaon scattering angle. According to Equation 2.11, this will contribute to the energy resolution $Error_{ang} \sim p_K q/m_H \times 5.3 \times 10^{-4} = 87$ keV.

The error of e′ momentum mainly comes from the uncertainty of momentum-SSD channel relation. From Figure 4.19 and Figure 4.20 the offset and slope parameters can be varied reasonably to shift the momentum at most 2 bins. Therefore a contribution of 300 keV from e′ momentum to energy resolution was accepted.

The other sources of error of missing mass are variation in beam energy and target energy straggling. The beam energy has been stabilized within 10^{-4}. It will then contribute about 180 keV. Our carbon target is very thin: $t = 22mg/cm^2 = 5.2 \times 10^{-4} X_0$. The uncertainty from target energy straggling is very small: ~ 37 KeV.

Table 4.6 breaks down the contributions to energy resolution and gives the total expected resolution.

The actual resolution of ${}^{12}_{\Lambda}$B binding energy, can be verified by the width of ground state peak in the spectrum. According to theoretical prediction (1.8), the ground state of

$^{12}_{\Lambda}$B is strongly excited. Although it is composed of two s_Λ spin doublet states, the energy separation of the two states is less than 200 keV and the member state with natural parity has only about 1/4 of the total strength. Furthermore, this peak is well separated from other significant peak structures, unlike the p_Λ states which have multiple peaks closely located. The width of this $^{12}_{\Lambda}$B ground state peak should reflect the actual missing mass resolution. Shown in 4.31 is the background subtracted $^{12}_{\Lambda}$B ground state binding energy spectrum in 300 keV/bin. A Gaussian fit to the peak gave a width of $\sim$ 920 keV (FWHM) with confidence level $\sim$94%. The fitting error for the ground state peak width is $\sim$ 100 keV. The shape of the ground state peak affect the width of Gaussian fitting, too. In a background substracated spectrum, the error in the background estimation will change the real shape of the ground state peak. To investigate this effect, a linear function plus a Gaussian distribution was used to fit the ground state peak in a very wide range (from left 10 MeV to 4 MeV). The FWHM of the Gaussian function in this case was 862 keV. It is $\sim$60 KeV less than fitting with a Gaussian only. This 60 keV was taken as the systmatic error of the $^{12}_{\Lambda}$B ground state missing mass resolution. Combined with the 100 keV fitting error, the total error of missing mass resolution is $\sim$116 keV.

To estimate the The energy resolution of Λ peak in CH_2 target runs was dominated by the contribution from beam position uncertainty and kaon scattering angle uncertainty. Beam rastering was used for CH_2 target runs to avoid melting target. The effect of 2.1 mm (Y) $\times$ 1.1 mm (X) beam raster on kaon momentum resolution was estimated by Monte Carlo simulation. First events were generated at target with positions spread according to the raster size, these events were then transported to the SOS focal plane through the SOS spectrometer by the Raytrace simulation. These events were re-

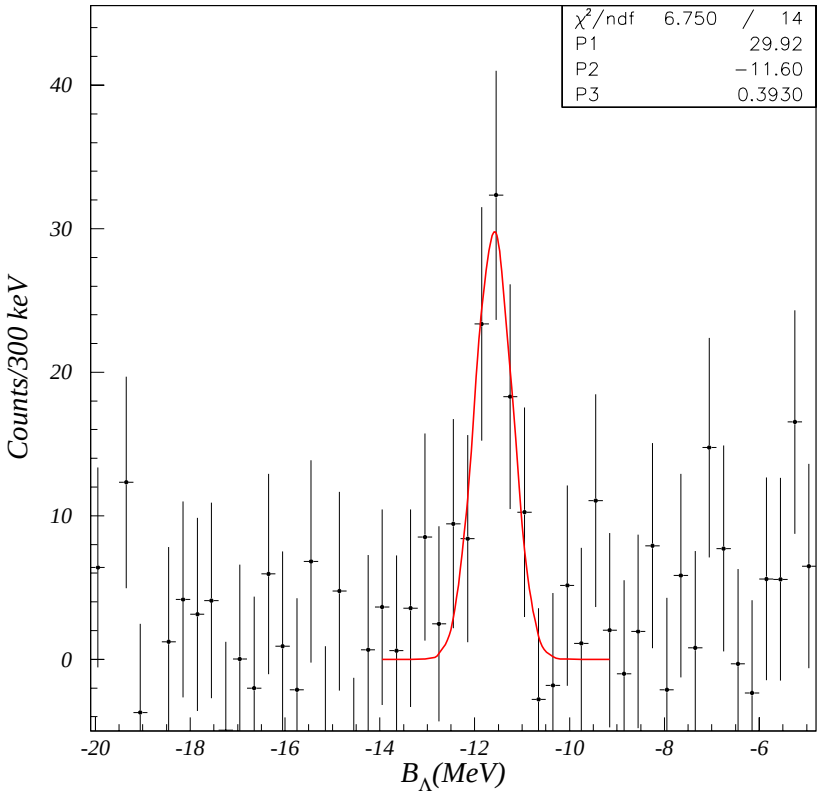

Figure 4.31: background subtracted ${}^{12}_{\Lambda}$B ground state binding energy spectrum in 300 keV/bin. It was fitted by a Gaussian function. The error bars are statistical errors only.

constructed back again to the target by the SOS reconstruction matrix. The distribution of the error of reconstructed momentum gave the contribution of beam rastering to kaon momentum resolution (Figure 4.32). A Gaussian fitting to the distribution had a FWHM of 1.30×10^{-3} for δp, which was 1.72 MeV (FWHM) when SOS central momentum was set at 1.2398 GeV/c. The contribution from kaon scattering angle uncertainty was more significant for p(e,e$'$K$^+$) reaction because of the smaller mass of Λ compared with $^{12}_{\Lambda}$B hypernucleus. It contributed 880 keV for p(e,e$'$K$^+$) kinematics . Thus we expect the total energy resolution will be 1.93 MeV (FWHM). This is consistent with the 1.93 MeV (FWNM) energy resolution of our Λ spectrum (Figure 4.29).

The analysis of Dalitz pair production from carbon target: C(e,e$^+$e$^-$e$'$)C (Figure 4.1) can also gives the approximate range of energy resolution. Due to the large mass of carbon nucleus compared with electron, carbon nuclear recoil momentum was very small and can be ignored. In addition, the e$^-$e$^+$ pair and the scattering e$'$ were all in very forward angles so they can be treated at 0°. Therefore the beam energy was reconstructed simply by the sum of the energies of the two electrons (the scattered electron e$'$ and the electron from pair production) in the electron arm and the positron (from the pair production) in the SOS. Figure 4.33 shows the distribution of beam energy obtained by this method, which has a 820 keV resolution (FWHM). This method used the momenta of two electrons in the ESPS rather than one electron in the (e,e$'$K) final state. It had an extra contribution of electron momentum resolution. Thus we may expect a better energy resolution for the (e,e$'$K) kinematics. On the other hand, the Dalitz pair events only came from two higher momentum SSD planes: plane 8 and 9, which had better energy resolution than the lower momentum planes due to optical properties of ESPS.

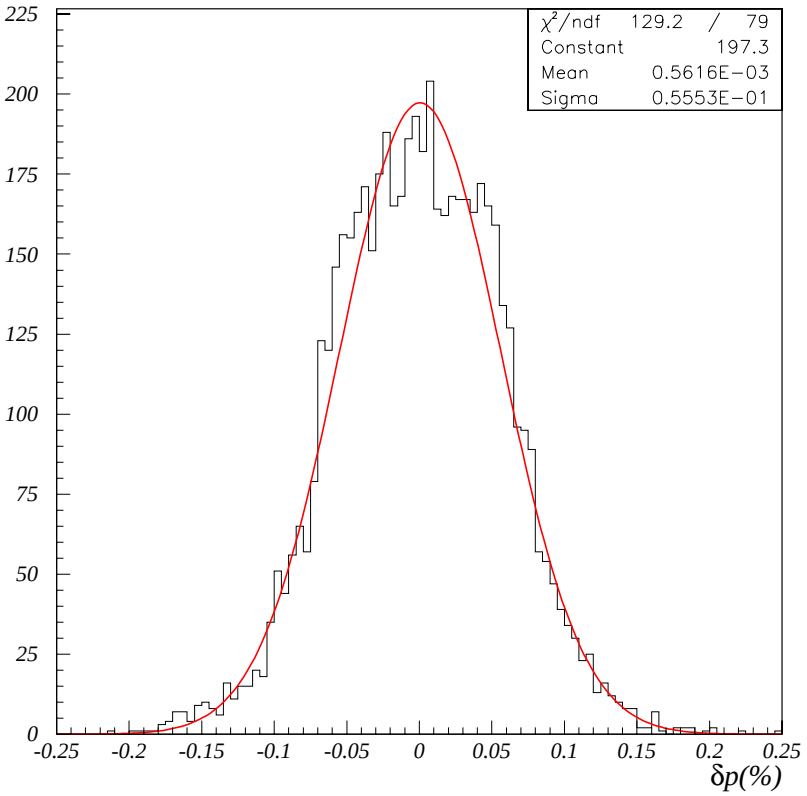

Figure 4.32: Simulated error distribution of reconstructed kaon momentum after beam position on the target was spread by the raster.

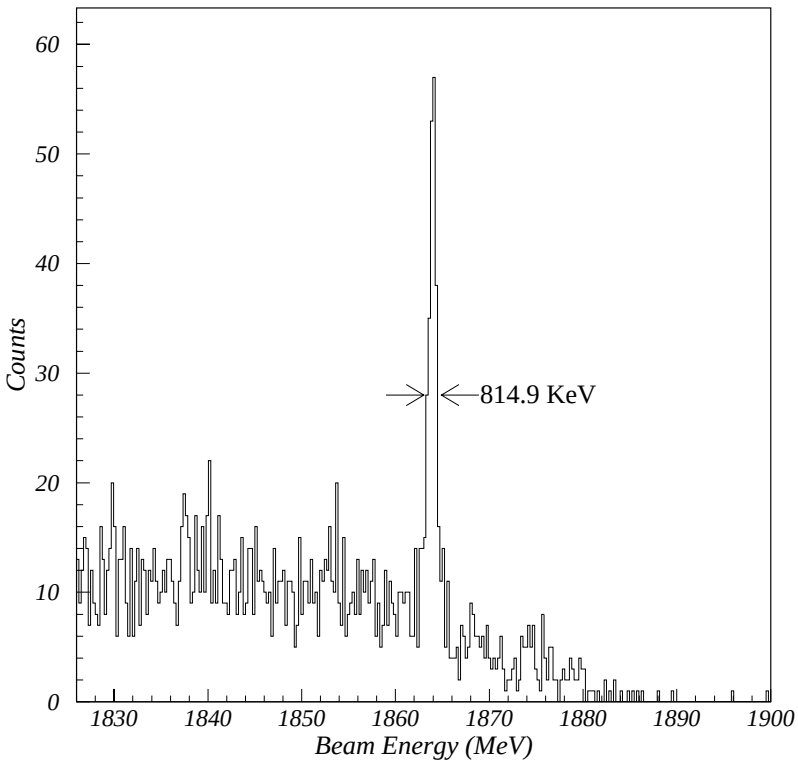

Figure 4.33: Calculated beam energy using the pair production data. The FWHM of the beam energy calculation is shown in the graph.

Therefore, the 820 keV (FWHM) resolution only gives the order of the actual missing mass resolution. It is consistent with 920 ± 120 keV (FWHM) resolution we got from ${}^{12}_{\Lambda}\mathrm{B}$ ground state.

CHAPTER 5

ELECTROPRODUCTION CROSS SECTION

In the previous chapter, we described the ${}^{12}_{\Lambda}$B binding energy spectrum in terms of count per energy bin. From the spectrum hypernuclear energy levels can be extracted. This is the primary goal of the present experiment. On the other hand, as a new production mechanism, the hypernuclear electroproduction cross section is also interesting. It will help improve our understanding about Λ-nucleus interaction. In this chapter I will describe the extraction of ${}^{12}_{\Lambda}$B electroproduction cross section.

To calculate the cross section, spectrometer acceptance and various correction factors have been studied. The correction factors including contributions from detector efficiencies, electronic and computer dead time, kaon decay and absorption in the spectrometer and efficiencies of cuts applied to data. The cut efficiencies have been studied in last chapter and summarized in Table 4.3.

5.1 HNSS Acceptance

5.1.1 SOS Solid Angle Acceptance

SOS solid angle acceptance is a function of particle momentum. Raytrace simulation was used to determine this function. The fiducial areas of various SOS focal plane detectors, the physical aperture of various magnetic elements, collimators and vacuum windows were coded in the Raytrace simulation with the actual dimensions from their

design drawings. The events which can't pass through the spectrometer or lie outside one of the collimators were rejected by the simulation. Events were generated at the target uniformly distributed over the largest possible solid angle. This solid angle scaled by the ratio of number of passing through events over all generated events gave the spectrometer acceptance.

The SOS detectors which restricted spectrometer acceptance were drift chambers, the four hodoscope planes and lucite Čerenkov. To determine the fiducial areas of these detectors, we compared the raytrace simulated particle X-Y profile at the corresponding collimator plane with real particle profile at the detector planes. According to this we adjust the offsets and X, Y boundaries of the active region. As an example, Figure 5.1 shows the consistence of raytrace simulated particle profile with distribution of real data from run 32535 at SOS entrance collimator and the last hodoscope plane S2X.

During the experiment, to suppress the high background positron triggers, S1X1, S1X2, S1X8, S1X9 were disabled before run 32421. after that, they were turned on. S2X1 was disabled for all the runs. However, because of the 3/4 SCIN trigger mode, the triggers were fired by other 3 hodoscope planes, so these disables scintillators didn't affect the total acceptance except run 32178–32421. During this run period we used S1X in veto. All events passing through these four scintillators were vetoed. This reduced the acceptance and the corresponding S1X collimator size in the Raytrace data card. Table 2.5 list the X,Y boundaries of fiducial area of these detectors.

To determine the relation of SOS solid angle acceptance to particle momentum, a Raytrace simulation was done with input particle momentum varying (δp) in a 3% step from -30% to 44%. which was much larger than the kinematics region of Λ and

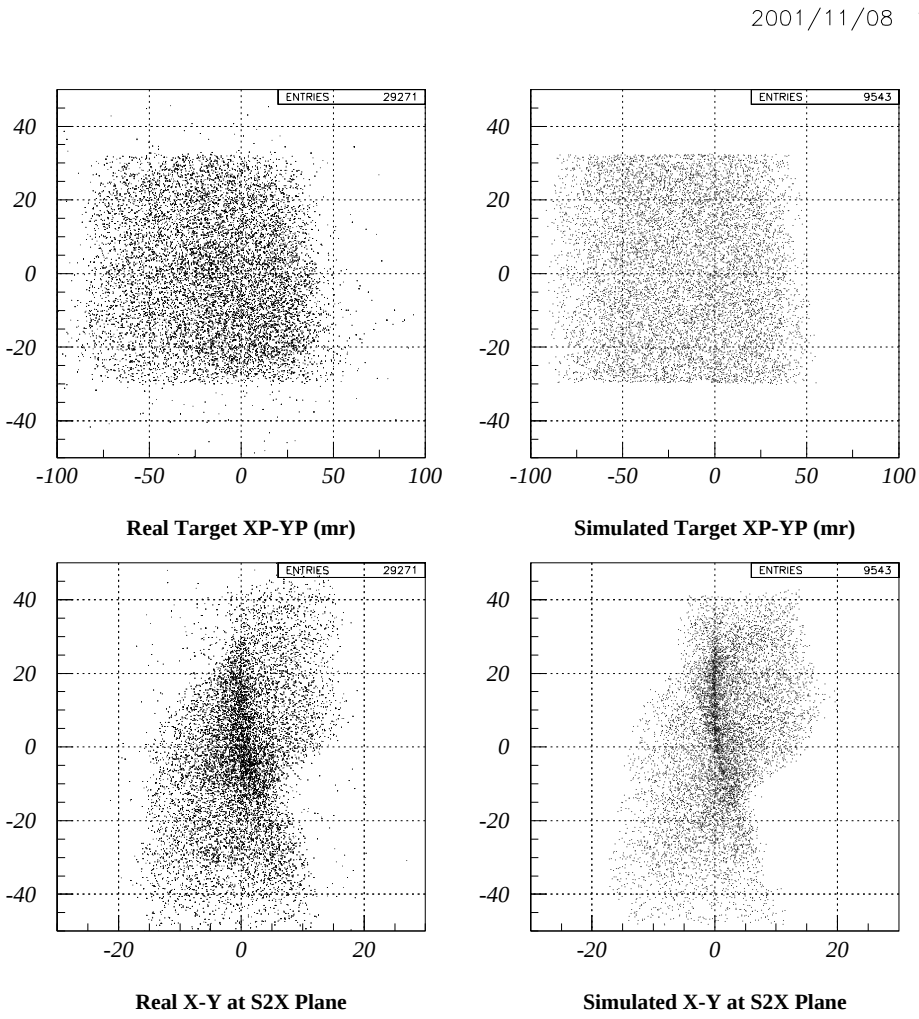

Figure 5.1: Comparisons of Raytrace simulated particle profiles with real data distributions. Top two panels are the reconstructed target angel distribution from data and the Raytrace simulated target pattern. Bottom two show the real particle profile at the last SOS hodoscope plane S2X and Raytrace simulated profile at same plane.

Table 5.1: SOS solid angle acceptance over a momentum range of -12% to 21% obtained by Raytrace simulation.

$\delta p(\%)$	1.864 GeV(msr)	1.721 GeV(msr)	1.864 GeV with $\overline{S}1X$ (msr)
-12.0	3.55	3.31	2.31
-9.0	4.78	4.21	3.92
-6.0	4.90	4.97	5.05
-3.0	4.99	5.11	5.07
0.0	5.03	4.93	5.05
3.0	4.93	5.01	5.00
6.0	5.00	4.93	4.99
9.0	4.95	4.90	4.98
12.0	4.89	4.97	4.98
15.0	4.44	4.62	4.33
18.0	3.92	4.15	3.31
21.0	3.55	3.70	2.37

$^{12}_{\Lambda}$B bounded states production ($-6\% < \delta p < 15\%$). For every δp, We generated 30000 events at the target. These events uniformly covered a cone with polar angle 0.1 radius and all had same momentum δp . The total solid angle coverage was 0.0314 sr. Table 5.1 lists the the SOS solid angle acceptance varying with particle momentum from -12% to 21%. We can see that the SOS acceptance is very close to 5 msr over kinematics range of Λ and $^{12}_{\Lambda}$B bounded states production. The systematic error is about 0.5 msr if taking acceptance as 5 msr according to the variation of acceptance at different δp points.

5.1.2 ESPS Virtual Photon Acceptance

One may recall the unpolarized (e,e$'K^+$) cross section Equation 1.12. It can be written in terms of virtual photon (VP) flux factor and the L/T unseparated photon

absorption cross section $\frac{d\sigma_\gamma}{d\Omega_k dp_k}$ as:

$$\frac{d^6\sigma}{d\Omega d\omega d\Omega_k dp_k} = \Gamma(e_1, \omega, \theta)\frac{d\sigma_\gamma}{d\Omega_k dp_k}. \tag{5.1}$$

In the case of discrete final nuclear states, scattering kaon momentum p_K can be calculated from e$'$ momentum, angle and kaon scattering angle. The cross section dependence on kaon momentum p_k vanishes. The double-differential photon absorption cross section $\frac{d\sigma_\gamma}{d\Omega_k dp_k}$ is reduced to $\frac{d\sigma_\gamma}{d\Omega_k}$. Thus the yield from a discrete nuclear state is:

$$N_s = \frac{L}{A}\rho dN_e\epsilon \int_{\Delta\Omega}\int_{\Delta\omega}\Gamma d\omega d\Omega \int_{\Delta\Omega_k}\frac{d\sigma_\gamma}{d\Omega_k}d\Omega_k \tag{5.2}$$

where ϵ is the correction factor. In our case, the kaon solid angle acceptance $\Delta\Omega_k$ is nearly independent of p_k in the kinematic region corresponding to the bound hypernuclear states, the above equation can be written as:

$$\begin{aligned} N_s &= \frac{L}{A}\rho dN_e\epsilon \int_{\Delta\Omega}\int_{\Delta\omega}\Gamma d\omega d\Omega \overline{\frac{d\sigma_\gamma}{d\Omega_k}} \int_{\Delta\Omega_k} d\Omega_k \\ &= \frac{L}{A}\rho dN_e\epsilon n_\gamma \Delta\Omega_k \overline{\frac{d\sigma_\gamma}{d\Omega_k}}, \end{aligned} \tag{5.3}$$

where $\overline{\frac{d\sigma_\gamma}{d\Omega_k}}$ is the average photon absorption cross section over SOS solid angel acceptance. $\Delta\Omega_k$ is SOS solid angle acceptance (5 msr). $n_\gamma = \int_{\Delta\Omega}\int_{\Delta\omega}\Gamma d\omega d\Omega$ is the number of virtual photons accepted by the ESPS per electron on target.

n_γ was also obtained by the Raytrace simulation. The integration over photon momentum ω (or e$'$ momentum $p_e = p_0 - \omega$) was carried out by sum over all e$'$ momentum within ESPS momentum range in a 1 MeV step. For every p_e, the integration of virtual

photon flux factor Γ over a 4π solid range gave the total number of VP per MeV per electron. The actual angular acceptance of ESPS was taken into account by the ratio of events which actually hit the detectors over the total generated events. This ratio was obtained from Raytrace simulation. The e$'$ events were generated at the target according to the virtual photon flux distribution Equation 1.13 covering the largest possible cone with a polar angle of 300 mr (there is basically no virtual photons outside this angle). Then from Raytrace we obtained the number of events which can pass through the ESPS and located at one of the SSD planes. The ratio was used to scale the integrated virtual photon flux to get the number of virtual photons accepted by the ESPS. Figure 5.2 shows this number versus e$'$ momentum. The sum over all VP momentum ω gave n_γ, which is 4.2×10^{-4}/e$'$ for 1.864 GeV, 3.8×10^{-4}/e$'$ for 1.721 GeV. The systematic error is dominant by the uncertainty of ESPS acceptance. It can be estimated from the difference of the areas of Raytrace simulated SSD hit pattern from the real hit pattern (Figure 4.18). It is 3%.

5.1.3 SSD Geometrical Acceptance

Due to the space requirement in the layout of the ESPS hodoscope, there existed some gaps between ESPS hodoscope elements. They can be seen in the SSD hit pattern (Figure 4.10). These gaps were from SSD channels which were not covered by corresponding hodoscope elements so were lost. The virtual photon acceptance calculated at last section needs to be corrected for this factor.

The hits in the gap regions were not completely zero due to the accidental coincidence between the SSD channels in the gap region and other hodoscope elements. A

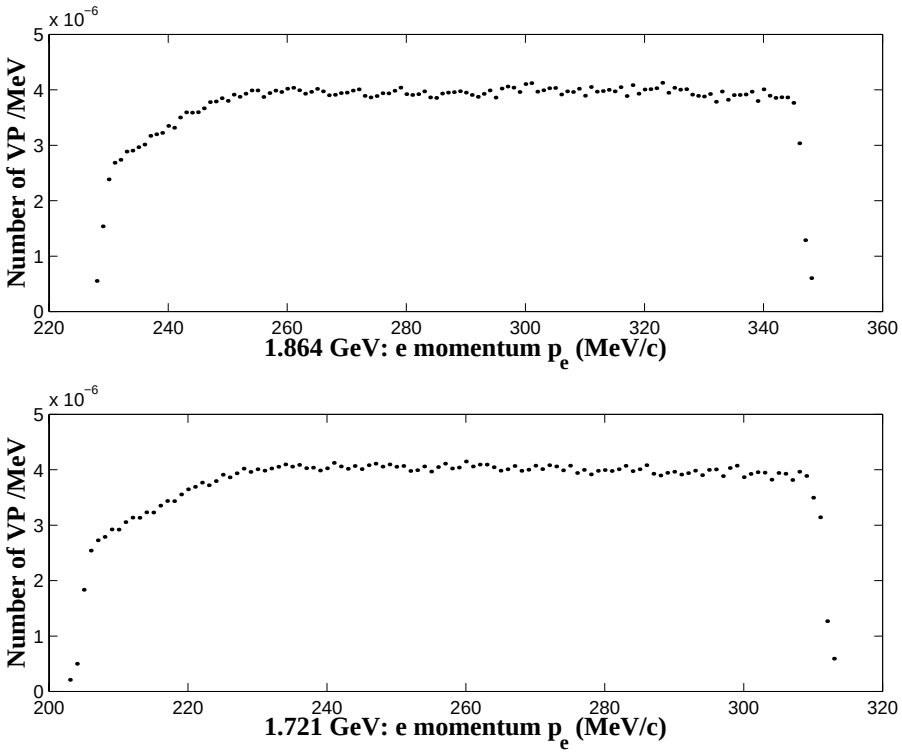

Figure 5.2: Number of virtual photons accepted by ESPS per MeV per electron versus e′ momentum.

normal SSD hit distribution was fitted for every SSD plane by fitting the hit pattern of SSD channels outside the gap region. This normal hit distribution represented the ideal hit pattern if there were no hodoscope gaps. The total number of counts under normal hit pattern was N_T. The channels with a hit number less than a proportion of the normal hit number were treated as inside the gap regions. Considering the about 30% fluctuation of the real hit pattern around normal hit distribution, we chose the ratio to be 70%. Then we had the number of counts N_G under normal hit pattern except these channels inside gaps. Thus the geometrical efficiency can be calculated as:

$$\text{geometrical effeciency} = \frac{N_G}{N_T}. \tag{5.4}$$

SSD channels within gaps were related to the ESPS optics. For the two beam energies, the geometrical efficiencies have a little difference. For 1.864 GeV, the average geometrical efficiency is 0.874 ± 0.003, while it is 0.847 ± 0.003 for 1.721 GeV.

5.2 Detector Efficiencies

5.2.1 ESPS Hodoscope Detection Efficiency

ESPS hodoscope detection efficiency was evaluated by the events which pass through SSD and overlapped two scintillators. Figure 5.3 illustrates the geometrical layout of SSD planes, scintillators and events crossing two overlapped scintillators. The detection efficiency of one of the scintillator can be evaluated by the events which have hits in the corresponding SSD channels and its overlap partner.

Following the same ESPS event selection procedure as described in Section 3.3,

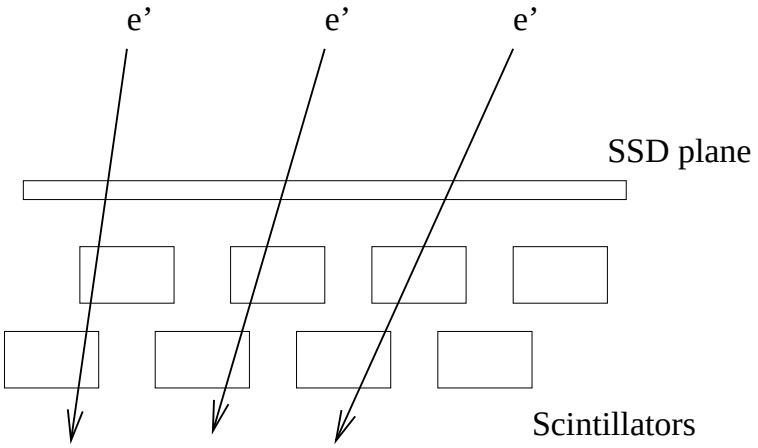

Figure 5.3: Schematic layout of one SSD plane and scintillators behind it. Arrow lines illustrate the events which pass through SSD and overlap region of two scintillators.

only events which satisfied the SSD-hodoscope channel correspondence and time coincidence were kept as real hits. But unlike in the data analysis, hits on two overlapped scintillators with time difference in the 3 ns gate were kept in the data separately. To determine the detection efficiency, we also need to know the number of events T in which one of the scintillators missed a hit. These events were identified by a hit in a SSD channel gate within the scintillator overlap region and one of the scintillator. The hit pattern of SSD channels for two overlapped scintillators have an overlapped area (Figure 5.4). The SSD channel gate was set according to the channels in the overlap area. Events which have hits within this gate and also from one of the scintillators should have passed through another scintillator. The loss of hit from another scintillator was due to the detection efficiency. The number of events S for which both scintillators had coincident hits over event number T for which at least one of the scintillators had a hit, S/T , gave the detection efficiency of that scintillator.

For some hodoscope channels, there were no overlapped pair. For these channels

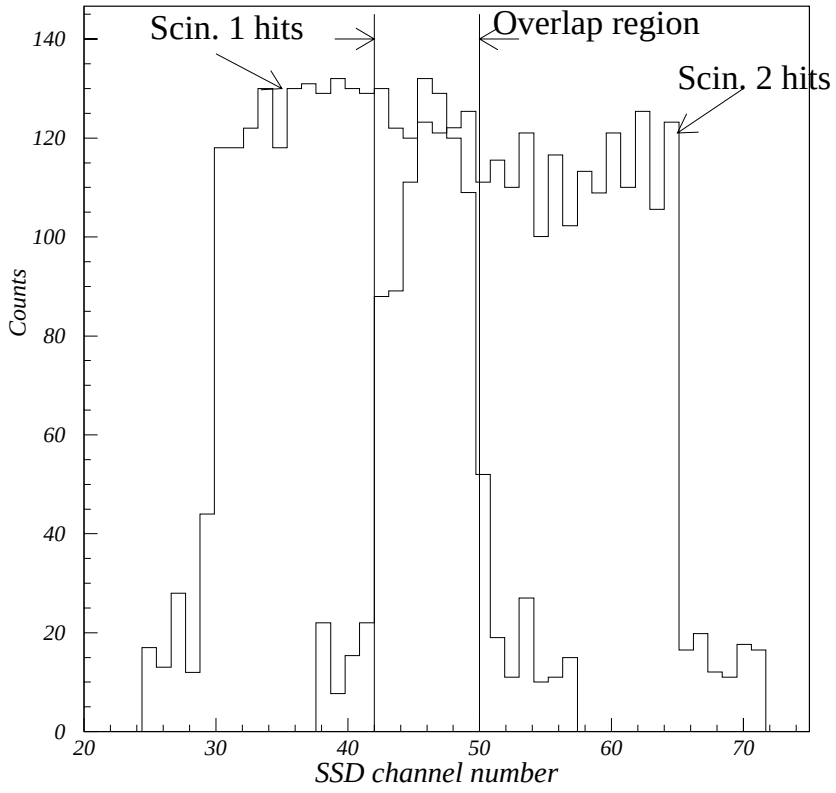

Figure 5.4: SSD channel number corresponding to two overlapped scintillators.

the efficiency can not be directly calculated by the above method. The efficiencies for these channels were estimated based on an observation of the relation between scintillator detection efficiency and pulse height ADC gain. The e′ which passed through the scintillators deposited about the same amount of energy. Thus the relative gain can be represented by the ADC amplitude above pedestal:

$$\text{Relative Gain} = \text{scintillator ADC peak positon} - \text{pedestal}. \tag{5.5}$$

The scintillator ADC pedestal had been very stable during the experiment and was ~ 800. Study of the correlation between gain and detection efficiency for those scintillators whose efficiencies can be calculated by the overlap channel method showed the positive correlation of detection efficiency with gain. When gain was large than 950, efficiencies were consistently around 98%, except for a few channels in the very high rate region. Fortunately, the channels without overlap were in the lower rate region. Therefore, for these scintillators, if their gains are more than 950, they can be assigned to have an efficiency of 98% with a 2% error. For channels with gain < 950, efficiencies were estimated by a scintillator with the same gain but had overlapped partners. Error was assigned as a larger value, 4%.

The efficiencies of the scintillators vary between 70% and 99%, while most of them have an efficiency of 90 to 99%. To determine the average efficiency of the whole ESPS hodoscope system, we used the Raytrace simulated event distribution on the ESPS focal plane and calculated the number of events which passed through every hodoscope elements. The event that passed through a scintillator took the efficiency of the the

scintillator. We took the center of the efficiency distribution for all the events from the simulation as the overall hodoscope detection efficiency. It is 96% $\pm$2% (σ).

5.2.2 SSD Detection Efficiency

SSD detection efficiency was evaluated by the events which passed through SSD and overlapping scintillator in the back. The reason to require two scintillator hits is to suppress accidental hits in the scintillator. The real events which passed through two scintillators were selected by requiring their time difference was within $\pm$5 ns (no SSD hit was required). All the events within this gate were counted as real events N_{scin}. The events which in addition fired SSD were counted as N_{ssd}. They were selected by requiring a hit within the corresponding SSD channel gate and SSD-hodoscope time gate. Figure 3.4 shows the SSD-hodoscope time difference spectrum. The accidental background in the true region, B_{ssd}, were estimated by the counts within $\pm$30 ns time gate under the line which connected the left and right background. The SSD detection efficiency was given as,

$$\epsilon = \frac{N_{ssd} - Bssd}{N_{scin}}. \tag{5.6}$$

SSD detection efficiency had rate dependence. Figure 5.5 shows the SSD efficiency drawn with SSD counting rate per channel. The rate dependence mainly came from the electronic dead time of the SSD front-end system. The double pulse resolution of the TEKZ chip was 100 ns, while a straight line fit of the SSD efficiency-SSD counting rate

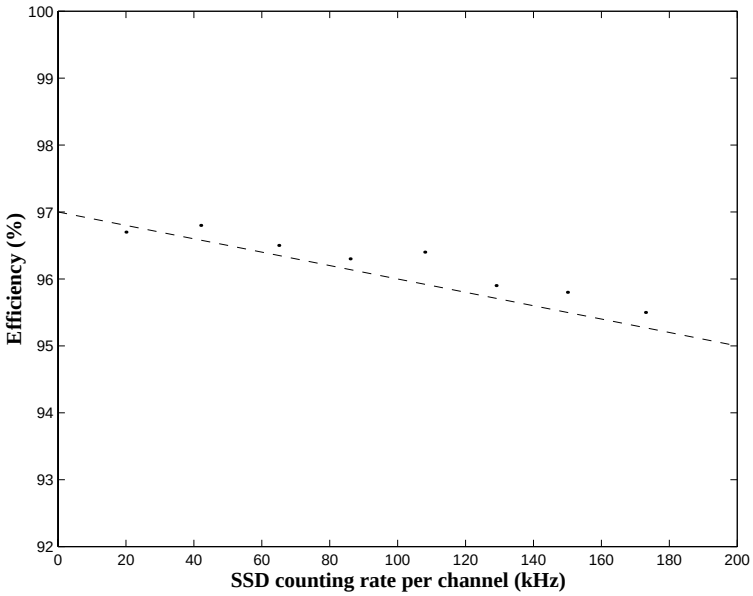

Figure 5.5: SSD efficiencies versus counting rate per channel. The overlaid straight line has the form of Equation eq:ssdrate with dead time $\tau = 100$ ns.

relation with the form of

$$\epsilon = \epsilon_0 - R\tau \tag{5.7}$$

with dead time $\tau = 100$ ns, where R is the channel rate, $\epsilon_0 = 0.97$, is consistent with the data points. Our average SSD channel rate was about 100 kHz. This gives a SSD detection efficiency of 96.0%, with an error of 0.3% .

5.3 Correction Factors

5.3.1 SOS Tracking Efficiency

The SOS tracking inefficiency accounts for events which don't have enough information from drift chambers to reconstruct a track. One source of the inefficiency is drift chamber detection inefficiency. If less than 5 DC planes fired in a drift chamber set of

Table 5.2: Detection efficiencies of SOS drift chamber planes.

SDC Plane No.	Low Rate Run	High Rate Run
1	99.67	99.56
2	99.78	99.67
3	99.59	99.52
4	99.45	99.32
5	99.77	99.69
6	99.66	99.47
7	99.74	99.83
8	99.57	99.66
9	99.29	99.67
10	99.24	99.63
11	99.67	99.74
12	99.24	99.69

6, the left-right ambiguity cannot be resolved and the track is not fit. Another source is too many wires firing due to noise hits. The tracking algorithm will try to fit the noise points and deviated from the real track. In this case, we tend to get tracks with big χ^2 per degree of freedom (p.d.f.) or low χ^2 p.d.f but multiple tracks. Because only one track is kept in the final analysis. Real tracks may be lost.

The procedure to evaluate a drift chamber plane detection efficiency is doing the tracking with all the hits from other planes except the plane for which we are studying efficiency. If the fitted track is single track and has a χ^2 less than 10 with the total fitting residue within 0.5 cm, this event is chosen as good track. This track is extrapolated to the wire plane we are studying efficiency to see if there is a wire on its track being fired. The ratio of tracks with wire firing on that plane to the total good events is the detection efficiency for that wire plane. Table 5.2 lists the detection efficiencies at low current run (32793) and high current run (34151). This calculation was done for 10000 good tracks. We can see all the planes have high detection efficiencies ϵ: $99.6\% \pm 2\%$ for high rate

run, $99.5\% \pm 2\%$ for low rate run.

Tracking algorithm needs at least 5 planes fired in one set of 6 DC planes to determine the track. The probability of having at least 6 planes fired is: $\epsilon^6 + C_6^5 \epsilon^5 (1-\epsilon)$. Thus for both low and high current, it is very close to 1.

The loss of DC efficiency due to noise hit was estimate by the χ^2 p.d.f. distribution of good events. Good events were selected by placing a SOS shower counter cut to exclude positrons, because positron events had a high rate and concentrated on a very small region of the focal plane. They formed hot spot on the wire plane thus there may be more multiple tracks than other particles. In addition, we required a good TOF β: $\beta > 0.6$ and $\beta < 1.3$ so that the particles were forward-going rather than cosmic rays which came from the back. Figure 5.6 shows the χ^2 p.d.f. distribution for the low (32793) and high current run (33380). The events with χ^2 p.d.f. less than 10 were treated as events with good tracking. The ratios of events with good tracking to the total events are both 0.978 for low and high beam current runs.

We also checked the possibility of multiple tracks, another source of tracking inefficiency with the above selected good events. Less than 10 multiple track events (~ 6 events) were found in 50000 events for high rate run 33380, no multiple track event was found in 50000 event for low rate run 32793.

Among these three sources of tracking inefficiencies, only the tracks with large χ^2 significantly affected DC detection efficiency. Therefore, we have a tracking efficiency of 0.978 with an error of 0.02.

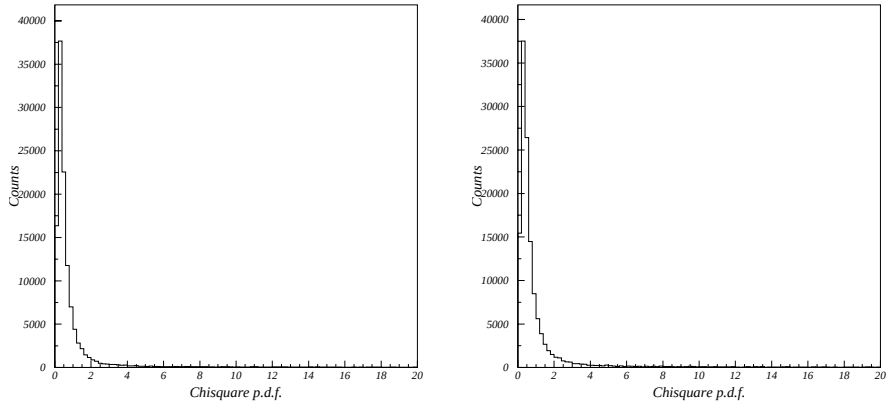

(a) Low rate run (b) High rate run

Figure 5.6: χ^2 p.d.f. distributions of SOS DC tracking.

5.3.2 SOS Trigger Efficiency

The SOS scintillator trigger SCIN (3/4 or 4/4) is required for all SOS trigger conditions. If one event misses hit on one (or two in 3/4 case) of the hodoscope planes, SOS trigger won't be formed and this event is lost. This causes trigger inefficiency. To evaluate SOS trigger efficiency, the hodoscope detection efficiency need to be studied first. The efficiency of each scintillator paddle was determined by the ratio of events which fired the paddle within total events which passed through the center area of the paddle based on tracking information. The outer 1.25 cm overlapping area was excluded to avoid ambiguity. The average of all paddles in a hodoscope plane gave the detection efficiency of the whole plane. For the runs before 32421, the disabled paddles in S1X were also excluded from the efficiency calculation.

Because of multiple scattering of particles in the front hodoscope planes S1X and

S1Y, it is difficult to determine the detection efficiency for the rear hodoscope planes S2X and S2Y. For low rate runs, the hodoscope detection efficiencies based on tracking are: S1X: 0.999, S1Y: 1.000, S2X: 0.938, S2Y: 0.967. For high rate runs, the efficiencies are: S1X: 0.998, S1Y: 0.999, S2X: 0.938, S2Y: 0.966. The detection efficiencies for the rear hodoscope planes appeared low. However, the efficiencies based on tracking are not correct for rear planes because the front hodoscope planes already deflected the particle trajectory [44]. The fraction of triggers for which the plane had a hit with good TDC signal can also be used as a measurement of overall efficiency of the hodoscope plane. From this track independent efficiency, we found the true hodoscope efficiency for the rear plane is comparable to the front planes. We estimated the rear plane has a efficiency of 0.98 with an error of 0.005.

The SCIN 3/4 trigger requires three of the four hodoscope planes fired, the trigger efficiency can be calculated as $\epsilon^4 + C_3^4\epsilon^3(1-\epsilon)$, where ϵ is the detection efficiency of one hodoscope plane. Using the numbers in the above, we got larger than 0.99 trigger efficiency for 3/4 trigger. For SCIN 4/4 trigger, we have a trigger efficiency of 0.96. The systematic error is less than 0.01.

In the 1.864 GeV runs period, we used lucite Čerenkov signal in trigger. Trigger will also be lost if a kaon passed through the lucite but failed to produce a signal due to detector inefficiency. But because in offline analysis we used a PID cut (lucite n.p.e.$>$ 1), tighter than the on-line trigger threshold, the loss of trigger efficiency was already included in the cut efficiency discussed previously.

5.3.3 Electronic and Computer Dead Time

Every time a logic gate in the trigger is activated, it remain open for a fixed time period. If another signal comes during this time, it is ignored. Events loss due to this reason is called electronic dead time. The number of events which is lost because of electronic dead time depend on event rate R and the width of the gate τ. There were more events lost by the electronic dead time at higher event rate and wider gate. For small dead time, the fraction of events which pass through the electronic gates to the total events is related to R and τ as:

$$\frac{N_{measured}}{N_{total}} = e^{-R\tau}. \tag{5.8}$$

In SOS trigger circuit, all gates were set to a width of 30 ns except the PID signals. The PID signals ELHI, ELLO, SHLO and SCER were 40 ns wide for PID efficiency. In the present experiment, the high positron rate produced high rate signals at the SCIN gate. Thus the most significant loss due to electronic dead time came from SCIN gate. At the high current (0.6 μA) 3/4 trigger mode, the signal rate incurred on the gate had the highest rate of $\sim$ 147 kHz. According to the equation above, it had a 0.44% dead time. It is very small compared with other correction factors. Therefore, SOS electronic dead time was not corrected in the cross section analysis.

In the SOS trigger circuit, there are 4 copies of the SOS pretrigger signal PRETRG with 4 different gate width 30, 30, 90 and 120 ns. These signals were used to check the SOS electronic dead time. But for our experiment, the SOS pretrigger was a sparsified signal from SCIN ANDed with PID signals, they cannot be used for electronic dead time

evaluation.

A more significant source of electronic dead time is from the electron arm. Single-hit TDCs were used for the ESPS hodoscope elements. Due to the high accidental electron rate, after the trigger signal from SOS started the TDC gate, an accidental electron hit may arrive in the TDC before the real coincidence electron hit. The TDC was already stopped when the real hit arrived. Consequently, the real hit was ignored. This dead time is called "coincidence blocking". The effect of coincidence blocking depended on the ESPS electron rate . At the ESPS arm, the real coincidence electron hit arrived about $\tau = 30$ ns after the SOS trigger signal had arrived. When scintillator rate was $R = 1$ MHz, coincidence blocking due to accidental hits was $R\tau = 0.03$. When the rate was at maximum 4 MHz, coincidence blocking increased to 0.12. The weighted average value of the efficiency due to coincidence blocking is 0.916 ± 0.02.

Due to the relative long processing time of events by the DAQ system, computer dead time was another source of dead time. Event will be lost when a hardware trigger is formed after the 8LM but the computer is busy processing the previous event so that the current trigger is vetoed by the BUSY signal from trigger supervisor (TS). The typical time required by DAQ computer to process an events is 300–400 μs in non-buffered mode. In buffered mode, computer can accept new triggers while the fastbus conversion is in progress, It only takes ~ 100 ns to process one events. Computer live time is measured by the ratio of events taken by the DAQ computer (SOS trigger) to the total triggers formed at 8LM (SOS pretrigger):

$$\text{Computer Live Time} = \frac{\text{SOS Trigger}}{\text{SOS Pretrigger}}. \tag{5.9}$$

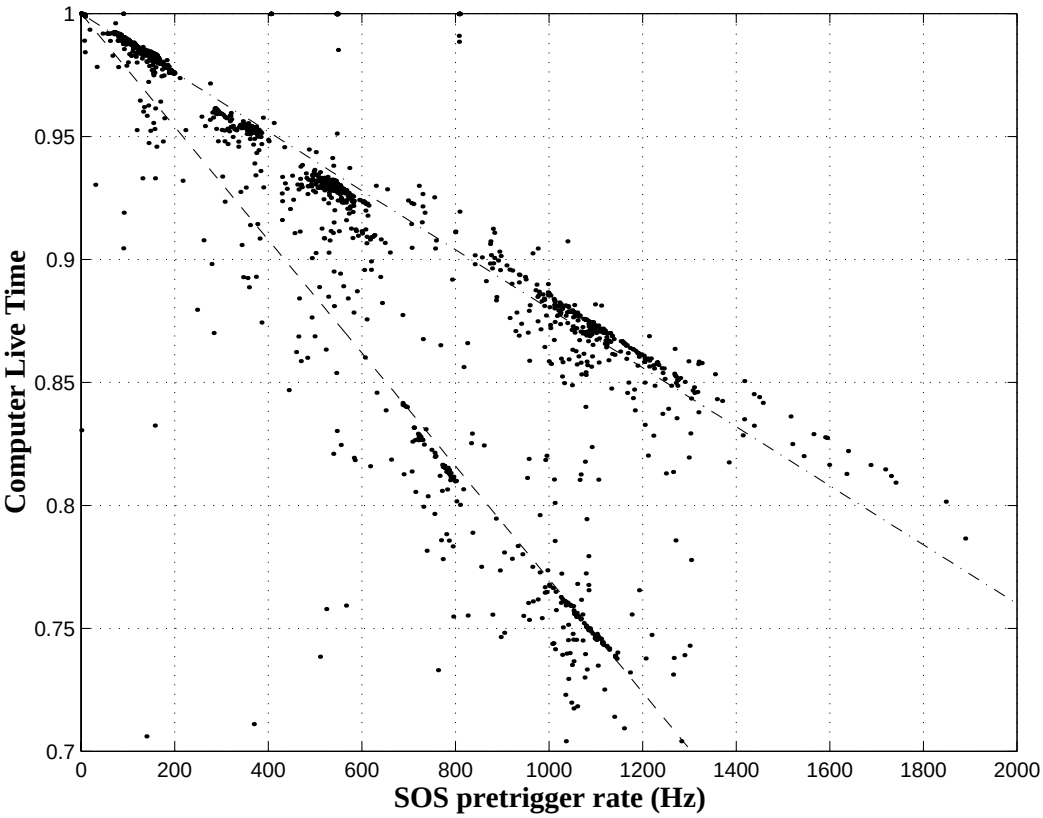

Figure 5.7: Computer live time versus SOS pretrigger rate. The overlaid two lines have the form of Equation 5.10, one with dead time $\tau = 230\mu$s, the other one with $\tau = 120\mu$s.

Like electronic live time, computer live time is related to the event processing time τ as:

$$\text{computer live time} = e^{-R\tau} \sim 1 - R\tau \tag{5.10}$$

for small dead time, where R is the pretrigger rate.

Figure 5.7 shows the computer live time vs. SOS pretrigger rate. The data points fall into two lines with different slopes: one has a slope of ~ 230 μs, corresponding to the time required by the computer to precess one event in unbuffered mode. In buffered mode, the time to process one event is ~ 120 μs. During 1.864 GeV run period, for 3/4 trigger, the computer live time is ~ 0.77 depend on trigger rate, while for 4/4 trigger,

computer live time is ~ 0.98. The computer live time for the 1.864 GeV beam energy CH_2 runs is 0.98 to 0.99. For 1.721 GeV runs low current carbon runs, the computer live time is ~ 0.98. For 1.721 GeV high current carbon runs, the computer live time is ~ 0.93.

5.3.4 Kaon Decay Correction

kaon is an unstable particle. It has an center of mass life time $\tau_k \sim 12.4$ ns ($c\tau_k \sim 371.3$ cm). Some kaons may decay in its flying path in the spectrometer and can not be detected. This factor must be corrected for the cross section.

The survival probability after kaon travels a distance of x is:

$$P(x) = e^{-\frac{m_k x}{p_k c\tau_k}}, \tag{5.11}$$

where m_k is the kaon mass and p_k is the kaon momentum. For the SOS spectrometer, when using 4/4 trigger, the x was the distance from target to the last hodoscope plane, because kaon decayed before the fourth hodoscope plane couldn't make the SCIN 4/4 trigger thus was lost. For 3/4 trigger case, kaons reached the aerogel detector after the front three hodoscope planes was not lost. The central path length from target to SOS focal plane was 752.3 cm. The additional travel distance from focal plane to the last hodoscope plane was 289.4 cm. Thus total central path length was 10.417 meters. We estimated a 0.327 survival probability for $p_k = 1.2398$ GeV runs and 0.290 for $p_k = 1.1195$ GeV runs. For 3/4 trigger the traveling distance was 10.12 meter, the survival probability were 0.338 and 0.301 for the two SOS momentum settings, respectively. Because the

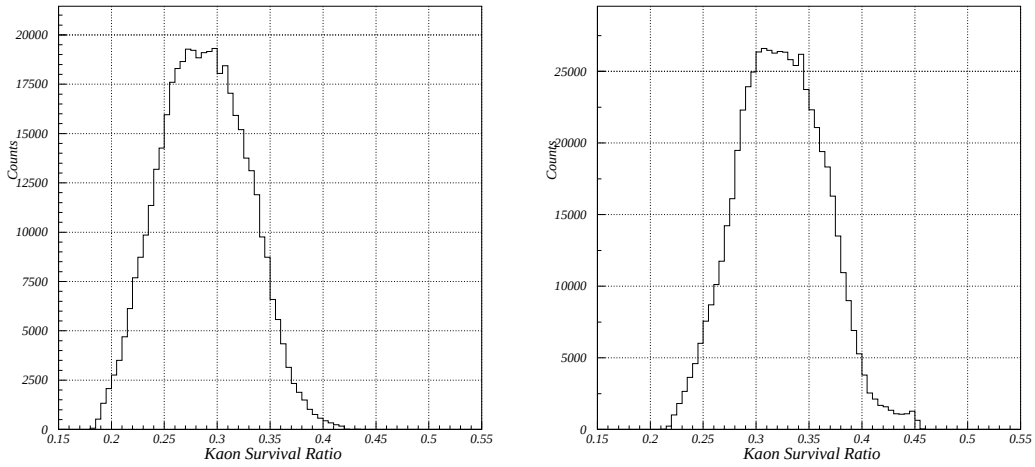

(a) 1.721 GeV runs

(b) 1.864 GeV runs

Figure 5.8: Distributions of kaon survival ratio for the two beam energies.

difference of survival probability between 4/4 and 3/4 triggers was only $\sim 1\%$. We can ignore the difference and consider it as a systematic error.

In reality, particles were not all traveling along the central path, thus Equation 3.10 was used to calculate the path length difference of different trajectories according to focal plane coordinates. Sum of the central path length and the actual traveling distance from focal plane to the S2X gave the total actual traveling distance for different particle trajectories. Figure 5.8 shows the survival probability distributions from two typical runs with the two SOS momentum settings. To avoid a event by event correction, we can use the weighted average as an overall correction factor. They are 0.32 for 1.864 GeV runs, 0.29 for 1.721 GeV runs.

In some cases, the decay products of kaon can still be identified as kaon if they do

not have enough momentum to trigger the aerogel Čerenkov counter and pass the TOF β cut, for example, $K^+ \rightarrow \mu^+ + \nu_\mu$ and $K^+ \rightarrow \pi^+ + \pi^0$, etc. These mimicked kaon events caused double counting because these events were supposed to be lost and already corrected by the decay factor. Simulation was done to estimate the number of these mimicked kaon events [55]. It was found that if kaon decays inside the SOS spectrometer, the decay products will not be identified as kaon because the decay products were light particles. If they have enough momentum to pass through the spectrometer they can not pass the PID cuts with such high momentum. Only $\sim 20\%$ kaon can decay in the detector hut. Within these events, the simulation shows only $\sim 6\%$ of them can be misidentified as kaon. Thus this "mimicked" kaons account to an $\sim 1.2\%$ decrease to the decay correction. We will consider it as a systematic error. The estimated total systematic error for the kaon decay correction is 3%.

5.3.5 Kaon Absorption Correction

When Kaons produced at the target pass through spectrometer windows and detector materials, they can interact with these materials by elastic or inelastic scattering and were lost. This has been studied in the previous Hall C kaon experiment E93018 which used the same SOS spectrometer [45]. The HNSS experiment had the advantage of less window material on the kaon path because the vacuum connection was used from the target to SOS exit. There were no target absorption, target and vacuum chamber windows, air gap between target chamber and SOS entrance window. The total radiation length of these materials was 6.57. Compared to the total radiation length of all the materials on the kaon path of 134.63 in E93018, the reduction of absorption materials in

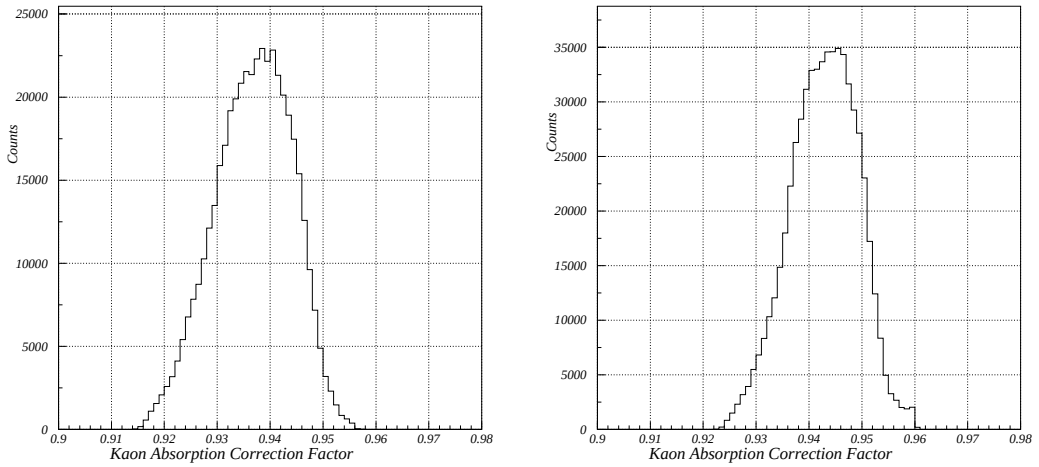

(a) 1.721 GeV runs (b) 1.864 GeV runs

Figure 5.9: Event distributions of kaon absorption corrections for the two beam energies.

HNSS was about 5%. For simplicity, we can use the same analysis as E93018 but treat the difference as a systematic error.

The effect of kaon absorption depends on kaon momentum p_K. Taking all the materials into account, the absorption correction can be expressed as [45]:

$$\text{absorption correction} = 1 - \frac{0.06962}{p_k^{0.99}}, \tag{5.12}$$

where p_K is in unit of GeV. Figure 5.9 shows the event-by-event absorption correction factor distribution. The overall correction factor for kaon absorption was obtained by average over all the events. It is 0.945 for 1.864 GeV runs, 0.940 for 1.721 GeV runs. The systematic error is 5% of 0.94, about 0.05.

Table 5.3 summarizes the correction factors for different run groups.

Table 5.3: Summary of correction factors for different run groups.

Corrections	1.864 GeV 3/4	1.864 GeV 4/4	1.721 GeV low current	1.721 GeV high current	Relative Error
SSD Geom. Accept.	0.874	0.874	0.847	0.847	0.004
ESPS Hodo. Det. Effi.	0.96	0.96	0.96	0.96	0.02
SSD Det. Efficiency	0.96	0.96	0.96	0.96	0.003
SOS Tracking Efficiency	0.98	0.98	0.98	0.98	0.02
SOS Trigger Efficiency	1.	0.96	0.96	0.96	
Coincidence Blocking	0.90	0.92	0.96	0.90	0.02
Computer Dead Time	0.78	0.98	0.98	0.93	0.02
Kaon Decay	0.32	0.32	0.29	0.29	0.03
Kaon Absorption	0.945	0.945	0.940	0.940	0.05

5.4 $^{12}_{\Lambda}$B Ground State Cross Section Extraction

5.4.1 Calculation of $^{12}_{\Lambda}$B Ground State Cross Section

From Equation 5.3, the average photoproduction cross section for $^{12}_{\Lambda}$B ground state in laboratory frame can be expressed as:

$$\overline{\frac{d\sigma_\gamma}{d\Omega_k}} = \frac{A}{L(\rho d)} \frac{N_s}{\epsilon N_e n_\gamma \Delta\Omega_k}. \tag{5.13}$$

The $\frac{A}{L(\rho d)}$ is the effective area of one scattering center. For carbon nuclei in CH_2 target

$$\frac{A}{L(\rho d)} = 2.53 \times 10^{-21}\mathrm{cm}^2 = 2.53 \times 10^3\mathrm{bar}. \tag{5.14}$$

For carbon nuclei in carbon target

$$\frac{A}{L(\rho d)} = 0.91 \times 10^{-21}\mathrm{cm}^2 = 0.91 \times 10^3\mathrm{bar}. \tag{5.15}$$

The N_e is the total electron charge on the target. We accumulated the charge of every run according to the measurement of BCM2. The systematic error for the charge measurement was $\sim 5\%$. The ϵ is the overall correction factor. N_s is the integrated counts in ${}^{12}_{\Lambda}$B ground state.

According to the different running conditions (high or low beam current, 3/4 or 4/4 trigger), CH_2 or carbon target and beam energies, we divided the runs into groups for the hypernuclear ground state cross section calculation. Table 5.4 lists the total charges, correction factors and their errors. The total systematic error is the quadrature of all the errors from correction factors, charges and acceptance. It was calculated as 0.25 of the calculated cross section value.

To estimate ground state counts N_s for the groups of runs, the ^{12}C(e,e$'$K$^+$) missing mass spectrum were plotted for all run groups. The missing mass spectrum of accidental backgrounds was estimated by scaling down the sum of events in 8 accidental coincidence peaks. Then a 5-order polynomial was used to fit the shape of the accidental background. We calculated the number of counts in the ${}^{12}_{\Lambda}$B ground state from the background subtracted spectrum. The counts included left and right one bin and the center bin in our 600 KeV/Bin missing mass spectrum. It was from -1.5 bin (-900 keV) to 1.5 bin (900 keV) of the peak center. According to our missing mass resolution of 920 keV (FWHM), it covered about $\pm 2.3\sigma$. The ground state counts are summarized in Table 5.4.

The cross sections calculated from Equation 5.13 were in Lab frame, while theorists generally express the cross section in CM frame. In order to compare with theory, it is convenient to transform the Lab cross section to CM cross section.

If θ_{CM} is the CM polar angle between scattered kaon and virtual photon, β_{CM}

Table 5.4: Numbers used in the $^{12}_{\Lambda}$B ground state cross section calculation.

Components	1.864 GeV 3/4 Carbon	1.864 GeV 4/4 Carbon	1.864 GeV CH_2	1.721 GeV Low Current	1.721 GeV High Current	Relative Error
SOS Acceptance (msr)	5.0	5.0	5.0	5.0	5.0	0.1
VP Flux ($\times 10^{-4}$)	4.2	4.2	4.2	3.8	3.8	0.03
Charge (mC)	177	62	235	99	212	0.05
Correction Factor	0.077	0.096	0.124	0.124	0.0055	0.24
Yield N_s	37.6	13.3	25.7	26.8	22.3	
CM Cross Section (nb)	149.9	122.5	134.2	132.0	121.9	
Statistical Error(nb)	40.6	59.3	38.6	39.7	34.5	

is the velocity of CM frame in the Lab coordinate system, β^*_K is the velocity of kaon in the CM frame, then the Lab differential cross section is correlated to CM by:

$$\frac{d\sigma_{Lab}}{d\Omega_K} = \frac{(1+\gamma^2+2\gamma\cos\theta_{CM})^{3/2}}{1+\gamma\cos\theta_{CM}}\frac{d\sigma_{CM}}{d\Omega^*_K}, \tag{5.16}$$

where $\gamma = \beta_{CM}/\beta^*_K$. To calculate γ, some kinematics variable have to be calculated at first.

The Lorenz invariants Q^2 and W are:

$$Q^2 = 4e_0e'\sin^2(\frac{\theta_e}{2}) \sim 0, \tag{5.17}$$

$$W = \sqrt{m^2_{carbon} + 2m_{carbon}\omega - Q^2}, \tag{5.18}$$

where ω is the energy of virtual photon: $\omega = e_0 - e'$. The velocity of CM frame β_{CM} can be expressed as:

$$\beta_{CM} = |\mathbf{q}|/(\omega + m_A) \tag{5.19}$$

and

$$\gamma_{CM} = \frac{1}{\sqrt{1 - \beta_{CM}^2}}, \tag{5.20}$$

where $|\mathbf{q}|$ is the amplitude of three momentum transfer, in our case, $|\mathbf{q}| = \omega$.

The kaon momentum in the CM frame $\mathbf{p_K^*}$ can be calculated by:

$$|\mathbf{p_K^*}| = \sqrt{\frac{(W^2 + m_K^2 - m_Y^2)^2}{4W^2} - m_K^2}. \tag{5.21}$$

β_K^* can be calculated from $|\mathbf{p_K^*}|$ as: $\beta_K^* = |\mathbf{p_K^*}|/\sqrt{m_K^2 + |\mathbf{p_K^*}|^2}$. Thus γ can be calculated.

The CM kaon scattering angle θ_{CM} is related to kaon scattering angle in the Laboratory θ_K by:

$$\tan\theta_{CM} = \frac{p_K \sin\theta_k}{\gamma_{CM}(p_K \cos\theta_k - \beta_{CM} E_K)}. \tag{5.22}$$

If we take p_K and θ_k to be the central momentum and angle (2.1°) of SOS, and take the scattered electron momentum p_e to be the central momentum of ESPS, we obtain the conversion factor of Lab to CM cross section on carbon target as is 0.787 for both beam energies.

5.4.2 Statistical Error of Cross Section

The statistical errors come from the statistical variation of the counts in the ground state peak and the uncertainty in the background estimation. By summing together events in 8 accidental peaks, the statistical error of the background estimate was reduced. If S_b ($\sim 1/8$) is the scaling factor of the summed background spectrum, e_b and e'_b are the statistical errors per bin of the background before and after the scaling, n_b is the number of counts per bin before the scaling. Then the relative statistical error before the scaling is:

$$\frac{e_b}{n_b} = \frac{1}{\sqrt{n_b}}. \tag{5.23}$$

The background after the scaling have the same relative error as before the scaling, so there is:

$$e'_b = S_b n_b \frac{1}{\sqrt{n_b}} = S_b \sqrt{n_b} \tag{5.24}$$

which is $\sqrt{S_b}$ times smaller than the error estimated from one accidental peak.

The error per bin for the background subtracted spectrum is the quadrature of the statistical error of the background included spectrum and the background error in the above equation. The quadrature of the errors of all the 5 bins gives total statistical errors. These results are summarized in Table 5.4.

Figure 5.10 plots the cross section values of ${}^{12}_{\Lambda}$B ground state obtained from various run groups. The average cross section for all these run groups is 132 nb/sr $\pm$19

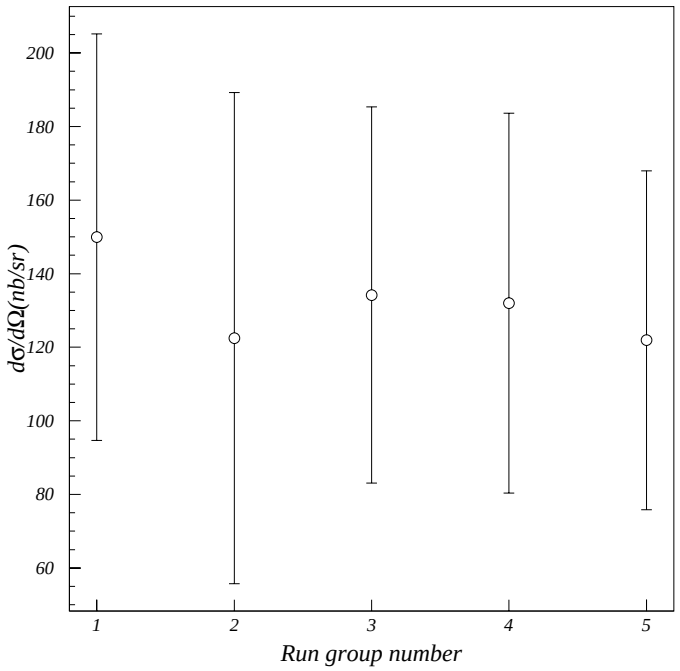

Figure 5.10: CM cross section values of ${}^{12}_{\Lambda}$B ground state obtained from various run groups.

(statistics)±16 (systematics). The cross section is the average cross section over our kaon angular acceptance, from 0° to 4.6°.

5.5 ^{12}C(γ^*,K$^+$) QF Cross Section Calculation

Since this is the first time the electroproduction (photoproduction) cross section of ${}^{12}_{\Lambda}$B ground state is measured experimentally, it is useful to do a QF Λ production cross section calculation to check the consistency of our cross section normalization with the existing experimental measurements [56, 46].

In the case of QF Λ, the dependence of cross section on kaon momentum p_K

cannot be dropped. From Equation 5.1 we have:

$$N_q = \frac{L}{A}\rho dN_e\epsilon \int_{\Delta\Omega}\int_{\Delta\omega} \Gamma d\omega d\Omega \int_{\Delta p_K}\int_{\Delta\Omega_K} \frac{d\sigma_\gamma}{d\Omega_K dp_k} d\Omega_k dp_k, \tag{5.25}$$

where N_q is the QF yield. We can change kaon momentum p_K to ^{12}C(γ^*,K$^+$) missing mass M_x in the integration. Because the SOS acceptance in the kinematic range of QF Λ can not be treated as constant any more, if we use the nominal SOS solid angel acceptance $\Delta\Omega_k = 5$ msr, the QF counts N_q has to be corrected for acceptance. Therefore, the QF Λ photoproduction cross section is

$$\frac{d\sigma}{d\Omega_k} \equiv \int \frac{d\sigma}{d\Omega_k dM_x} dM_x = \frac{A}{L(\rho d)} \frac{N_{qc}}{\epsilon N_e n_\gamma \Delta\Omega_k}, \tag{5.26}$$

where the N_{qc} is the acceptance corrected QF Λ yield within the missing mass range starting from the emission threshold. The acceptance correction was done according to the shape of the missing mass spectrum of the accidental background. Because ^{12}C(γ^*,K$^+$) QF production also contained contribution from Σ^0/Σ^-, we used the ratio from [46] to separate our Λ cross section from the total QF cross section. To compare with previous data, the cross section number was scaled according to a scaling function of Q^2 [57].

5.5.1 ^{12}C(γ^*,K$^+$) QF Yield and Cross Section

To calculate the QF ^{12}C(γ^*,K$^+$) cross section, the 1.721 GeV high current runs 33087–33390 was used because This was the longest carbon run period with the same run condition.

The missing mass spectrum was calculated with ^{12}C(e,e′K$^+$) kinematics. After subtracting the background, we got the uncorrected QF spectrum in missing mass scale. Acceptance correction was carried out by using the fitted missing mass spectrum shape of background. We normalized all our acceptance within the missing mass range to the bound states region where we have known acceptance

If n is the QF count per bin before correction, n_c is the count per bin after correction, b is the count of background per bin, M is the count of background per bin in the bound states region where we've determined our nominal acceptance, then $n_c = nM/b$.

Acceptance correction was done from threshold missing mass 11.37 GeV to 11.60 GeV. Beyond this range, the correction was more than 60% of the nominal acceptance so the correction error became unacceptable. After acceptance correction, a 5-order polynomial was fitted from the correct QF distribution. An integration of the polynomial within missing mass range 11.37 GeV to 11.60 GeV yielded a count of 1774. This is the acceptance corrected QF yield. The area in the tail of the distribution beyond 11.6 GeV which was not included in the integration contributed $\sim 10\%$ of the total yield.

We can use the same correction factors, SOS acceptance and electron listed in Table 5.4 for 1.721 GeV high current runs for QF cross section calculation. But there is an additional correction of 0.82 due to ESPS multiplicity in the data. This multiplicity factor should be taken into account for QF calculation but not for bounded states. Because events from multiplicity were spread out in the missing mass spectrum as background. But when we integrate the QF region, these multiplicity events will still contribute. The total QF cross section is 5.91 μb/sr in Laboratory frame and 4.55 μb/sr in CM frame.

5.5.2 Statistical and Systematic Errors of the Cross Section

If δn and δb are the errors per bin for the uncorrected QF and background, respectively, δn_c is the error for corrected QF, then

$$\delta n_c = M \frac{\delta nb - \delta bn}{b^2}. \tag{5.27}$$

δn can be calculated as the quadrature of the errors of the total spectrum and that of the background δb.

The sum of square of the errors of every bin from missing mass M_x=11.37 GeV to 11.60 GeV gives total statistical error 75 counts, which is about 4.2% of the total yield.

The systematic error of the yield is from the tail of QF distribution outside the missing mass range, from missing mass 11.37 GeV to 11.60 GeV. As mentioned before, this area is about 10% of the total yield. Combine the errors from correction factor, SOS acceptance and charge, The total systematic error is 17% of the total yield.

5.5.3 Comparison with Previous Experiment Result

In JLab E93018 and E91016, the ^{12}C(e,e'K$^+$) QF cross section at $Q^2 = 0.39\ GeV^2$, Lab γ-K angle $\theta_{\gamma K} = 0$ was measured as described in [58]. Monte Carlo simulation (SIMC) was used to extract the QF cross section of Λ and Σ^0/Σ^-. The simulation used two body Fermi gas model and published nuclear response function to model the nucleus. The Λ portion was separated from the total QF cross section as 1.72 ± 0.13 μb/sr (CM). The ratio of Λ to the total QF cross section is 0.504±0.04. Compare the QF cross section with H(e,e'K$^+$)Λ cross section of 0.41 ± 0.02 μb/sr from E91016, the

effective proton number of 4.2±0.41 was obtained. This was in agreement with published result of [56] on ^{12}C(γ,K$^+$) reaction using real γ which gave an effective proton number of 4.2 ± 0.6.

We used the same Λ to the total QF ratio as [46] to seperate our Λ cross section, assuming that the Λ to Σ^0/Σ^- cross section ratio in the QF production remain unchanged from $Q^2 = 0.38\ GeV^2$ (E91016) to $Q^2 \sim 0$ (E89009). The Λ QF cross section is then 2.28 ± 0.31 μb/sr.

The cross section value in [58] is at $Q^2 = 0.39$ (GeV/c)^2, $W = 12.62$ GeV, while in E89009, $Q^2 = 0$, $W = 12.54$ GeV. To compare the cross section, we used a scaling $f(Q^2) = 1/(Q^2 + 2.67)^2$ for p(γ^*,K)Λ reaction from [57]. After scaling the cross section to $Q^2 = 0$, the estimated cross section for carbon QF Λ cross section from E91016 is 2.26 ± 0.17 μb/sr. This is in good agreement with our result of 2.28 μb/sr.

On the other hand, if we scale the elementary p($\gamma*$,K)Λ cross section from E91016, 0.41 μb/sr, to $Q^2 = 0$, we get 0.54 ± 0.026 μb/sr for the elementary process. Comparing this with the QF cross section of E89009, we have an effective proton number of 4.2±0.61. In [56], the cross section was measured up to photon energy 1.1 GeV which was lower than ours. But the cross section seems flat at higher photon energy. Their cross section is an average of photon-kaon angle from 10 to 40 degrees. Thus the cross section is smaller than ours as our cross section at average angle of 2.1°.

CHAPTER 6

RESULTS AND DISCUSSIONS

JLab experiment E89009 obtained the ${}^{12}_{\Lambda}$B excitation energy spectrum from a ^{12}C target with virtual photon energy $\omega \sim 1.5$ GeV and kaon scattering angles θ_K from 0° to 4.6°. The experimental spectrum is shown in Figure 4.30 in binding energy scale. The accidental background of the spectrum can be estimated with good statistics by the out-of-time events, and the spectrum after background subtraction is shown in Figure 6.1. The error bars represent statistical unceratinties including the contribution from background subtraction.

Two prominent peaks, one at $B_\Lambda \approx 11.6$ MeV and the other near the Λ emission threshold, are clearly evident in the spectrum. They correspond to the s_Λ ground state and p_Λ substitution states, respectively. The ground state peak is actually composed of two states 1^- and 2^-. They are the spin-doublet (non-spin-flip and spin-flip) of s_Λ coupled to ground state $(p_{3/2})_p^{-1}$ ^{11}B core. Due to the weak ΛN spin-spin interaction, their separation predicted by all theories is around 150 keV, too close to be resolved by our experimental resolution. Due to the large spin-flip amplitude in the electroproduction, it is believed that the 2^- state dominates in this peak. The p_Λ peak represents a complicated composition of high spin stretched states (2^+s and 3^+), with Λ remaining in the p-shell and coupled to $(p_{3/2})_p^{-1}$ ^{11}B core. The 3^+ state has the largest strength in the electroproduction. These states are near each other and the predictions of their

positions vary among different models, depending on descriptions of the spin-dependent effective ΛN interaction. The 2^- in the ground state and 3^+ p-shell substitution state can only be produced by eletroproduction or photoproduction.

Strength is observed between the ground state doublet and the composite p-shell peak (see figures 4.30 and 6.1). We note that this has been seen also in the ${}^{12}_{\Lambda}$C spectrum obtained from (π^+,K$^+$) reactions at KEK E369 (Figure 1.3). They are believed to be formed by a series of ^{11}B core excited states coupled with a Λ at s-shell. However, the (e,e′K$^+$) reaction populates different core excitation states. Such low-lying core excitation states are highly interesting, as the Λ can be used as a probe to study nuclear interior structure. Unfortunately, our data does not have sufficient statistics to explore this. The states are embedded in the statistical fluctuations of the data thus it is hard to claim any individual structure. Nonetheless, we believe that the visible strength observed in the spectrum is from these core excitations.

Above threshold, there seem to be wide peaked structures over the continuous quasi-free distribution. These are believed to be the unbound states of ${}^{12}_{\Lambda}$B. They are close together. These states decay predominantly via nucleon emission to form hyperfragments which then decay weakly through the $\Lambda \rightarrow \pi + N$ or $\Lambda + N \rightarrow N + N$ channels, therefore, are unstable.

Existing theories which calculate the ${}^{12}_{\Lambda}$B level structure and excitation strengths are due to Motoba [24] and Millener [13]. Motoba's calculation is a complete one, which includes elementary strangeness production process as p(γ, K$^+$)Λ, the proton pick-up process from ^{12}C nucleus, and the Λ-core coupling process. Thus, this calculation is able to predict both the level structures and their strengths. Both non-spin-flip and spin-flip

amplitudes were treated carefully. However, for simplicity, a ^{11}C wave function that was fitted for the calculation of $^{12}_{\Lambda}$C spectrum from the ^{12}C(π^+,K$^+$)$^{12}_{\Lambda}$C reaction in place of the ^{11}B core was used. This naturally ignored Coulomb effects and charge symmetry breaking between the two core nuclei. Thus, Motoba's level positions are considered to be incorrect. However, due to the close symmetry between $^{12}_{\Lambda}$C and $^{12}_{\Lambda}$B, the calculated strengths for the corresponding levels are considered to be valid.

Millener's calculation is focused on properly treating the ^{11}B core nuclear structure and the spin-dependent ΛN interaction by fitting to the level transitions observed from γ spectroscopy data, in particular that of the p-shell transition from the recent experiment results from the $^{13}_{\Lambda}$C system [59]. Thus, his level predictions are generally believed more reliable in terms of spacing. However, his calculation did not included the elementary process of $p(\gamma, K^+)\Lambda$, and thus cannot predict excitation strengths of the level structure. In order to compare the E89009 spectrum to this calculation, Motoba's strength predictions were applied to the corresponding levels in Millener's prediction.

The positions, relative strengths, and spin-parity (J^π) assignments of the states calculated by Motoba, et al. are shown in Figure 6.1(a) [24]. Since the ground state peak of E89009 spectrum is composed of two inseparable 1^- and 2^- states and we are interested in the level spacings between different states, the predicted position of the 2^- ground state was put at the center of ground state peak in the experimental spectrum. The heights of the lines denote the relative strengths of the states. The states above $B_\Lambda = 0$ emission threshold are unbounded states. The dashed curve is the predicted spectral shape by spreading the bound states with our missing mass resolution of 920 keV (FWHM). The unbound states are particle-unstable, and were smeared by a large

width of 2.5 MeV (FWHM) to simulate their large escape widths. The whole excitation function was scaled by a common factor to fit the height of the experimental spectrum. One can see that the predicted and the experimental spectra have quite similar overall features, even in the quasi-free region, where the "bumps" can possibly be explained by unbound hypernuclear states. However, the energy separation of the predicted s-shell and p-shell Λ states is apparently not correct, because Motoba's calculation took ^{11}C as the nuclear core.

As discussed above, to compare the spectrum with Millener's calculation, we used the energy levels from Millener's calculation but assigned them excitation strengths according to Motoba's calculation for the same states. This predicted spectrum is shown in Figure 6.1(b) (dashed curve). One can see that the overall spectrum is more consistent with the data. The position of p_Λ peak is closer represented best by Millerner's prediction. Note that the two calculations predict the relative positions of 3^+ and 2_2^+ differently. This difference is the result of different models of the Λ one body potential used in their calculations. Due to experimental energy resolution, we can't resolve the 2^+s and 3^+ states. But the strength of this peak is anticipated to come from these two strongly excited states. The wider-than-predicted p-shell Λ peak in the experimental spectrum seems to suggest a more complex structure near threshold. Configuration mixing is expected to be significant for the p-shell hypernuclear states. Calculations using configuration mixing will result in a splitting of the total strength among many states. However, a large fraction of the strength still resides in the 3^+ state. Obviously, further studies with better resolution and yield will be very important.

From the E89009 spectrum, the binding energies of the peaks representing the

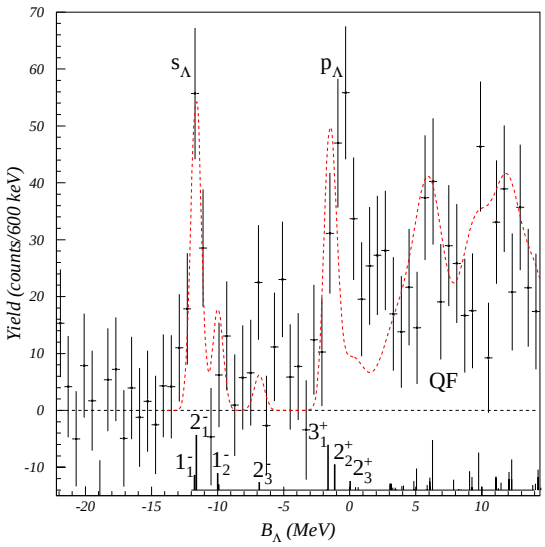

(a) Comparison with Motoba's calculation

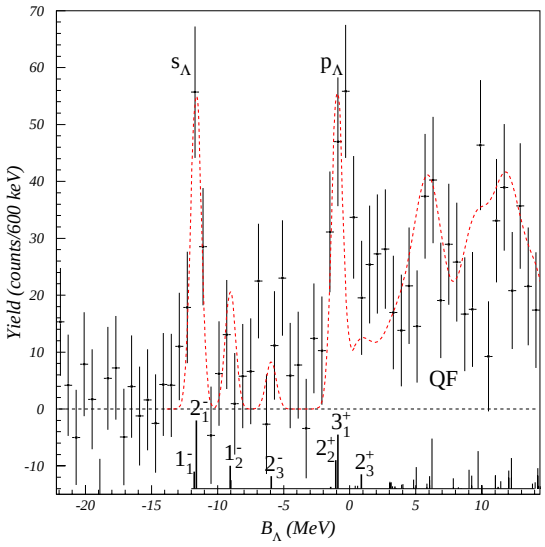

(b) Comparison with Millener's calculation

Figure 6.1: Background subtracted $^{12}_{\Lambda}$B binding energy spectrum and comparisons with theoretical predictions. The horizontal scale is Λ binding energy. The zero is the particle emission threshold. "QF" in the figures denote the quasi-free region above $B_\Lambda = 0$. Error bars are statistical only. The dashed curves are theoretically predicted spectral shapes from the two calculations indicated.

Table 6.1: Binding energies of s_Λ and p_Λ states of ${}^{12}_{\Lambda}$B obtained from the HNSS spectrum and comparison with Millerner's calculation [60]. The quoted uncertainties are statistical only. The systematic uncertainty is 180 keV (Section 4.9).

State (J^π)	E_x (MeV) Theoretical	E_x (MeV) Experimental	B_Λ (MeV) Experimental
1^-_1	0.00		
2^-_1	0.165	0.00 ($2^-/1^-$)	-11.6 ± 0.11
3^+	10.87	11.11±0.19 ($3^+/2^+$s)	−0.49±0.16

ground state doublet and the compound substitution states of ${}^{12}_{\Lambda}$B can be extracted. This is because we calibrated the absolute scale of hypernuclear mass by the known masses of the Λ and Σ. This is in contrast to the (K^-, π^-) or (π^+,K^+) reactions, in which only the Λ peak could be seen due to the limited acceptance of the spectrometers. The ground state peak in the E89009 spectrum was fit by a Gaussian function. For the substitution state, since the 2^+_2 state is very close to the most strongly excited 3^+ state (their energy separation is only $\sim$ 170 keV by Millener's calculation), and the 2^+_3 state is $\sim$ 800 keV above and has only about one third of the strength of the 3^+ state, we also fitted the p-state peak with one single Gaussian. The center of the Gaussian function was extracted. Table 6.1 lists the binding energies of these two peaks from the E89009 spectrum. Their excitation energies are listed to be compared with Millener's calculation.

The E89009 spectrum can also be compared with its mirror ${}^{12}_{\Lambda}$C spectrum obtained by the (π^+,K^+) reaction from KEK E369 (Figure 1.3). The E369 spectrum has better statistics but poorer resolution (1.45 MeV). The meson-induced spectrum excites only natural parity states. Thus, although the overall shape of the spectrum is similar to the

E89009 spectrum, the spin assignments are different. Comparison of the energy levels of the same spin-parity states will give valuable information about the Charge Symmetry Breaking effect.

CHAPTER 7

SUMMARY AND CONCLUSION

Experiment E89009 at Jlab is the first hypernuclear spectroscopy experiment to use the (e,e′K) reaction. A ${}^{12}_{\Lambda}$B spectrum was observed from carbon target. The missing mass resolution of the spectrum, 920 ± 120 keV, is consistent with expectation based on spectrometer and beam performance , and is the best ever achieved for direct measurements of hypernuclear spectra. The previous best resolution was ∼1.45 MeV for a ${}^{12}_{\Lambda}$C hypernucleus in the (π^+,K^+) reaction from KEK E369 experiment. This demonstrates that electroproduction can be used effectively for high precision hypernuclear spectroscopic studies [61].

Comparisons of the ${}^{12}_{\Lambda}$B spectrum with theoretical predictions have shown the overall structure to be consistent with expectation. The relative excitation strengths of the hypernuclear states are consistent with Motoba's calculation, while the energy separation of the p-shell and s-shell Λ states is better represented by Millener's calculation. The unnatural parity states were expected to be strongly excited from electroproduction.and this is experimental spectrum from the (e,e′K^+) reaction is needed by theorists.

In the present experiment, the absolute hypernuclear mass scale was calibrated by the known masses of the Λ and Σ rather than only the excitation energy relative to the ground state. Thus the binding energies of ${}^{12}_{\Lambda}$B ground state peak and the p-shell Λ state peak were found to be 11.6 MeV and 0.49 MeV, respectively.

The photoproduction cross section of the $^{12}_{\Lambda}$B ground state was also extracted and found to be 132 nb/sr $\pm$19 (statistic) $\pm$16 (systematic) at $\theta_K \sim 2^\circ$. The large statistical uncertainty is due to limited statistics. The value is consistent with the theoretically predicted 112 nb/sr cross section for the 2^- state at $\theta_K = 0^\circ$.

The HNSS was used in the experiment to detect scattered particles. The spectrometer detected near zero degree scattered electrons. This method increased the virtual photon flux accepted by the electron spectrometer. However, it also allowed in extremely high rate of bremsstrahlung electrons causing a high accidental background rate. Valuable information was obtained from the present experiment for designing future experiments to tag small angle electrons.

In conclusion, the excitation strength and spectral shape of the $^{12}_{\Lambda}$B hypernuclear spectrum obtained from the present experiment are in general consistent with theories. Although the experiment had to face severe background problem caused by detecting near zero degree scattered electrons, the source of the background rates on different targets have been well understood. Experience learned about how to handle this high background rate in detector hardware and in data analysis. Sub-MeV resolution was obtained by using the high quality primary electron beam. The way to improve the current missing mass resolution by increase kaon arm spectrometer momentum resolution has been identified. Therefore, the present experiment demonstrates hypernuclear electroproduction as a remarkable tool to investigate hypernuclei in a deeper and broader range and with better resolution than hadronic reaction mechanism.

As a new phase of hypernuclear spectroscopy experiments using (e,e$'$K$^+$) reaction, JLab E01011 has already been approved and is prepared to run in JLab Hall C

[33]. Tremendously valuable information on electroproduction was gained from E89009. The new proposed experiment has a much improved experimental setup. The electron spectrometer will detect about 2.5 degree scattered electrons. This will reduce the rate of forward electrons from bremsstrahlung by almost four orders of magnitude, while the virtual photon flux will be reduced by only a factor of 30. A new high resolution kaon spectrometer (HKS) will be built to replace the SOS used in the present experiment. As a result, the hypernuclear yield from the experiment is expected to increase by a factor of about 50 and the energy resolution may reach 350 keV (FWHM). This will allow us to resolve detailed hypernuclear energy structures and extend the spectroscopy study to well beyond the p-shell.

BIBLIOGRAPHY

[1] H. C. Bhang et al., *Nucl. Phys.*, A639:269c, 1998.

[2] M. Danysz and J. Pniewski, *Philos. Mag.*, 44:348, 1953.

[3] B. F. Gibson and E. V. Hungerford, *Physics Reports*, 257:349, 1995.

[4] H. Takahashi, Observation of Lambpha and Λ–Λ interaction. In *Bulletin of The American Physical Society, First Joint Meeting of The Nuclear Physics Divisions of APS and JPS*, volume 46, page 56, Hawaii, October 2001. American Institute of Physics.

[5] H. Outa et al., *Prog. Theor. Phys. Suppl.*, 117:177, 1994.

[6] T. Nagae et al., *Phys. Rev. Lett.*, 80:1605, 1998.

[7] C. B. Dover, In B. F. Gibson and W. R. Gibbs, editors, *LAMPF Workshop on (π,K) Physics*, page 3, Los Alamos, NM, 1990. AIP.

[8] C. Bennhold et al., Hypernuclear physics with photons. In L. Tang and O. Hashimoto, editors, *Proc. of Jlab sponsored Workshop on Hypernuclear Physics with Electromagnetic Probes*, page 1, Hampton, VA, December 1999. Hampton University.

[9] R. H. Dalitz and A. Gal, *Ann. Phys*, 116:167, 1978.

[10] D. J. Millener, A. Gal, and C. B. Dover, *Phys. Rev.*, C31:499, 1985.

[11] T. Motoba et al., In *Physics with GeV Electrons and Gamma-Rays, Sendai, Japan, 2001*, page 107. Universal Academy press, Inc., 2001.

[12] Y. Yamamoto et al., *Prog. Theor. Phys. Suppl.*, 117:361, 1994.

[13] D. J. Millener, In L. Tang and O. Hashimoto, editors, *Proc. of Jlab sponsored Workshop on Hypernuclear Physics with Electromagnetic Probes*, page 79, Hampton, VA, December 1999. Hampton University.

[14] M. M. Nagels et al., *Phys. Rev.D*, 12:744, 1975.

[15] R. E. Chrien and C. B. Dover, *Annu. Rev. Nucl. Part. Sci.*, 39:113, 1989.

[16] D. J. Millener, C. B. Dover, and A. Gal, *Phys. Rev.C*, 38:2700, 1988.

[17] H. Hochi, *Phys. Rev.C*, 64:4302, 2001.

[18] T. Motoba, *Nucl. Phys.*, A639:135c, 1998.

[19] T. Yamada et al., *Phys. Rev.C*, 38:854, 1988.

[20] S. Ajimura et al., *Nucl. Phys.*, A639:93c, 1998.

[21] E. Hiyama, *Phys. Rev.C*, 59:2351, 1999.

[22] H. Tamura et al., *Phys. Rev. Lett.*, 84:5963, 2000.

[23] K. Tanida et al., *Phys. Rev. Lett.*, 86:1982, 2001.

[24] T. Motoba et al., *Prog. Theor. Phys. Suppl.*, 117:123, 1994.

[25] C. B. Dover and D. J. Millener, In B. Frois and I. Sick, editors, *Modern Topics in Electron Scattering*, page 609, Singapore, 1991. World Scientific.

[26] D. J. Millener et al., *Phys. Rev. Lett.*, 54:1237, 1985.

[27] P. H. Pile et al., *Phys. Rev. Lett.*, 66:2585, 1991.

[28] T. Hasegawa et al., *Phys. Rev. Lett.*, 74:224, 1995.

[29] T. Hasegawa et al., *Phys. Rev.C*, 53:1210, 1996.

[30] E. V. Hungerford, *Prog. Theor. Phys. Suppl.*, 117:135, 1994.

[31] S. S. Hsiao and S. R. Cotanch, *Phys. Rev.C*, 28:1668, 1983.

[32] C. E. Hyde-Wright, W. Bertozzi, and J. M. Finn, In *Proc. 1985 CEBAF Summer Workshop*, page 1, Newport News, VA, 1985.

[33] O. Hashimoto, L. Tang, J. Reinhold, and S. Nakamura, A high-resolution high-efficiency spectrometer system for Λ hypernuclear spectroscopy at JLab. Proposal for Jlab E01011, 2000.

[34] P. Ġueye, E89009 colloboration meeting, February 1998.

[35] C. Yan et al., *Nucl. Instr. and Meth.*, A365:261, 1995.

[36] P. Ġueye, *Status of the Actual Beam Position Mointors in the Hall C Beamline.* Jlab Hall C Internal Report (unpublished).

[37] P. Ġueye, M. Tiefenback, and C. Yan, *Hall C Beam Energy measurement.* Jlab Hall C Internal Report (unpublished).

[38] C. Armstrong, *Beam Current Measurement in Hall C.* Jlab Hall C Internal Report (unpublished), 1996.

[39] C. Yan, *Calculation for Setting Parameters of Hall C Target Raster.* Hall C internal report (unpublished), 1996.

[40] W. R. Leo, *Techniques for Nuclear and Particle Physics Experiments.* Springer-Verlag, 1994.

[41] Y. Tsai, *Rev. Mod. Phys.*, 46:815, 1974.

[42] J. E. Spencer and H. A. Enge, *Nucl. Inst. and Meth.*, 49:181, 1967.

[43] Compiled by W. J. Cummings, *SOS Handbook.* Jlab Hall C Internal Report (unpublished), 1996.

[44] J. Arrington, PhD thesis, California Institute of Technology, 1998.

[45] R. M. Mohring, PhD thesis, University of Maryland, 1999.

[46] W. Hinton, PhD thesis, Hampton University, 2000.

[47] T. Miyoshi et al., *Submitted to Nucl. Inst. and Meth.*, 2002.

[48] K. Lan et al., *IEEE Trans. Nucl. Sci.*, 1999.

[49] C. Armstrong, *Hall C analysis engine routine flow.* Hall C internal report (unpublished), 1995.

[50] D. F. Geesaman, *Tracking in the SOS Spectromenter.* Jlab Hall C Internal Report (unpublished), 1993.

[51] C. Armstrong, *Hall C Time-of-Flight Fitting Code.* Jlab Hall C Internal Report (unpublished), 1995.

[52] K. Assamagan, D. Dutta, and P. Welch, *Hall C Matrix Element Optimization Package (CMOP).* Jlab Hall C Internal Report (unpublished), 1997.

[53] S. B. Kowalski and H. A. Enge, The ion-optical program Raytrace. *Nucl. Instr. and Meth.*, A258:407, 1987.

[54] L. Tang, C. Yan, and E. V. Hungerford, *Nucl. Inst. and Meth.*, A366:259, 1995.

[55] G. Niculescu, PhD thesis, Hampton University, 1998.

[56] H. Yamazaki et al., *Phys. Rev. C*, 52:R1157, 1995.

[57] C. J. Bebek et al., *Phys. Rev. D*, 15:594, 1977.

[58] J. Cha, PhD thesis, Hampton University, 2000.

[59] S. Ajimura et al., *Phys. Rev. Lett.*, 86:4255, 2001.

[60] L. Tang et al., First experiment on spectroscopy of Λ-hypernuclei by electroproduction at JLab. In *Proceedings of 8th Conference on Mesons and Light Nuclei, AIP Conference Proceedings 603*, page 173, Prague, Czech Republic, July 2001.

[61] T. Miyoshi et al. (HNSS Collaboration), High resolution spectroscopy of the ${}^{12}_{\Lambda}B$ hypernucleus produced by the (e,e′K$^+$) reaction, in preparation to submit to Phys. Rev. Lett., 2002.

VITA

Lulin Yuan was born in Xiangfan, China, on September 29, 1969. He received his Bachelor of Science degree in System Science in 1991 after four years of study in the Department of Physics, Beijing Normal University, Beijing, China. After that, he continued his study in the same university until he received his Master of Science degree in System Science in 1994. He worked as a Research Associate in the Institute of System Science, Chinese Academy of Sciences for two years before he came to Hampton University, Hampton, Virginia, in 1997 to pursue his Ph.D. degree in nuclear physics. He received his Ph.D. degree in August 2002. His dissertation is on the electroproduction of hypernuclei. In 2000, he was married to Xiaoyan Lin. He and his family currently reside at 214 Fieldstone Lane, #202, Newport News, VA 23602.